Universidade Federal de Goiás
Escola de Engenharia Elétrica, Mecânica e de Computação
Programa de Pós Graduação em Engenharia Mecânica

Almério José Venâncio Pains Soares Pamplona

Viscoelasticity of pipes and the effect of unsteady friction during water hammer using the Smoothed Particle Hydrodynamics (SPH) method

(Viscoelasticidade de tubulações e o efeito do atrito não estacionário durante o golpe de aríete utilizando o método de Hidrodinâmica de Partículas Suavizadas – SPH)

Goiânia
2025

UNIVERSIDADE FEDERAL DE GOIÁS
ESCOLA DE ENGENHARIA ELÉTRICA, MECÂNICA E DE COMPUTAÇÃO

TERMO DE CIÊNCIA E DE AUTORIZAÇÃO (TECA) PARA DISPONIBILIZAR VERSÕES ELETRÔNICAS DE TESES

E DISSERTAÇÕES NA BIBLIOTECA DIGITAL DA UFG

Na qualidade de titular dos direitos de autor, autorizo a Universidade Federal de Goiás (UFG) a disponibilizar, gratuitamente, por meio da Biblioteca Digital de Teses e Dissertações (BDTD/UFG), regulamentada pela Resolução CEPEC nº 832/2007, sem ressarcimento dos direitos autorais, de acordo com a Lei 9.610/98, o documento conforme permissões assinaladas abaixo, para fins de leitura, impressão e/ou download, a título de divulgação da produção científica brasileira, a partir desta data.

O conteúdo das Teses e Dissertações disponibilizado na BDTD/UFG é de responsabilidade exclusiva do autor. Ao encaminhar o produto final, o autor(a) e o(a) orientador(a) firmam o compromisso de que o trabalho não contém nenhuma violação de quaisquer direitos autorais ou outro direito de terceiros.

1. Identificação do material bibliográfico

[x] Dissertação [ ] Tese [ ] Outro*:_____

*No caso de mestrado/doutorado profissional, indique o formato do Trabalho de Conclusão de Curso, permitido no documento de área, correspondente ao programa de pós-graduação, orientado pela legislação vigente da CAPES.

Exemplos: Estudo de caso ou Revisão sistemática ou outros formatos.

2. Nome completo do autor

Almério José Venâncio Pains Soares Pamplona

3. Título do trabalho

Viscoelasticity of pipes and the effect of unsteady friction during water hammer using the Smoothed Particle Hydrodynamics (SPH) method

(*Viscoelasticidade de tubulações e o efeito do atrito não estacionário durante o golpe de aríete utilizando o método de Hidrodinâmica de Partículas Suavizadas – SPH*).

4. Informações de acesso ao documento (este campo deve ser preenchido pelo orientador)

Concorda com a liberação total do documento [x] SIM [ ] NÃO[1]

[1] Neste caso o documento será embargado por até um ano a partir da data de defesa. Após esse período, a possível disponibilização ocorrerá apenas mediante:
a) consulta ao(à) autor(a) e ao(à) orientador(a);
b) novo Termo de Ciência e de Autorização (TECA) assinado e inserido no arquivo da tese ou dissertação.
O documento não será disponibilizado durante o período de embargo.
Casos de embargo:
- Solicitação de registro de patente;
- Submissão de artigo em revista científica;
- Publicação como capítulo de livro;
- Publicação da dissertação/tese em livro.

Obs. Este termo deverá ser assinado no SEI pelo orientador e pelo autor.

Documento assinado eletronicamente por **Andreia Aoyagui Nascimento**, **Professora do Magistério Superior**, em 16/04/2025, às 16:40, conforme horário oficial de Brasília, com fundamento no § 3º do art. 4º do Decreto nº 10.543, de 13 de novembro de 2020 .

Documento assinado eletronicamente por **Almério José Venâncio Pains Soares Pamplona**, **Usuário Externo**, em 16/04/2025, às 16:50, conforme horário oficial de Brasília, com fundamento no § 3º do art. 4º do Decreto nº 10.543, de 13 de novembro de 2020 .

A autenticidade deste documento pode ser conferida no site https://sei.ufg.br/sei/controlador_externo.php?acao=documento_conferir&id_orgao_acesso_externo=0, informando o código verificador **5318025** e o código CRC **926949DE**.

Referência: Processo nº 23070.005978/2025-04 SEI nº 5318025

Almério José Venâncio Pains Soares Pamplona

Viscoelasticity of pipes and the effect of unsteady friction during water hammer using the Smoothed Particle Hydrodynamics (SPH) method

(Viscoelasticidade de tubulações e o efeito do atrito não estacionário durante o golpe de aríete utilizando o método de Hidrodinâmica de Partículas Suavizadas – SPH)

Dissertation presented to the Stricto Sensu Programa de Pós Graduação em Engenharia Mecânica at the Escola de Engenharia Elétrica, Mecânica e de Computação in the Universidade Federal de Goiás, as a partial requirement to obtain the Master's Degree in Mechanical Engineering.
Concentration Field: Fluid and Solid Dynamics.
Advisor: Andreia Aoyagui Nascimento.
Co-advisor: Joel Roberto Guimarães Vasco.

Goiânia
2025

Ficha de identificação da obra elaborada pelo autor, através do
Programa de Geração Automática do Sistema de Bibliotecas da UFG.

Pamplona, Almério José Venâncio Pains Soares
Viscoelasticity of pipes and the effect of unsteady friction during water hammer using the Smoothed Particle Hydrodynamics (SPH) method [manuscrito] : Viscoelasticidade de tubulações e o efeito do atrito não estacionário durante o golpe de aríete utilizando o método de Hidrodinâmica de Partículas Suavizadas – SPH / Almério José Venâncio Pains Soares Pamplona. - 2025.
CXLIII, 143 f.

Orientador: Prof. Andreia Aoyagui Nascimento; co-orientador Joel Roberto Guimarães Vasco.
Dissertação (Mestrado) - Universidade Federal de Goiás, Escola de Engenharia Elétrica, Mecânica e de Computação (EMC), Programa de Pós-graduação em Engenharia Mecânica, Goiânia, 2025.
Bibliografia. Apêndice.
Inclui siglas, símbolos, lista de figuras, lista de tabelas.

1. Hydraulic Transient (Transiente Hidráulico). 2. Transient Friction (Atrito não estacionário). 3. Viscoelasticity Effect (Efeito Viscoelástico). 4. Smoothed Particle Hydrodynamics (Hidrodinâmica de Partículas Suavizadas). I. Nascimento, Andreia Aoyagui, orient. II. Título.

CDU 621

UNIVERSIDADE FEDERAL DE GOIÁS

ESCOLA DE ENGENHARIA ELÉTRICA, MECÂNICA E DE COMPUTAÇÃO

ATA DE DEFESA DE DISSERTAÇÃO

Ata nº **03** da sessão de Defesa de Dissertação de **Almério José Venâncio Pains Soares Pamplona**, que confere o título de Mestre em **Engenharia Mecânica**, na área de concentração em **Dinâmica dos Fluidos e dos Sólidos**.

Aos **vinte e oito de março de dois mil e vinte e cinco**, a partir das **15h00min**, **de forma virtual através da plataforma Google Meet**, realizou-se a sessão pública de Defesa de Dissertação intitulada **"Viscoelasticity of pipes and the effect of unsteady friction during water hammer using the Smoothed Particle Hydrodynamics (SPH) method"** (*Viscoelasticidade de tubulações e o efeito do atrito não estacionário durante o golpe de aríete utilizando o método de Hidrodinâmica de Partículas Suavizadas – SPH*) . Os trabalhos foram instalados pela Orientadora, Professora Doutora **Andreia Aoyagui Nascimento (EMC/UFG)** com a participação dos demais membros da Banca Examinadora: Professor Doutor **Aristeu da Silveira Neto (FEMEC/UFU)**, Professor Doutor **Joel Roberto Guimarães Vasco (EECA/UFG)**; membro titular externo, Professor Doutor **Alexandre Kepler Soares (ENC/UNB)**. Durante a arguição os membros da banca **não fizeram** sugestão de alteração do título do trabalho. A Banca Examinadora reuniu-se em sessão secreta a fim de concluir o julgamento da Dissertação, tendo sido o candidato **aprovado** pelos seus membros. Proclamados os resultados pela Professora Doutora **Andreia Aoyagui Nascimento**, Presidente da Banca Examinadora, foram encerrados os trabalhos e, para constar, lavrou-se a presente ata que é assinada pelos Membros da Banca Examinadora, aos **vinte e oito de março de dois mil e vinte e cinco.**

TÍTULO SUGERIDO PELA BANCA

Documento assinado eletronicamente por **Andreia Aoyagui Nascimento**, **Professora do Magistério Superior**, em 16/04/2025, às 14:53, conforme horário oficial de Brasília, com fundamento no § 3º do art. 4º do Decreto nº 10.543, de 13 de novembro de 2020 .

Documento assinado eletronicamente por **Aristeu da Silveira Neto**, **Usuário Externo**, em 16/04/2025, às 16:57, conforme horário oficial de Brasília, com fundamento no § 3º do art. 4º do Decreto nº 10.543, de 13 de novembro de 2020.

Documento assinado eletronicamente por **Joel Roberto Guimaraes Vasco**, **Professor do Magistério Superior**, em 16/04/2025, às 18:25, conforme horário oficial de Brasília, com fundamento no § 3º do art. 4º do Decreto nº 10.543, de 13 de novembro de 2020 .

Documento assinado eletronicamente por **Demostenes Ferreira Filho**, **Coordenador de Curso**, em 22/04/2025, às 12:25, conforme horário oficial de Brasília, com fundamento no § 3º do art. 4º do Decreto nº 10.543, de 13 de novembro de 2020 .

A autenticidade deste documento pode ser conferida no site https://sei.ufg.br/sei/controlador_externo.php?acao=documento_conferir&id_orgao_acesso_externo=0, informando o código verificador **5317432** e o código CRC **E4DE2133**.

Referência: Processo nº 23070.005978/2025-04 SEI nº 5317432

ACKNOWLEDGEMENTS

In this brief space, I would like to express my gratitude to everyone who has helped me—directly and indirectly—on my journey, enabling me to complete this work and reach my current position. Although this is a small gesture compared to what they have done for me, I hope to repay their kindness someday.

First, I want to thank God for the life and opportunities He has provided me. Second, I extend my heartfelt appreciation to my family—Suelma, Gilvan, and Ariston—for their unwavering support of all my projects, no matter how complicated or demanding.

I am also grateful to my friend Arlam for the countless hours we spent discussing and analyzing the models, the mathematical foundations, and various abstract aspects of the project. A special thank you goes to my friends Gabriel and Vitor for their assistance with equipment for running simulations and for their support during my travels to conferences.

I want to thank my advisors, Andreia and Joel, for believing in both me and the project and for their invaluable support through all the challenges I faced. I appreciate the Postgraduate Program in Mechanical Engineering for its academic and financial assistance.

Finally, I would like to extend my gratitude to those I may not have mentioned here—there are many who have played significant roles in my life and who continue to do so.

"The greatest enemy of knowledge is not ignorance, it is the illusion of knowledge."
(Stephen Hawking)

RESUMO

Um golpe de aríete é um rápido aumento de pressão em tubulações causado por mudanças repentinas na velocidade do escoamento, como fechamento de válvulas. Esses surtos podem resultar em falhas graves em sistemas de transporte de fluidos caso não controlados. Métodos tradicionais, como o Método das Características (MOC), ajudam a prever o golpe de aríete, mas enfrentam desafios, incluindo restrições quanto ao número de Courant e problemas de balanço de massa e momentum em geometrias complexas. O método Smoothed Particle Hydrodynamics (SPH) oferece uma alternativa promissora, permitindo modelagem sem malha e flexibilidade para simular esses transientes hidráulicos. Este estudo emprega um código *in-house* baseado no método Corrected Smoothed Particle Hydrodynamics (CSPH) que usa renormalização da função kernel para tratamento de fronteiras. Modelos de atrito transiente são incluídos para aumentar a precisão na modelagem do golpe de aríete em tubos metálicos. Para tubos plásticos, essa abordagem é combinada com um modelo viscoelástico baseado num modelo mecânico de Kelvin-Voigt. A configuração numérica consiste em um sistema reservatório-tubo-válvula para validar os métodos baseados em SPH. As simulações avaliam os efeitos do atrito transiente e da viscoelasticidade na propagação de ondas de pressão. Utiliza-se a Metodologia de Superfície de Resposta (RSM) para identificar configurações ótimas e como parâmetros numéricos afetam as simulações. Os resultados mostram que o CSPH captura efetivamente a taxa de amortecimento de pressão da onda, mas falha em estimar a velocidade da onda devido à perda de momentum dada a redução da massa específica causada pela renormalização. Para corrigir isso, introduz-se o CSPH Compensado (CCSPH), que simula com precisão as taxas de amortecimento de ondas de pressão, celeridade da onda e formas da onda, tanto em tubos elásticos quanto viscoelásticos. Também validou-se um código interno do Método de Características (MOC) para comparação com o CCSPH. Ambos os métodos demonstraram precisão e eficiência computacional semelhantes.

Palavras-chaves: Transitório Hidráulico; Atrito Transitório; Viscoelasticidade; Smoothed Particle Hydrodynamics.

ABSTRACT

A water hammer is a rapid pressure surge in pipelines caused by sudden flow velocity changes, such as when valves close. These surges can result in serious failures in fluid transport systems if not controlled. Traditional methods, like the Method of Characteristics (MOC), help predict water hammer but face challenges, including Courant number constraints and mass and momentum balance issues in complex geometries. The Smoothed Particle Hydrodynamics (SPH) method offers a promising alternative, enabling mesh-free modeling and improved flexibility for simulating these hydraulic transients. This study employs an in-house code based on the Corrected Smoothed Particle Hydrodynamics (CSPH) method that uses kernel function renormalization for boundary treatment. Unsteady friction models are included to enhance accuracy in modeling water-hammer in metal pipes. For plastic pipes, this approach is combined with a mechanical Kelvin-Voigt-based viscoelastic model. The numerical setup consists of a reservoir-tube-valve system to validate the SPH-based methods. Simulations assess the effects of unsteady friction and viscoelasticity on pressure wave propagation. Response Surface Methodology (RSM) is used to identify optimal configurations and how numerical parameters affect the simulations. Results show that CSPH effectively captures the wave pressure damping ratio but fails to estimate wave speed due to momentum loss from density reductions in renormalization. To correct this, one introduces the Compensated CSPH (CCSPH), which accurately simulates pressure wave damping ratios, wave speeds, and waveforms in elastic and viscoelastic pipes. One also validated an in-house Method of Characteristics (MOC) code for comparison with CCSPH. Both methods demonstrated similar accuracy and computational efficiency.

Keywords: Water Hammer; Transient Friction; Viscoelasticity; Smoothed Particle Hydrodynamics.

LIST OF FIGURES

LIST OF TABLES

LIST OF ABBREVIATIONS AND ACRONYMS

CLL Cell-linked List

CSPH Corrected Smoothed Particles Hydrodynamics

CSPH-R CSPH implemented with the unsteady friction model as per Ramos et al. (2004)

CSPH-V CSPH implemented with the unsteady friction model as per Vitkovsky et al. (2000)

CSPH-VH CSPH implemented with the unsteady friction model as per Vardy and Hwang (1993)

CSPH-VISC CSPH implemented with the viscoelastic model of Covas et al. (2005)

CSPH-R-VISC CSPH implemented with the unsteady friction model as per Ramos et al. (2004) and the viscoelastic model of Covas et al. (2005)

CSPH-V-VISC CSPH implemented with the unsteady friction model as per Vitkovsky et al. (2000) and the viscoelastic model of Covas et al. (2005)

CSPH-VH-VISC CSPH implemented with the unsteady friction model as per Vardy and Hwang (1993) and the viscoelastic model of Covas et al. (2005)

CCSPH Compensated Corrected Smoothed Particles Hydrodynamics

CCSPH-R CCSPH implemented with the unsteady friction model as per Ramos et al. (2004)

CCSPH-V CCSPH implemented with the unsteady friction model as per Vitkovsky et al. (2000)

CCSPH-VH CCSPH implemented with the unsteady friction model as per Vardy and Hwang (1993)

CCSPH-VISC CCSPH implemented with the viscoelastic model of Covas et al. (2005)

CCSPH-R-VISC CCSPH implemented with the unsteady friction model as per Ramos et al. (2004) and the viscoelastic model of Covas et al. (2005)

CCSPH-V-VISC CCSPH implemented with the unsteady friction model as per Vitkovsky et al. (2000) and the viscoelastic model of Covas et al. (2005)

CCSPH-VH-VISC CCSPH implemented with the unsteady friction model as per Vardy and Hwang (1993) and the viscoelastic model of Covas et al. (2005)

CWSM Corrected Wave Speed Measurement

DFT Discrete Fourier Transform

FD Finite Difference

FFT Fast Fourier Transform

FV Finite Volume

GSPH Ghost Smoothed Particles Hydrodynamics

LBM Lattice Boltzmann Method

MASE Mean Absolute Scaled Error

MOC Method of Characteristics

MOC-R MOC implemented with the unsteady friction model as per Ramos et al. (2004)

MOC-V MOC implemented with the unsteady friction model as per Vitkovsky et al. (2000)

MOC-VH MOC implemented with the unsteady friction model as per Vardy and Hwang (1993)

MOC-VISC MOC implemented with the viscoelastic model of Covas et al. (2005)

MOC-R-VISC MOC implemented with the unsteady friction model as per Ramos et al. (2004) and the viscoelastic model of Covas et al. (2005)

MOC-V-VISC MOC implemented with the unsteady friction model as per Vitkovsky et al. (2000) and the viscoelastic model of Covas et al. (2005)

MOC-VH-VISC MOC implemented with the unsteady friction model as per Vardy and Hwang (1993) and the viscoelastic model of Covas et al. (2005)

NRMSE Normalized Root Mean Square Error

PE Polyethylene

PVC Polyvinyl Chloride

ODE Ordinary Differential Equation

PDE	Partial Differential Equation
SPH	Smoothed Particles Hydrodynamics
SPH-R	SPH implemented with the unsteady friction model as per Ramos et al. (2004)
SPH-V	SPH implemented with the unsteady friction model as per Vitkovsky et al. (2000)
SPH-VH	SPH implemented with the unsteady friction model as per Vardy and Hwang (1993)
SPH-VISC	SPH implemented with the viscoelastic model of Covas et al. (2005)
SPH-R-VISC	SPH implemented with the unsteady friction model as per Ramos et al. (2004) and the viscoelastic model of Covas et al. (2005)
SPH-V-VISC	SPH implemented with the unsteady friction model as per Vitkovsky et al. (2000) and the viscoelastic model of Covas et al. (2005)
SPH-VH-VISC	SPH implemented with the unsteady friction model as per Vardy and Hwang (1993) and the viscoelastic model of Covas et al. (2005)
RMSE	Root Mean Square Error
RMSPE	Root Mean Square Percentual Error
RSM	Response Surface Methodology
WDS	Water Distribution System
WSM	Wave Speed Measurement

LIST OF SYMBOLS

a	wave speed
$\langle a \rangle$	estimated wave speed
b	viscous layer thickness
b_p	pipe-wall thickness
B_m	constant of the unsteady friction model of Trikha (1975)
B_p	MOC coefficient that encapsulates numerical terms for $+a$
B_{p1}	MOC coefficient that composes the term B_p
B_m	MOC coefficient that encapsulates numerical terms for $-a$
B_{m1}	MOC coefficient that composes the term B_m
B_{MOC}	matrix with the main coefficients of the Water Hammer PDE, h and u_1
$\mathbb{C}$	complex field or domain
c_{RG}	Runge-Kutta linear coefficient
C_0	consistency of zero order
C_1	consistency of first order
C_2	consistency of second order
C^*	dimensionless coefficient for the unsteady model of Vardy and Brown (2003)
C_h	hydraulic capacitance
C_k	one half of the kinetic energy of the fluid to the potential energy stored in the fluid
C_p	MOC coefficient that encapsulates numerical terms for $+a$
C_{p1}	MOC coefficient relative to the unsteady friction that composes the term C_p
C_{p2}	MOC coefficient relative to the viscoelasticity that composes the term C_p

C_m	MOC coefficient that encapsulates numerical terms for $-a$
C_{p1}	MOC coefficient relative to the unsteady friction that composes the term C_m
C_{p2}	MOC coefficient relative to the viscoelasticity that composes the term C_m
C_{or}	coefficient of discharge
C_t	characterizes the valve-closure
C_0^∞	compactly supported set of smooth functions
d	pipe diameter
d_{or}	orifice diameter
$\mathcal{D}$	a subset in the complex domain $\mathbb{C}$
$\mathcal{D}$	bounded linear function
$\mathbf{e}_j$	j-th unit vector that compose a vector space basis in Eulerian frame
e	specific internal energy
$\mathbf{E}_j$	j-th unit vector that compose a vector space basis in Lagrangian frame
E	total energy
f	arbitrary variable or function in Eulerian Frame
$\overline{f}$	average value of a function
$\langle f_0 \rangle$	estimated frequency by interpolation
$\left\langle \overline{f}_0 \right\rangle$	average of estimated frequency by interpolation
f_{ba}	arbitrary variable difference relative to particles b and a
f_s	signal acquisition frequency
$\mathbf{f}_{external}$	external force
f_f	signal frequency
f_{max}	maximum value of a function
f_{min}	minimum value of a function
f_u	unsteady friction coefficient

$f_{u,L}$	unsteady friction coefficient when unsteady shear stress reaches its maximum value
$\mathbf{f}_W$	weight force
F	arbitrary variable or function in Lagrangian Frame, or a general PDE
$\mathbf{F}_{MOC}$	vector with the unsteady friction and viscoelastic components of the Water Hammer PDE
F_p	general PDE relative to $\partial u/\partial x$
F_q	general PDE relative to $\partial u/\partial t$
F_R	lumped boundary resistance due to wall shear and any other constriction
F_R^*	dimensionless lumped boundary resistance
F_τ	hoop stress difference relative to the initial instant
g	gravitational acceleration
G	relaxation modulus or Young modulus
G_∞	relaxation modulus infimum value
G_{dB}	discrete Fourier transformed signal in decibels
$\mathbf{g}$	gravitational acceleration field
h	pressure head or piezometric pressure
h_{ba}	relative piezometric head between particles b and a
h^0	initial pressure or piezometric head
$h_{reservoir}$	piezometric head at the interface between the reservoir and the pipe
h_s	smoothing length
$h_{s,ab}$	smoothing length average value from particles a and b
h_{valve}	piezometric head at the interface between the valve and the pipe
H_w	arbitrary window function
i	imaginary number, $i = \sqrt{-1}$
$\mathbf{J}^\Gamma$	local entropy flux
k_{RG}	Runge-Kutta component

K	unsteady friction coefficient of the models by Brunone and Golia (1990) and Vitkovsky et al. (2000)
K_1	unsteady friction coefficient relative to the local acceleration of the model by Ramos et al. (2004)
K_2	unsteady friction coefficient relative to the advection acceleration of the model by Ramos et al. (2004)
K_c	compact set
K_s	one-dimensional steady-state resistance coefficient
K_t	correcting coefficient to measure the additional unsteady effects on boundary resistance and momentum flux of absolute local velocity
K_u	unsteady flow coefficient of boundary resistance and momentum flux of absolute local velocity
L	pipe length
m	mass
M	order of a distribution
M_f	total number of discrete points of a function after zero padding
$\mathbf{M}_j$	j-th moment of the kernel
$\mathbf{n}$	unit normal vector
$\mathbb{N}$	natural field or domain
N	order of a distribution
$\mathcal{N}_a$	neighborhood set of the particle a.
N_f	total number of discrete points of a function
N_{neigh}	number of neighbor particles
N_{part}	total number of particles
$\mathcal{N}_{Voigt}$	set of Voigt elements
N_w	length of the windowed signal
$\mathcal{O}$	order of an approximation or order of computational operations (big O)
p	pressure

p^*	dimensionless pressure
$\overline{p}$	pressure average value
$\widehat{p}$	Fourier transformed value of pressure
p_d	probability of having an entirely randomly or a quasi-ordered distribution of particles
p_f	target peak of a windowed signal in the frequency domain
q	heat
r	pipe cross-section radius
r_s	normalized distance of a neighbor particle within a support domain
$\mathbb{R}$	real field or domain
$\mathcal{R}_+$	subset of the real field with only positive values
R	pipe initial radius value at a point x_1
R_h	hydraulic radius
R_θ	counterclockwise linear rotation transformation
Re	Reynolds number
s	pipe surface area
s_n	pipe cross-section surface area perpendicular to the pipe's center axis
s_l	pipe lateral surface area
s_{MOC}	parameter for MOC parametrization
t	time
t_0	initial instant
t^*	instant immediately preceding t
$t^{'}$	instant of time defined as $t - \flat$
t_c	valve closing time
t_d	diffusion time
t_p	elapsed time since the beginning of the unsteadiness

t_w	water hammer time scale
T_b	instantaneous temperature at the boundaries
T_m	constant of the unsteady friction model of Trikha (1975)
$\boldsymbol{u}$	velocity field
u_j	j-th velocity field component
u_0	velocity temporal mean value
$u^{'}$	velocity temporal fluctuation value
u^*	dimensionless velocity temporal mean value
$u^{*'}$	dimensionless velocity temporal fluctuation value
u_j^t	j-th velocity field component at instant t
$\widehat{u}_j$	Fourier transformed value of the j-th velocity field component
$\overline{u}_j^0$	j-th cross-section average velocity field component at the steady-state
u_{ba}	relative velocity between particles b and a
$\mathbf{U}_{MOC}$	vector with the main components of the Water Hammer PDE, h and u_1
$u_{i,reservoir}$	velocity at the interface between the reservoir and the pipe
$u_{1,valve}$	velocity at the interface between the valve and the pipe
V	volume
$\boldsymbol{x}$	position vector in Eulerian frame
x_j	j-th position vector component in Eulerian frame or RSM independent variables
x_{ab}	distance vector between particles a and b
x_j^*	j-th dimensionless position vector component in Eulerian frame
$\mathbf{X}$	position vector in Lagrangian frame
y	response variable
Y_m	m-th component of the unsteady friction model of Trikha (1975)
X_j	j-th position vector component in Lagrangian frame

w	work
w_d	distribution
$\mathbf{w}_j$	j-th unit vector that compose a vector space basis in Eulerian frame
W	smoothing or kernel function
α_d	smoothing function coefficient for a dimension d
α_f	nearest discrete function value in a signal windowed peak in frequency domain
α_p	pipe-wall constrain coefficient
α_Π	artificial viscosity coefficient to smoothing numerical perturbations
β_j	j-th RSM model coefficient
β_f	nearest discrete function value in a signal windowed peak in frequency domain
β_{or}	diameter ratio of orifice diameter to pipe diameter
β^Γ	arbitrary positive coefficient
β_Π	artificial viscosity coefficient to avoid unrealistic particles penetration
γ	specific entropy
γ_f	nearest discrete function value in a signal windowed peak in frequency domain
δ	infinitesimal value of some variable
δ_D	Dirac function
ϵ	internal pipe wall's absolute roughness or random error
ε	logarithmic radius strain
ε_0	elastic strain
ε_r	retarded strain
ζ	bulk modulus
ζ_b	bulk viscosity
θ	pipe inclination angle

ι	creep compliance
ι_0	elastic creep compliance
κ	exponential coefficient of the coefficient C^*
κ_s	multiple of the smoothing length to define the support length of a support domain
λ	quasi-stationary friction factor
μ	dynamic viscosity
ν	kinematic viscosity
ν_{lam}	laminar kinematic viscosity
ν_w	kinematic viscosity at the wall
ρ	density
$\overline{\rho}_{ab}$	density average value from particles a and b
ϱ	dimensionless parameter to assess the applicability of asymmetric and quasi-steady turbulence models
ϱ_{MOC}	MOC coefficient relative the viscoelasticity
σ_Γ	local rate of entropy production
τ	shear stress
τ_0	constant shear stress
τ_h	hoop stress
τ_s	quasi-stationary shear stress or friction
τ_t	unsteady shear stress or friction
$\tau_{t,L}$	maximum unsteady shear stress or friction
ϕ_e	function that indicates the error relative to the distribution of the particles
ϕ_{or}	valve maneuvering function
ψ	dimensionless time
ψ_d	elements of $\mathcal{D}$ with support

ψ_L	dimensionless instant when he unsteady shear stress reaches its maximum value
ω	oscillation frequency, $\omega = 2\,\pi\,f_f$
$\widehat{\omega}_0$	frequencies of a discretized sinusoidal signal
$\widehat{\omega}_0^*$	least-square estimated frequency
Γ	total entropy
Γ_e	total entropy exchange with the surroundings of a control volume
Γ_i	total entropy within a control volume
Δt	time step
Δx	spatial step
Θ_H	high-frequency coefficient
Θ_L	low-frequency coefficient
Π_{ab}	artificial viscosity in SPH
Υ	resistance coefficient
Φ	weighting function that accounts for prior velocity variations
Ω	arbitrary manifold or finite volume or a non-empty open set
Ω_s	kernel support
$\flat$	arbitrary instant

TABLE OF CONTENTS

1 INTRODUCTION

Water hammer is a hydraulic phenomenon characterized by rapid pressure surges in pipelines, typically caused by sudden changes in flow velocity due to valve closure or sudden stops in pump operation. During hydraulic transient, the kinetic energy near the flow interruption decreases to zero, converting it mainly into a pressure potential energy. This sudden increase in pressure potential energy can lead to pipe rupture. Additionally, the overpressure propagates as a wave along the pipeline. These pressure surges, if not properly managed, can lead to damaging effects on pipeline systems and equipment (JUNG et al., 2007).

The study and understanding of water hammers have deep historical roots, dating back to ancient civilizations that developed complex water conveyance systems for irrigation and domestic use (GHIDAOUI et al., 2005). With the advent of the scientific age and the mathematical advancements, the understanding of fluid flow, including water hammer, underwent significant theoretical abstraction, leading to advancements in hydraulic engineering. The development of high-speed digital computers marked another notable transformation in the study and application of fluid engineering principles (GHIDAOUI et al., 2005).

The Industrial Revolution and the subsequent increase in urbanization and industrialization further emphasized the importance of understanding and controlling transient fluid flows, including water hammer. The development of hydroelectric power generation and the construction of long pipelines for fluid transport highlighted the need for accurate modeling and prediction of hydraulic transients (GHIDAOUI et al., 2005).

Another aspect is the risks posed by rapid pressure changes. Failures in managing water hammers can lead to catastrophic consequences, as evidenced by historical incidents such as the burst penstock of the Oigawa Power Station in Japan or the collapse of the Lütschinen Hydroelectric Power Plant penstock in Switzerland (CHAUDHRY, 2014). As a result, engineers and researchers have continuously strived to develop better theoretical and numerical models to predict and mitigate the effects of water hammer in various systems, from power generation to water distribution networks.

Unsteady friction (BRUNONE et al., 1991a; BRUNONE et al., 1991b; VARDY; HWANG, 1993; VITKOVSKY et al., 2000; RAMOS et al., 2004) and viscoelastic (RIEUTORD; BLANCHARD, 1979; RIANDE et al., 2000; SHAW; MACKNIGHT, 2005; COVAS et al., 2004; COVAS et al., 2005; SOARES et al., 2008) models are products of the efforts to advance fluid dynamics theory, which enhanced the ability to model and simulate water hammer phenomena. These models consider the complex interactions between fluid flow,

pipe material properties, and transient effects, leading to more accurate predictions of pressure surges in pipelines.

However, theoretical analysis has limitations, which forced numerical advancements in hydraulic transient analysis. They have significantly contributed to the comprehension and prediction of water hammer phenomena. In this scenario, the Method of Characteristics (MOC) has been a key traditional approach due to its accuracy, simplicity, numerical efficiency, and programming simplicity (GHIDAOUI et al., 2005). However, the MOC has limitations, such as the limited Courant number to the unity value, non-assured mass and momentum conservation, and simulation inaccuracy of variable cross-sectional pipelines. Additionally, the MOC can be computationally intensive for implicit schemes (PAL et al., 2021).

An alternative numerical method, the Smoothed Particle Hydrodynamics (SPH) method, has been developed to address limitations in fluid dynamics simulations. SPH is a mesh-free Lagrangian method known for its ability to handle complex geometries and free surfaces. It has been successfully used to model fluid flows, solids with large deformations (LIU et al., 2003a), and pore-scale modeling for diffusion and dispersion (ZHU; FOX, 2001; ZHU; FOX, 2002). SPH has shown broad applicability in various fields, including astrophysics, coastal and offshore engineering, solid mechanics, biology, and hydraulic and naval engineering (SZEWC et al., 2012; PALYANOV et al., 2016; SHUTOV; KLYUCHANTSEV, 2019; ALTOMARE et al., 2022; XU et al., 2023). Additionally, SPH has advantages over traditional methods when applied to water hammer problems.

One advantage of SPH is its programming simplicity to couple unsteady friction and viscoelastic models. The unsteady friction model is added directly to the continuity equation without significantly changing the unsteady friction discretized form. The viscoelastic model is added directly to the momentum balance and requires one old time-step saved data to update the current time-step. SPH also offers better scalability and efficiency for simulating large-scale systems than traditional mesh-based methods due to its Langragian nature (XU et al., 2023). Additionally, SPH can easily handle free surface flows, making it suitable for modeling scenarios where air entrainment or cavitation may occur. The SPH method conserves mass and momentum and has a broader applicability range for Courant numbers (PAN et al., 2022).

SPH has already shown accurate results for scenarios with quasi-stationary (HOU et al., 2012; JUNIOR et al., 2020) and unsteady friction (PAN et al., 2022). Pal et al. (2021) mentioned that SPH had some limitations regarding complex boundary conditions such as nodal junctions, surge tanks or air chambers, and pumps. However, Song et al. (2023) extended the SPH model to attend to water distribution systems, making the method suitable for several hydraulic transient scenarios.

1.1 Justification

The unstoppable increase in cities and industries growth, accompanied by the increasing complexity of fluid systems distribution and the safety risk that hydraulic transients pose to these systems, makes the accurate modeling and prediction of hydraulic transients unprecedented. Several theoretical and numerical models have been proposed to address this necessity. However, there is still room for improvement, especially in the case of numerical schemes, when it comes to accuracy and problem complexity.

The SPH method has shown potential in various engineering, astronomical, and biological fields, including the water hammer phenomena. It successfully included unsteady friction models and extended its applicability to water distribution systems instead of reservoir-pipe-valve schemes only. Nevertheless, to the author's knowledge, there is still no work on the viscoelasticity aspects of a polymer pipeline that uses the SPH method combined with a viscoelastic model. Hence, it is interesting to utilize the advantages of SPH, such as the mesh-less nature, to develop a numerical scheme that accounts for the viscoelastic effects of pipelines in hydraulic transients.

1.2 Objectives

The current work's general goal is to apply the SPH method to simulate water hammer problems, particularly those involving a reservoir-tube-valve configuration, and evaluate the SPH aspects within these problems.

Specifically, by combining unsteady friction models and viscoelastic models, the one seeks to enhance the accuracy of the simulations and validate the numerical results with experimental data. Additionally, one intends to perform an extensive analysis of critical parameters in the SPH method using response surface statistical methods, aiming to further improve the understanding and predictive capabilities of water hammer phenomena.

2 LITERATURE REVIEW

This section aims to provide a concise historical review of the development of hydraulic transients or water hammers, along with a discussion of the most noteworthy computational fluid dynamics studies used to investigate the issue. The primary objective of this review is to identify the critical variables and conditions associated with hydraulic transients.

Menabrea (1858) and Michaud (1878) were the first ones to study the water hammer phenomenon. Michaud (1878) examined the design and use of air chambers and safety valves to mitigate the water hammer in hydrogeneration plants. Later, Weston (1885) and Carpenter (1893) performed experiments to develop an expression relating pressure and velocity. However, they did not succeed due to the use of short pipelines.

Frizell (1898) and Joukowski (1898) successfully and independently found

$$\Delta p = \pm \rho \, a \, \Delta \overline{u}_1 \tag{2.1}$$

or

$$\Delta h = \pm \frac{a}{g} \, \Delta \overline{u}_1 \tag{2.2}$$

by examining experimental results performed in long pipelines, varying from 305 m to 9.45 km with relatively small diameters ($L \gg d$). Note that a is the acoustic wave speed, $p = \rho \, g \, (h - z)$ is the static pressure, z is the elevation of the pipe centerline from a given datum, h is the pressure head, ρ is the density, $\overline{u}_1$ is the cross-sectional average velocity, and g is the gravitational acceleration. Δ represents the quantity difference, for instance $\Delta p = p_{max} - p_{reservoir}$, where p_{max} is the maximum static pressure and $p_{reservoir}$ is the static pressure at the reservoir. Furthermore, the positive sign indicates a flow moving downstream, while the negative associates a flow toward upstream.

Frizell (1898) researched the impact of branch lines, wave reflections, and successive waves on speed regulation. In a separate study, Joukowski (1898) explored the propagation of pressure waves in pipes and the reflection of waves from the open end of a branch. He investigated the usage of air chambers, surge tanks, and safety valves to manage water hammer pressures. Additionally, Joukowski (1898) determined that the maximum pressure rise occurred for closing times $t_c \leq 2L/a$, with L as the pipeline's length.

Later, Allievi (1903), Allievi (1909) formalized a general theory for hydraulic transients using the balance equations, showing in his work that the advective term of the momentum equation is negligible relative to the transient one. Furthermore, Allievi

(1903), Allievi (1909) proved that the maximum pressure does not exceed two times the static head, $h \leq 2\,h^0$. He also related the closure time with the maximum pressure by introducing two parameters to characterize pipelines and valve behavior,

$$C_k = \frac{a\,\overline{u}_1^0}{2\,g\,h^0} \tag{2.3}$$

and

$$C_t = \frac{a\,t_c}{2\,L} \tag{2.4}$$

where $\overline{u}_1^0$ is the cross-section average velocity at the steady-state, C_k represents one half of the kinetic energy of the fluid to the potential energy stored in the fluid and the pipe walls at pressure head h^0, while C_t characterizes the valve-closure.

Longer, faster, and more complex pipelines emerged due to the fossil fuel in the industry. As a result, refinements in the theory came up. Jaeger (1933) applied the basis from Allievi (1903) in compound pipelines. Rich (1945) applied Laplace-Mellin transformations on the balance equations, facilitating the interpretation of a wider range of operations modes, such as branched-conduit problems. Parmakian (1963) compiled the hydraulic transient developments in his book, including the graphical analysis method. Streeter and Lai (1963), Streeter and Wylie (1967), and Chaudhry (1987) worked on more refinements. Their combined efforts have resulted in the classical mass and momentum balance equations for one-dimensional water hammer flows:

$$\frac{\partial h}{\partial t} + \frac{a^2}{g}\frac{\partial u_1}{\partial x_1} = 0, \tag{2.5}$$

$$\frac{\partial u_1}{\partial t} + g\,\frac{\partial h}{\partial x_1} + \frac{4}{\rho\,d}\tau = 0, \tag{2.6}$$

where τ is the shear stress at the pipe wall, d is the pipe internal diameter, x_1 is the spatial coordinate along the pipeline, and t is the temporal coordinate. The conditions to obtain Eq. (2.5) and (2.6) are a slightly compressible one-dimensional fluid flow in a pipeline with linearly elastic walls, uniform pressure at the end sections of the control volume, negligible radial velocity due to radial expansion and contraction, and negligible advective and slope terms. Furthermore, the density and cross-section area variations are indirectly considered by assuming the wave velocity a to have a finite value.

The first application of the shear stress term was as the quasi-stationary form. Schönfeld (1949) applied a Heaviside and a Fourier transformations on the time component of the one-dimensional balance equations on tubes with hydraulic transient, considering a flow resistance. Schönfeld (1949) approximated the transformed solution, finding a simple

equation, in which the resistance depends on the instantaneous acceleration. Daily et al. (1956) used Schönfeld's result as the base for their classical empirical transient friction model, which depends on the coefficient K, a measure of deviations, due to unsteadiness, of the wall shear momentum flux. This remark is supported by the extended thermodynamics approach used by Axworthy et al. (2000).

Examining unsteady wall friction through experimental data reveals inconsistencies in the behavior of friction coefficients K during accelerating and decelerating flows. Early findings suggested that unsteady wall friction decreased in decelerating flows (DAILY et al., 1956), contrary to later findings by Shuy (1997), who observed an increase. That spurred discussions, particularly by Vardy and Brown (1997), who introduced the time scale hypothesis to explain these variances by considering the duration of experimental conditions. The stability analysis of Ghidaoui and Kolyshkin (2001) concurs with the time scale hypothesis. Moreover, the stability analysis shows that, while other experiments belong to the stable domain, the experiments of Shuy (1997) belong to the unstable domain.

The scale hypothesis has its fundaments on the possibility of deriving Daily et al. (1956)'s proposed model from unsteady pipe flow with constant acceleration (VARDY; BROWN, 1997). Then, the constant acceleration model is approximately valid for problems with time-dependent acceleration, provided that the time scale of the transient event greatly exceeds the rising time, which is a measure of time required for the vorticity diffusion through the shear layer ($L/d \gg T_d$). This condition ensures sufficient mixing such that the acceleration history pattern is destroyed, and only the instantaneous acceleration significantly affects the wall shear stress (GHIDAOUI et al., 2005).

Additionally, Axworthy et al. (2000) demonstrated that Daily et al. (1956)'s proposed model complies with the second law of thermodynamics as per the theory of extended irreversible thermodynamics. That holds for scenarios involving significant fast transients, where the time scale is notably shorter than the radial diffusion time scale of vorticity. During this brief time scale, the turbulence strength and structure remain unchanged, resulting in no additional acceleration history being developed aside from instantaneous acceleration.

The efforts to refine unsteady friction models have focused on accommodating both rapid and gradual transient conditions. Brunone et al. (1991b) added the Coriolis correction coefficient to the energy balance equation for water hammer and defined a constitutive equation for the new term. Vitkovsky et al. (2000) and Ramos et al. (2004) refined Brunone et al. (1991b)'s model. The Coriolis correction coefficient added significant correction for unsteady friction when the flow is accelerated and small correction when the flow is decelerated (GHIDAOUI et al., 2005).

The constitutive equation in the Coriolis correction coefficient depends on a constant

named K in the models proposed by Brunone et al. (1991b) and Vitkovsky et al. (2000), and K became two constants, K_1 and K_2, in the model proposed by Ramos et al. (2004). Brunone et al. (1991b) proposed an empirical method to estimate K by fitting the decay of measured pressure head history. Vardy and Brown (1997) derived a theoretically-based expression for determining K, which was also used by Ramos et al. (2004) to estimate K_1, and K_2. However, the reliability of the expression introduced by Vardy and Brown (1997) is based on the steady-state turbulence models to represent unsteady turbulence (GHIDAOUI et al., 2005).

Zielke (1968) applied the Laplace transformation on the axial components of Navier-Stokes equations instead of what Schönfeld (1949) did, implementing the Fourier transformation on the time component. As a result, Zielke (1968) derived a wall shear expression for unsteady laminar flow, which depends on the velocity profile history weighted by a function in an integral convolution. Zielke (1968) proposed an expression for the weighting function, but it had a high computational cost. Trikha (1975) proposed a three-exponential-terms approximation, reducing the memory consumption and the computational time.

The model proposed by Zielke (1968) is based on a fully developed flow, in which the advective term is negligible and the velocity profile remains axisymmetric during the transient. Vardy and Hwang (1993) extended Zielke (1968)'s model to a low Reynolds number turbulent water hammer flows in smooth pipes. Vardy and Brown (1995) generalized the model for high and low Reynolds numbers, as well as laminar flow. Vardy and Brown (2003) later refined their model by assuming a linear turbulent kinematic viscosity within the wall shear layer, which becomes uniform in the core region, and by considering the turbulent eddy viscosity to be time-variant.

Vardy and Brown (1995) demonstrated that when the acceleration varies slowly, their model closely approximates instantaneous acceleration model within the relevant time scale where the weighting function is significant. Furthermore, in the time interval where the weighting function decreases significantly with the Reynolds number, instantaneous acceleration model becomes more precise for highly turbulent flows (GHIDAOUI et al., 2005).

In addition to the wall shear, during the hydraulic transient, polyethylene (PE) or polyvinyl chloride (PVC) pipes can deform significantly, dumping the pressure waves. Such influence is due to the viscoelastic mechanical nature of polymers (SHAW; MACKNIGHT, 2005; COVAS et al., 2005). The behavior of plastic pipes can be described by an instantaneous-elastic response, which is accounted for in the elastic wave speed, and a retarded-viscoelastic response. Using the Boltzmann superposition principle (BOLTZMANN, 1874), Rieutord and Blanchard (1979) and Gally et al. (1979) coupled the retarded-viscoelastic behavior by adding a time-dependent term into the mass-balance

equation, Eq. (2.5). Rieutord and Blanchard (1979) evaluated the relaxation time effects on a three-Kelvin-Voigt element. Meanwhile, Gally et al. (1979) determined experimentally the creep-function values, verifying the model within a single PE pipeline.

Meißner (1977) assumed a complex nature for the pressure variable in Eqs. (2.5) and (2.6), and a convolutional relationship between the pipe wall deformation and a creep function. Applying these assumptions to the water hammer balance equations, Meißner (1977) derived a complex wave speed expression, including elastic and viscoelastic responses. Schönfeld (1949)'s analysis introduced the concept of flow impedance, defined as the ratio between complex pressure and discharge. Wylie (1965) further developed this concept into the Impedance Method, which was later expanded by Hirschmann (1978) and Hirschmann (1979) to include the viscoelastic properties of pipe walls. Franke and Seyler (1983) incorporated Meißner (1977)'s wave speed formulas into unsteady fluid equations and utilized the Impedance Method to solve steady-oscillatory flows. Suo and Wylie (1989) expanded the Impedance Method by utilizing the Impulse Response, which involves correlating a complex impulse input with a complex output through convolution with the impulse function. Subsequently, Suo and Wylie (1990) employed the Impulse Response Method to characterize pipe-wall viscoelasticity in oscillatory and non-periodic flows.

In order to enhance the water hammer numerical methods, Covas et al. (2004) first focuses on the experimental analysis and characterization of viscoelastic behavior in PE pipes during hydraulic transients. The PE pipe showed significant pressure attenuation and wave delay, indicating its viscoelastic nature. The pressure wave's amplitude decreased exponentially, and the wave phase shifted. Measurements highlighted a lag in the strain response to pressure changes, characterized by an initial elastic response followed by gradual viscoelastic strain. Mechanical hysteresis was observed, with the strain response differing during loading and unloading. Creep tests revealed time-dependent strain behavior under a constant load, with the creep compliance function showing significant creep that increased with temperature.

Then, Covas et al. (2005) analyzed the experimental data using the viscoelastic model introduced by Rieutord and Blanchard (1979) coupled with wall shear models. Covas et al. (2005) examined the effects of unsteady friction and viscoelasticity separately to calibrate their numerical models. They found significant discrepancies between numerical results and experimental data for unsteady friction with neglected viscoelastic effects. Including only the viscoelastic effects, the model showed good agreement with experimental data, although the calibrated creep function varied with the initial flow rate. That highlighted the importance of incorporating the viscoelastic effect in plastic pipe models.

Further efforts to understand the unsteady friction and the viscoelasticity con-

tributions for hydraulic transient phenomena were employed. For instance, Duan et al. (2010) found that initial transient stages show comparable contributions from unsteady friction and viscoelastic effects on pressure head attenuation. Over time, viscoelastic effects become dominant, impacting damping and phase shift of the pressure wave. Furthermore, the viscoelastic effect is critical when the viscoelastic retardation time is shorter than the wave travel time along the pipeline.

Later, Gong et al. (2016) introduced a robust method for calibrating the creep function of viscoelastic pipelines and the elastic wave speed using frequency-domain analysis of hydraulic transients. This approach is computationally efficient and offers accurate evaluations, aiding in better system design and safe operation of viscoelastic pipeline systems. Additionally, Wu et al. (2022) compared energy dissipation in 1D and 2D models of viscoelastic pipes, finding that the friction term's contribution increases with Reynolds numbers while the viscoelastic term's impact remains relatively constant. Finally, Vardy (2023) highlighted that while skin friction and viscoelasticity are dominant factors, other effects like bubbly flows and fluid-structure interaction also play significant roles. Accurate numerical modeling requires consideration of these factors to avoid misinterpretation of results.

About the numerical models, there are several different schemes developed to obtain an approximated solution for the hydraulic transient equations. The Method of Characteristics (MOC) is the most popular due to its accuracy, simplicity, numerical efficiency, and programming simplicity (GHIDAOUI et al., 2005). However, it is possible to find studies using the Finite Difference (FD) and Finite Volume (FV) techniques. Recently, a few works using the Smoothed Particle Hydrodynamics (SPH) method also appeared.

MOC is a method developed specifically to solve hyperbolic partial differential equations (PDE) by reducing them to a family of ordinary differential equations (ODE) (COURANT; HUBERT, 1962). Specifically for water hammer equations, one reduces them to a family of time-dependent ODEs by fixing the curved characteristic lines through $\mathrm{d}x/\mathrm{d}t = \overline{u}_1 + a$, which coincides with Courant-Friedrich-Lewy's stability condition.

The initial application of the MOC in hydraulic transients can be traced back to Gray (1953), who first used it to compute pressure and velocity in a frictionless pipe system with fixed time (Δt) and space (Δx) intervals. Lister (1960) expanded on this by investigating the fixed-grid method and the method of specified time intervals, ultimately finding that the fixed-grid method simplifies programming and thus gained popularity. Lai (1961) later incorporated frictional losses into the MOC, while Streeter (1963) developed boundary conditions for valve operations within the MOC framework. Streeter and Lai (1963)'s experimental validation of the MOC for different valve closure times further solidified its practical utility.

One fundamental challenge of the MOC is its fixed relationship between space

and time steps, a requirement that can create numerical difficulties in complex systems with many pipe segments or variable wave speeds. Perkins et al. (1964) highlighted that the fixed-grid method is numerically stable only for Courant's numbers less than unity. Efficiently resolving device behavior with the fixed scheme requires the same time step for all pipes, making it challenging to satisfy the Courant's condition $a\,\Delta t/\Delta x \leq 1$.

Various interpolation techniques were developed to address these challenges. Space-line interpolations, proposed by Lister (1960), approximate the head and flow at the base of the characteristic line, allowing different time steps for specific pipes and enabling faster codes with manageable errors. Vardy (1976) introduced reachout-space-line interpolation for pipe networks, though this method also requires boundary interpolation, generating and propagating errors over time.

Wiggert and Sundquist (1977) combined space-line and space reach-out interpolation to mitigate limitations, while Goldberg and Wylie (1983) developed the more accurate time-line interpolation method, using previous time-step data for interpolation. Lai (1988)'s multimode scheme combined various interpolation techniques, offering extensive flexibility in choosing Δt and Δx. Sibetheros et al. (1991) demonstrated that a spline strategy adapts MOC grids to complex domains, anticipating transient conditions at unknown points based on general behavior knowledge.

Despite these advances, interpolation is inherently non-physical, introducing numerical errors such as dissipation and dispersion. These errors result from numerical approximations of the advection term in balance equations, creating false or artificial diffusion. Although these errors persist, MOC methods efficiently account for the advection term in momentum equations, maintaining correct wave speeds on average (PAL et al., 2021).

Ghidaoui and Karney (1994) analyzed a wave speed adjustment method to ensure characteristic lines pass through grid points from known to unknown time levels. Karney and Ghidaoui (1997) introduced a hybrid interpolation technique combining various approaches, optimizing memory use, execution speed, and discretization flexibility in pipe networks. Ghidaoui et al. (1998) proposed an integrated-energy approach to control discretization errors associated with interpolation methods. Shimada et al. (2006) developed an exact method for computing numerical errors in interpolation methods, noting that interpolation distorts physics, particularly in short pipes, requiring tiny time steps and increased computational times.

Tian et al. (2008) applied the MOC to moderate valve-induced water hammer effects in parallel pipe systems, finding that damping torque effectively reduces pressure vibrations due to valve closure. Bergant et al. (2008a) and Bergant et al. (2008b) incorporated fluid-structure interaction (FSI) and other transient processes into the MOC, addressing parameters like unsteady friction, cavitation, viscoelasticity, and representing leakages and

blockages. Afshar and Rohani (2008) proposed an implicit MOC model to overcome the limitations of widely used MOC models, simulating transient flow problems and comparing results favorably with explicit MOC schemes. Jang et al. (2016) developed a quasi-2D approach based on the MOC to reduce computational nodes by proposing 1D characteristic equations for pressure and discharge. This method achieved equivalent results to those obtained with an explicit 2D solution

Despite its many advantages, the MOC has notable disadvantages. According to Pal et al. (2021), the approach must be artificially modified if the Courant number is not set to unity, and mass and momentum balance are not assured for non-uniform Courant numbers. Interpolation, though necessary, is non-physical and tends to cause artificial damping of the solution. Including the advective acceleration term is difficult, potentially inducing errors, especially when aiming for $a\,\Delta t/\Delta x = 1$.

The momentum and mass balance equations cannot be satisfied even in the absence of interpolation, making MOC particularly applicable to systems with constant celerity, which is a core assumption of the model. In practical scenarios, celerity is not static and fluctuates over time. However, since both the time step and celerity are treated as fixed, adjustments must be made to the spatial step throughout the simulation to maintain the condition $a\,\Delta t/\Delta x = 1$. This is often overlooked in typical implementations. Explicit schemes are easier to program and execute but are conditionally stable and computationally inaccurate with larger spatial steps or variable cross-sectional areas. On the other hand, implicit schemes, though unconditionally stable, are more complex and computationally demanding (PAL et al., 2021).

As an alternative, Lagrangian-based methods, such as Lattice Boltzmann Method (LBM) and SPH, have significantly advanced the modeling of unsteady flows, including water hammer phenomena. The LBM, a modern computational fluid dynamics (CFD) approach based on kinetic theory, has been widely used for modeling various fluid dynamics scenarios. Cheng et al. (1998) first used LBM for unsteady flow, followed by Wu et al. (2008), who developed a practical and straightforward LBM model. Budinski (2016) applied LBM to model a one-dimensional hydraulic transient, using an adaptive grid independent of the Courant number. This approach showed excellent agreement with results obtained from MOC, validating its accuracy. Budinski also provided a detailed derivation of boundary conditions for various hydraulic elements, including straight pipes, branching pipes, valve-end pipes, reservoirs, surge tanks, and air chambers.

Louati et al. (2019) extended the application of LBM to two-dimensional water hammer modeling, comparing results with a fifth-order Finite Volume (FV) scheme. They noted that higher-order finite difference and finite volume methods are challenging to implement with complex boundary conditions. Despite this, LBM schemes emerged as a viable alternative, offering computational speed and accuracy comparable to MOC for

low-frequency water hammer waves. However, Louati et al. (2019) noted that it loses stability and performance for high-frequency cases due to the neglected high-order terms of the equivalent macroscopic equations considered during the LBM numerical formulation.

Concomitantly, SPH methods have become increasingly popular. Hou et al. (2012) were the first to utilize SPH for simulating rapid pipeline filling. Their approach addressed boundary deficiency issues associated with conventional SPH methods by introducing a dynamic SPH pressure boundary condition. That allowed for the effective capture of the deceleration phase of filling, demonstrating good agreement with rigid column theory.

The corrective smoothed-particle method (CSPH), introduced by Hou et al. (2012) and Junior et al. (2020) and based on Chen et al. (1999), further advanced SPH for water hammer simulation in reservoir, pipe, and valve systems. This method utilized a corrective kernel estimate of SPH to approximate spatial derivatives, yielding outcomes comparable to MOC results. Hou et al. (2012) also observed that the smoothing length is a critical parameter affecting numerical accuracy and efficiency. Smaller lengths result in dispersion errors, while wider lengths cause numerical dissipation. An optimal range is between $0.9\,\Delta x_1$ and $1.5\,\Delta x_1$, where Δx_1 is the distance between particles. Additionally, Hou et al. (2015) employed a second-order accurate CSPM to model the dynamic interaction between air bubbles and water in a dead-end pipe, demonstrating accuracy and efficiency.

Most recently, Pan et al. (2022) combined the SPH method with unsteady friction models using virtual and mirror particles to improve boundary accuracy. Pan et al. (2022) noted that the implicit scheme of the model proposed by Brunone and Golia (1990), Brunone et al. (1991a) and Brunone et al. (1991b) is more stable and accurate than the explicit scheme, especially when neglecting artificial viscosity. Furthermore, Pan et al. (2022) analyzed extensively the critical numerical parameters for the SPH method. As a result, they observed:

a. Although artificial viscosity helps control numerical oscillations, it can lead to excessive dissipation, suggesting optimal values of viscosity parameters as $\alpha = 1.0$ and $\beta = 2.0$.

b. Fewer particles lead to more significant numerical dissipations. Thus, smoothing length near 1.0 times the distance interval is recommended for accurate simulations.

c. The cubic spline function presented more stability than other smoothing functions.

d. The Euler scheme is shown to have the same accuracy as the second-order Runge-Kutta scheme but requires fewer computational resources.

e. Compared to Godunov and MOC schemes, SPH is more accurate and stable for Courant numbers of less than one.

Song et al. (2023) extended the SPH capabilities to handle complex boundary conditions in water distribution systems (WDS). Song et al. (2023) combined the SPH and MOC methods, developing the SPH-WHWDS approach. This approach included specific equations for pipes, valves, reservoirs, surge tanks, air chambers, and pumps. The researchers obtained accurate results for a simple reservoir-pipe-valve experiment and a complex looped WDS. Song et al. (2023)' models predicted protection devices' behavior, such as air chambers, with similar accuracy to the pure MOC method.

Despite their advances, both LBM and SPH methods encounter challenges. LBM can exhibit instability and inaccuracy when dealing with high-frequency water hammer waves. Similarly, it can be challenging for SPH to implement complex boundary conditions, but there have been recent developments presenting alternative solutions for this issue. Furthermore, selecting the optimal parameters for artificial viscosity and particle smoothing can be challenging and may require additional computational effort.

3 MATHEMATICAL MODELLING

3.1 Basic definitions

Chaudhry (2014) introduced the following basic terminology of the hydraulic transient field:

Definition 3.1.1 *A flow that maintains constant temporal mean values of its properties, such as pressure and velocity, at a given point over time is known as a steady flow. In contrast, an unsteady flow is characterized by continuous changes with time in the flow conditions, like the temporal mean values of its properties over a short period of time.*

Definition 3.1.2 *A transient flow is an intermediate state between two steady states, e.g. when the flow conditions change from one steady-state to another steady-state.*

Definition 3.1.3 *Column separation is a phenomenon that occurs when a liquid column in a pipeline separates from the main flow. This typically occurs when the pressure within the pipeline drops below atmospheric pressure, which causes cavity vapor to form and detach the liquid column.*

Definition 3.1.4 *Hydraulic transient is a phenomenon of unsteady flow that results in pressure fluctuations caused by sudden changes in flow velocity.*

3.2 The Transport Theorem

The hydraulic transient model is commonly represented by a set of one-dimensional modified Navier-Stokes equations described by Chaudhry (2014) and Thorley (1991). To establish such a system, it is necessary to rearrange the Transport Theorem, Theorem 3.2.1.

Thus, suppose a fluid region holds the continuum principle, embodying manifold properties. Then, let's call the fluid region Ω and fix its rectangular coordinates, (x_1, x_2, x_3). Hence, a fluid flow is defined as a continuous, differentiable, and invertible transformation between the particles moving within the fluid region and the fluid region itself (ŁUKASZEWICZ; KALITA, 2016).

Definition 3.2.1 *Consider a manifold $\Omega \in \mathbb{R}^3$, with a particle P occupying a position $\boldsymbol{X} = (X_1, X_2, X_3)$ at the instant $t = 0$. Then a fluid flow is the transformation $\boldsymbol{x} : \Omega(0) \to \Omega(t)$, such that*

$$\boldsymbol{x} = \boldsymbol{x}(\boldsymbol{X}, t) \quad \text{and} \quad \boldsymbol{X} = \boldsymbol{X}(\boldsymbol{x}, t)\,, \tag{3.1}$$

and $J = J(\boldsymbol{X}, t)$*, its Jacobian, satisfies* $0 < J < \infty$*.*

The illustration in Fig. 3.1 shows how fluids move in two different frames of reference: Eulerian (Fig. 3.1a) and Lagrangian (Fig. 3.1b). Control volumes ($\Omega(t)$), which stay fixed in space, are used in the Eulerian frame of reference. That means that the spatial coordinates ($\boldsymbol{x}$) do not change relative to the inertial reference. In contrast, the Lagrangian frame of reference moves with the flow of the fluid. As a result, the material coordinates ($\boldsymbol{X}$) change over time relative to the inertial reference. The transformation between them (Fig. 3.1c) is given by Definition 3.2.1. Furthermore, in Fig. 3.1, the spatial and material coordinates at a specific time t_j are represented by $\boldsymbol{x}_{t_j}$ and $\boldsymbol{X}_{t_j}$, respectively. Velocities $\boldsymbol{u}_{t_j}$ and $\boldsymbol{U}_{t_j}$ are defined similarly. Additionally, the Eulerian and Lagrangian coordinate systems are respectively denoted by $(\mathbf{e}_1, \mathbf{e}_2, \mathbf{e}_3)$ and $(\mathbf{E}_1, \mathbf{E}_2, \mathbf{E}_3)$.

As a manifold, the motion state at a specific point $\boldsymbol{x}$ and time t of Ω is defined by various functions such as $\rho = \rho(\boldsymbol{x}, t)$, $\boldsymbol{u} = \boldsymbol{u}(\boldsymbol{x}, t)$, $p = p(\boldsymbol{x}, t)$, which represent hydrodynamic variables such as density, velocity, and pressure.

Definition 3.2.2 *The velocity* $\boldsymbol{u}$ *at time* t *of a particle initially at* $\boldsymbol{X}$ *is given as*

$$\boldsymbol{u}(\boldsymbol{x}, t) = \boldsymbol{U}(\boldsymbol{X}, t) = \frac{\mathrm{d}}{\mathrm{d}t}\boldsymbol{x}(\boldsymbol{X}, t)\,, \quad \boldsymbol{x} = \boldsymbol{x}(\boldsymbol{X}, t)\,, \tag{3.2}$$

with $\mathrm{d}(\cdot)/\mathrm{d}t$ *representing an ordinary derivative operator.*

Definition 3.2.2 is a direct consequence of the fluid flow transformation according to Łukaszewicz and Kalita (2016). The other hydrodynamic variables also have a representation in material coordinates. For instance, consider an initial coordinate $\boldsymbol{X}$ and an arbitrary variable f. Then, applying the transformation:

$$f(\boldsymbol{x}, t) = f(\boldsymbol{x}(\boldsymbol{X}, t), t) = F(\boldsymbol{X}, t)\,. \tag{3.3}$$

Furthermore, the ordinary derivative operator is reserved for the material coordinates, whereas the partial derivative is applied to local variables. That is another consequence of Eq. (3.1), which further develops into the material derivative operator.

Definition 3.2.3 *Consider an arbitrary manifold* $\Omega(t)$ *moving with the fluid, where* $\boldsymbol{X}$ *is the initial position, and* $\boldsymbol{x}$ *is a position such that* $\boldsymbol{x} = \boldsymbol{x}(\boldsymbol{X}, t)$*. Thus, the material derivative of a scalar or vector function* f *of position and time is given as*

Figure 3.1: An arbitrary fluid particle moving within a manifold Ω defined in a fluid region. The Eulerian frame of reference in the fluid region is represented by the fixed system $(\mathbf{e}_1, \mathbf{e}_2, \mathbf{e}_3)$, while the Lagrangian frame is represented by the system $(\mathbf{E}_1, \mathbf{E}_2, \mathbf{E}_3)$, which serves as a inertial reference.

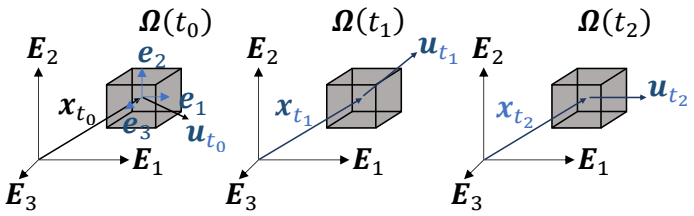

(a) Eulerian frame of reference

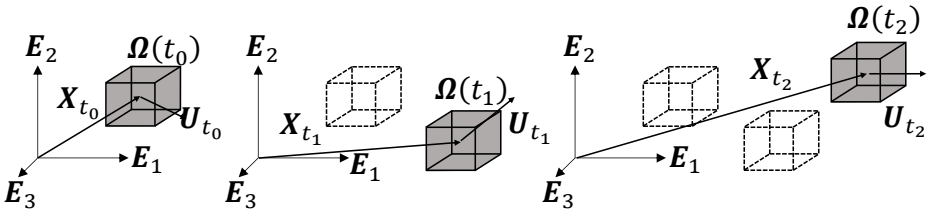

(b) Lagrangian frame of reference

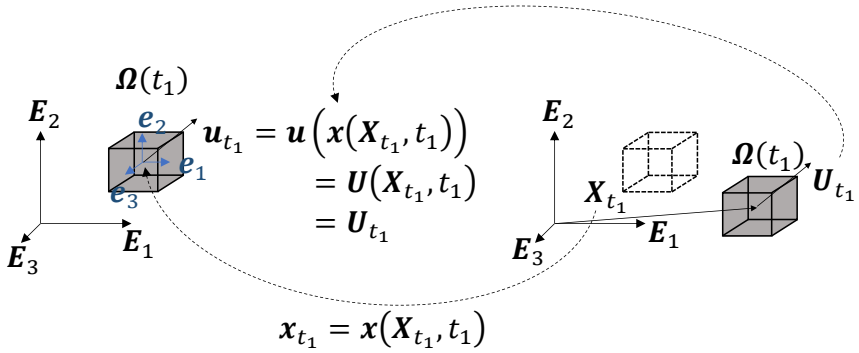

(c) Transformation

Source: Modified from Rapp (2017).

$$\frac{D}{Dt} f(\boldsymbol{x}, t) = \frac{\mathrm{d}}{\mathrm{d}t} F(\boldsymbol{X}, t) = \frac{\mathrm{d}}{\mathrm{d}t} f(\boldsymbol{x}(\boldsymbol{X}, t)) = \frac{\partial}{\partial t} f(\boldsymbol{x}, t) + (\boldsymbol{u}(\boldsymbol{x}, t) \cdot \nabla) f(\boldsymbol{x}, t). \tag{3.4}$$

The fluid flow map and material derivative serve as essential tools in demonstrating the Transport Theorem. Moreover, one can use them to alter the theorem to derive the hydraulic transient equations.

Theorem 3.2.1 *Let $\Omega(t)$ denote an arbitrary manifold that is moving with the fluid and let $f(\boldsymbol{x}, t)$ be a scalar or vector function of position and time. The Transport Theorem states that*

$$\begin{aligned}&\frac{\mathrm{d}}{\mathrm{d}t}\int_{\Omega(t)} f\left(\boldsymbol{x},t\right)\mathrm{d}\boldsymbol{x}=\\&\int_{\Omega(t)}\left\{\frac{\partial}{\partial t}f\left(\boldsymbol{x},t\right)+\boldsymbol{u}\left(\boldsymbol{x},t\right)\cdot\nabla f\left(\boldsymbol{x},t\right)+f\left(\boldsymbol{x},t\right)\nabla\cdot\boldsymbol{u}\left(\boldsymbol{x},t\right)\right\}\mathrm{d}\boldsymbol{x}.\end{aligned}\tag{3.5}$$

Consider the transformation $\boldsymbol{x}:\Omega(0)\rightarrow\Omega(t)$, such that $\boldsymbol{x}=\boldsymbol{x}(\boldsymbol{X},t)$. Then

$$\int_{\Omega(t)} f\left(\boldsymbol{x},t\right)\mathrm{d}\boldsymbol{x}=\int_{\Omega(0)} f\left(\boldsymbol{x}(\boldsymbol{X},t),t\right)J\left(\boldsymbol{X},t\right)\mathrm{d}\boldsymbol{X}=\int_{\Omega(0)} F\left(\boldsymbol{X},t\right)J\left(\boldsymbol{X},t\right)\mathrm{d}\boldsymbol{X}.\tag{3.6}$$

As a result,

$$\begin{aligned}\frac{\mathrm{d}}{\mathrm{d}t}\int_{\Omega(t)} f\left(\boldsymbol{x},t\right)\mathrm{d}\boldsymbol{x}&=\frac{\mathrm{d}}{\mathrm{d}t}\int_{\Omega(0)} F\left(\boldsymbol{X},t\right)J\left(\boldsymbol{X},t\right)\mathrm{d}\boldsymbol{X}\\&=\int_{\Omega(0)}\left\{\frac{\mathrm{d}}{\mathrm{d}t}F\left(\boldsymbol{X},t\right)J\left(\boldsymbol{X},t\right)+F\left(\boldsymbol{X},t\right)\frac{\mathrm{d}}{\mathrm{d}t}J\left(\boldsymbol{X},t\right)\right\}\mathrm{d}\boldsymbol{X}.\end{aligned}\tag{3.7}$$

The first part of the right-hand side of the Eq. (3.7) can be expanded using the material derivative definition. Hence,

$$\begin{aligned}&\int_{\Omega(0)}\frac{\mathrm{d}}{\mathrm{d}t}F\left(\boldsymbol{X},t\right)J\left(\boldsymbol{X},t\right)\mathrm{d}\boldsymbol{X}=\\&=\int_{\Omega(0)}\left\{\frac{\partial}{\partial t}f\left(\boldsymbol{x}(\boldsymbol{X},t),t\right)+\mathbf{u}\left(\boldsymbol{x}(\boldsymbol{X},t),t\right)\cdot\nabla f\left(\boldsymbol{x}(\boldsymbol{X},t),t\right)\right\}J\left(\boldsymbol{X},t\right)\mathrm{d}\boldsymbol{X}\\&=\int_{\Omega(t)}\left\{\frac{\partial}{\partial t}f\left(\boldsymbol{x},t\right)+\mathbf{u}\left(\boldsymbol{x},t\right)\cdot\nabla f\left(\boldsymbol{x},t\right)\right\}\mathrm{d}\boldsymbol{x}.\end{aligned}\tag{3.8}$$

For the second part of Eq. (3.7), the time derivative of the Jacobian must be developed. Thus, using indices notation

$$\begin{aligned}
\frac{\mathrm{d}}{\mathrm{d}t} J\left(\boldsymbol{X}, t\right) &= \frac{\mathrm{d}}{\mathrm{d}t}\left[\det\left(\frac{\partial x_j}{\partial X_j}\right)\right] = \det\left[\frac{\mathrm{d}}{\mathrm{d}t}\left(\frac{\partial x_j}{\partial X_j}\right)\right] \\
&= \det\left[\frac{\partial}{\partial X_j} u_j\left(\boldsymbol{x}(\boldsymbol{X}, t), t\right)\right] \\
&= \det\left[\frac{\partial}{\partial x_j} u_j\left(\boldsymbol{x}(\boldsymbol{X}, t), t\right) \frac{\partial x_j}{\partial X_j}\right] \\
&= \nabla \cdot \mathbf{u}\left(\boldsymbol{x}(\boldsymbol{X}, t), t\right) J\left(\boldsymbol{X}, t\right),
\end{aligned} \tag{3.9}$$

which means that

$$\begin{aligned}
&\int_{\Omega(0)} \left\{F\left(\boldsymbol{X}, t\right) \frac{\mathrm{d}}{\mathrm{d}t} J\left(\boldsymbol{X}, t\right)\right\} \mathrm{d}\boldsymbol{X} = \\
&= \int_{\Omega(0)} \left\{F\left(\boldsymbol{X}, t\right) \nabla \cdot \mathbf{u}\left(\boldsymbol{x}(\boldsymbol{X}, t), t\right) J\left(\boldsymbol{X}, t\right)\right\} \mathrm{d}\boldsymbol{X} \\
&= \int_{\Omega(t)} \left\{f\left(\boldsymbol{x}, t\right) \nabla \cdot \mathbf{u}\left(\boldsymbol{x}, t\right)\right\} \mathrm{d}\boldsymbol{x}.
\end{aligned} \tag{3.10}$$

Hence, adding Eqs. (3.8) and (3.10), one obtains

$$\int_{\Omega(t)} \left\{\frac{\partial}{\partial t} f\left(\mathbf{x}, t\right) + \mathbf{u}\left(\mathbf{x}, t\right) \cdot \nabla f\left(\mathbf{x}, t\right) + f\left(\mathbf{x}, t\right) \nabla \cdot \mathbf{u}\left(\mathbf{x}, t\right)\right\} \mathrm{d}\boldsymbol{x}, \tag{3.11}$$

which is the right hand-side of Eq. (3.7). Thus, Eq. (3.7) is equal to Eq. (3.5), proving the Transport Theorem.

The Transport Theorem provides the necessary tools to formulate the hydraulic transient equations. The first step is to define the problem, which involves considering a fluid control volume within a pipe with a non-uniform circular cross-section, as shown in Fig. 3.2. The hydrodynamic variables depend on x_1 and t, including the cross-section surface area (s). The weight force ($\boldsymbol{f}_W$) is located at the control volume center, whereas the pressure forces (ps) are on the control surfaces $s_{n,1}$ and $s_{n,2}$. Additionally, friction tension (τ) acts on the lateral surfaces.

Let's take Eq. (3.5). Then, apply the integral over the control volume of Fig. 3.2b, considering that an arbitrary scalar or vector function f depends on x_1 and t. That implies:

Figure 3.2: Physical model used to develop the hydraulic transient mathematical model.

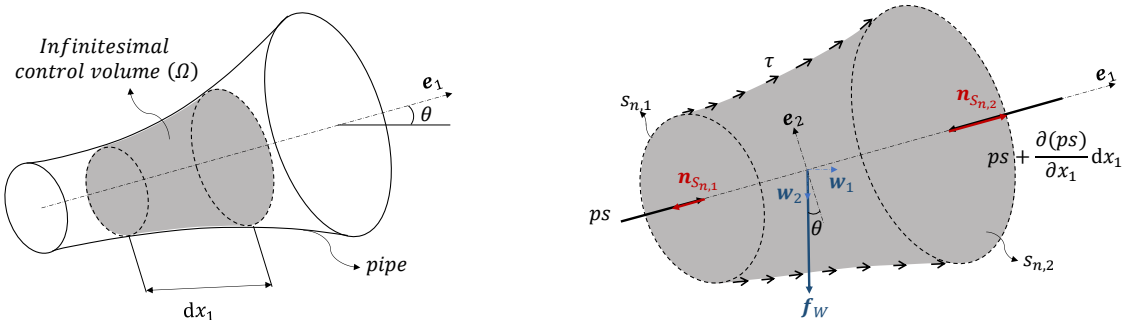

(a) (b)

Source: Own authorship.

$$\frac{\mathrm{d}}{\mathrm{d}t}\int_{\Omega(t)} f\left(x_1,t\right)\mathrm{d}\boldsymbol{x} = \frac{\mathrm{d}}{\mathrm{d}t}\int_{L(t)} f\left(x_1,t\right)s\left(x_1,t\right)\mathrm{d}x_1$$

$$= \int_{L(0)}\left\{\frac{\mathrm{d}}{\mathrm{d}t}F\left(X_1,t\right)S\left(X_1,t\right)J\left(X_1,t\right) + F\left(X_1,t\right)\frac{\mathrm{d}}{\mathrm{d}t}S\left(X_1,t\right)J\left(X_1,t\right) + F\left(X_1,t\right)S\left(X_1,t\right)\frac{\mathrm{d}}{\mathrm{d}t}J\left(X_1,t\right)\right\}\mathrm{d}X_1$$

$$\begin{aligned}&\frac{\mathrm{d}}{\mathrm{d}t}\int_{\Omega(t)} f\left(x_1,t\right)\mathrm{d}\boldsymbol{x}\\ &= \int_{L(t)}\left\{\frac{D}{Dt}f\left(x_1,t\right)s\left(x_1,t\right) + f\left(x_1,t\right)\frac{D}{Dt}s\left(x_1,t\right) + f\,s\,\frac{\partial}{\partial x_1}u_1\left(x_1,t\right)\right\}\mathrm{d}x_1,\end{aligned} \tag{3.12}$$

where the integral subscript $L(t)$ represent an arbitrary linear path along $\mathbf{e}_1$-axis within the control volume $\Omega(t)$.

3.3 Continuity Equation

Definition 3.3.1 *Let $\rho = \rho\left(x_1,t\right)$ be the fluid density at point x_1 and time t. Hence, the mass of the finite volume $\Omega(t)$ in Fig 3.2b is*

$$m = \int_{\Omega(t)} \rho\left(x_1,t\right)\mathrm{d}\boldsymbol{x}. \tag{3.13}$$

The mass balance states that the mass of fluid in a material volume Ω remains unchanged as Ω moves with the fluid; that is,

$$\frac{\mathrm{d}}{\mathrm{d}t}\int_{\Omega(t)} \rho\left(x_1,t\right)\mathrm{d}\boldsymbol{x} = 0. \tag{3.14}$$

From the Transport Theorem in Eq. (3.12), it follows that:

$$\int_{L(t)} \left\{ s \frac{D\rho}{Dt} + \rho \frac{Ds}{Dt} + \rho\, s \frac{\partial u_1}{\partial x_1} \right\} \mathrm{d}x_1 = 0. \tag{3.15}$$

The localization theorem, which is also a lemma of general properties of the integral in Zorich (2004), states that if the integral of a nonnegative function $\mathbf{f} : L \to \mathbb{R}$ over the interval L equals zero, then $\mathbf{f}(x) = 0$ at almost all points of the interval L. This statement remains valid if the interval L in it is replaced by any admissible Jordan-measurable set. Hence, Eq. (3.15) becomes

$$\frac{1}{\rho}\frac{D\rho}{Dt} + \frac{1}{s}\frac{Ds}{Dt} + \frac{\partial u_1}{\partial x_1} = 0. \tag{3.16}$$

Consider that the fluid is slightly compressible (CHAUDHRY, 2014). As a result, the fluid density is related to pressure by

$$\frac{1}{\rho}\frac{D\rho}{Dt} = \frac{1}{\zeta}\frac{Dp}{Dt}, \tag{3.17}$$

where ζ is the bulk modulus. Then, substituting Eq. (3.17) into Eq. (3.16), one gets

$$\frac{1}{\zeta}\frac{Dp}{Dt} + \frac{1}{s}\frac{Ds}{Dt} + \frac{\partial u_1}{\partial x_1} = 0. \tag{3.18}$$

The pipe in Fig. 3.2b has a circular cross-sectional area. Admit that its radius is a function of position x_1 and time t. Hence

$$\frac{Ds}{Dt} = 2\,\pi\, r \frac{Dr}{Dt}, \tag{3.19}$$

where r is the cross-section radius and R is the initial radius value at a point x_1. Then, let's use the logarithmic radius strain (ε), also known as true strain or Hencky strain (HENCKY, 1928), then its time variation is

$$\frac{D\varepsilon}{Dt} = \frac{D}{Dt}\left[\ln\left(\frac{r}{R}\right)\right] = \frac{1}{r}\frac{Dr}{Dt}. \tag{3.20}$$

Consider that the pipe is rigidly anchored with expansion joints throughout, then the axial stresses in the pipe the pipe's inertia become negligible. Hence, the surface time variation can be written as

$$\frac{Ds}{Dt} = 2\, s \frac{D\varepsilon}{Dt}. \tag{3.21}$$

Substituting Eq. (3.21) in Eq. (3.18), one gets

$$\frac{1}{\zeta}\frac{Dp}{Dt} + 2\,\frac{D\varepsilon}{Dt} + \frac{\partial u_1}{\partial x_1} = 0, \tag{3.22}$$

which is the general continuity equation 1-D form for a hydraulic transient of a slightly compressible fluid in control volume within a deformable pipe.

3.4 Principle of Momentum Conservation

Definition 3.4.1 *The principle of momentum conservation states that the rate of change of momentum of a material volume is equal to the resultant force on the volume*

$$\frac{\mathrm{d}}{\mathrm{d}t}\int_{\Omega(t)} \rho\,\boldsymbol{u}\,\mathrm{d}\boldsymbol{x} = \sum_{j}^{N} \boldsymbol{f}_{external,i}, \tag{3.23}$$

where $\boldsymbol{f}_{external,i}$ is the j-th external force of the finite N forces acting on the material volume (ŁUKASZEWICZ; KALITA, 2016).

Figure 3.2b shows three external forces within the control volume. These forces derived from pressure (p) acting perpendicularly on cross-section surfaces (s_n), shear stress (τ) parallel to the lateral surface (s_l), and a gravitational field on the control volume. The surface force ($\boldsymbol{f}_s$) can be defined as

$$\boldsymbol{f}_s = \int_{s(t)} \mathbf{T}\mathrm{d}\mathbf{s}, \tag{3.24}$$

where $\mathbf{T}$ is the stress tensor. Assuming, by the Cauchy Principle, that the stress tensor is a linear function of the surface's normal vector,

$$\mathbf{T}\left(\boldsymbol{x}, t, \mathbf{n}\right) = \mathbf{n}\left(\boldsymbol{x}\ , t\right) \cdot \boldsymbol{\sigma}\left(\boldsymbol{x}, t\right), \tag{3.25}$$

where $\mathbf{n}$ is the normal vector such that $\mathbf{n}\left(\boldsymbol{x}, t\right) = \left(\mathbf{e}_1, \mathbf{e}_2, \mathbf{e}_3\right)$, and $\boldsymbol{\sigma}$ is a second order tensor. Considering the problem as a one-dimensional one, Eq. (3.24)) becomes

$$\boldsymbol{f}_s = -\int_{s(t)} \begin{bmatrix} 1\,\mathbf{e}_1 & 1\,\mathbf{e}_2 & 1\,\mathbf{e}_3 \end{bmatrix} \begin{bmatrix} p & 0 & 0 \\ \tau & 0 & 0 \\ 0 & 0 & 0 \end{bmatrix} \begin{bmatrix} 1\,\mathbf{e}_1 \\ 1\,\mathbf{e}_2 \\ 1\,\mathbf{e}_3 \end{bmatrix} \mathrm{d}s. \tag{3.26}$$

Now, one splits the total surface integral into an integral on the normal surface and an integral on the lateral surface, while transforming the rectangular coordinates in cylindrical coordinates:

$$\begin{aligned}\boldsymbol{f}_s = &- \int_{s_n(t)} \begin{bmatrix}1\,\mathbf{e}_r & 1\,\mathbf{e}_\theta & 1\,\mathbf{e}_1\end{bmatrix} \begin{bmatrix}0 & 0 & 0\\ 0 & 0 & 0\\ 0 & 0 & p\end{bmatrix} \begin{bmatrix}0\,\mathbf{e}_r\\ 0\,\mathbf{e}_\theta\\ 1\,\mathbf{e}_1\end{bmatrix} \mathrm{d}s_n \\ &- \int_{s_l(t)} \begin{bmatrix}1\,\mathbf{e}_r & 1\,\mathbf{e}_\theta & 1\,\mathbf{e}_1\end{bmatrix} \begin{bmatrix}0 & 0 & \tau\\ 0 & 0 & 0\\ 0 & 0 & 0\end{bmatrix} \begin{bmatrix}1\,\mathbf{e}_r\\ 0\,\mathbf{e}_\theta\\ 0\,\mathbf{e}_1\end{bmatrix} \mathrm{d}s_l.\end{aligned} \tag{3.27}$$

Then, one applies the Divergence Theorem on the normal surface integral and opens de lateral surface integral components, obtaining

$$\boldsymbol{f}_s = - \int_{\Omega(t)} \frac{\partial p}{\partial x_1}\,\mathrm{d}\boldsymbol{x} - \int_{s_l(t)} \tau\,\frac{d}{2}\,\mathbf{e}_1\,\mathrm{d}\theta\mathrm{d}x_1, \tag{3.28}$$

$$\boldsymbol{f}_s = - \int_{L(t)} \frac{\partial p}{\partial x_1}\,s\,\mathbf{e}_1\,\mathrm{d}x_1 - \int_{L(t)} \tau\,\pi\,d\,\mathbf{e}_1\,\mathrm{d}x_1, \tag{3.29}$$

where s is the cross-section surface area, d is the control volume diameter The gravitational forces ($\boldsymbol{f}_W$) can be represented as

$$\boldsymbol{f}_W = \int_{\Omega(t)} \rho\,\mathbf{g}\,\mathrm{d}\boldsymbol{x}, \tag{3.30}$$

where $\mathbf{g}$ is the gravitational acceleration. Considering that $\mathbf{g}$ is defined on the coordinate system $(\mathbf{w}_1, \mathbf{w}_2, \mathbf{w}_3)$, Fig. 3.2b, one should apply a rotation of θ degrees to obtain its form on the coordinate system $(\mathbf{e}_1, \mathbf{e}_2, \mathbf{e}_3)$. Then

$$\mathbf{g_e} = \mathbf{R}_\theta\,\mathbf{g_w} = \begin{bmatrix}\cos(\theta) & -\sin(\theta) & 0\\ \sin(\theta) & \cos(\theta) & 0\\ 0 & 0 & 0\end{bmatrix} \begin{bmatrix}0\\ g\\ 0\end{bmatrix} = g \begin{bmatrix}-\sin(\theta)\\ \cos(\theta)\\ 0\end{bmatrix} \tag{3.31}$$

where $\mathbf{g_e}$ and $\mathbf{g_w}$ are the gravitational acceleration vectors defined on $(\mathbf{e}_1, \mathbf{e}_2, \mathbf{e}_3)$ and $(\mathbf{w}_1, \mathbf{w}_2, \mathbf{w}_3)$, respectively. Additionally, $\mathbf{R}_\theta$ is a counterclockwise linear rotation transformation. As a result, the Eq. (3.30) can be rewritten as

$$\boldsymbol{f}_W = \int_{\Omega(t)} \rho\,g\,\left[-\sin(\theta)\,\mathbf{e}_1 + \cos(\theta)\,\mathbf{e}_2 + 0\,\mathbf{e}_3\right]\mathrm{d}\boldsymbol{x}. \tag{3.32}$$

Since, the flow major direction is the $\mathbf{e}_1$-axis, the body force becomes

$$\boldsymbol{f}_W = - \int_{L(t)} \rho\,g\,s\,\sin(\theta)\,\mathbf{e}_1\,\mathrm{d}x_1. \tag{3.33}$$

Therefore, Eq. (3.23) can be rewritten, substituting Eq. (3.29) and (3.33) as the external forces:

$$\frac{\mathrm{d}}{\mathrm{d}t}\int_{L(t)} \rho\, s\, u_1\, \mathbf{e}_1\, \mathrm{d}x_1 = -\int_{L(t)} \frac{\partial p}{\partial x_1}\, s\, \mathbf{e}_1\, \mathrm{d}x_1 - \int_{L(t)} \tau\, \pi\, d\, \mathbf{e}_1\, \mathrm{d}x_1 - \int_{L(t)} \rho\, g\, s\, \sin(\theta)\, \mathbf{e}_1\, \mathrm{d}x_1. \tag{3.34}$$

Then, applying the Transport Theorem, Eq. (3.12) on the left-hand side of Eq. (3.34), one gets

$$\begin{aligned} &\int_{L(t)} u_1 \left\{ \frac{D(\rho\, s)}{Dt} + \rho\, s\, \frac{\partial u_1}{\partial x_1} \right\} \mathrm{d}x_1 + \int_{L(t)} \rho\, s\, \frac{Du_1}{Dt} \mathrm{d}x_1 = \\ &= -\int_{L(t)} \frac{\partial p}{\partial x_1}\, s\, \mathrm{d}x_1 - \int_{L(t)} \tau\, \pi\, d\, \mathrm{d}x_1 - \int_{L(t)} \rho\, g\, s\, \sin(\theta)\, \mathrm{d}x_1, \end{aligned} \tag{3.35}$$

where u_1 is the velocity field component on $\mathbf{e}_1$-axis. The continuity equation implies, Eq. (3.15), that the first integral on the left-hand side of Eq. (3.35) has a value of zero. By moving each term from the right-hand side to the left-hand side and combining them into a single integral, it is also determined to be zero. Hence

$$\frac{Du_1}{Dt} + \frac{1}{\rho}\frac{\partial p}{\partial x_1} + \frac{\pi\, d\, \tau}{\rho\, s} + g\, \sin(\theta) = 0. \tag{3.36}$$

3.5 The Elastic Wave Speed

The elastic wave speed is a crucial parameter in hydraulic transients. To estimate its value, the physical model in Fig. 3.2b requires simplification. Assume that a pressure wave, entering the control volume, transports the hydrodynamic properties with a quasi-uniform speed, a. The flow velocity and mass flow rate present negligible changes compared to the propagation speed, a (THORLEY, 1991). Shear stress has an insignificant influence in this context. The pipe inclines at $\theta = 0$. Furthermore, consider that the fluid is slightly compressible. Thus, the density experiences almost no variation along the control volume and time (CHAUDHRY, 2014).

The energy equation is an additional tool to show the elastic wave speed since the pressure fluctuation is caused by some external event that forces the kinetic energy to transform into work done by pressure.

Definition 3.5.1 *The first law of thermodynamics in classical hydrodynamics states that the increase of total energy in a material volume is the sum of the heat transferred and the work done on the volume.*

$$\frac{\mathrm{d}E}{\mathrm{d}t} = \frac{\mathrm{d}W}{\mathrm{d}t} + \frac{\mathrm{d}Q}{\mathrm{d}t}. \tag{3.37}$$

where E is the total energy, W is the work and Q is the heat (ŁUKASZEWICZ; KALITA, 2016).

Hydraulic transients are isothermal, which indicates that there is no thermal energy involved. The total energy comprises both kinetic and internal energy. Compression and expansion of the control volume generate work while the internal energy remains balanced and constant over time. Hence,

$$\frac{\mathrm{d}}{\mathrm{d}t}\int_{L(t)} \rho\, s \left(\frac{1}{2}u_1^2 + e\right) \mathrm{d}x_1 = -\frac{\mathrm{d}}{\mathrm{d}t}\int_{L(t)} p\, s \,\mathrm{d}x_1 \tag{3.38}$$

where e is the specific internal energy. Consider that wave speed is responsible for carrying properties and kinetic energy, while internal energy remains unchanged over time. Thus

$$\int_{L(t)} \frac{u_1^2}{2}\left\{\frac{D\,(\rho\, s)}{Dt} + \rho\, s\, \frac{\partial u_1}{\partial x_1}\right\}\mathrm{d}x_1 + \int_{L(t)} \rho\, s\, a\, \frac{Du_1}{Dt}\mathrm{d}x_1 = -\int_{L(t)} s\, \frac{Dp}{Dt} + p\, s\, \left(\frac{1}{s}\frac{Ds}{Dt} + \frac{\partial u}{\partial x_1}\right)\mathrm{d}x_1$$

$$\rho\, a\, \frac{Du_1}{Dt} = -\frac{Dp}{Dt} - p\left(\frac{1}{s}\frac{Ds}{Dt} + \frac{\partial u}{\partial x_1}\right)$$

$$\rho\, a \frac{\partial u_1}{\partial t} + \rho\, a^2 \frac{\partial u_1}{\partial x_1} = -\frac{Dp}{Dt} + \frac{p}{\rho}\frac{D\rho}{Dt}. \tag{3.39}$$

Using the fact that the fluid is slightly compressible, $(p/\rho)\, D\rho/Dt \ll Dp/Dt$, and that local velocities variations are much smaller than the wave speed, $\partial u_1/\partial t \ll a\, \partial u_1/\partial x_1$, the equation reduces to

$$\rho\, a^2 \frac{\partial u_1}{\partial x_1} = -\frac{Dp}{Dt}. \tag{3.40}$$

The Eq. (3.40) shows that the total time rate of pressure is directly proportional to the advective acceleration the fluid experiences due to the elastic pressure fluctuation. Coupling it in the continuity equation and considering only elastic deformation (ε_0), one obtains

$$\frac{1}{\zeta}\frac{Dp}{Dt} + 2\,\frac{D\varepsilon_0}{Dt} - \frac{1}{\rho\, a^2}\frac{Dp}{Dt} = 0,$$

$$a = \left\{\frac{1}{\rho}\left[\frac{1}{\zeta} + 2\,\frac{D\varepsilon_0}{Dt}\frac{Dt}{Dp}\right]^{-1}\right\}^{1/2}, \tag{3.41}$$

which is the elastic wave speed.

3.6 Hydraulic Transient Equations

In hydraulic engineering, it is a standard procedure to calculate pipeline pressures based on the piezometric head, h, above a specified datum. The pressure intensity, p, can be expressed as

$$p = \rho\, g\, (h + z)\,, \tag{3.42}$$

in which z is the elevation of the pipe centerline above the specified datum.

The calculations for fluid flow are based on the assumption of a fluid that is slightly compressible, with pipe walls that are slightly deformable. To address the variation of density, a finite wave velocity is taken into account. However, in the case of an incompressible fluid with rigid pipe walls, the wave velocity becomes infinite, resulting in instantaneous changes (CHAUDHRY, 2014). For horizontal pipe $Dz/Dt = 0$. Hence, with these assumptions,$Dp/Dt = \rho\, g\, Dh/Dt$, and Eq. (3.22) and (3.36) become

$$\frac{1}{\zeta}\frac{Dh}{Dt} + \frac{2\,a^2}{g}\,\frac{D\varepsilon}{Dt} + \frac{a^2}{g}\,\frac{\partial u_1}{\partial x_1} = 0, \tag{3.43}$$

$$\frac{Du_1}{Dt} + g\frac{\partial h}{\partial x_1} + \frac{\pi\, d\, \tau}{\rho\, s} = 0. \tag{3.44}$$

Let's assume that $s = \pi\, d^2/4$. Then, substitute that in the friction term, besides the elastic wave velocity, Eq.(3.41), in the continuity equation. That results into

$$\frac{Dh}{Dt} + \frac{2\,a^2}{g}\,\left(\frac{D\varepsilon}{Dt} - \frac{D\varepsilon_0}{Dt}\right) + \frac{a^2}{g}\,\frac{\partial u_1}{\partial x_1} = 0, \tag{3.45}$$

$$\frac{Du_1}{Dt} + g\frac{\partial h}{\partial x_1} + \frac{4\,\tau}{\rho\, d} = 0. \tag{3.46}$$

According to Covas (2003), the instantaneous strain (ε) can be decomposed into

$$\varepsilon = \varepsilon_0 + \varepsilon_r, \tag{3.47}$$

where ε_0 is the elastic strain, while ε_r is a retarded strain. From this model, one can have a purely elastic material, such as metal or concrete, or a viscoelastic material, like Polyethylene pipes. For pure elastic conduct, the continuity equation is simplified to

$$\frac{Dh}{Dt} + \frac{a^2}{g}\,\frac{\partial u_1}{\partial x_1} = 0. \tag{3.48}$$

Conversely, a viscoelastic pipe is modeled by

$$\frac{Dh}{Dt} + \frac{2\,a^2}{g}\,\frac{D\varepsilon_r}{Dt} + \frac{a^2}{g}\,\frac{\partial u_1}{\partial x_1} = 0, \tag{3.49}$$

3.7 Unsteady Friction Models

Fig 3.3 illustrates two velocity profiles in a pipeline system. Velocity profile 1 depicts the steady-state flow velocity profile before the downstream valve is closed, while velocity profile 2 represents the flow velocity profile after the downstream valve is closed and the pressure wave has passed through the position of velocity profile 2. The fluid region within the pipeline is composed of three regions: the viscous layer (blue layer), the vortex sheet (orange layer), and the core region (white center)

When the downstream valve is closed, a pressure wave is produced, which nullifies the mean velocity and generates a vortex sheet at the end section of the pipe due to the velocity inversion near the wall region. Even though the mean velocity is canceled out, there is still some motion in the pipe cross-section, particularly near the wall. The velocity profile in the core remains (profile 2) unchanged and retains its steady-state shape (COVAS, 2003; MARTINS et al., 2016), as observed in Fig. 3.3

Figure 3.3: Inversion of the velocity profile for the total closure of the downstream valve along the pipeline. The velocity profile 2 is the one after the velocity profile 1 encounters the pressure wave.

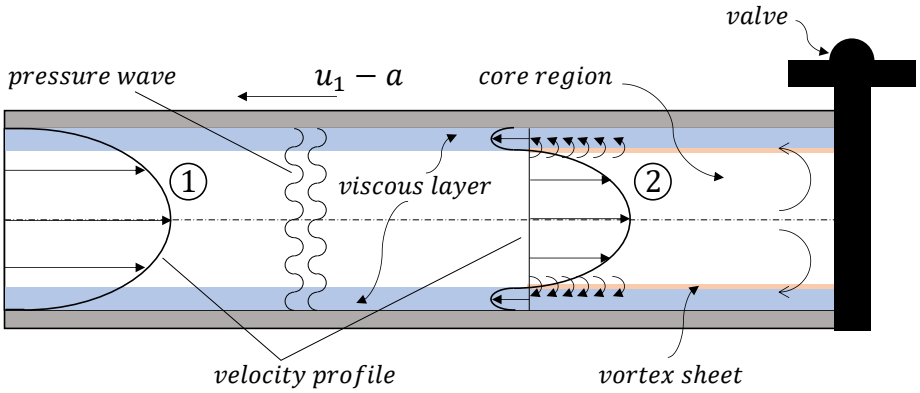

Source: Adapted from Covas (2003).

When a pressure wave moves to the reservoir and returns, it changes the direction of the velocity. The average velocity becomes negative, but the profile retains its steady-state shape in the core region. Additionally, there is always a diffusion towards the core (MARTINS et al., 2016). When the pressure wave reaches the valve, the cycle starts again.

The velocity distribution in a pipe is affected by two distinct zones - the viscous layer and the core region. The viscous layer, being less inert, tends to respond more quickly to changes, while the core region, being more inert, tends to retain the memory of past

velocity distributions. These zones exhibit different behaviors and have an impact on the friction losses in the momentum equation.

As a result, friction has no steady-state behavior. Hence, consider that friction decomposes into two terms - a quasi-stationary (τ_s) and a unsteady (τ_t) components - such that $\tau = \tau_s + \tau_t$. The quasi-stationary friction stress is described as:

$$\tau_s = \frac{1}{8}\,\rho\,\lambda\,|u_1|u_1, \tag{3.50}$$

where λ is the quasi-stationary friction factor. Swamee (1993) proposes the following approximation for λ:

$$\lambda = \left\{ \left(\frac{64}{Re}\right)^8 + 9.5\left[\ln\left(\frac{\epsilon}{3.7\,d} + \frac{5.74}{Re^{0.9}}\right) - \left(\frac{2500}{Re}\right)^6\right]^{-16} \right\}^{1/8}, \tag{3.51}$$

where Re is the Reynolds number,

$$Re = \frac{u_1\,d}{\nu}, \tag{3.52}$$

and ϵ is the internal pipe walls' absolute roughness (m).

According to Covas (2003), there are five major types of unsteady friction models: (1) weights of past-time local accelerations; (2) instantaneous mean velocity; (3) instantaneous acceleration; (4) local and advective acceleration, and (5) velocity profiles. Whereas Ghidaoui et al. (2005) resumed them in two types: experimental and analytical models.

3.7.1 Empirical-based Models

Assuming a uniform cross-section, elastic, and smooth pipe containing a flow composed by a fluid with Newtonian properties, the shear stress can be expressed in its isotropic and deviatoric form as

$$\boldsymbol{\tau} = \zeta_b\,(\nabla\cdot\boldsymbol{u})\,\mathbf{I} + \mu\left[\nabla\boldsymbol{u} + (\nabla\boldsymbol{u})^T - \frac{2}{3}\,(\nabla\cdot\boldsymbol{u})\,\mathbf{I}\right], \tag{3.53}$$

using Stokes's constitutive equation. The bulk and dynamic viscosity are denoted by ζ_b and μ, respectively. By integrating the divergence of Eq. (3.53) and focusing only on the component along the $\mathbf{e}_1$ axis, since one considers $u_2 \approx u_3 \approx 0$, one obtains:

$$\int_{L(t)} (\nabla\cdot\boldsymbol{\tau})\,\mathbf{e}_1\,s\,\mathrm{d}x_1 = \int_{L(t)} \left[\left(\zeta_b + \frac{1}{3}\mu\right)\frac{\partial}{\partial x_1}\,(\nabla\cdot\boldsymbol{u}) + \mu\nabla^2 u_1\right]\,\mathbf{e}_1\,s\,\mathrm{d}x_1. \tag{3.54}$$

Then, assume an incompressible flow with significant velocity spatial variation along the pipe cross-section, specially near the pipe wall due to the viscous effect. Transforming the rectangular coordinates in cylindrical coordinates, Eq. (3.54) becomes

$$\int_{L(t)} \mu \frac{1}{r} \frac{\partial}{\partial r} \left(r \frac{\partial u_1}{\partial r} \right) s \, \mathrm{d}x_1. \tag{3.55}$$

Thus, Eq. (3.55) simplifies Eq. (3.36) to

$$\rho \frac{\partial u_1}{\partial t} + \frac{\partial p}{\partial x_1} - \rho \nu \frac{1}{r} \frac{\partial}{\partial r} \left(r \frac{\partial u_1}{\partial r} \right) = 0, \tag{3.56}$$

where ν is the kinematic viscosity. Considering that a harmonic potential pressure difference induces the flow, one can apply the Fourier transformation relative to time on Eq. (3.56) and obtain

$$\frac{\partial \widehat{p}}{\partial x_1} = -\rho \, i \, \omega \, \widehat{u}_1 + \rho \nu \frac{1}{r} \frac{\partial}{\partial r} \left(r \frac{\partial \widehat{u}_1}{\partial r} \right), \tag{3.57}$$

where i is the imaginary number, ω is the oscillation frequency and $\widehat{f}$ is the corresponding Fourier transformed value of an arbitrary absolutely integrable function.

Schönfeld (1949) found several solutions for laminar and turbulent regimes of the ordinary differential equation, Eq. (3.57), observing two typical types of solution. For high frequencies, resistance is negligible concerning inertia, resulting in

$$\frac{\partial \widehat{p}}{\partial x_1} = -\left(1 + \Theta_H\right) i \, \omega \, \rho \, \widehat{u}_1, \tag{3.58}$$

which, after the inverse Fourier transformation, becomes

$$\rho \frac{\partial u_1}{\partial t} + \frac{\partial p}{\partial x_1} + \rho \, \Theta_H \frac{\partial u_1}{\partial t} = 0 \tag{3.59}$$

where Θ_H is the high-frequency coefficient, which is an asymptotic approximation of Bessel functions, in the case of pipes with circular cross-section, or tangent functions, in the case of rectangular cross-section pipes. For low frequencies, one must consider the resistance influence, implying the solution for Eq. (3.56) is

$$\rho \frac{\partial u_1}{\partial t} + \frac{\partial p}{\partial x_1} + \Upsilon \, u_1 + \rho \, \Theta_L \frac{\partial u_1}{\partial t} = 0, \tag{3.60}$$

where Θ_L is the low-frequency coefficient, obtained similarly to Θ_H. Schönfeld (1949) suggested that Υ, the resistance coefficient, can be approximated as $\rho \, g \, u_1 / \left(R_h \, C_h^2 \right)$, where R_h is the hydraulic radius, and C_h is the hydraulic capacitance or the steady flow Chézy

coefficient. Compared with the quasi-stationary shear stress, Eq. (3.50), one could say that g/C_h^2 is equivalent to the friction factor, λ.

Consider the same uniform cross-section, elastic, and smooth pipe containing a incompressible flow composed by a fluid with Newtonian properties. However, decompose the velocity field into a base (u_0, temporal mean value) and a fluctuation $\left(u^{'}\right)$ velocity component. Additionally, encapsulate the lumped boundary resistance due to wall shear and any constrictions into F_R instead of using any constitutive relationship. Then apply a dimensionless process on the Navier-Stokes equation, considering $p^* = 2\,p/\left(\rho\,\overline{u}_1^2\right)$, $u^* = u_0/\overline{u}_1$, $u^{*\,'} = u^{'}/\overline{u}_1$, $x_1^* = x_1/L$, and $F_R^* = 2\,F_R/\left(\rho\,\overline{u}_1^2\right)$. Furthermore, $\overline{u}_1$ is the velocity average value relative to the pipe's cross-section surface, and L is the pipe length. As a result, one obtains

$$\rho\,\frac{\partial u_1}{\partial t} + \frac{\rho}{2}\,\frac{\partial\left(u_1\,u_1\right)}{\partial x_1} + \frac{\partial p}{\partial x_1} + F_R = 0$$

$$\rho\,\frac{\partial u_0}{\partial t} + \rho\,\frac{\partial u^{'}}{\partial t} + \frac{\rho}{2}\,\frac{\partial\left(u_0\,u_0\right)}{\partial x_1} + \rho\,\frac{\partial\left(u_0\,u^{'}\right)}{\partial x_1} + \frac{\rho}{2}\,\frac{\left(\partial u^{'}\,u^{'}\right)}{\partial x_1} + \frac{\partial p}{\partial x_1} + F_R = 0,$$

$$\frac{2\,L}{\overline{u}_1}\left(\frac{\partial u^*}{\partial t} + \frac{\partial u^{*\,'}}{\partial t}\right) + \frac{\partial p^*}{\partial x_1^*} + L\,F_R^* + \frac{\partial\left(u^*\,u^*\right)}{\partial x_1^*} + 2\,\frac{\partial\left(u^*\,u^{*\,'}\right)}{\partial x_1^*} + \frac{\partial\left(u^{*\,'}\,u^{*\,'}\right)}{\partial x_1^*} = 0,$$

$$\frac{2\,L}{\overline{u}_1}\,\frac{\partial u_1^*}{\partial t} + \frac{\partial p^*}{\partial x_1^*} + K_s + K_t = 0, \tag{3.61}$$

where K_s is the one-dimensional steady-state resistance coefficient,

$$K_s = L\,F_R^*, \tag{3.62}$$

K_t is the correcting coefficient to measure the additional unsteady effects on boundary resistance and momentum flux of absolute local velocity,

$$K_t = \frac{\partial\left(u^*\,u^*\right)}{\partial x_1^*} + 2\,\frac{\partial\left(u^*\,u^{*\,'}\right)}{\partial x_1^*} + \frac{\partial\left(u^{*\,'}\,u^{*\,'}\right)}{\partial x_1^*}, \tag{3.63}$$

and $K_u = K_s + K_t$ is the unsteady flow coefficient of boundary resistance and momentum flux of absolute local velocity. Comparing Eq. (3.61) with the dimensionless form of Eq. (3.60),

$$\frac{2\,L}{\overline{u}_1}\,\frac{\partial u_1^*}{\partial t} + \frac{\partial p^*}{\partial x_1^*} + \frac{L}{d}\;u_1^{*\,2} + \frac{2\,L}{\overline{u}_1}\Theta_L\,\frac{\partial u_1^*}{\partial t} = 0, \tag{3.64}$$

one obtains

$$K_u = \frac{L}{d}\ u_1^{*\,2} + \frac{2\,L}{\overline{u}_1}\,\Theta_L\,\frac{\partial u_1^*}{\partial t}, \tag{3.65}$$

where $R_h = d/4$ for a circular pipe, and $C_h = \sqrt{8\,g/\lambda}$. Assume that $K_u = 8\,\pi\,d\,L\tau/\left(\rho\,\overline{u}_1^2\,\pi\,d^2\right)$ (GHIDAOUI et al., 2005), then Eq. (3.65) can be rewritten as

$$\tau = \frac{1}{8}\,\rho\,\lambda\,u_1^2 + \frac{\rho\,d}{4}\,\Theta_L\,\frac{\partial u_1}{\partial t}, \tag{3.66}$$

where Θ_L is usually assigned as K. The shear stress quasi-stationary or steady-state component is retrieved similarly to Eq. (3.50), while the unsteady shear stress depends on the local acceleration and a constant determined experimentally.

Daily et al. (1956) model, Eq. (3.66), is insufficient to simulate every aspect of the hydraulic transient phenomena. Hence, to enhance the unsteady shear stress model, one needs definitions from Extend Irreversible Thermodynamics and Classical Irreversible Thermodynamics (JOU et al., 2010). That requires defining the second law of thermodynamics.

Definition 3.7.1 *The second law of thermodynamics states that all natural processes increase entropy, which increases disorder. Idealized reversible processes do not produce entropy, and known transformations cannot destroy entropy. Thus, the rate of change of the entropy* (Γ) *of a control volume* (Ω) *is defined as*

$$\frac{\mathrm{d}\Gamma}{\mathrm{d}t} = \frac{\mathrm{d}\Gamma_e}{\mathrm{d}t} + \frac{\mathrm{d}\Gamma_j}{\mathrm{d}t}. \tag{3.67}$$

It includes the rate of entropy exchange $(\mathrm{d}\Gamma_e/\mathrm{d}t)$ *with the surroundings, which can be zero, positive or negative, and the rate of processes occurring within* Ω $(\mathrm{d}\Gamma_j/\mathrm{d}t)$*. Furthermore, the non-negative quantity,* $\mathrm{d}\Gamma_j/\mathrm{d}t \geq 0$*, is zero at equilibrium or for reversible transformations and positive for irreversible processes (JOU et al., 2010).*

It is possible to define a local specific entropy γ, a local entropy flux $\mathbf{J}^\Gamma$, and a local rate of production σ^Γ respectively, without any loss of generality, as

$$\Gamma = \int_{\Omega(t)} \rho\,\gamma\,\mathrm{d}\boldsymbol{x}, \tag{3.68}$$

$$\frac{\mathrm{d}\Gamma_e}{\mathrm{d}t} = -\int_{s(t)} \mathbf{J}^\Gamma \cdot \mathbf{n}\,\mathrm{d}s, \tag{3.69}$$

$$\frac{\mathrm{d}\Gamma_j}{\mathrm{d}t} = \int_{\Omega(t)} \sigma^\Gamma\,\mathrm{d}\boldsymbol{x}. \tag{3.70}$$

As a result, the balance of the entropy can be rewritten as

$$\frac{\mathrm{d}}{\mathrm{d}t}\int_{\Omega(t)}\rho\,\gamma\,\mathrm{d}\boldsymbol{x}=-\int_{s(t)}\mathbf{J}^{\Gamma}\cdot\mathbf{n}\,\mathrm{d}s+\int_{\Omega(t)}\sigma^{\Gamma}\,\mathrm{d}\boldsymbol{x}, \tag{3.71}$$

which, after applying the Transport and Gauss Theorems, becomes

$$\frac{D}{Dt}\left(\rho\,\gamma\right)=-\rho\,\gamma\,\frac{\partial u_1}{\partial x_1}-\frac{\partial J_1^{\Gamma}}{\partial x_1}+\sigma^{\Gamma} \tag{3.72}$$

in a one-dimensional context with $\sigma^{\Gamma}\geq 0$. Axworthy et al. (2000) considered $\rho\,\gamma\,\partial u_1/\partial x_1$ equivalent to $-q/T_b$, where q is the time rate of specific heat transfer and T_b is the instantaneous temperature. In the present text, q is considered negligible.

Classical Irreversible Thermodynamics (CIT) can compute system entropy using temperature, mass, density, and specific internal energy. For steady flow, CIT confirms the second law. However, local and advective accelerations are significant at or near the wavefront for unsteady flows, requiring nonequilibrium assumptions at the local scale. Extended Irreversible Thermodynamics (EIT) considers dissipative fluxes in addition to conserved variables to address this. Equation

$$\gamma=\gamma\left(e_j,u_1\right) \tag{3.73}$$

represents the equation of state, assuming negligible temperature changes and that density changes correspond to the acoustic wave speed. It treats internal energy (e_j) and velocity as intensive properties. From the exact differential of Eq. (3.73) concerning t, one obtains

$$\frac{D}{Dt}\left(\rho\,\gamma\right)=\alpha_1\,\frac{Dh}{Dt}+\alpha_2\frac{Du_1}{Dt}, \tag{3.74}$$

where

$$\alpha_1=\frac{\partial}{\partial e_j}\left(\rho\,\gamma\right)\frac{\partial e_j}{\partial h}\quad\text{and}\quad\alpha_2=\frac{\partial}{\partial u_1}\left(\rho\,\gamma\right). \tag{3.75}$$

From Eq. (3.72) and Eq. (3.74), one obtains

$$\alpha_1\,\frac{Dh}{Dt}+\alpha_2\frac{Du_1}{Dt}=-\frac{\partial J_1^{\Gamma}}{\partial x_1}+\sigma^{\Gamma}, \tag{3.76}$$

which, using Eq. (3.48), can be rewritten as

$$\alpha_2\frac{\partial u_1}{\partial t}+\left[\alpha_2\,u_1-\alpha_2\left(\frac{a^2}{g}\right)\right]\frac{\partial u_1}{\partial x_1}=-\frac{\partial J_1^{\Gamma}}{\partial x_1}+\sigma^{\Gamma}. \tag{3.77}$$

The EIT model is compatible with CIT when α_2 tends to zero or the velocity time rate is zero. Considering $\alpha_2 = 0$, $\alpha_1 = -g^2\,h\,/a^2$ and $J_1^\Gamma = -g\,u_1\,h$ are possible solutions, which lead to Eq. (3.77) becoming

$$\alpha_2 \frac{Du_1}{Dt} - g\,u_1 \frac{\partial h}{\partial x_1} = \sigma^\Gamma. \tag{3.78}$$

EIT follows a standard procedure of expanding the coefficient in a Taylor series around the static equilibrium, neglecting the second or higher-order terms, resulting in the expression of α_2 as

$$\alpha_2 = \alpha_2\Big|_{u_1=0} + u_1 \frac{\partial \alpha_2}{\partial u_1}\Big|_{u_1=0}. \tag{3.79}$$

Assume that $\alpha_2|_{u_1=0} = 0$ and use Eq. (3.46), then Eq. (3.78) can be rewritten as

$$\sigma^\Gamma = \left[\left(1 + \frac{\partial \alpha_2}{\partial u_1}\Big|_{u_1=0}\right)\frac{\partial u_1}{\partial t} + \left(1 + \frac{\partial \alpha_2}{\partial u_1}\Big|_{u_1=0}\right) u_1 \frac{\partial u_1}{\partial x_1} + \frac{4}{\rho\,d}\tau\right] u_1, \tag{3.80}$$

which satisfies the entropy inequality ($\sigma^\Gamma \geq 0$) if

$$\left(1 + \frac{\partial \alpha_2}{\partial u_1}\Big|_{u_1=0}\right)\frac{\partial u_1}{\partial t} + \left(1 + \frac{\partial \alpha_2}{\partial u_1}\Big|_{u_1=0}\right) u_1 \frac{\partial u_1}{\partial x_1} + \frac{4}{\rho\,d}\tau = \beta^\Gamma\,u_1, \quad \beta^\Gamma \geq 0, \tag{3.81}$$

reducing the generated entropy to $\sigma^\Gamma = \beta^\Gamma\,u_1^2$, with β^Γ as an arbitrary positive coefficient. Additionally, a system reaches thermodynamic equilibrium once $\delta\sigma^\Gamma = 0$. Thus,

$$\delta\sigma^\Gamma = 2\,\beta^\Gamma\,u_1\,\delta u_1 + u_1^2\,\delta\beta^\Gamma \tag{3.82}$$

is null when $u_1 = 0$ provided that $\delta\beta^\Gamma$ is not of $O\left(u^{-m}\right)$, where $m \geq 2$. Using the fact that CIT compatibility with EIT happens in the limit of $\partial\alpha_2/\partial u_1|_{u_1=0} = 0$, and the steady-state condition, then Eq. (3.81) reduces to

$$\beta^\Gamma = \frac{4}{\rho\,d}\tau_s. \tag{3.83}$$

That ensures $\beta^\Gamma \geq 0$ and $\delta\beta^\Gamma$ with an order greater than $O\left(u^{-m}\right)$, where $m \geq 2$. Substituting Eq. (3.83) in Eq. (3.81), one obtains

$$\tau = \tau_s - \frac{\rho\,d}{4}\left[\left(1 + \frac{\partial \alpha_2}{\partial u_1}\Big|_{u_1=0}\right)\frac{\partial u_1}{\partial t} + \left(1 + \frac{\partial \alpha_2}{\partial u_1}\Big|_{u_1=0}\right) u_1 \frac{\partial u_1}{\partial x_1}\right], \tag{3.84}$$

which leads to

$$\tau_t = K\frac{\rho\, d}{4}\left(\frac{\partial u_1}{\partial t} + u_1\,\frac{\partial u_1}{\partial x_1}\right), \tag{3.85}$$

where $K = -\left(1 + \partial\alpha_2/\partial u_1|_{u_1=0}\right)$. Equation (3.85) is similar to the one proposed by Daily et al. (1956), Eq. (3.66), but with a specific form for the coefficient Θ_L. Brunone and Golia (1990), Brunone et al. (1991a), Brunone et al. (1991b), Vitkovsky et al. (2000), and Ramos et al. (2004) proposed models that agree with Eq. (3.85). Brunone and Golia (1990), Brunone et al. (1991a), Brunone et al. (1991b) suggested a model proportional to the wave speed,

$$\tau_t = K\frac{\rho\, d}{4}\left(\frac{\partial u_1}{\partial t} - a\,\frac{\partial u_1}{\partial x_1}\right), \tag{3.86}$$

improved by Vitkovsky et al. (2000) with the influence of the velocity inversion,

$$\tau_t = K\frac{\rho\, d}{4}\left(\frac{\partial u_1}{\partial t} + a\,\mathrm{sign}\,(u_1)\,\frac{\partial u_1}{\partial x_1}\right). \tag{3.87}$$

On the other hand, Ramos et al. (2004) proposed a model that separately controls local acceleration and advection,

$$\tau_t = \frac{\rho\, d}{4}\left(K_1\frac{\partial u_1}{\partial t} + K_2\, a\,\mathrm{sign}\,(u_1)\,\frac{\partial u_1}{\partial x_1}\right). \tag{3.88}$$

where K_1 and K_2 are experimental-determined coefficients.

Instantaneous acceleration models based on Eq. (3.85) satisfy the second law of thermodynamics, and K serves as a positive relaxation time that accounts for unsteady shear stress. However, K derived from $\partial\alpha_2/\partial u_1|_{u_1=0}$, meaning that it also depends on x_1 and t, does not account for the radial diffusion effect due to the vortex layer formed between the wall and core regions, which is a natural limitation of EIT theory models. These models are limited to short-timescale phenomena and do not cover long-timescale events, such as the diffusion effect (JOU et al., 2010; AXWORTHY et al., 2000).

3.7.2 Analytical-based Models

Zielke (1968) developed a weighted past-time local accelerations equation for the unsteady friction component considering: (i)a fully developed laminar flow; (ii) negligible advective terms; (iii) negligible influence of the mass storage on velocity profile; (iv) axisymmetric velocity profiles. Through the application of assumptions (i), (ii), (iii), and (iv) on the cylindrical coordinate form of Eqs. (3.44) and (3.48), and subsequent use of Laplace transformation analyses, Appendix A, Zielke (1968) derived

$$\tau_t = \frac{4\,\rho\,\nu}{d}\int_0^t \frac{\partial}{\partial t} u_1\left(t^*\right)\,\Phi\left(t-t^*\right)\mathrm{d}t^*, \tag{3.89}$$

where ν is the kinematic viscosity, t^* is the instant immediately preceding t, and $\Phi\left(t-t^*\right)$ is a weighting function that accounts for prior velocity variations, defined as:

$$\Phi\left(t-t^*\right) = C\sum_{i=1}^{\infty}\exp\left[\eta_j\left(t-t^*\right)\right], \tag{3.90}$$

with C and η_j being constants contingent upon modeled problem.

Equation (3.89) includes the effect of local accelerations from the initial moment to the current time. However, this integration can be computationally intensive, leading Trikha (1975) to create an exponential series approximation for the weighted function. Using the weighted function described in Eq. (3.90) and applying it to Eq. (3.89), Trikha (1975) obtained

$$Y_m\left(t\right) = \begin{cases} 0, & t = 0, \\ Y_{m,t^*}\,\exp\left(-B_m\psi\right) + T_m\left(u_1^t - u_1^{t^*}\right), & t > 0. \end{cases} \tag{3.91}$$

after separating the integral into three components. B_m and T_m are constants computed by minimizing the squared error between Φ and Y_m. Additionally, u_1^t represents the current velocity, and $u_1^{t^*}$ denotes the velocity at the previous instant.

Later, Vardy and Hwang (1993) further simplified the approximation expression into

$$\tau_t = \frac{4\,\nu\,\rho}{d}\left[Y_1\left(t\right) + Y_2\left(t\right)\right]. \tag{3.92}$$

Zielke (1968) initially developed his model for laminar flows, but Arlt (1983) experimentally demonstrated its potential for extension to turbulent flows. Vardy and Hwang (1993) provided a theoretical justification by considering a flow within a laminar ring that encloses a uniform velocity central core, Fig. 3.4. The authors assumed similar axioms to Zielke (1968) and added the assumption of a linear time-invariant eddy viscosity within the wall shear layer, which becomes uniform in the core region. Consequently, for a moderate unsteady turbulent flow, Vardy and Hwang (1993) obtained a weighted function as follows:

$$\Phi\left(\psi\right) = \frac{\lambda\,Re}{4}\sum_{i=1}^{\infty}\exp\left[-\frac{\psi}{16}\left(i\,\pi\,\lambda\,Re\right)^2\right], \tag{3.93}$$

where ψ is the dimensionless time defined as

$$\psi = \frac{4\,\nu}{d^2}\left(t-t^*\right). \tag{3.94}$$

Figure 3.4: Model proposed by Vardy and Hwang (1993). It has a core region with a uniform velocity profile and a laminar ring region, near the wall, where the velocity profile is subjected to the viscous effect.

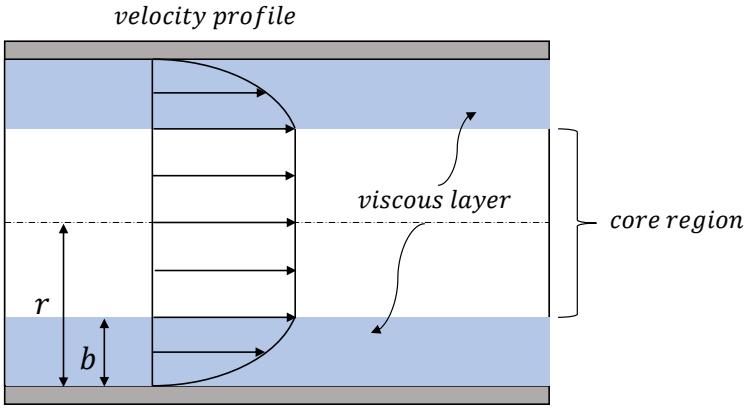

Source: Adapted from Vardy and Hwang (1993).

Vardy and Hwang (1993) demonstrated that only two terms of Y_m provide sufficient accuracy compared to the model suggested by Zielke (1968) when applied to their moderate unsteady turbulent flow model. As a result, Vardy and Hwang (1993) created the Tab. 3.1 with pre-calculated values for the constants B_m and T_m for specific ranges of values defined by $\lambda_R\, Re = 0.25\, \lambda\, Re$.

Table 3.1 – Values of the coefficients B_m and T_m for several ranges defined by $\lambda_R Re$.

$\lambda_R Re$	T_1	T_2	B_1	B_2
250.000	250.000	74.000	4.400×10^5	4.200×10^5
500.000	260.000	65.000	5.600×10^5	1.150×10^5
1000.000	350.000	65.000	9.800×10^5	4.120×10^5
2000.000	470.000	65.000	2.800×10^5	1.620×10^5

The model developed by Vardy and Hwang (1993) was validated for a moderate range of Reynolds number ($< 10^5$), which fit the numerical experiments set up in the present work. Furthermore, Vardy and Hwang (1993) pointed out that the dependence on historical conditions decreases as the product $\lambda\, Re$ increases since the thickness of the laminar layer decreases ($b/r \approx 4/(\lambda\, Re)$), reducing the required time for vorticity diffusion to influence the whole layer. That emphasizes the importance of the Reynolds number and the dimensionless time scale on hydraulic transient behavior.

According to the findings of Ghidaoui et al. (2005), practical water hammer flows satisfy assumptions (i), (ii), and (iii), while consideration (iv) has applicability limitations. Additionally, Das and Arakeri (1998) discovered nonstationary helical vortices that resulted in alternating flow reversal between the bottom and top sides of the pipe when Re and dimensionless time exceeded specific thresholds. This asymmetric behavior has also been observed by Brunone et al. (2000).

The linear stability analysis of Ghidaoui and Kolyshkin (2001) showed that hydraulic transient flow behavior is significantly affected by Reynolds number and wave dimensionless time scale. The inflection points in velocity profiles and large gradients near the pipe wall can cause instabilities, leading to fluctuations in wall shear stress and increased turbulence. These instabilities can cause hydraulic transients to become unstable, and they are characterized by their asymmetry and their association with Reynolds number and wave dimensionless time scale.

Besides the assumption (iv), the considerations (v) and (iv) also have their applicability limitations. They can be resumed as a quasi-steady turbulence consideration, which states that the flow characteristics remain similar to its state-steady previous features during the wave propagation. Thus, to understand the limits of the model proposed by Vardy and Hwang (1993), Vardy and Brown (1995), Vardy and Brown (2003) in Fig. 3.4, assume that in Fig. 3.3, the flow is in a steady-state turbulent regime, and the valve is closed. A pressure wave travels towards the reservoir, reversing the velocity field near the wall after passing point x. That generates a vortex sheet and a shear pulse around the pipe perimeter at x due to the disparity between the fluid within the viscous layer and the core region.

The shear pulse modifies the flow structure as it travels through the viscous layer and core region. This can cause an asymmetric velocity profile and significant changes in turbulence properties. It takes time for the wave to completely diffuses and impact the flow structure, especially in the core region. Ghidaoui et al. (2002) estimated this diffusion time, based on the viscous sublayer estimated by He and Jackson (2000), as

$$t_d = \frac{2\,d}{\overline{u}_1\sqrt{\lambda}}, \tag{3.95}$$

where $\overline{u}_1$ its the longitudinal average velocity. Based on Eq. (3.95), Ghidaoui et al. (2002) developed a dimensionless parameter to assess the applicability of asymmetric and quasi-steady turbulence models:

$$\varrho = \frac{2\,d}{\overline{u}_1\sqrt{\lambda}}\frac{a}{L}, \tag{3.96}$$

where L is the pipe length, and $t_w = a/L$ is the water hammer time scale.

The variable ϱ is used to quantify the number of wave cycles occurring within a pipe before the wall shear pulse causes a disturbance that affects the pre-existing turbulent characteristics throughout the entire cross-section of the pipe. Hence, Ghidaoui et al. (2002) proposed the classification:

a. Regime I occurs when $\varrho \gg 1$. In this scenario, the turbulence in the flow remains similar to the steady-state flow over many cycles, making the quasi-steady turbulence and axisymmetry assumptions acceptable;

b. Regime II is characterized by ϱ having an order of 1, which indicates that the water hammer time scale and delay in turbulence are comparable. Therefore, the quasi-steady turbulence and axisymmetry assumptions become questionable in this case;

c. In regime III, $\varrho \ll 1$, which implies low wave frequency, negligible flow inertia, and water hammer effects. Thus, the quasi-steady turbulence assumption is highly applicable. However, regime III is no longer a water hammer regime.

Although the analytical model has applicability limitations in turbulent regimes, Vardy and Brown (1995) and Vardy and Brown (2003) still improved their model by approximating the weighting function before Laplace inverse transformation instead of after the operation as Zielke (1968) and Vardy and Hwang (1993) did. The updated expression is:

$$\Phi = \frac{d}{4\,\nu_{lam}}\sqrt{\frac{\nu_w}{\pi\,t}}\exp\left(-\frac{4\,Re^{\kappa}\,\nu_{lam}}{12.86\,d^2}t\right) = \frac{1}{2}\sqrt{\frac{\nu_w}{\pi\,\psi\,\nu_{lam}}}\exp\left(-\frac{\psi}{C^*}\right), \tag{3.97}$$

where ν_{lam} is the laminar kinematic viscosity, ν_w is the kinematic viscosity at the wall, $C^* = 12.86/Re^{\kappa}$, $\psi = 4\,\nu_{lam}\,t^*/d^2$, $t^* = t_p - t$, t_p is the elapsed time since the beginning of the unsteadiness and κ is defined as

$$\kappa = \log_{10}\left(\frac{15.29}{Re^{0.0567}}\right). \tag{3.98}$$

Applying Eq. 3.97 in Eq. 3.89 and assuming a uniform acceleration, the unsteady shear stress reduces to the following dimensionless form:

$$f_u \equiv \frac{\tau_t}{\frac{1}{4}\rho\,d\,\frac{\partial u_1}{\partial t}} \approx 2\sqrt{C^*}\mathrm{erf}\left(\sqrt{\frac{\psi}{C^*}}\right), \tag{3.99}$$

where f_u is the unsteady friction coefficient, and $\mathrm{erf}\,(\cdot)$ is an error function. It is worth noting that the error function has definite lower and upper limits. When $\psi = 0$, the error function is zero, while when $\psi \to \infty$, the function approaches one. The function approaches

unity quickly, surpassing 0.99 for $\sqrt{\psi/C^*} > 1.823$. This implies that the unsteady shear stress reaches its maximum value when

$$\sqrt{\psi/C^*} > 1.823 \rightarrow \psi_L \approx 3.323\, C^*. \tag{3.100}$$

The magnitude of limiting shear stress is

$$f_{u,L} = 2\sqrt{C^*} \quad \text{or} \quad \tau_{t,L} = \frac{1}{2}\rho\, d\, \sqrt{C^*}\, \frac{\partial u_1}{\partial t}. \tag{3.101}$$

Based on equation Eq. (3.101), one observes that the model proposed by Vardy and Brown (1995) and Vardy and Brown (2003) retrieves the empirical-based model, implying that the empirical coefficient (K) is similar to the unsteady friction coefficient (f_u). Additionally, Vardy and Brown (2003) highlighted that the accuracy of Eq. (3.2) as an approximation for Eq. (3.89) improves when t has small values or the scale of the flow disturbance greatly exceeds the radial diffusion of vorticity across the shear layers. Furthermore, the decrease in the time interval where $\Phi(\psi)$ is significant with Reynolds number suggests that Eq. (3.2) becomes more precise for highly turbulent flows.

3.8 Linear Viscoelastic Model

Viscoelastic materials have both viscous and elastic properties when deformed. They exhibit three stress-strain properties: relaxation modulus ($G(t)$), creep compliance ($\iota(t)$), and hysteresis.

One can gauge the extent of relaxation modulus by consistently applying strain (ε_0) to a material for a set period from t_0. Over time, the resulting stress gradually diminishes until it eventually levels off, as depicted in Fig. 3.5. The relaxation modulus is a function that relates stress and strain through

$$\tau(t) = \begin{cases} 0, & t < t_0 \\ G(t - t_0)\, \varepsilon(t), & t \geq t_0 \end{cases} \tag{3.102}$$

and behaves as in

$$\lim_{t \to \infty} G(t - t_0) = G_\infty, \tag{3.103}$$

where G_∞ is the relaxation modulus infimum value.

The creep compliance determination involves subjecting a material to constant stress (τ_0) over a period of time from t_0. Figure 3.6 illustrates the resulting time-dependent

strain, which increases gradually. The relationship between stress and strain is established by the creep compliance, expressed in

$$\varepsilon(t) = \begin{cases} 0, & t < t_0 \\ \iota(t - t_0)\,\tau(t), & t \geq t_0 \end{cases} \tag{3.104}$$

and exhibiting behavior similar to that of

$$\lim_{t\to\infty} \iota(t - t_0) = \infty, \tag{3.105}$$

Figure 3.5: Stress and strain histories in the relaxation modulus test.

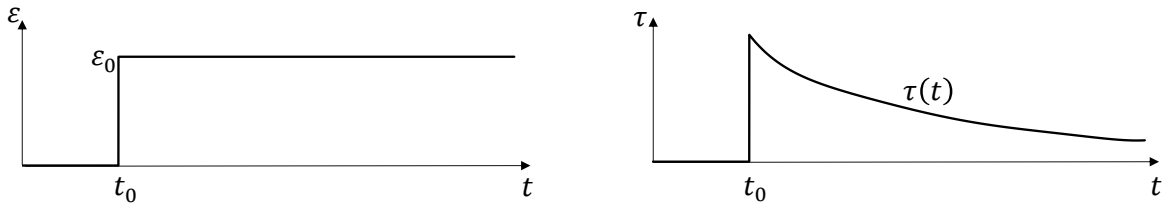

(a) strain history (b) stress history

Source: Adapted from Banks et al. (2010).

Figure 3.6: Stress and strain histories in the creep compliance test.

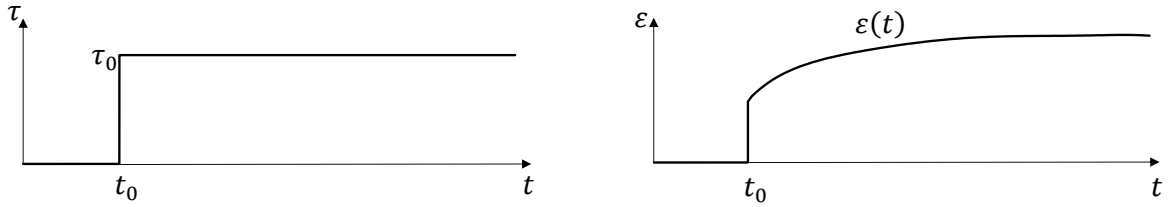

(a) stress history (b) strain history

Source: Adapted from Banks et al. (2010).

A viscoelastic material exhibits different behaviors during the loading and unloading phases. For example, in a material that can be modelled by the Kelvin-Voigt mechanical model, Fig. 3.7, the stress-strain curve increases monotonically during loading and decreases in the opposite direction during unloading. This results in the material exhibiting hysteresis. The Kelvin-Voigt material displays hysteresis due to its ability to remember whether it is being loaded or unloaded (BANKS et al., 2010).

According to the Boltzmann superposition principle (BOLTZMANN, 1874), two stress increments, τ_0 and τ_1, applied at different times, $t = 0$ and $t = t_1$, respectively, act independently, and the resultant strains add linearly, Fig. 3.8. Thus

$$\varepsilon(t) = \tau_0\,\iota(t) + \tau_1\,\iota(t - t_1). \tag{3.106}$$

Figure 3.7: Stress and strain curves during cyclic loading-unloading of a a material that can be modelled by the Kelvin-Voigt mechanical model.

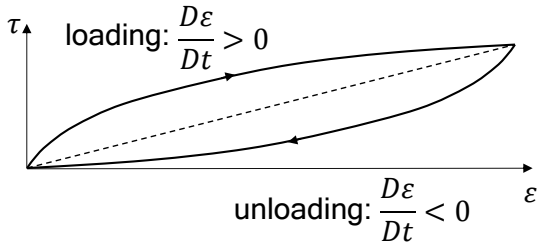

Source: Adapted from Banks et al. (2010).

That applies not only to two stress increments but also to a more general experiment consisting of discrete stress increments applied at different times,

$$\varepsilon(t) = \sum_{j=0}^{n} \tau_j \, \iota(t - t_j), \quad j = 1, 2, \ldots, n. \tag{3.107}$$

Figure 3.8: Linear addition of strains resulting from sequentially applied stresses.

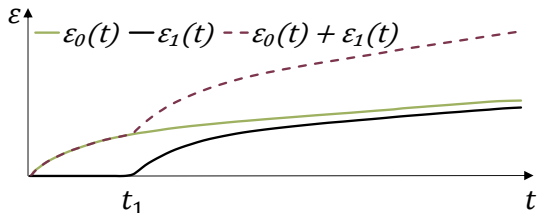

Source: Adapted from Shaw and MacKnight (2005).

The summation of individual τ_j, where $j = 1, 2, \ldots, n$, represents the total stress. For continuous stress application, the increment of applied stress is the derivative of τ_j multiplied by the increment of time $\mathrm{d}\flat$. The summation can be replaced by integration, resulting in

$$\varepsilon(t) = \int_{-\infty}^{t} \iota(t - \flat) \, \frac{D}{D\flat} \tau(\flat) \, \mathrm{d}\flat. \tag{3.108}$$

The variable t in the Eq. (3.108) denotes the time at which the strain is observed. The integration variable $\flat$ considers the stress history for the analysis. The lower limit of integration is $-\infty$, as the complete stress history plays a role in the observed strain. The upper limit is t since stresses applied after this point have no significant impact on the observed strain. Hence, integrating Eq. (3.108) by parts, it becomes

$$\varepsilon(t) = \iota(t-\flat)\ \tau(\flat)\Big|_{-\infty}^{t} - \int_{-\infty}^{t} \tau(\flat)\ \frac{D}{D\flat}\iota(t-\flat)\,\mathrm{d}\flat. \tag{3.109}$$

If the sample is initially unstressed, then $\tau(-\infty)$ must be zero. Considering such initial state and setting $t-\flat$ to t', Eq. (3.108) becomes

$$\varepsilon(t) = \iota(0)\ \tau(t) + \int_{0}^{t} \tau(t-t')\ \frac{D}{Dt'}\iota(t')\,\mathrm{d}t'. \tag{3.110}$$

To create the creep compliance function model, one must define the ideal mechanical elements: the Hookean spring, Fig. 3.9a, and the Newtonian dashpot, Fig. 3.9b. A Hookean spring is made of a homogenous and isotropic material, demonstrating linear-elastic behavior and a constant Poisson's ratio. When subjected to an instantaneous strain, it produces instantaneous stress

$$\tau(t) = G\,\varepsilon(t), \tag{3.111}$$

where G is the relaxation modulus or the Young modulus. However, most real materials with elasticity do not strictly follow Hooke's law due to inertia and a small time dependence.

Figure 3.9: Ideal mechanical elements.

(a) Hookean spring (b) Newtonean dashpot

Source: Own authorship.

The Newtonean dashpot consists of a leaky piston in a cylinder filled with a Newtonean viscous liquid. When subjected to a homogeneous, isotropic, isentropic, and incompressible flow, the shear stress along the cylinder cross-section is described by

$$\tau(t) = \mu\,\frac{D}{Dt}\varepsilon(t), \tag{3.112}$$

where μ represents the liquid dynamic viscosity.

The Voigt model, Fig. 3.10, assumes that a viscoplastic material's behavior can be approximated by a parallel composition of a Hookean spring and a Newtonian dashpot. As a result, the strain is equal in both mechanical elements, and the stress is the sum

of the stresses in the two components. Therefore, using Eq. (3.111) and Eq. (3.112), the stress applied on a Voigt element can be calculated using

$$\tau\left(t\right) = G\,\varepsilon\left(t\right) + \mu\,\frac{D}{Dt}\varepsilon\left(t\right). \tag{3.113}$$

Figure 3.10: Schematic of a Voigt element.

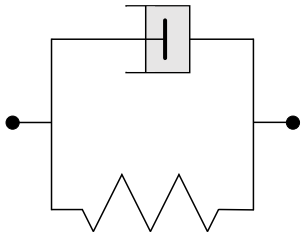

Source: Own authorship.

In a creep experiment context, the Voigt model is under constant stress (τ_0). Hence, Eq. (3.113) reduces to

$$\frac{G}{\mu}\,\varepsilon\left(t\right) + \frac{D}{Dt}\varepsilon\left(t\right) = \frac{\tau_0}{\mu}. \tag{3.114}$$

Then, using the integrating factor $\exp\left(t\,G/\mu\right)$, one obtains

$$\int_{\varepsilon(0)}^{\varepsilon(t)} \frac{D}{Dt'}\left[\varepsilon\left(t'\right)\,\exp\left(t'\,\mu/G\right)\right]\mathrm{d}t' = \frac{\tau_0}{\mu}\int_0^t \exp\left(t'\,G/\mu\right)\mathrm{d}t',$$

$$\varepsilon\left(t\right) = \frac{\tau_0}{G}\left[1 - \exp\left(-t\,G/\mu\right)\right], \tag{3.115}$$

which can be rewritten as

$$\iota\left(t\right) = \iota\left[1 - \exp\left(-t\,G/\mu\right)\right], \tag{3.116}$$

using the definition from Eq. (3.104). In Eq. (3.116), $\iota\left(t\right) = \varepsilon\left(t\right)/\tau_0$ and $\iota = 1/G$. Furthermore, the Voigt model can be generalized into the Kelvin-Voigt model, which is a composition of Voigt elements in series, Fig. 3.11. Using the Boltzmann superposition principle, the creep compliance of a Kelvin-Voigt model is

$$\iota\left(t\right) = \iota_0 + \sum_{j=1}^{n} \iota_j\left[1 - \exp\left(-t\,G_j/\mu_j\right)\right], \tag{3.117}$$

where $\iota_j = 1/G_j$, with $j = 0, 1, 2, \cdots n$.

Figure 3.11: Schematic of the Kelvin-Voigt model.

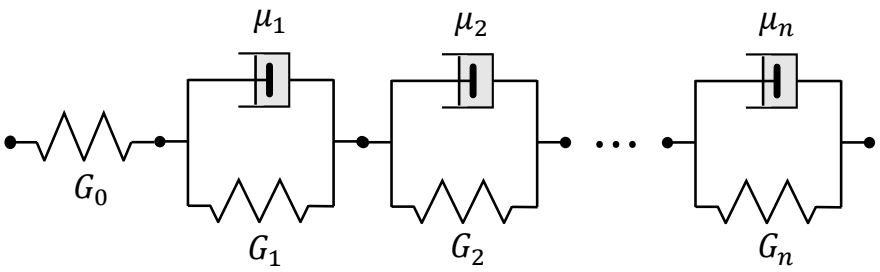

Source: Own authorship.

If the pipe material is homogeneous and isotropic, has linear viscoelastic behavior for small strains, and Poisson's ratio is constant, the mechanical behavior depends only on a creep function. Additionally, if the wall thickness is at least ten times less than the pipe radius, the hoop stress (τ_h) can be determined using

$$\tau_h\left(x_1, t\right) = \frac{\alpha_p\, d\, \rho\, g\, h\left(x_1, t\right)}{2\, b_p}, \tag{3.118}$$

which applied in Eq. (3.110) leads to

$$\varepsilon\left(t\right) = \frac{\alpha_p\, d\, \rho\, g}{2\, b_p}\, \left[h\left(x_1, t\right) - h^0\left(x_1\right)\right]\, \iota_0 + \frac{\alpha_p\, d\, \rho\, g}{2\, b_p}\, \int_0^t \left[h\left(x_1, t - t'\right) - h^0\left(x_1\right)\right] \frac{D}{Dt'} \iota\left(t'\right) \mathrm{d}t' \tag{3.119}$$

where α_p is the pipe-wall constrain coefficient, d is the pipe internal diameter, ρ is the density, g is the gravity acceleration, b_p is the pipe-wall thickness, $h\left(t\right)$ and h^0 are the piezometric head at t and $t = 0$, respectively, ι is the creep compliance function. Consider

$$F_\tau\left(x_1, t\right) = \frac{\alpha_p\, d\, \rho\, g}{2\, b_p}\, \left[h\left(x_1, t\right) - h^0\left(x_1\right)\right], \tag{3.120}$$

and apply Eq. (3.117) in Eq. (3.119), then Eq. (3.119) can be rewritten as

$$\varepsilon\left(r\right) = \iota_0\, F_\tau\left(x_1, t\right) + \sum_{j=1}^{n} \int_0^t F_\tau\left(x_1, t - t'\right)\, \frac{\iota_j\, G_j}{\mu_j} \exp\left(\frac{t'\, G_j}{\mu_j}\right) \mathrm{d}t' \tag{3.121}$$

where the first term at the right-hand side is the elastic strain (ε_0) and the component in the integral is the retarded strain (ε_t).

Applying the time derivative on the retarded strain j-th component, leads to

$$\frac{D}{Dt}\varepsilon_{r,j}\left(x_1,t\right)=\frac{D}{Dt}\int_0^t F_\tau\left(x_1,t-t'\right)\,\frac{\iota_j\,G_j}{\mu_j}\exp\left(\frac{t'\,G_j}{\mu_j}\right)\mathrm{d}t'$$

$$=\frac{D}{Dt}\left[-\frac{\iota_j\,G_j}{\mu_j}\int_t^0 F_\tau\left(x_1,y\right)\exp\left(\frac{\left(y-t\right)\,G_j}{\mu_j}\right)\mathrm{d}y\right]$$

$$=\frac{D}{Dt}\left[-\frac{\iota_j\,G_j}{\mu_j}\exp\left(\frac{-t\,G_j}{\mu_j}\right)\int_0^t F_\tau\left(x_1,y\right)\exp\left(\frac{y\,G_j}{\mu_j}\right)\mathrm{d}y\right]$$

$$\frac{D}{Dt}\varepsilon_{r,j}\left(x_1,t\right)=-\frac{\iota_j\,G_j^2}{\mu_j^2}\exp\left(\frac{-t\,G_j}{\mu_j}\right)\int_0^t F_\tau\left(x_1,y\right)\exp\left(\frac{y\,G_j}{\mu_j}\right)\mathrm{d}y$$

$$+\frac{\iota_j\,G_j}{\mu_j}\exp\left(\frac{-t\,G_j}{\mu_j}\right)\frac{D}{Dt}\int_0^t F_\tau\left(x_1,y\right)\exp\left(\frac{y\,G_j}{\mu_j}\right)\mathrm{d}y$$

$$=-\frac{\iota_j\,G_j^2}{\mu_j^2}\exp\left(\frac{-t\,G_j}{\mu_j}\right)\int_0^t F_\tau\left(x_1,y\right)\exp\left(\frac{y\,G_j}{\mu_j}\right)\mathrm{d}y$$

$$+\frac{\iota_j\,G_j}{\mu_j}\exp\left(\frac{-t\,G_j}{\mu_j}\right)F_\tau\left(x_1,y\right)\exp\left(\frac{y\,G_j}{\mu_j}\right)$$

$$=-\frac{\iota_j\,G_j^2}{\mu_j^2}\int_0^t F_\tau\left(x_1,y\right)\exp\left(\frac{\left(y-t\right)\,G_j}{\mu_j}\right)\mathrm{d}y+\frac{\iota_j\,G_j}{\mu_j}F_\tau\left(x_1,y\right)$$

$$=-\frac{\iota_j\,G_j^2}{\mu_j^2}\int_t^0 F_\tau\left(x_1,t-t'\right)\exp\left(\frac{-t'\,G_j}{\mu_j}\right)\left(-1\right)\mathrm{d}t'+\frac{\iota_j\,G_j}{\mu_j}F_\tau\left(x_1,t\right)$$

$$=-\frac{G_j}{\mu_j}\int_0^t F_\tau\left(x_1,t-t'\right)\,\frac{\iota_j\,G_j}{\mu_j}\exp\left(\frac{-t'\,G_j}{\mu_j}\right)\mathrm{d}t'+\frac{\iota_j\,G_j}{\mu_j}F_\tau\left(x_1,t\right)$$

$$\frac{D}{Dt}\varepsilon_{r,j}\left(x_1,t\right)=\frac{\iota_j\,G_j}{\mu_j}F_\tau\left(x_1,t\right)-\frac{G_j}{\mu_j}\,\varepsilon_{r,j}\left(x_1,t\right)\tag{3.122}$$

To calculate the j-th retarded strain in the right-hand side of Eq. (3.122), one uses a Taylor series expansion for approximation. First, one splits the j-th retarded strain into two components:

$$\varepsilon_{r,i}\left(x_1,t\right)=\underbrace{\int_0^{\Delta t}F_\tau\left(x_1,t-t'\right)\,\frac{\iota_j\,G_j}{\mu_j}\,\exp\left(\frac{-t'\,G_j}{\mu_j}\right)\,\mathrm{d}t'}_{A}$$
$$+\underbrace{\int_{\Delta t}^{t}F_\tau\left(x_1,t-t'\right)\,\frac{\iota_j\,G_j}{\mu_j}\,\exp\left(\frac{-t'\,G_j}{\mu_j}\right)\,\mathrm{d}t'}_{B} \tag{3.123}$$

Next, one adjusts the integral limits to incorporate a past value and expands component A using a Taylor series. This process yields

$$A=-\int_t^{t-\Delta t}F_\tau\left(x_1,t''\right)\,\frac{\iota_j\,G_j}{\mu_j}\,\exp\left[\frac{\left(t''-t\right)\,G_j}{\mu_j}\right]\,\mathrm{d}t''$$

$$A=-F_\tau\left(x_1,t''\right)\,\iota_j\,\exp\left[\frac{\left(t''-t\right)\,G_j}{\mu_j}\right]\Bigg|_t^{t-\Delta t}$$

$$+\,\frac{\iota_j\mu_j}{G_j}\,\frac{D}{Dt''}F_\tau\left(x_1,t''\right)\exp\left[\frac{\left(t''-t\right)\,G_j}{\mu_j}\right]\Bigg|_t^{t-\Delta t}$$

$$\underbrace{-\int_t^{t-\Delta t}\frac{D^2}{Dt''^2}F_\tau\left(x_1,t''\right)\,\frac{\mu_j}{G_j}\,\exp\left[\frac{\left(t''-t\right)\,G_j}{\mu_j}\right]\,\mathrm{d}t''}_{\text{second order}\approx 0}$$

$$A\approx\iota_j\left[F_\tau\left(x_1,t\right)-F_\tau\left(x_1,t-\Delta t\right)\exp\left(\frac{-\Delta t\,G_j}{\mu_j}\right)\right]$$
$$-\,\frac{\iota_j\mu_j}{G_j}\,\frac{D}{Dt}F_\tau\left(x_1,t\right)\,\left[1-\exp\left(\frac{-\Delta t\,G_j}{\mu_j}\right)\right]. \tag{3.124}$$

Changing the integral limits of the component B, one gets

$$B=\int_{\Delta t}^{t}F_\tau\left(x_1,t-t'\right)\,\frac{\iota_j\,G_j}{\mu_j}\,\exp\left(\frac{-t'\,G_j}{\mu_j}\right)\,\mathrm{d}t'$$

$$B=\int_0^{t-\Delta t}F_\tau\left(x_1,t-\Delta t-y\right)\,\frac{\iota_j\,G_j}{\mu_j}\,\exp\left[\frac{\left(-y-t'\right)\,G_j}{\mu_j}\right]\,\mathrm{d}y$$

$$B=\varepsilon_{r,i}\left(x_1,t-\Delta t\right)\,\exp\left(\frac{-\Delta t\,G_j}{\mu_j}\right). \tag{3.125}$$

Substituting Eq. (3.124) and Eq. (3.125) in Eq. (3.122), one obtains

$$\frac{D}{Dt}\varepsilon_{r,j}\left(x_1,t\right)=\frac{\alpha_p\,d\,\rho\,g}{2\,b_p}\left\{\frac{\iota_j\,G_j}{\mu_j}\left[h\left(x_1,t-\Delta t\right)-h^0\left(x_1\right)\right]\exp\left(\frac{-\Delta t\,G_j}{\mu_j}\right)\right.$$

$$\left.+\iota_j\frac{D}{Dt}h\left(x_1,t\right)\left[1-\exp\left(\frac{-\Delta t\,G_j}{\mu_j}\right)\right]\right\}-\varepsilon_{t,j}\left(x_1,t-\Delta t\right)\exp\left(\frac{-\Delta t\,G_j}{\mu_j}\right) \tag{3.126}$$

3.9 Model's summary

This section provides a detailed summary of the mathematical model for analyzing hydraulic transients in viscoelastic pipes. It is formulated in a Lagrangian framework and takes into account the impact of unsteady friction. Hence,

$$\frac{Dh}{Dt}+\frac{2\,a^2}{g}\,\frac{D\varepsilon_r}{Dt}+\frac{a^2}{g}\,\frac{\partial u_1}{\partial x_1}=0, \tag{3.127}$$

$$\frac{Du_1}{Dt}+g\frac{\partial h}{\partial x_1}+\frac{4\,\tau}{\rho\,d}=0, \tag{3.128}$$

where u_1 is the velocity along the pipe's center axis, h is the pressure load, a is the wave speed, g is the gravitational acceleration, ε_r is the retarded strain, ρ is the fluid density, d is the pipe internal diameter, τ is the friction, and $D\left(\cdot\right)/Dt$ is the material derivative. The friction can be modelled by any of the following 3 models:

$$\tau=\frac{1}{8}\,\rho\,\lambda\,|u_1|u_1+K\frac{\rho\,d}{4}\left(\frac{\partial u_1}{\partial t}+a\,\mathrm{sign}\left(u_1\right)\,\frac{\partial u_1}{\partial x_1}\right), \tag{3.129}$$

$$\tau=\frac{1}{8}\,\rho\,\lambda\,|u_1|u_1+\frac{\rho\,d}{4}\left(K_1\frac{\partial u_1}{\partial t}+K_2\,a\,\mathrm{sign}\left(u_1\right)\,\frac{\partial u_1}{\partial x_1}\right), \tag{3.130}$$

or

$$\tau=\frac{1}{8}\,\rho\,\lambda\,|u_1|u_1+\frac{4\,\nu\,\rho}{d}\left[Y_1\left(t\right)+Y_2\left(t\right)\right], \tag{3.131}$$

where Y_m are defined as

$$Y_m\left(t\right)=\begin{cases}0, & t=0,\\ Y_{m,t^*}\,\exp\left(-B_m\psi\right)+T_m\left(u_1^t-u_1^{t^*}\right), & t>0.\end{cases} \tag{3.132}$$

Note that λ is Darcy's friction coefficient ν is the fluid kinematic viscosity, t^* represents the instant before t, $\psi=4\,\nu\left(t-t^*\right)/d^2$, and the values for the coefficients B_m and T_m

are given by Tab. 3.2, in which $\lambda_R\, Re = 0.25\, \lambda\, Re$. Additionally, K, K_1, and K_2 are experimentally determined coefficients.

Table 3.2 – Values of the coefficients B_m and T_m for several ranges defined by $\lambda_R Re$.

$\lambda_R Re$	T_1	T_2	B_1	B_2
250.000	250.000	74.000	4.400×10^5	4.200×10^5
500.000	260.000	65.000	5.600×10^5	1.150×10^5
1000.000	350.000	65.000	9.800×10^5	4.120×10^5
2000.000	470.000	65.000	2.800×10^5	1.620×10^5

The last component is the retarded strain time derivative in Eq. (3.127), which is defined as the summatory of

$$\frac{D}{Dt}\varepsilon_{r,j}\left(x_1, t\right) = \frac{\iota_j}{\natural_j} F_\tau\left(x_1, t\right) - \frac{1}{\natural_j}\varepsilon_{r,j}\left(x_1, t\right), \tag{3.133}$$

where F_τ is defined as

$$F_\tau\left(x_1, t\right) = \frac{\alpha_p\, d\, \rho\, g}{2\, b_p}\left[h\left(x_1, t\right) - h^0\left(x_1\right)\right], \tag{3.134}$$

in which j stand for the number Voigt elements composing the chosen Kelvin-Voigt model, G is the relaxation modulus, ι is the creep compliance, α_p is the pipe-wall constrain coefficient, b_p is the pipe-wall thickness, h^0 is the pressure load at $t = 0$, μ_j are the viscosity of Newtonean dashpots in the Voigt elements, $\natural = \mu/G$ and Δt is the time step. Furthermore, the retarded strain is defined as

$$\begin{aligned}\varepsilon_{r,j}\left(x_1, t\right) \approx \iota_j & \left[F_\tau\left(x_1, t\right) - F_\tau\left(x_1, t - \Delta t\right) \exp\left(-\frac{\Delta t}{\natural_j}\right)\right] - \\ & \iota_j\, \natural_j\, \frac{D}{Dt} F_\tau\left(x_1, t\right)\left[1 - \exp\left(-\frac{\Delta t}{\natural_j}\right)\right] + \\ & \varepsilon_{r,j}\left(x_1, t - \Delta t\right) \exp\left(-\frac{\Delta t}{\natural_j}\right).\end{aligned} \tag{3.135}$$

4 SMOOTHED PARTICLES HYDRODYNAMIC METHOD (SPH)

Gingold and Monaghan (1977) and Lucy (1977) developed the Smoothed Particle Hydrodynamic method initially and independently to solve astrophysical problems. Later, Monaghan (1983) extended to fluid mechanics, while Libersky et al. (1993) extended SPH to solid mechanics and Monaghan (1992) covered heat transfer and magnetic phenomena.

The SPH method is a meshless and Lagrangian approach that uses a set of irrotational particles to discretize the continuum domain. These particles move according to balance equations without any mesh connectivity (LIU; LIU, 2003a; SIGALOTTI et al., 2021). The SPH method achieves interpolation without connectivity by using integral convolution representation for field function approximation, replacing integral representations with summations over neighboring particles in a local domain called the support domain. This interpolation repeats at every time step, depending on the current local distribution of particles (adaptability). The particle approximations produce a set of ordinary differential equations (ODEs) in discretized form concerning time (LIU; LIU, 2003a).

The SPH method offers advantages over traditional grid-based numerical methods, particularly its adaptive nature. This method is not affected by mesh distortions, making it suitable for simulations of large material deformations (LIU; LIU, 2003a). Additionally, the SPH method performs precisely the advection, allowing for accurate tracking of material history information without numerical diffusion (SIGALOTTI et al., 2021).

The classical SPH method has slow numerical convergence due to loss of particle consistency, which is defined as:

Definition 4.0.1 *Consistency refers to how well an approximation can replicate an exact equation. When using polynomials for assessment, an approximation has consistency C_n if it accurately reproduces a polynomial of order n (LIU; LIU, 2006; SIGALOTTI et al., 2021).*

To address the inconsistency issue, corrections and modifications have been proposed over the years. One proposed solution is the Corrective Smoothed Particle Method (CSPM)(CHEN et al., 1999), which uses Taylor series expansions to restore particle consistency, resulting in improved stability. This method restores C_1 kernel consistency everywhere except at the boundaries, where the kernel consistency drops to C_0.

Therefore, the present chapter covers the fundamentals of the SPH method and some of the corrections needed to improve its stability and accuracy.

4.1 The SPH Method Fundamentals

The SPH method is based on the properties of the Dirac function (δ_D), which is rigorously defined as a distribution:

Definition 4.1.1 *Let $\Omega \subseteq \mathbb{R}^n$ be a non-empty open set. A distribution $w_d \in \mathcal{D}'(\Omega)$ is a bounded linear functional on $\mathcal{D} = C_0^\infty$. More specifically, $w_d : \mathcal{D} \to \mathbb{C}$ is a linear map, and if $K_s \subseteq \Omega$ is any compact set, then there are $M = M(K_c) \geq 0$ and $N = N(K_c) \geq 0$ such that*

$$|w_d(\varphi_d)| \leq M \sup_{\boldsymbol{x} \in \Omega, |j| \leq N} \left| \frac{\partial^j}{\partial \boldsymbol{x}^j} \varphi_d(\boldsymbol{x}) \right|, \tag{4.1}$$

for all $\varphi_d \in \mathcal{D}$ with support as a subset of K_c ($\operatorname{supp}(\varphi_d) \subseteq K_d$). $\mathcal{D}'(\Omega)$ in the space of all distributions on Ω and C_0^∞ is the vector space of smooth functions with compact support, also known as test functions (DUISTERMAAT; KOLK, 2010).

Therefore, δ_D distribution is a linear functional on $\mathcal{D}(\Omega)$ and is defined by

$$\delta_D(\varphi_d) = \varphi_d(0), \tag{4.2}$$

for every test function $\varphi_d \in \mathcal{D}(\Omega)$. The δ_D distribution is a distribution of order zero ($M = 1$ and $N = 0$) having a compact support being $\{0\}$. Furthermore, δ_D distribution is constrained to satisfy the identity

$$\int_\Omega \delta_D(\boldsymbol{x}) \, \mathrm{d}\boldsymbol{x} = 1. \tag{4.3}$$

As a result, the Lebesgue integral concerning the δ_D distribution satisfies

$$f(\boldsymbol{x}) = \int_\Omega f(\boldsymbol{x}_b) \, \delta_D(\boldsymbol{x} - \boldsymbol{x}_b) \, \mathrm{d}\boldsymbol{x}_b \tag{4.4}$$

for all continuous compactly supported functions $f \in \mathcal{D}(\Omega)$, such that $f : \mathbb{R}^n \to \mathbb{R}$. One consequence of the convolution operation in Eq. (4.4) is given by the Titchmarsh convolution theorem (HöRMANDER, 1998):

Theorem 4.1.1 *Let $f \in \mathcal{D}(\Omega)$ and $w_d \in \mathcal{D}'(\Omega)$, then*

$$\operatorname{supp}\left(\int_\Omega f(\boldsymbol{x}_b) \, w_d(\boldsymbol{x} - \boldsymbol{x}_b) \, \mathrm{d}\boldsymbol{x}_b \right) \subseteq \operatorname{supp}(f) + \operatorname{supp}(w_d). \tag{4.5}$$

Theorem 4.1.1 guarantees that $f(\boldsymbol{x})$ in Eq. (4.4) has a support within the supports of f and δ_D. However, numerically, one cannot calculate directly the δ_D distribution but needs to approximate it. Hence, kernel functions (W) are used to construct a kernel approximation of Eq. (4.4), as described in

$$\langle f(\boldsymbol{x})\rangle = \int_{\Omega} f(\boldsymbol{x}_b)\, W(\|\boldsymbol{x}-\boldsymbol{x}_b\|, h_s)\, \mathrm{d}\boldsymbol{x}_b, \tag{4.6}$$

where $\langle f(\boldsymbol{x})\rangle$ is the smoothed estimate of $f(\boldsymbol{x})$, and h_s is the smoothing length. Let $K_c \subseteq \Omega$ be a compact set with the neighborhood defined by $\|\boldsymbol{x}-\boldsymbol{x}_b\| \leq \kappa_s h_s$ as its compact support ($\mathrm{supp}\,[W(\|\boldsymbol{x}-\boldsymbol{x}_b\|, h_s)]$), with $\boldsymbol{x}_b, \boldsymbol{x} \in K_c$, and $\kappa_s, h_s \in \mathbb{R}_+$ where κ_s is a constant related to the kernel function. Then, the distribution W is bell-shaped and must satisfy the following conditions within K_c (LIU; LIU, 2003a; SIGALOTTI et al., 2021):

1. Normalization:

$$\int_{K_c} W(\|\boldsymbol{x}-\boldsymbol{x}_b\|, h_s)\, \mathrm{d}\boldsymbol{x}_b = 1; \tag{4.7}$$

2. Equality to the Dirac delta distribution:

$$\lim_{h_s\to 0} W(\|\boldsymbol{x}-\boldsymbol{x}_b\|, h_s) = \delta_D(\boldsymbol{x}-\boldsymbol{x}_b); \tag{4.8}$$

3. Positive definiteness: $W(\|\boldsymbol{x}-\boldsymbol{x}_b\|, h_s) > 0$ for every non-zero $\boldsymbol{x}_b \in \mathrm{supp}(K_c)$;

4. Evenness: $W(\|\boldsymbol{x}-\boldsymbol{x}_b\|, h_s) = W(-\|\boldsymbol{x}-\boldsymbol{x}_b\|, h_s)$;

5. Monotonically decreasing behavior: if, whenever $\boldsymbol{x}_a \leq \boldsymbol{x}_b$, then $W(\|\boldsymbol{x}-\boldsymbol{x}_a\|, h_s) \geq W(\|\boldsymbol{x}-\boldsymbol{x}_b\|, h_s)$;

6. Compact condition: $W(\|\boldsymbol{x}-\boldsymbol{x}_b\|, h_s) = 0$ when $\|\boldsymbol{x}-\boldsymbol{x}_b\| \geq \kappa_s h_s$.

7. Smoothness:the smoothing function should be sufficiently smooth.

Modern SPH applications use kernels with compact support, where W is 0 except within a sphere of radius $k h_s$ from the center $\boldsymbol{x}$.

The Kernel approximation has a truncation error of order $O(h_s^2)$. To assess this, expand $f(x_b)$ in the integrand of Eq. (4.6) in the Taylor series about $\boldsymbol{x}$, which gives

$$\begin{aligned}\langle f(\boldsymbol{x})\rangle = f(\boldsymbol{x}) \int_{\Omega} W(\|\boldsymbol{x}-\boldsymbol{x}_b\|, h_s)\, \mathrm{d}\boldsymbol{x}_b + \\ + \sum_{j=1}^{\infty} \frac{1}{j!} \nabla^{(j)} f(\boldsymbol{x}) :: \ldots : \int_{\Omega} (\boldsymbol{x}_b-\boldsymbol{x})^j\, W(\|\boldsymbol{x}-\boldsymbol{x}_b\|, h_s)\, \mathrm{d}\boldsymbol{x}_b\end{aligned} \tag{4.9}$$

where ∇^j represents the product of the ∇ operator j times concerning the coordinate $\boldsymbol{x}$, and the symbol $:: \ldots :$ is utilized to denote the jth-order inner product. Additionally, $(\boldsymbol{x}_b - \boldsymbol{x})^j$ is a tensor of rank j. Considering the normalization property of the kernel function in Eq. (4.7), then Eq. (4.9) can be rewritten as

$$\langle f(\boldsymbol{x}) \rangle = f(\boldsymbol{x}) + \sum_{j=1}^{\infty} \frac{1}{j!} \nabla^{(j)} f(\boldsymbol{x}) :: \ldots : \int_{\Omega} (\boldsymbol{x}_b - \boldsymbol{x})^j \; W(\|\boldsymbol{x} - \boldsymbol{x}_b\|, h_s) \, \mathrm{d}\boldsymbol{x}_b \tag{4.10}$$

Thus, $\langle f(\boldsymbol{x}) \rangle$ becomes $f(\boldsymbol{x})$ only if the family of consistency relations is satisfied for the moments of the kernel, as shown in

$$\mathbf{M}_j = \int_{\Omega} (\boldsymbol{x}_b - \boldsymbol{x})^j \; W(\|\boldsymbol{x} - \boldsymbol{x}_b\|, h_s) \, \mathrm{d}\boldsymbol{x}_b = \mathbf{0}^{(j)} \tag{4.11}$$

for $j \in \mathbb{N}$, where $\mathbf{0}^{(j)}$ is the null tensor of rank j. The normalization property ensures consistency C_0. When $j = 1$, the kernel moment is null due to symmetry, ensuring consistency C_1. This holds for all odd values of j. However, for even values of j, the moments are not necessarily null, so consistency C_2 is not guaranteed, and the kernel approximation has a truncation error of order $O(h_s^2)$ since $\|\boldsymbol{x}_b - \boldsymbol{x}\|^2 \leq \kappa_s \, h_s^2$.

To solve partial differential equations, the gradient form of the kernel approximation is required. Thus, applying the kernel approximation on the $\nabla f(\boldsymbol{x})$, one obtains

$$\langle \nabla f(\boldsymbol{x}) \rangle = \int_{\Omega} [\nabla f(\boldsymbol{x}_b)] \; W(\|\boldsymbol{x} - \boldsymbol{x}_b\|, h_s) \, \mathrm{d}\boldsymbol{x}_b. \tag{4.12}$$

Considering the identity

$$\nabla f(\boldsymbol{x}_b) = \nabla [f(\boldsymbol{x}_b) \; W(\|\boldsymbol{x} - \boldsymbol{x}_b\|, h_s)] - f(\boldsymbol{x}_b) \; \nabla W(\|\boldsymbol{x} - \boldsymbol{x}_b\|, h_s), \tag{4.13}$$

and substituting Eq. (4.13) in Eq. (4.12), one gets

$$\begin{aligned} \langle \nabla f(\boldsymbol{x}) \rangle &= \int_{\Omega} \{\nabla [f(\boldsymbol{x}_b) \; W(\|\boldsymbol{x} - \boldsymbol{x}_b\|, h_s)] - f(\boldsymbol{x}_b) \; \nabla W(\|\boldsymbol{x} - \boldsymbol{x}_b\|, h_s)\} \, \mathrm{d}\boldsymbol{x}_b, \\ &= \int_s [f(\boldsymbol{x}_b) \; W(\|\boldsymbol{x} - \boldsymbol{x}_b\|, h_s)] \, \mathbf{n} \, \mathrm{d}s - \int_{\Omega} f(\boldsymbol{x}_b) \; \nabla W(\|\boldsymbol{x} - \boldsymbol{x}_b\|, h_s) \, \mathrm{d}\boldsymbol{x}_b \end{aligned} \tag{4.14}$$

When the support domain is within the problem domain, Fig. 4.1a, the integral over the boundary of the support domain reduces to zero. However, if the boundary of the support domain overlaps the problem domain, Fig. 4.1b, the surface integral may not vanish due

to the truncated kernel function (LIU; LIU, 2003a). As a result, for points with support domains inside the problem domain, Eq. (4.14) simplifies to

$$\langle \nabla f(\boldsymbol{x}) \rangle = -\int_{\Omega} f(\boldsymbol{x}_b)\ \nabla W(\|\boldsymbol{x}-\boldsymbol{x}_b\|, h_s)\,\mathrm{d}\boldsymbol{x}_b \tag{4.15}$$

Figure 4.1: Schematic of the SPH kernel approximation with a compactly supported kernel function.

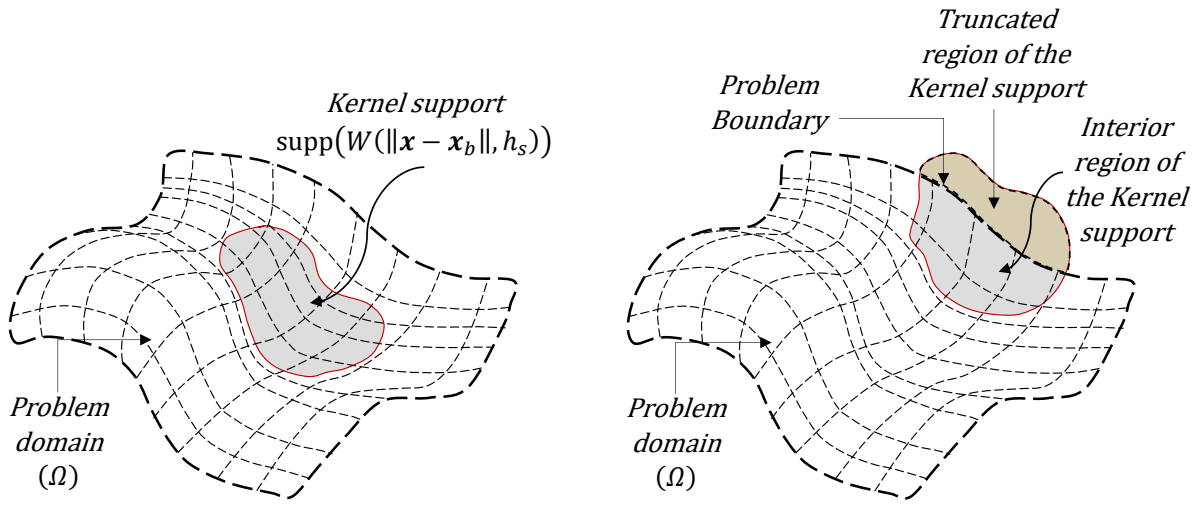

(a) Support domain within the problem domain

(b) Support domain intersects the problem domain

Source: Own authorship.

By expanding the integrand $f(\boldsymbol{x}_b)$ in Eq. (4.15) into a Taylor series, and taking the gradient concerning $\boldsymbol{x}$ instead of $\boldsymbol{x}_b$, vanishing the negative sign, one obtains

$$\begin{aligned}\langle \nabla f(\boldsymbol{x}) \rangle = f(\boldsymbol{x}) \int_{\Omega} \nabla W(\|\boldsymbol{x}-\boldsymbol{x}_b\|, h_s)\,\mathrm{d}\boldsymbol{x}_b \\ + \nabla f(\boldsymbol{x}) \cdot \int_{\Omega} (\boldsymbol{x}_b - \boldsymbol{x})\ \nabla W(\|\boldsymbol{x}-\boldsymbol{x}_b\|, h_s)\,\mathrm{d}\boldsymbol{x}_b \\ + \sum_{j=2}^{\infty} \frac{1}{j!} \nabla^{(j)} f(\boldsymbol{x}) :: \ldots : \int_{\Omega} (\boldsymbol{x}_b - \boldsymbol{x})^j\ \nabla W(\|\boldsymbol{x}-\boldsymbol{x}_b\|, h_s)\,\mathrm{d}\boldsymbol{x}_b\end{aligned} \tag{4.16}$$

Therefore, the kernel consistency relations given by

$$\nabla \mathbf{M}_0 = \int_\Omega \nabla W\left(\|\boldsymbol{x} - \boldsymbol{x}_b\|, h_s\right) \mathrm{d}\boldsymbol{x}_b = \mathbf{0}^1,$$

$$\nabla \mathbf{M}_1 = \int_\Omega \left(\boldsymbol{x}_b - \boldsymbol{x}\right) \nabla W\left(\|\boldsymbol{x} - \boldsymbol{x}_b\|, h_s\right) \mathrm{d}\boldsymbol{x}_b = \mathbf{0}^2, \tag{4.17}$$

$$\nabla \mathbf{M}_j = \int_\Omega \left(\boldsymbol{x}_b - \boldsymbol{x}\right)^j \nabla W\left(\|\boldsymbol{x} - \boldsymbol{x}_b\|, h_s\right) \mathrm{d}\boldsymbol{x}_b = \mathbf{0}^{j+1},$$

for $j = 2, 3, \cdots$, must be exactly fulfilled for an exact approximation to the gradient (SIGALOTTI et al., 2021).

The integral representation and the kernel approximation deal with the continuum domain. The SPH method uses Lagrangian particles to discretize the problem domain. The particles may be, in general, disordered due to the advection effect and are irrotational and undeformable, carrying material properties such as position, velocity, temperature, mass, and others. The initial discretization is based on dividing the problem domain into N subdomains (Ω_k), each containing a Lagrangian particle at a chosen position $\boldsymbol{x}_k$ within Ω_k, Fig. 4.2. The interaction among the particles is guaranteed by the kernel function, whose influence is within the kernel support (Ω_s), centered at the observation position $\boldsymbol{x}_a$. Numerical integration is performed over the intersection set between Ω_s and the finite model domain Ω, with the intersection set elements being the neighbors around particle a or subdomain Ω_a (SIGALOTTI et al., 2021).

Figure 4.2: Schematic of the SPH particle discretization with a compactly supported kernel function. The red particle is the observation particle a, while the blue ones are the neighbors particles around particle a.

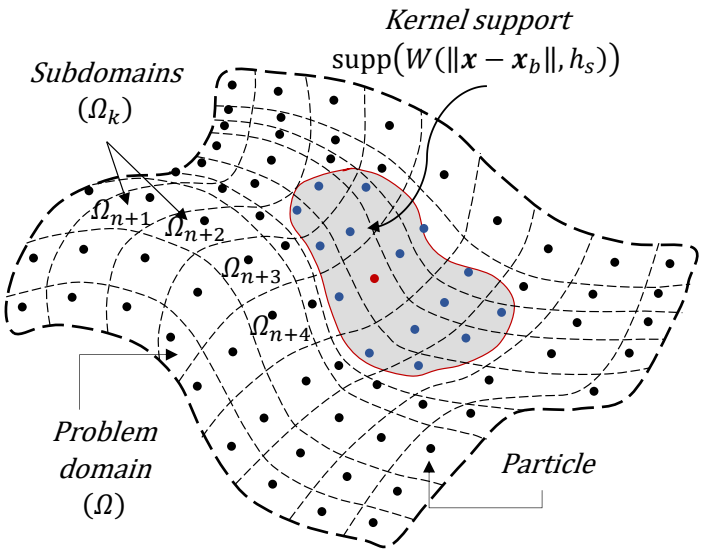

Source: Own authorship.

Using the mean value theorem

$$
\begin{aligned}
f_a &= \langle f(\boldsymbol{x}_a) \rangle \\
&= \sum_{b=1}^{N_{neigh}} \int_{\Omega_b} f(\boldsymbol{x}_b)\, W(\|\boldsymbol{x}_a - \boldsymbol{x}_b\|, h_s)\, \mathrm{d}\boldsymbol{x}_b \\
&\approx \sum_{b=1}^{N_{neigh}} f(\boldsymbol{x}_b)\, W(\|\boldsymbol{x}_a - \boldsymbol{x}_b\|, h_s)\, \Delta V_b
\end{aligned}
\tag{4.18}
$$

where the subscript b denotes the neighbor particles around particle a, N_{neigh} is the total number of neighbor particles, Ω_b is the subdomain containing the neighbor particles around particle a, and ΔV_b is the volume of Ω_b. Considering $N_{neigh} = n_a$, $\mathcal{N}_a = \{1, 2, \ldots, n_a\}$, $W(\|\boldsymbol{x}_a - \boldsymbol{x}_b\|, h_s) = W_{ab}$, and $\Delta V_b = m_b/\rho_b$, where m_b and ρ_b are the mass and density of each neigbor particle, respectively, then the particle approximation in Eq. (4.17) can be rewritten as

$$
f_a = \sum_{b \in \mathcal{N}_a} f_b\, W_{ab}\, \frac{m_b}{\rho_b}. \tag{4.19}
$$

Similarly, the particle approximation of the gradient of f_a is

$$
(\nabla f)_a = \sum_{b \in \mathcal{N}_a} f_b\, \nabla_a W_{ab}\, \frac{m_b}{\rho_b}, \tag{4.20}
$$

where ∇_a is the gradient concerning $\boldsymbol{x}_a$, being represented as

$$
\nabla_a W_{ab} = \frac{\boldsymbol{x}_{ab}}{r_{ab}} \frac{\partial W_{ab}}{\partial r_{ab}}, \tag{4.21}
$$

where $r_{ab} = \|\boldsymbol{x}_a - \boldsymbol{x}_b\|$ and $\boldsymbol{x}_{ab} = \boldsymbol{x}_a - \boldsymbol{x}_b$.

The particle approximation of the gradient has two more stable forms (LIU; LIU, 2003a). These involve placing the density inside the gradient operator, resulting in the identities

$$
\nabla f(\boldsymbol{x}) = \frac{1}{\rho} \left\{ \nabla \left[\rho\, f(\boldsymbol{x}) \right] - f(\boldsymbol{x})\, \nabla \rho \right\}, \tag{4.22}
$$

and

$$
\nabla f(\boldsymbol{x}) = \rho \left\{ \nabla \left[\frac{f(\boldsymbol{x})}{\rho} \right] + \frac{f(\boldsymbol{x})}{\rho^2}\, \nabla \rho \right\}. \tag{4.23}
$$

By applying a similar process used to obtain the particle approximation of Eq. (4.20) to the gradient components of Eq. (4.22) and Eq. (4.23), the equations become

$$\begin{aligned}(\nabla f)_a &= \frac{1}{\rho_a}\left\{\sum_{b\in\mathcal{N}_a}\rho_b\, f_b\,\nabla_a W_{ab}\,\frac{m_b}{\rho_b} - f_a\sum_{b\in\mathcal{N}_a}\rho_b\,\nabla_a W_{ab}\frac{m_b}{\rho_b}\right\},\\ &= \sum_{b\in\mathcal{N}_a}(f_b - f_a)\,\nabla_a W_{ab}\,\frac{m_b}{\rho_a},\end{aligned} \tag{4.24}$$

and

$$\begin{aligned}(\nabla f)_a &= \rho_a\left\{\sum_{b\in\mathcal{N}_a}\frac{f_b}{\rho_b}\,\nabla_a W_{ab}\,\frac{m_b}{\rho_b} + \frac{f_a}{\rho_a^2}\sum_{b\in\mathcal{N}_a}\rho_b\,\nabla_a W_{ab}\,\frac{m_b}{\rho_b}\right\},\\ &= \rho_a\sum_{b\in\mathcal{N}_a}\left(\frac{f_b}{\rho_b^2} + \frac{f_a}{\rho_a^2}\right)\nabla_a W_{ab}\,m_b.\end{aligned} \tag{4.25}$$

4.2 The Kernel Function

The kernel function is a distribution responsible for determining the pattern for the function approximation. Additionally, it defines the dimension of the support domain of particles and determines the consistency and, therefore, the accuracy of the kernel and particle approximations.

The normalization of the kernel function ensures zero-th-order consistency in approximating a continuous function. By having compact support, a global operation is transformed into a local one, and the positive definiteness of the kernel ensures physical coherence, such as positive density and energy.

The monotonically decreasing behavior ensures that the nearest particles have a greater influence on the concerned particle. The kernel evenness feature contributes by ensuring that particles with the same distance from the central particle but in different positions have a similar influence in the support domain.

The relationship between kernel smoothness and particle disorder sensitivity suggests that increased smoothness results in reduced disorder sensitivity. Additionally, higher accuracy is observed for well-ordered particles (MONAGHAN, 1992; FULK, 1994).

The first two kernels introduced were the bell-shaped kernel by Lucy (1977), Fig. 4.3, and the Gaussian kernel by Gingold and Monaghan (1977), Fig. 4.4. The bell-shaped kernel is defined by

$$W\left(\|\boldsymbol{x}-\boldsymbol{x}_b\|, h_s\right) = W\left(r_s, h_s\right) = \alpha_d \begin{cases} \left(1+3\,r_s\right)\left(1-r_s\right)^3, & 0 \leq r_s \leq 1, \\ 0 & r_s \geq 1, \end{cases} \tag{4.26}$$

with α_d being $5/2h_s$, $5/\pi\,h_s^2$, and $105/16\,\pi\,h_s^3$ in one, two, and three-dimensional space to ensure normalization across all dimensions. Additionally, $r_s = \|\boldsymbol{x}-\boldsymbol{x}_b\|/h_s$ represents the relative distance between two particles in the support domain. To exemplify how to calculate the coefficient α_d, consider the one-dimensional case of the bell-shaped kernel

$$\begin{aligned} \alpha_1 &= \left[\int_0^{h_s} \left(1+3\,\frac{x_1}{h_s}\right)\left(1-\frac{x_1}{h_s}\right)^3 \mathrm{d}x_1\right]^{-1} \\ &= \left[\left(-\frac{3\,r_s^5}{5\,h_s^4} + \frac{2\,r_s^4}{h_s^3} - \frac{2\,r_s^3}{h_s^2} + r_s\right)_0^{h_s}\right]^{-1} \\ &= \frac{5}{2\,h_s}. \end{aligned} \tag{4.27}$$

Considering cylindrical coordinates for the two-dimensional case, with r as the radius and θ as the angular coordinate, one obtains

$$\begin{aligned} \alpha_2 &= \left[\int_0^{2\,\pi}\int_0^{h_s} \left(1+3\,\frac{r}{h_s}\right)\left(1-\frac{r}{h_s}\right)^3 r\mathrm{d}r\mathrm{d}\theta\right]^{-1} \\ &= \left[2\,\pi\,\left(-\frac{r_s^6}{2\,h_s^4} + \frac{8\,r_s^5}{5\,h_s^3} - \frac{3\,r_s^4}{2\,h_s^2} + \frac{r_s^2}{2}\right)_0^{h_s}\right]^{-1} \\ &= \frac{5}{\pi\,h_s^2}. \end{aligned} \tag{4.28}$$

For the three-dimensional case, consider spherical coordinates, with r as the radius, and θ and ϕ as the angular coordinates. Then the coefficient is calculated as

$$\alpha_3 = \left[\int_0^{2\,\pi}\int_0^{\pi}\int_0^{h_s}\left(1+3\,\frac{r}{h_s}\right)\left(1-\frac{r}{h_s}\right)^3 r^2\,\sin(\theta)\,\mathrm{d}r\mathrm{d}\theta\mathrm{d}\phi\right]^{-1}$$

$$= \left[4\,\pi\,\left(-\frac{3\,r_s^7}{7\,h_s^4}+\frac{4\,r_s^6}{3\,h_s^3}-\frac{6\,r_s^5}{5\,h_s^2}+\frac{r_s^3}{3}\right)_0^{h_s}\right]^{-1} \tag{4.29}$$

$$= \frac{105}{16\,\pi\,h_s^3}.$$

Figure 4.3: The kernel and its first and second derivatives used by Lucy (1977).

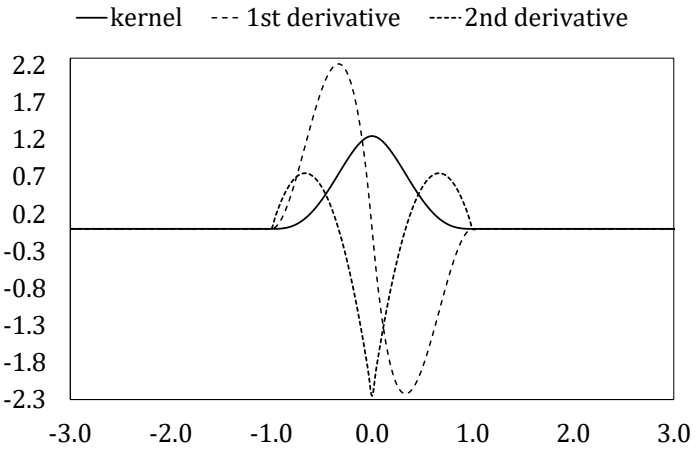

Source: Own authorship.

The Gaussian kernel proposed by Gingold and Monaghan (1977) is given by

$$W(r_s, h_s) = \alpha_d\,\exp\left(-r_s^2\right), \tag{4.30}$$

with the coefficient α_d taking values of $1/\pi^{1/2}\,h_s$, $1/\pi\,h^2$ and $1/\pi^{3/2}\,h^3$ in one, two, and three-dimensional space, respectively. This distribution maintains its smoothness under high-order derivatives, ensuring high stability and accuracy. However, it lacks compact support, resulting in global influence, hence a high computational cost.

The Gaussian kernel stability inspired the development of similar kernels with compact support. The cubic-spline kernel, Fig. 4.5, is one of these developed kernels, being defined as

$$W(r_s, h_s) = \alpha_s\begin{cases}\frac{2}{3} - r_s^2 + \frac{1}{2}\,r_s^3, & 0 \le r_s < 1,\\ \frac{1}{6}\,(2-r_s)^3, & 1 \le r_s < 2,\\ 0, & r_s \ge 2\end{cases} \tag{4.31}$$

Figure 4.4: The kernel and its first and second derivatives used by Gingold and Monaghan (1977).

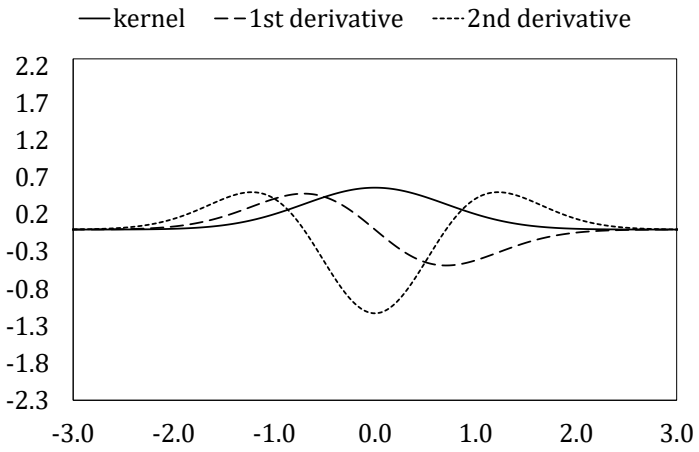

Source: Own authorship.

with α_d as $1/h_s$, $15/7\,\pi\,h_s^2$, and $3/2\,\pi\,h_s^3$ in one, two, and three-dimensional spaces, respectively. Furthermore, it is the most commonly used smoothing distribution in SPH. It resembles the Gaussian kernel but has reduced stability due to its second derivative being piecewise linear and its definition being piecewise continuous (MONAGHAN; LATTANZIO, 1985; LIU; LIU, 2003a).

Figure 4.5: The cubic-spline kernel and its derivatives proposed by Monaghan and Lattanzio (1985).

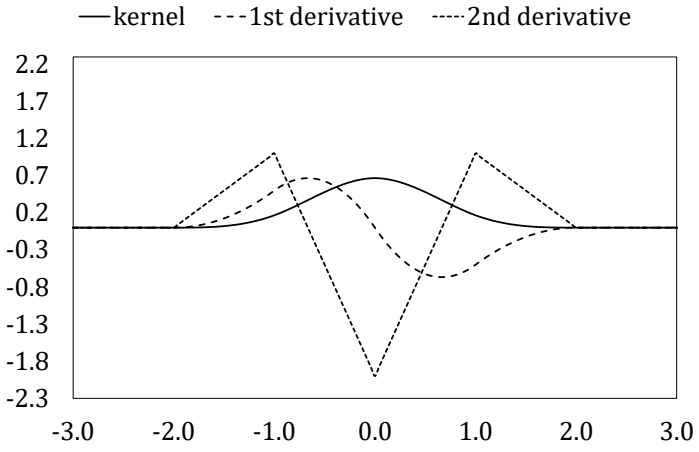

Source: Own authorship.

Independent of the kernel, the SPH method requires neighborhood discrimination for each particle in the problem domain. The algorithm to accomplish this task is called the nearest neighbor search, which is not exclusive to the SPH method. There are several algorithms. The simplest one is the all-pair-wise, which consists of calculating the pair-wise

distance between the concerned particle and every other particle. This procedure requires a number of interactions on the order of $\mathcal{O}\left(N_{part}^2\right)$, where N_{part} is the total number of particles in the problem domain (LIU; LIU, 2003a; KHORASANIZADE; SOUSA, 2019).

The cell-linked list (CLL) is an alternative approach where one splits the problem domain into cells of a specific size, Fig. 4.6, and the neighbor particles are stored based on the cell they belong to. When using a uniform grid, the effort for CLL is on the order of $\mathcal{O}\left(N_{part}\right)$. However, with the adaptive SPH method, the grid must be non-uniform. Hence, the effort increases to the order of $\mathcal{O}\left(N_{part}^2\right)$ (KHORASANIZADE; SOUSA, 2019). Furthermore, when setting up a support domain with a radius of $\kappa_s\, h_s$, where κ_s is a constant real value, the algorithm searches through 3, 9, and 27 cells for one, two, and three-dimensional space, respectively. Thus, the reduces significantly compared with the all-pair-wise algorithm.

Figure 4.6: In a two-dimensional space, one uses a linked-list algorithm to search for the nearest neighboring particles. The support domain has a dimension of $\kappa_s\, h_s$ for the particles, and the smoothing length is spatially constant.

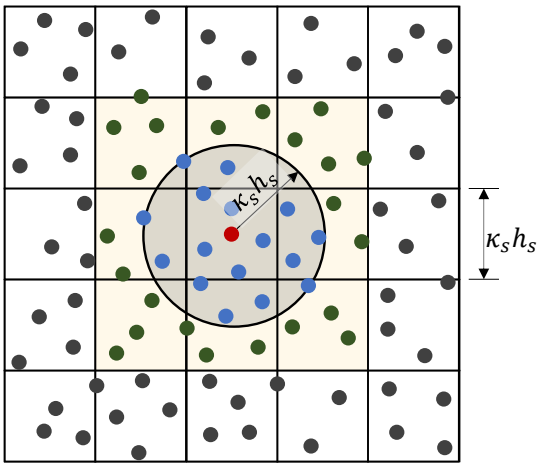

Source: Adapted from Liu and Liu (2003a).

There are several data structures, each with different performances to store the cell identification and the particles. One of the data structures is already in the name of the CLL algorithm, the linked list. It consists of an array of linked lists. Each element of the array represents a cell. Additionally, the linked lists are composed of particles such that each particle is a node that points to the next particle within the same cell, Fig. 4.7.

The sliding dynamic vector is a data structure that consists of an array called PartsSorted, where particles are sorted by the cell they belong to, and another array called CellsBegin, which stores the indices where a cell begins in the PartsSorted array, Fig. 4.8. The static matrix is a data structure where each row represents a cell, and the particles in the cell are listed in the columns. The total number of particles in each cell is saved in the

Figure 4.7: Data structure: linked list

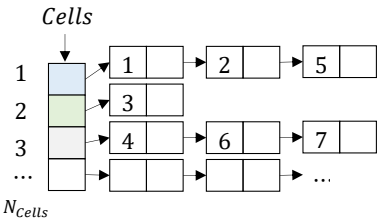

Particles	Cells
1	1
2	1
3	2
4	3
5	1
6	3
7	3

Source: Own authorship.

first column of the matrix. However, the main drawback is that this structure requires a fixed amount of memory, even if some cells have more columns than particles, Fig. 4.9.

Figure 4.8: Data structure: sliding vector

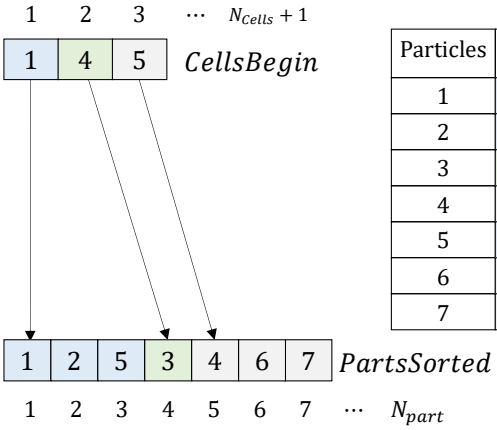

Particles	Cells
1	1
2	1
3	2
4	3
5	1
6	3
7	3

Source: Own authorship.

Figure 4.9: Data structure: static matric

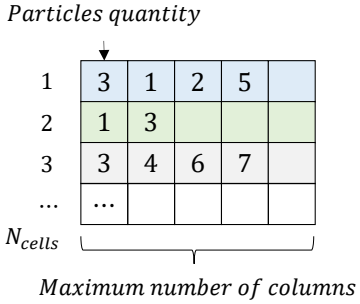

Particles	Cells
1	1
2	1
3	2
4	3
5	1
6	3
7	3

Source: Own authorship.

One employs The tree method to search for the nearest neighbor by mapping particles into a tree data structure and using the $\kappa_s h_s$ maximum distance between parent and children particles as the criterion. Common trees used in SPH include two-, quad-, and octrees in one-, two-, and three-dimensional spaces, respectively. Other options include kd-trees, ball trees, and b-trees. The advantage of the tree method is the efficient step order required to build the tree and search for neighbors, especially for adaptive SPH methods since the effort does not depend on the smoothing length. Building the tree requires $\mathcal{O}\left(N_{part}\ \log\left(N_{part}\right)\right)$ steps, while finding neighbors takes at most $\mathcal{O}\left(N_{part}\right)$ steps (BENTLEY, 1975; KHORASANIZADE; SOUSA, 2019).

Figure 4.10: Tree structure and tree search algorithm in two-dimensional space. The tree is constructed by recursively splitting the maximal problem domain into octants that contain particles, until the leaves on the tree are individual particles. The tree search algorithm is performed by checking if the volume of the search cube (shaded area) for a given particle overlaps with the volume represented by the current node.

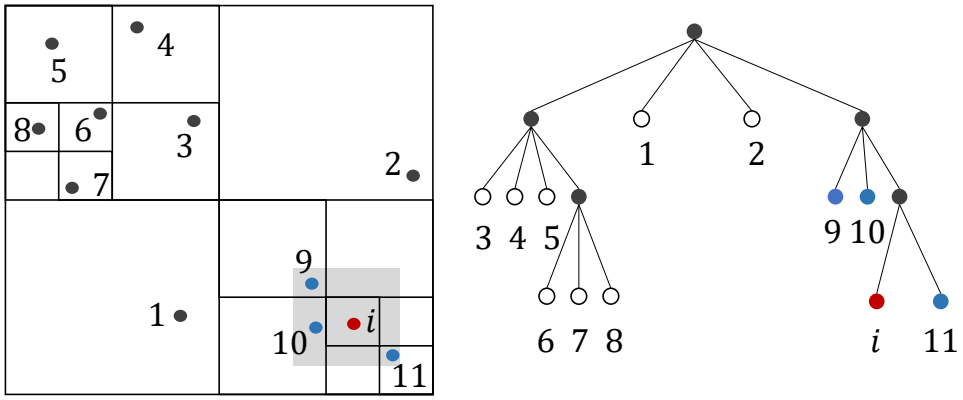

Source: Adapted from Liu and Liu (2003a).

4.3 Balance Equations

There are two approximation forms for the mass balance in the problem domain: the first form results from the direct application of the SPH method on the density function, while the second form is an approximation of the continuity equation. Hence, using Eq. (4.19), the density is represented as

$$\rho_a = \sum_{b \in \mathcal{N}_a} \rho_b W_{ab} \frac{m_b}{\rho_b} = \sum_{b \in \mathcal{N}_a} m_b W_{ab} \tag{4.32}$$

Equation (4.32) conserves the mass exactly, locally and globally, because the integration of the density over the support or problem domains is exactly the total mass of all the particles, locally or globally, respectively. However, near the problem boundaries

and edges, the summation approach suffers from insufficient particles within the support domain. As a result, the density of the concerned particles on or near the boundaries is smoothed out and thus leads to spurious results. Boundary treatments, like ghost particles or consistency recovery, can be employed to mitigate the spurious results due to truncated support domains near the boundaries. Furthermore, the summation approach requires the calculation of the density before other parameters, which increases the computational cost relative to the continuity equation approach (LIU; LIU, 2003a).

The continuity equation approach results from the gradient approximation application, Eq. (4.24), on Eqs. (3.48) and (3.49). Thus, Eq. (4.24) becomes

$$\left\langle \frac{Dh}{Dt} \right\rangle_a^{t+1} = -\frac{a^2}{g} \sum_{b \in \mathcal{N}_a} u_{ba}^t \frac{\partial W_{ab}^t}{\partial x_{1,a}^t} \frac{m_b^t}{\rho_b^t}, \tag{4.33}$$

while Eq. (3.49) with Eqs. (3.123) and (3.126) becomes

$$\begin{aligned} \left\langle \frac{Dh}{Dt} \right\rangle_a^{t+1} = \left\{ 1 + \frac{a^2\, \alpha_p\, d\, \rho_a^t}{b_p} \sum_{m \in \mathcal{N}_{Voigt}} \iota_k \left[1 - \exp\left(\frac{-\Delta t\, G_k}{\mu_k} \right) \right] \right\}^{-1} \left\{ -\frac{a^2}{g} \sum_{b \in \mathcal{N}_a} u_{ba}^t \frac{\partial W_{ab}^t}{\partial x_{1,a}^t} \frac{m_b^t}{\rho_b^t} \right. \\ -\frac{a^2\, \alpha_p\, d\, \rho_a^t}{b_p} \sum_{m \in \mathcal{N}_{Voigt}} \left[\frac{\iota_k\, G_k}{\mu_k} \left(h_a^{t-1} - h_{0,a}^t \right) \exp\left(\frac{-\Delta t\, G_k}{\mu_k} \right) \right. \\ \left. \left. -\varepsilon_{r,m,a}^{t-1} \exp\left(\frac{-\Delta t\, G_k}{\mu_k} \right) \right] \right\} \end{aligned} \tag{4.34}$$

where a is the pressure wave speed, α_p is the pipe-wall constrain coefficient, d is the pipe internal diameter, ρ density, b_p is the pipe-wall thickness, h_0 and h are the piezometric head at t = 0 and t, respectively, ι is the creep compliance function, G is the Young modulus, μ is the Voigt's dashpot element dynamic viscosity, and $\mathcal{N}_{Voigt}$ is the set of Voigt elements in the Kelvin-Voigt model for the pipe viscoelasticity property. Additionally, the subscript a represents the concerned particle at the position of $x_{1,a}$, while the superscripts t and $t-1$ mean a variable at time t and $t - \Delta t$. The symbol u_{ba} represents $u_{1,b} - u_{1,a}$.

The continuity equation approach also has the truncated support domain error near the problem boundaries. However, one can apply the same mitigation techniques to solve the spurious results. Furthermore, one can not guarantee the exact mass conservation locally or globally. Nevertheless, the method has a relatively low computational cost as it can be computed alongside parameters.

The momentum can be approximated by applying Eq. (4.24) to the gradient elements in Eq. (3.46). Thus

$$\left\langle \frac{Du_1}{Dt} \right\rangle_a^{t+1} = -g \sum_{b \in \mathcal{N}_a} h_{ba}^t \frac{\partial W_{ab}^t}{\partial x_{1,a}^t} \frac{m_b^t}{\rho_b^t} - \frac{\pi \, d \, \tau_a^t}{\rho \, s}, \tag{4.35}$$

where $h_{ba} = h_b - h_a$. Considering that the advective term of the material derivative is negligible, the friction component of the models proposed by Vitkovsky et al. (2000), Ramos et al. (2004), and Vardy and Hwang (1993) can be approximated as

$$\tau_a^t = \frac{1}{8} \rho \, \lambda \, |u_{1,a}^t| u_{1,a}^t + K \frac{\rho \, d}{4} \left(\left\langle \frac{Du_1}{Dt} \right\rangle_a^{t-1} + a \, \mathrm{sgn}\left(u_a^t\right) \sum_{b \in \mathcal{N}_a} u_{ba}^t \frac{\partial W_{ab}^t}{\partial x_{1,a}^t} \frac{m_b^t}{\rho_b^t} \right), \tag{4.36}$$

$$\tau_a^t = \frac{1}{8} \rho \, \lambda \, |u_{1,a}^t| u_{1,a}^t + \frac{\rho \, d}{4} \left(K_1 \left\langle \frac{Du_1}{Dt} \right\rangle_a^{t-1} + K_2 \, a \, \mathrm{sgn}\left(u_1^t\right) \sum_{b \in \mathcal{N}_a} u_{ba}^t \frac{\partial W_{ab}^t}{\partial x_{1,a}^t} \frac{m_b^t}{\rho_b^t} \right), \tag{4.37}$$

and

$$\tau_a^t = \frac{1}{8} \rho \, \lambda \, |u_{1,a}^t| u_{1,a}^t + \frac{4 \, \nu \, \rho_a}{d} \left[Y_1^t + Y_2^t \right], \tag{4.38}$$

where

$$Y_m^t = \begin{cases} 0 & t = 0, \\ Y_m^{t-1} \, \exp\left(-B_m \, \phi\right) + T_m \, \Delta t \left\langle \frac{Du_1}{Dt} \right\rangle_a^{t-1} & t > 0, \end{cases} \tag{4.39}$$

respectively. The variables K, K_1, and K_2 are obtained through experimentation, while λ is calculated using Eq. (3.51). The function $\mathrm{sgn}\,(\cdot)$ returns the sign of a variable, ν represents kinematic viscosity, and B_m and T_m are coefficients that can be found in Table. 3.1.

4.4 Corrections for the SPH Method

4.4.1 Artificial Viscosity

To accurately simulate the shock problems of hydrodynamics, it is necessary to utilize treatments or methods that enable algorithms to model shock waves. Failure to do so results in unphysical oscillations in the numerical results around the shocked regions. Although a shock wave is not a physical discontinuity, it is a very narrow transition zone with a thickness typically on the order of a few molecular mean-free paths. The balance of mass, momentum, and energy across a shock front necessitates the simulation of the transformation of kinetic energy into heat energy. Physically, a form of viscous dissipation

can represent this energy transformation (LIU; LIU, 2003a; NEJAD-ASGHAR et al., 2008).

Monaghan (1989) proposed the most commonly utilized artificial viscosity method in SPH simulations. It plays a dual role in the simulation process by dissipating kinetic energy at shock fronts and preventing unrealistic particle penetration. The artificial viscosity proposed by Monaghan (1989) is

$$\Pi_{ab} = \begin{cases} \frac{-\alpha_\Pi \, a_{ab} \, \phi_{\Pi_{ab}} + \beta_\Pi \, \phi^2_{\Pi_{ab}}}{\overline{\rho}_{ab}} & \boldsymbol{u}_{ab} \cdot \boldsymbol{x}_{ab} < 0, \\ 0 & \boldsymbol{u}_{ab} \cdot \boldsymbol{x}_{ab} \geq 0, \end{cases} \tag{4.40}$$

where α_Π and β_Π are constants typically around 1.0. Furthermore, $\phi_{\Pi_{ab}}$ is defined as

$$\phi_{\Pi_{ab}} = \frac{h_{s,ab} \, \boldsymbol{u}_{ab} \cdot \boldsymbol{x}_{ab}}{r^2_{ab} + 0.01 \, h^2_{s,ab}} \tag{4.41}$$

with $h_{s,ab} = 0.5 \, (h_{s,a} + h_{s,b})$, $a_{ab} = 0.5 \, (a_a + a_b)$, $\overline{\rho}_{ab} = 0.5 \, (\rho_a + \rho_b)$. Reenforcing, that a is the pressure wave speed. Additionally, the artificial viscosity is added directly to the momentum equation. Thus, Eq. (4.35) can be rewritten as

$$\left\langle \frac{Du_1}{Dt} \right\rangle^{t+1}_a = -g \sum_{b \in \mathcal{N}_a} \left(h^t_{ba} + \frac{1}{g} \Pi^t_{ab} \right) \frac{\partial W^t_{ab}}{\partial x^t_{1,a}} \frac{m^t_b}{\rho^t_b} - \frac{\pi \, d \, \tau^t_a}{\rho \, s} \tag{4.42}$$

4.4.2 Correted SPH Method

Sigalotti et al. (2021) highlighted that the particle approximation has two types of error: the smoothing error and particle discretization. The first error type has an order $\mathcal{O}\left(h^m_s\right)$, where $m \in \mathbb{Z}$ depends on the order of completeness enforced in the kernel. The smoothing error is independent of the particle distribution, and most kernels have $m = 2$. The second error type has an order $\mathcal{O}\left(\phi_e \left(N_{neigh}\right)\right)$, where $\phi_e \left(N_{neigh}\right)$ is a function that indicates the error relative to the distribution of the particles. Monaghan (1992) conjectured that quasi-ordered particles have an error order of $\mathcal{O}\left(\log\left(N_{neigh}\right)/N_{neigh}\right)$ while randomly distributed particles have $\mathcal{O}\left(N^{-1/2}_{neigh}\right)$.

Zhu et al. (2015) noticed that reducing the smoothing length to zero while increasing the number of neighbor particles infinitely, which includes enlarging the total number of particles toward infinity, leads to a completely consistency condition. Furthermore, Zhu et al. (2015) proposed that the smoothing error is proportional to $\mathcal{O}\left(N^{-m\,\sharp}_{part}\right)$, and the particle discretization error is proportional to $\mathcal{O}\left(N^{1-3\,\sharp}_{part}\right)$, where $\sharp \approx 3 + m/p_d$, with p_d being the probability of having an entirely randomly or a quasi-ordered distribution of particles.

Read et al. (2010) reported that the terms related to consistency C_0 in SPH particle approximation are irreducible when $N_{part} \to \infty$ and $h_s \to 0$ while N_{neigh} remains constant. Hence, Read et al. (2010) suggested, as a convergence criterion, that the discretization error must decrease faster than the smoothing error. Additionally, Sigalotti et al. (2021) showed that the particle approximation does not affect the mass and momentum balance if and only if C_0 and C_1 are guaranteed. Therefore, the classical SPH method needs corrections to ensure consistency of types C_0 and C_1.

Chen et al. (1999) proposed a stable and general scheme for estimating the kernel of a function. The scheme uses the Taylor series expansion of the function about any arbitrary point in its domain of definition. Thus, expanding $f(\boldsymbol{x})$ about the point $\boldsymbol{x}_a$ gives

$$f(\boldsymbol{x}) = f(\boldsymbol{x}_a) + (\boldsymbol{x}_a - \boldsymbol{x}) \cdot \nabla f(\boldsymbol{x}_a) + \frac{1}{2}(\boldsymbol{x}_a - \boldsymbol{x}) \otimes (\boldsymbol{x}_a - \boldsymbol{x}) : \nabla \otimes (\nabla f(\boldsymbol{x}_a)) + \mathcal{O}\left[(\boldsymbol{x}_a - \boldsymbol{x})^3\right]. \tag{4.43}$$

Multiplying Eq. (4.43) by $W_a = W(\boldsymbol{x}_a - \boldsymbol{x}, h_s)$ and integrating the result over the domain, one obtains

$$\int_\Omega f(\boldsymbol{x})\, W_a \mathrm{d}\boldsymbol{x} = f(\boldsymbol{x}_a) \int_\Omega W_a \mathrm{d}\boldsymbol{x} + \nabla f(\boldsymbol{x}_a) \cdot \int_\Omega (\boldsymbol{x}_a - \boldsymbol{x})\, W_a \mathrm{d}\boldsymbol{x} + \frac{1}{2}\nabla \otimes (\nabla f(\boldsymbol{x}_a)) : \int_\Omega (\boldsymbol{x}_a - \boldsymbol{x}) \otimes (\boldsymbol{x}_a - \boldsymbol{x})\, W_a \mathrm{d}\boldsymbol{x} + \mathcal{O}\left[(\boldsymbol{x}_a - \boldsymbol{x})^3\right], \tag{4.44}$$

which can be solved as

$$\langle f(\boldsymbol{x}_a) \rangle = \frac{\int_\Omega f(\boldsymbol{x})\, W_a \mathrm{d}\boldsymbol{x}}{\int_\Omega W_a \mathrm{d}\boldsymbol{x}}, \tag{4.45}$$

if one neglects the derivative terms. Then, for the first derivates, one multiply Eq. (4.43) by ∇W_a and proceeds similarly. It results in

$$\int_\Omega f(\boldsymbol{x})\, \nabla W_a \mathrm{d}\boldsymbol{x} = f(\boldsymbol{x}_a) \int_\Omega \nabla W_a \mathrm{d}\boldsymbol{x} + \nabla f(\boldsymbol{x}_a) \cdot \int_\Omega (\boldsymbol{x}_a - \boldsymbol{x})\, \nabla W_a \mathrm{d}\boldsymbol{x} + \frac{1}{2}\nabla \otimes (\nabla f(\boldsymbol{x}_a)) : \int_\Omega (\boldsymbol{x}_a - \boldsymbol{x}) \otimes (\boldsymbol{x}_a - \boldsymbol{x})\, \nabla W_a \mathrm{d}\boldsymbol{x} + \mathcal{O}\left[(\boldsymbol{x}_a - \boldsymbol{x})^3\right],$$

$$\langle \nabla f(\boldsymbol{x}_a) \rangle \cdot \int_\Omega (\boldsymbol{x}_a - \boldsymbol{x})\, \nabla W_a \mathrm{d}\boldsymbol{x} = \int_\Omega \left[f(\boldsymbol{x}) - f(\boldsymbol{x}_a)\right] \nabla W_a \mathrm{d}\boldsymbol{x} \tag{4.46}$$

Equation (4.46) in the three-dimensional space represents a set coupled in three equations. Equation (4.44)'s right-hand side's second term disappears completely for points far from the domain's boundaries, owing to the symmetry of the kernel. This implies that Eq. (4.45)'s estimate is second-order for unbounded domains. However, for points near a boundary, Eq. (4.45) provides only a first-order approximation because Eq. (4.43)'s right-hand side's second term is no longer nullified. The same holds for the kernel approximation of the derivatives. As a result, the entire method achieves C_1 kernel consistency far from the boundaries and C_0 kernel consistency for points close to or on the boundary (SIGALOTTI et al., 2021).

The particle approximation of Eq. (4.45) is

$$f_a = \left(\sum_{b \in \mathcal{N}_a} W_{ab} \frac{m_b}{\rho_b} \right)^{-1} \left(\sum_{b \in \mathcal{N}_a} f_b W_{ab} \frac{m_b}{\rho_b} \right), \tag{4.47}$$

while the particle approximation of Eq. (4.46) is

$$\nabla f_a = \mathbb{A}^{-1} \sum_{b \in \mathcal{N}_a} (f_a - f_b) \frac{(\boldsymbol{x}_a - \boldsymbol{x}_b)}{r_{ab}} \frac{\partial W_{ab}}{\partial r_{ab}} \frac{m_b}{\rho_b}, \tag{4.48}$$

where $\mathbb{A}$ is a 3×3 matrix defined as

$$A_{ij} = \sum_{b \in \mathcal{N}_a} (x_{i,a} - x_{i,b}) \frac{(x_{j,a} - x_{j,b})}{r_{ab}} \frac{\partial W_{ab}}{\partial r_{ab}} \frac{m_b}{\rho_b}. \tag{4.49}$$

Therefore, Eqs (4.33), (4.34) and (4.42) can be rewritten as

$$\left\langle \frac{Dh}{Dt} \right\rangle_a^{t+1} = -\frac{a^2}{g} \left(\sum_{b \in \mathcal{N}_a} x_{ba}^t \frac{\partial W_{ab}^t}{\partial x_{1,a}^t} \frac{m_b^t}{\rho_b^t} \right)^{-1} \left(\sum_{b \in \mathcal{N}_a} u_{ba}^t \frac{\partial W_{ab}^t}{\partial x_{1,a}^t} \frac{m_b^t}{\rho_b^t} \right), \tag{4.50}$$

$$\left\langle \frac{Dh}{Dt} \right\rangle_a^{t+1} = \left\{ 1 + \frac{a^2\,\alpha_p\,d\,\rho_a^t}{b_p} \sum_{k\,\in\,\mathcal{N}_{Voigt}} \iota_k \left[1 - \exp\left(\frac{-\Delta t\,G_k}{\mu_k} \right) \right] \right\}^{-1}$$

$$\left\{ -\frac{a^2}{g} \left(\sum_{b\,\in\,\mathcal{N}_a} x_{ba}^t \frac{\partial W_{ab}^t}{\partial x_{1,a}^t} \frac{m_b^t}{\rho_b^t} \right)^{-1} \left(\sum_{b\,\in\,\mathcal{N}_a} u_{ba}^t \frac{\partial W_{ab}^t}{\partial x_{1,a}^t} \frac{m_b^t}{\rho_b^t} \right) - \cdots \right. \tag{4.51}$$

$$\cdots - \frac{a^2\,\alpha_p\,d\,\rho_a^t}{b_p} \sum_{m\,\in\,\mathcal{N}_{Voigt}} \left[\frac{\iota_k\,G_k}{\mu_k} \left(h_a^{t-1} - h_{0,a}^t \right) \exp\left(\frac{-\Delta t\,G_k}{\mu_k} \right) \right.$$

$$\left. \left. -\varepsilon_{r,k,a}^{t-1} \exp\left(\frac{-\Delta t\,G_k}{\mu_k} \right) \right] \right\},$$

and

$$\left\langle \frac{Du_1}{Dt} \right\rangle_a^{t+1} = -g \left(\sum_{b\,\in\,\mathcal{N}_a} x_{ba}^t \frac{\partial W_{ab}^t}{\partial x_{1,a}^t} \frac{m_b^t}{\rho_b^t} \right)^{-1} \left(\sum_{b\,\in\,\mathcal{N}_a} \left(h_{ba}^t + \frac{1}{g} \Pi_{ab}^t \right) \frac{\partial W_{ab}^t}{\partial x_{1,a}^t} \frac{m_b^t}{\rho_b^t} \right) - \frac{\pi\,d\,\tau_a^t}{\rho\,s}, \tag{4.52}$$

respectively.

4.4.3 Ghost Particles

Boundary conditions in the SPH method can be effectively managed using ghost or virtual particles, as proposed by Monaghan (1994). These ghost particles are strategically placed at positions adjacent to the domain boundary to exert repulsive forces on nearby real particles, thus preventing unphysical penetration beyond the boundary.

Ghost particles are categorized into type-I and type-II (LIU; LIU, 2003a). Type-II ghost particles are symmetrically arranged with respect to the adjacent real particles at the boundary. They share the same physical attributes as real particles, with the exception of their velocities, which are directed oppositely. However, this configuration alone is inadequate to avert altogether the risk of real particles penetrating the boundary, necessitating the inclusion of type I particles. These type-I ghost particles generate the requisite repulsive forces to ensure that real particles remain confined within the domain.

Type-I particles play a role in the smoothing function and contribute to the particle-based representation of real particles; however, they are omitted from simulations focused on determining particle positions and physical variables. As demonstrated in Fig. 4.11, the discretization domain is established by integrating ghost particles into the framework.

Figure 4.11: A particle distribution near some boundaries with ghost particles application.

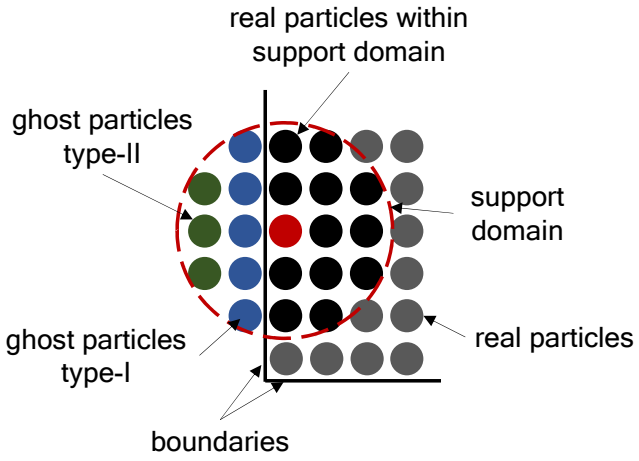

Source: Own authorship.

In the present study, the employed particles were of type-II since the particles do not move throughout the simulation but may suffer changes in their pressure head and velocity. Furthermore, the SPH applied with ghost particle boundary treatment is called GSPH.

4.5 Temporal Integration

Gingold and Monaghan (1977) and Lucy (1977) originally developed the SPH method as an explicit numerical scheme. Later, other authors like Hopp-Hirschley and Nieken (2019) and Shimizu et al. (2022) developed implicit schemes, especially for incompressible flows. The most explicit scheme applied in the SPH method is the Forward Euler Scheme, which is a time dimension approximation, using Taylor Series expansion and neglecting higher-order derivatives. Hence, considering a scalar smooth function $f(\boldsymbol{x}, t)$, expand it around an arbitrary time point t, then

$$f(\boldsymbol{x}, t+\Delta t) = f(\boldsymbol{x}, t) + \Delta t \frac{D}{Dt} f(\boldsymbol{x}, t) + \frac{\Delta t}{2!} \frac{D^2}{Dt^2} f(\boldsymbol{x}, t) + \mathcal{O}\left(t^3\right),$$

$$\langle f(\boldsymbol{x}, t+\Delta t) \rangle = f(\boldsymbol{x}, t) + \Delta t \frac{D}{Dt} f(\boldsymbol{x}, t), \tag{4.53}$$

which, from a Lagrangian perspective and using the SPH notation, can be represented as

$$f_a^{t+1} = f_a^t + \Delta t \left\langle \frac{Df}{Dt} \right\rangle_a^t. \tag{4.54}$$

However, it is a time integration method with a truncation error of the order of $\mathcal{O}(t^2)$.

The Runge-Kutta scheme is more accurate than the Forward Euler scheme. However, it usually requires a narrow time step for stability in regions of clustered grids or particles (ALLAMPALLI et al., 2009). Consider the interval $[0, t]$ and divide it into N_{time} subintervals as $[t_n, t_{n+1}]$ with $n = 0, 1, \ldots, N_{time} - 1$. From the mean value theorem for integrals and the fundamental theorem of calculus, one has

$$f(\boldsymbol{x}_a, t_{n+1}) - f(\boldsymbol{x}_a, t_n) = \int_{t_n}^{t_{n+1}} \frac{D}{Dt} f[f(\boldsymbol{x}_a, t), t] \, \mathrm{d}t = \Delta t \frac{D}{Dt} f[f(\boldsymbol{x}_a, \xi), \xi] \tag{4.55}$$

where $\Delta t = t_{n+1} - t_n$ and $\xi \in [t_n, t_{n+1}]$. Approximating $D\{f[f(\boldsymbol{x}_a, \xi), \xi]\}/Dt$ by the liner combination of values $D\{f[f(\boldsymbol{x}_a, \xi_1), \xi_1]\}/Dt, \ldots, D\{f[f(\boldsymbol{x}_a, \xi_m), \xi_m]\}/Dt$ on the interval $[t_n, t_{n+1}]$, then one arrives at the general form of Runge-Kutta method:

$$f_a^{t+1} = f_a^t + \Delta t \sum_{j=1}^{m} c_{RG,j} \frac{D}{Dt} f[f(\boldsymbol{x}_a, \xi_j), \xi_j] \tag{4.56}$$

where $c_{RG,i}$ are the linear coefficients of the linear combination. Equation (4.56) can be rewritten as

$$f_a^{t+1} = f_a^t + \Delta t \sum_{j=1}^{m} c_{RG,j} \, k_{RG,j}, \tag{4.57}$$

where the terms $k_{RG,i}$ are

$$\begin{cases} k_{RG,1} = \frac{D}{Dt} f[f(\boldsymbol{x}_a, t_n), t_n] \\ k_{RG,2} = \frac{D}{Dt} f[f(\boldsymbol{x}_a, t_n) + (y_{21} \, k_{RG,1}) \, \Delta t, \, t_n + z_2 \, \Delta t] \\ k_{RG,3} = \frac{D}{Dt} f[f(\boldsymbol{x}_a, t_n) + (y_{31} \, k_{RG,1} + y_{32} \, k_{RG,2}) \, \Delta t, \, t_n + z_3 \, \Delta t] \\ \vdots \\ k_{RG,m} = \frac{D}{Dt} f[f(\boldsymbol{x}_a, t_n) + (y_{m1} \, k_{RG,1} + \ldots + y_{m,m-1} \, k_{RG,m-1}) \, \Delta t, \, t_n + z_m \, \Delta t] \end{cases} \tag{4.58}$$

The Runge-Kutta method is consistent if and only if

$$\sum_{j=1}^{m} c_{RG,j} = 1. \tag{4.59}$$

Additionally, the order of the truncation error depends on other requirements that are resumed into

$$\sum_{j=1}^{n-1} y_{nj} = c_n, \tag{4.60}$$

with $n = 2, \ldots, m$, which is neither sufficient nor necessary (ISERLES, 1996). Butcher (2008) showed that the number of stages of a Runge-Kutta scheme must satisfy the condition $m \geq q$, and if $q \geq 5$, then $m \geq q + 1$, with q as the truncation order, $\mathcal{O}\left(t^{q+1}\right)$.

To deduce the fourth-order Runge-Kutta scheme, assume the following coefficients: $z_1 = 0$, $z_2 = 1/2$, $z_3 = 1/2$, $z_4 = 1$, $y_{21} = 1/2$, $y_{32} = 1/2$, $y_{43} = 1$, and $y_{ij} = 0$, otherwise. Applying the coefficients into Eq. (4.60), one verifies that they are consistent. Then, expand $k_{RG,j}$, function that indicates the error relative to the distribution of the particles, into a Taylor Series and neglect the higher-order derivatives, one obtains

$$\begin{aligned} k_{RG,2} &= \frac{D}{Dt} f\left[f_a^t + \frac{\Delta t}{2}\frac{D}{Dt} f\left(f_a^t,\, t_n\right),\, t_n + \frac{\Delta t}{2}\right] \\ &= \frac{D}{Dt} f\left(f_a^t,\, t_n\right) + \frac{\Delta t}{2}\frac{D^2}{Dt^2} f\left(f_a^t,\, t_n\right), \end{aligned} \tag{4.61}$$

$$\begin{aligned} k_{RG,3} &= \frac{D}{Dt} f\left(f_a^t + \frac{\Delta t}{2}\, k_{RG,2},\, t_n + \frac{\Delta t}{2}\right) \\ &= \frac{D}{Dt} f\left(f_a^t,\, t_n\right) + \frac{\Delta t}{2}\frac{D}{Dt} k_{RG,2} \\ &= \frac{D}{Dt} f\left(f_a^t,\, t_n\right) + \frac{\Delta t^2}{2}\frac{D^2}{Dt^2} f\left(f_a^t,\, t_n\right) + \frac{\Delta t^3}{4}\frac{D^3}{Dt^3} f\left(f_a^t,\, t_n\right), \end{aligned} \tag{4.62}$$

$$\begin{aligned} k_{RG,4} &= \frac{D}{Dt} f\left(f_a^t + \Delta t\, k_{RG,3},\, t_n + \Delta t\right) \\ &= \frac{D}{Dt} f\left(f_a^t,\, t_n\right) + \Delta t\, \frac{D}{Dt} k_{RG,3} \\ &= \frac{D}{Dt} f\left(f_a^t,\, t_n\right) + \Delta t\, \frac{D^2}{Dt^2} f\left(f_a^t,\, t_n\right) + \frac{\Delta t^3}{2}\frac{D^3}{Dt^3} f\left(f_a^t,\, t_n\right) + \frac{\Delta t^4}{4}\frac{D^4}{Dt^4} f\left(f_a^t,\, t_n\right), \end{aligned} \tag{4.63}$$

where $f_a^t = f\left(\boldsymbol{x}_a, t_n\right)$. Combine Eqs. (4.61), (4.62), and (4.63) into Eq. (4.57) for four stages, resulting in

$$f_a^{t+1} = f_a^t + \Delta t\,\left(c_{RG,1} + c_{RG,2} + c_{RG,3} + c_{RG,4}\right)\frac{D}{Dt}f\left(f_a^t,\, t_n\right)$$

$$+ \Delta t^2\,\left(\frac{c_{RG,2}}{2} + \frac{c_{RG,3}}{2} + c_{RG,4}\right)\frac{D^2}{Dt^2}f\left(f_a^t,\, t_n\right) \tag{4.64}$$

$$+ \Delta t^3\,\left(\frac{c_{RG,3}}{4} + \frac{c_{RG,4}}{2}\right)\frac{D^3}{Dt^3}f\left(f_a^t,\, t_n\right) + \Delta t^4\,\frac{c_{RG,4}}{4}\,\frac{D^4}{Dt^4}f\left(f_a^t,\, t_n\right).$$

Now, expand f_a^{t+1} in a Taylor series around t,

$$f_a^{t+1} = f_a^t + \Delta t\,\frac{D}{Dt}f\left(f_a^t,\, t_n\right) + \frac{\Delta t^2}{2}\frac{D^2}{Dt^2}f\left(f_a^t,\, t_n\right) + \frac{\Delta t^3}{6}\frac{D^3}{Dt^3}f\left(f_a^t,\, t_n\right)$$

$$+ \frac{\Delta t^4}{24}\frac{D^4}{Dt^4}f\left(f_a^t,\, t_n\right) + \mathcal{O}\left(\Delta t^5\right), \tag{4.65}$$

and compare the expansion with Eq. (4.64). Hence, one obtains a system of constrains on the coefficients

$$\begin{cases} c_{RG,1} + c_{RG,2} + c_{RG,3} + c_{RG,4} = 1 \\ \frac{1}{2}c_{RG,2} + \frac{1}{2}c_{RG,3} + c_{RG,4} = \frac{1}{2} \\ \frac{1}{4}c_{RG,3} + \frac{1}{2}c_{RG,4} = \frac{1}{6} \\ \frac{1}{4}c_{RG,4} = \frac{1}{24} \end{cases} \tag{4.66}$$

whose solution is $c_{RG,1} = 1/6$, $c_{RG,2} = 1/3$, $c_{RG,3} = 1/3$, and $c_{RG,4} = 1/6$. Therefore, the fourth-order Runge-Kutta method can be explicitly written as

$$f_a^{t+1} = f_a^t + \Delta t\left(\frac{1}{6}k_{RG,1} + \frac{1}{3}k_{RG,2} + \frac{1}{3}k_{RG,3} + \frac{1}{6}k_{RG,4}\right), \tag{4.67}$$

with

$$\begin{cases} k_{RG,1} = \frac{D}{Dt}f\left(f_a^t,\, t_n\right) \\ k_{RG,2} = \frac{D}{Dt}f\left(f_a^t + \frac{1}{2}\,\Delta t\, k_{RG,1},\, t_n + \frac{1}{2}\,\Delta t\right) \\ k_{RG,3} = \frac{D}{Dt}f\left(f_a^t + \frac{1}{2}\,\Delta t\, k_{RG,2},\, t_n + \frac{1}{2}\,\Delta t\right) \\ k_{RG,4} = \frac{D}{Dt}f\left(f_a^t + \,\Delta t\, k_{RG,3},\, t_n + \Delta t\right) \end{cases} \tag{4.68}$$

5 METHOD OF CHARACTERISTICS (MOC)

MOC is a method based on transforming partial differential equations (PDE) into ordinary differential equations (ODE) by assuming the existence of a solution along a fixed characteristic line in the PDE's solution domain. The solution, in this case, is a constant value.

Implementing the Method of Characteristics (MOC) necessitates a geometric understanding of first-order partial differential equations (PDEs). According to Courant and Hubert (1989), consider a general differential equation denoted by

$$F\left(x, t, u, p, q\right) = 0, \tag{5.1}$$

where $F_p^2 + F_q^2 \neq 0$, with the shorthand notation $p = \partial u/\partial x$ and $q = \partial u/\partial t$. Therefore, for each integral surface passing through the point P with coordinates x, t, u, the values of p and q, which define the location of the tangent plane at that point, must fulfill the condition specified in Eq. (5.1). The tangent plane of an integral surface at the point P is confined to positions that are part of the manifold defined by Eq. (5.1). This manifold typically represents a one-parameter family for a specific point $P : (x, t, u)$. If F is linear concerning p and q, the collection of potential tangent planes creates an axial pencil of planes that intersect along a straight line known as the Monge axis. Assume that the family of planes constitutes an enveloping Monge cone at each point P under consideration. In the context of the (x, t, u)-space, the differential equation manifests geometrically as a cone field, analogous to how a direction field represents a first-order ODE. To identify a solution, one must locate a surface that tangentially intersects the corresponding Monge cone (or aligns within the cone field) at every point within its domain.

In particular, there are curves described by ODEs called characteristics curves that are tangent to the Monges axes as degenerations of Monge cones.

Moving to the hydraulic transient equations, Eqs. (3.49) and (3.46), one first rewrites them as

$$\frac{\partial}{\partial t}\begin{bmatrix} h \\ u_1 \end{bmatrix} + \begin{bmatrix} u_1 & \frac{a^2}{g} \\ g & u_1 \end{bmatrix} \frac{\partial}{\partial x_1}\begin{bmatrix} h \\ u_1 \end{bmatrix} = -\begin{bmatrix} \frac{a^2}{g}\frac{D\varepsilon_r}{Dt} \\ \frac{4\,\tau}{\rho\, d} \end{bmatrix}, \tag{5.2}$$

or

$$\frac{\partial \mathbf{U}_{moc}}{\partial t} + \mathbf{B}_{moc}\frac{\partial \mathbf{U}_{moc}}{\partial x_1} = \mathbf{F}_{moc}, \tag{5.3}$$

where the eigenvalues of matrix $\mathbf{B}_{moc}$ are $u_1 \pm a$. Then, assume that the integral surface $\mathbf{U}_{moc}(x_1, t)$ of the differential equation is required to possess at the point $P(x_1, t, \mathbf{U}_{moc})$, a tangent plane whose normal has direction numbers $p = \partial \mathbf{U}_{moc}/\partial x_1$ and $q = \partial \mathbf{U}_{moc}/\partial t$ and -1 connected by the linear equation $q + \mathbf{B}_{moc} p = \mathbf{F}_{moc}$. According to this equation, the tangent plane of all integral surfaces through the point $(x_1, t, \mathbf{U}_{moc})$ belong to a single pencil plane whose axis is given by the relations

$$\frac{\mathrm{d}x_1}{\mathrm{d}s_{moc}} = \pm a, \quad \frac{\mathrm{d}t}{\mathrm{d}s_{moc}} = 1, \quad \frac{\mathrm{d}\mathbf{U}_{moc}}{\mathrm{d}s_{moc}} = \mathbf{F}_{moc}, \tag{5.4}$$

at the point P, where s_{moc} is a parameter and assuming that the eigenvalues of matrix $\mathbf{B}_{moc}$ are null, i.e., $u_1 \pm a = 0$. These pencils and their axis are the Monge pencils and Monge axes. Equation (5.4) can be rewritten as

$$\frac{\mathrm{d}x_1}{\mathrm{d}t} = \pm a, \quad \frac{\mathrm{d}\mathbf{U}_{moc}}{\mathrm{d}t} = \mathbf{F}_{moc}, \tag{5.5}$$

The point P and the direction of the Monge axis through P constitute a characteristic line element. In the $(x_1, t, \mathbf{U}_{moc})$-space, the directions of the Monge axes constitute a direction field. The integral curves derived from this direction field are governed by the ODEs in Eq. (5.5) and are referred to as characteristic curves. Thus, integrating the PDE in Eq. (5.3) is the same as finding surfaces that align with the Monge field at every point, i.e., surfaces whose tangent plane at every point belongs to the Monge pencil.

To conceptualize this idea, consider a homogeneous variant of Eq. (5.3) with a specified initial condition. The solution to this equation represents the transportation of the initial profile without alteration, effectively maintaining the shape of the initial waveform as it propagates along the characteristics with a velocity defined by $\mathrm{d}x_1/\mathrm{d}t = a$, as illustrated in Fig. 5.1. This concept can be further extended to a numerical grid built by characteristic lines, Fig. 5.2. Along these lines, one can effectively integrate and discretize the hydraulic transient equations.

Using Eq. (5.5), and considering the advective terms negligible due to $u_1 \ll a$, Eq. (5.3) can be rewritten as

$$\frac{\mathrm{d}h}{\mathrm{d}t} \pm \frac{a}{g}\frac{\mathrm{d}u_1}{\mathrm{d}t} \pm \frac{4\,a\,\tau}{\rho\,d} + \frac{2\,a^2}{g}\,\frac{\partial \varepsilon_r}{\partial t} = 0. \tag{5.6}$$

Then, multiplying Eq. (5.6) by $\mathrm{d}t$ and integrating it along the characteristic lines results in

$$\int_{i-1,t}^{i,t+1} \mathrm{d}h + \int_{i-1,t}^{i,t+1} \frac{a}{g}\mathrm{d}u_1 + \int_{i-1,t}^{i,t+1} \frac{4\,a\,\tau}{\rho\,d}\mathrm{d}t + \int_{i-1,t}^{i,t+1} \frac{2\,a^2}{g}\,\frac{\partial \varepsilon_r}{\partial t}\mathrm{d}t = 0, \tag{5.7}$$

and

Figure 5.1 – Initial profile, characteristic lines, and solution at various times.

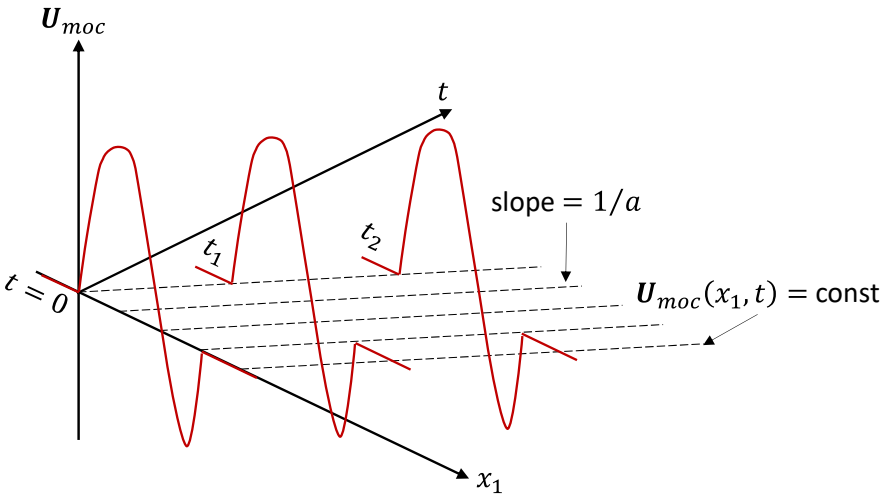

Source: Own Authorship.

Figure 5.2 – Numerical grid based on straight characteristic lines.

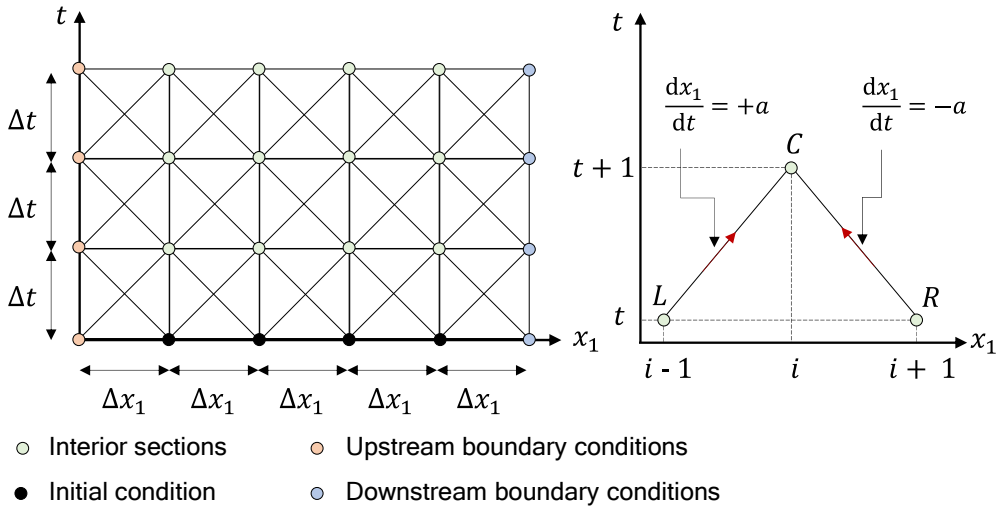

Source: Modified from Covas (2003).

$$\int_{i+1,t}^{i,t+1} \mathrm{d}h - \int_{i+1,t}^{i,t+1} \frac{a}{g} \mathrm{d}u_1 - \int_{i+1,t}^{i,t+1} \frac{4\,a\,\tau}{\rho\,d} \mathrm{d}t + \int_{i+1,t}^{i,t+1} \frac{2\,a^2}{g} \frac{\partial \varepsilon_r}{\partial t} \mathrm{d}t = 0. \tag{5.8}$$

Thus

$$h_i^{t+1} - h_{i-1}^t + \frac{a}{g}\left(u_{1,i}^{t+1} - u_{1,i-1}^t\right) + \frac{a\,\Delta t\,\lambda}{2\,g\,d}\left|u_{1,i-1}^t\right| u_{1,i}^{t+1} + \int_{i-1,t}^{i,t+1} \frac{4\,a\,\tau_t}{\rho\,d} \mathrm{d}t + \tag{5.9}$$

$$\frac{a^2\,\alpha_p\,d\,\rho\,\Delta t}{b_p} \sum_{m \in \mathcal{N}_{Voigt}} \frac{\iota_m\,G_m}{\mu_m}\left(h_i^t - h_i^0\right) - \frac{G_m}{\mu_m} \varepsilon_{r,m,i}^{t+1} = 0,$$

$$h_i^{t+1} - h_{i+1}^t - \frac{a}{g}\left(u_{1,i}^{t+1} - u_{1,i+1}^t\right) - \frac{a\,\Delta t\,\lambda}{2\,g\,d}\left|u_{1,i+1}^t\right| u_{1,i}^{t+1} + \int_{i+1,t}^{i,t+1} \frac{4\,a\,\tau_t}{\rho\,d}\mathrm{d}t + \frac{a^2\,\alpha_p\,d\,\rho\,\Delta t}{b_p} \sum_{m\,\in\,\mathcal{N}_{Voigt}} \frac{\iota_m\,G_m}{\mu_m}\left(h_i^t - h_i^0\right) - \frac{G_m}{\mu_m}\varepsilon_{r,m,i}^{t+1} = 0. \tag{5.10}$$

Considering the models of Vardy and Hwang (1993), Vitkovsky et al. (2000), and Ramos et al. (2004) for the unsteady friction term and rearranging Eq. (5.9) and (5.10), one obtains the following scheme:

$$+a: \quad h_i^{t+1} = C_p - B_p\,u_i^{t+1}, \tag{5.11}$$

$$-a: \quad h_i^{t+1} = C_m + B_m\,u_i^{t+1}. \tag{5.12}$$

where C_p, C_m, B_p, and B_m are coefficients that encapsulates the numerical schemes for the steady and unsteady friction terms, besides the viscoelastic model. Their description are

$$C_p = \frac{1}{\varrho_{moc}}\left\{h_{i-1}^t + \left[\frac{a}{g} - (1-\epsilon_{MOC})\,\frac{a\,\Delta t\,\lambda_{i-1}}{2\,g\,d}\left|u_{1,i-1}^t\right|\right] u_{1,i-1}^t - C_{p1} - C_{p2}\right\}, \tag{5.13}$$

$$B_p = \frac{1}{\varrho_{moc}}\left(B_{p1} + \epsilon_{MOC}\frac{a\,\Delta t\,\lambda_{i-1}}{2\,g\,d}\left|u_{1,i-1}^t\right|\right), \tag{5.14}$$

$$C_m = \frac{1}{\varrho_{moc}}\left\{h_{i+1}^t - \left[\frac{a}{g} - (1-\epsilon_{MOC})\,\frac{a\,\Delta t\,\lambda_{i+1}}{2\,g\,d}\left|u_{1,i+1}^t\right|\right] u_{1,i+1}^t + C_{m1} - C_{m2}\right\}, \tag{5.15}$$

$$B_m = \frac{1}{\varrho_{moc}}\left(B_{m1} + \epsilon_{MOC}\frac{a\,\Delta t\,\lambda_{i+1}}{2\,g\,d}\left|u_{1,i+1}^t\right|\right), \tag{5.16}$$

where the subscripts $i+1$ and $i-1$ in λ_{i-1} and λ_{i+1} mean that the Reynolds number is computed using $u_{1,i-1}^t$ and $u_{1,i+1}^t$, respectively. The coefficient $\epsilon_{MOC} \in [0.0, 1.0]$, which is adopted as zero in the current work. Furthermore, the variables C_{p1}, C_{m1}, C_{p2}, C_{m2}, B_{p1}, B_{m1}, and ϱ_{moc} are detailed in Tab. 5.1. The integration of local acceleration in the models by Vitkovsky et al. (2000) and Ramos et al. (2004) employed a first-order explicit central discretization scheme. The advective terms were handled similarly.

Table 5.1 – Definition of the variables C_{p1}, C_{m1}, C_{p2}, C_{m2}, B_{p1}, B_{m1}, and ϱ_{moc}.

Unsteady Friction		
No unsteady friction	$C_{p1} = C_{m1} = 0$	$B_{p1} = B_{m1} = \dfrac{a}{g}$
Vardy and Hwang (1993)	$C_{p1} = C_{m1} = \dfrac{16\,a\,\nu\,\Delta t}{g\,d^2}\left[Y_1^{t-1}\exp\left(-B_1\psi\right) + Y_2^{t-1}\exp\left(-B_2\psi\right) - \left(T_1+T_2\right)u_{1,i}^t\right]$	$B_{p1} = B_{m1} = \dfrac{a}{g}\left[1 + \dfrac{16\,a\,\nu\,\Delta t}{g\,d^2}\left(T_1+T_2\right)\right]$
Vitkovsky et al. (2000)	$C_{p1} = \dfrac{a\,K}{2\,g}\left[-u_{1,i}^{t-1} + \operatorname{sgn}\left(u_{1,i-1}^t\right)\left\lvert u_{1,i+1}^t - u_{1,i-1}^t\right\rvert\right]$ $C_{m1} = \dfrac{a\,K}{2\,g}\left[-u_{1,i}^{t-1} + \operatorname{sgn}\left(u_{1,i+1}^t\right)\left\lvert u_{1,i+1}^t - u_{1,i-1}^t\right\rvert\right]$	$B_{p1} = B_{m1} = \dfrac{a}{g}\left(1 + \dfrac{K}{2}\right)$
Ramos et al. (2004)	$C_{p1} = \dfrac{a}{2\,g}\left[-K_1\,u_{1,i}^{t-1} + K_2\operatorname{sgn}\left(u_{1,i-1}^t\right)\left\lvert u_{1,i+1}^t - u_{1,i-1}^t\right\rvert\right]$ $C_{m1} = \dfrac{a}{2\,g}\left[-K_1\,u_{1,i}^{t-1} + K_2\operatorname{sgn}\left(u_{1,i+1}^t\right)\left\lvert u_{1,i+1}^t - u_{1,i-1}^t\right\rvert\right]$	$B_{p1} = B_{m1} = \dfrac{a}{g}\left(1 + \dfrac{K_1}{2}\right)$
Viscoelasticity		
Linear-elastic	$C_{p2} = C_{m2} = 0$	$\varrho_{moc} = 1$

continued on next page

continued from previous page

Covas (2003)

$$C_{p2} = C_{m2} = \frac{a^2\,\alpha_p\,d\,\rho\,\Delta t}{b_p} \sum_{k\,\in\,\mathcal{N}_{Voigt}} \frac{\iota_k\,G_k}{\mu_k} \Big\{ -h_i^0 + \left[1 - \frac{\mu_k}{\Delta t\,G_k}\left(1 - \exp\left(-\frac{\Delta t\,G_k}{\mu_k}\right)\right)\right] h_i^0 + \left[\exp\left(-\frac{\Delta t\,G_k}{\mu_k}\right) - \frac{\mu_k}{\Delta t\,G_k}\left(1 - \exp\left(-\frac{\Delta t\,G_k}{\mu_k}\right)\right)\right]\left(h_i^t - h_i^0\right) - \frac{G_k}{\mu_k}\varepsilon_{r,k,i}^t \exp\left(-\frac{\Delta t\,G_k}{\mu_k}\right)\Big\}.$$

$$\varrho_{moc} = 1 + \sum_{k\,\in\,\mathcal{N}_{Voigt}} \iota_k \left[1 - \exp\left(-\frac{\Delta t\,G_k}{\mu_k}\right)\right]$$

From Eqs. (5.11) and (5.12), the pressure head and the velocity can be calculated in the interior points of the numerical domain as

$$h_i^{t+1} = \frac{B_m\,C_p + B_p\,C_m}{B_p + B_m}, \tag{5.17}$$

$$u_{1,i}^{t+1} = \frac{C_p - C_m}{B_p + B_m}. \tag{5.18}$$

The boundary at the interface between the reservoir and the pipe is characterized by either a constant or time-varying pressure head. Notably, no intermediate point, such as a ghost cell, is present before this boundary. Consequently, Eqs. (5.19) and (5.20) can be reformulated as

$$h_{reservoir}^{t+1} = \text{constant or } f\,(t)\,, \tag{5.19}$$

$$u_{1,reservoir}^{t+1} = \frac{h_{reservoir}^{t+1} - C_m}{B_m}, \tag{5.20}$$

where $h_{reservoir}$ and $u_{1,reservoir}$ are the piezometric pressure and velocity, respectively, at the interface between the reservoir and the pipe.

The valve maneuvering function characterizes the downstream boundary or the interface between the pipe and the valve, and similar to the upstream boundary, there is no intermediate point after this boundary. As a result, Eqs. (5.19) and (5.20) can be reformulated as

$$h_{valve}^{t+1} = C_p - B_p \, u_{1,valve}^{t+1}, \tag{5.21}$$

$$u_{1,valve}^{t+1} = \phi_{or} \, u_{1,valve}^{0} \sqrt{\frac{h_{valve}^{t}}{h_{valve}^{0}}}, \tag{5.22}$$

where ϕ_{or} is the valve maneuvering function, h_{valve} and $u_{1,valve}$ are the piezometric pressure and velocity, respectively, at the interface between the valve and the pipe. Additionally, the superscript 0 indicates the variable's initial value.

6 COMPUTATIONAL EXPERIMENT

6.1 Experimental Setup

This section leverages experimental data from three studies to validate and calibrate numerical models focusing on hydraulic transient phenomena. Experiment 1, conducted by Martins et al. (2016), investigated water hammer effects within a 'reservoir-pipe-valve' setup at the Laboratory of Hydraulics and Environment (LHE), IST, Lisbon. Experiment 2, by Soares et al. (2017), replicated this setup, varying flow conditions. Experiment 3, by Covas et al. (2005), explored transient behavior in a high-density polyethylene pipeline at Imperial College London, UK. These experiments provide comprehensive datasets essential for refining and validating numerical models, particularly those employing SPH coupled with transient friction and viscoelastic models.

Martins et al. (2016) conducted experiments at the Laboratory of Hydraulics and Environment (LHE), Department of Civil Engineering, Architecture, and Geo-resources (DECivil), of Instituto Superior Técnico (IST), Lisbon, aimed to investigate water hammer phenomena. The experimental setup comprised a typical "reservoir-pipe-valve" configuration, Fig. 6.1, consisting of a copper pipe with a total length (L) of 15.22 m, an inner diameter (d) of 0.02 m, and a wall thickness (e) of 1.00 mm. The pipe received water from a 60-liter hydropneumatic vessel acting as a constant head reservoir. Transient events were generated by rapidly closing an electromechanical quarter-turn ball valve at the end of the pipe. The data acquisition system (DAS) included an oscilloscope (PicoScopeTM), a trigger-synchronizer, two pressure transducers (PT1 and PT2), a potentiometer connected to the valve stem, electrical power sources, and a laptop computer.

Figure 6.1: Experiment pipe rig: "reservoir-pipe-valve" configuration.

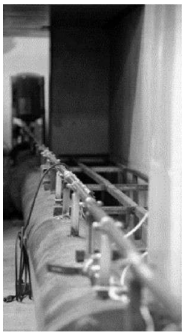

(a) Pipe view

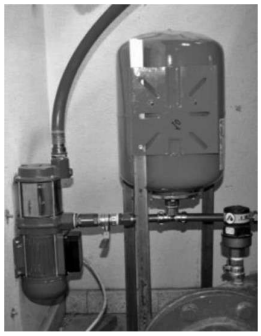

(b) Reservoir

(c) Ball valve

Source: Adapted from Martins et al. (2016).

Pressure transducers PT1 and PT2, positioned immediately upstream of the valve and at the pipe midsection, respectively, allowed high-frequency data acquisition up to 3.00

kHz. To minimize noise, signal averaging techniques were employed. Three initial discharges (Q_0) were tested: 71.70×10^{-6} m^3/s, 96.10×10^{-6} m^3/s, and 120.60×10^{-3} m^3/s. Despite variations in discharge, the system response to transient conditions remained consistent due to the smooth walls, small inner diameter, and short length of the copper pipe. Tests focused on the highest discharge to analyze the largest piezometric head amplitude.

Soares et al. (2017) conducted their research at the same laboratory, replicated the 'reservoir-pipe-valve' setup described in Martins et al. (2016). The experimental rig featured a straight copper pipe with identical dimensions to the experiment of Martins et al. (2016). Two valves were installed at the downstream end, one for generating water hammer and the other for controlling initial discharge. The DAS, including an oscilloscope, trigger-synchronizer, laptop, and two strain-gauge type pressure transducers, enabled high-frequency acquisition rates up to 3.00 kHz. Tests were conducted over Reynolds numbers (Re) from 5411 to 14961, with corresponding discharges (Q_0) from 85.00×10^{-6} m^3/s to 133.00×10^{-6} m^3/s, under non-cavitating flow, and for $Re = 8913$ to $Re = 14961$, with corresponding discharges from 140.00×10^{-6} m^3/s to 235.00×10^{-6} m^3/s, under cavitating flows.

Experiment 3, conducted by Covas et al. (2005) at Imperial College London, UK, utilized a 277 m high-density polyethylene (HDPE) pipeline to study transient behavior, Fig. 6.2. The pipeline, made of SDR11 PE100 NP16, featured a nominal diameter of 63.00 mm and a wall thickness of 6.20 mm. The experimental setup included a centrifugal pump, a pressurized tank, and a globe valve for flow control. Data acquisition involved strain-gauge-type pressure transducers (from T1 to T8), strain gauges (SG1, SG5, SG8), and a notebook computer. Pipe-wall viscoelasticity was observed during transient events, characterized by creep behavior determined through creep tests. The setup aimed to analyze novel leak detection techniques and validate hydraulic transient solvers.

Figure 6.2: Imperial College experimental facility

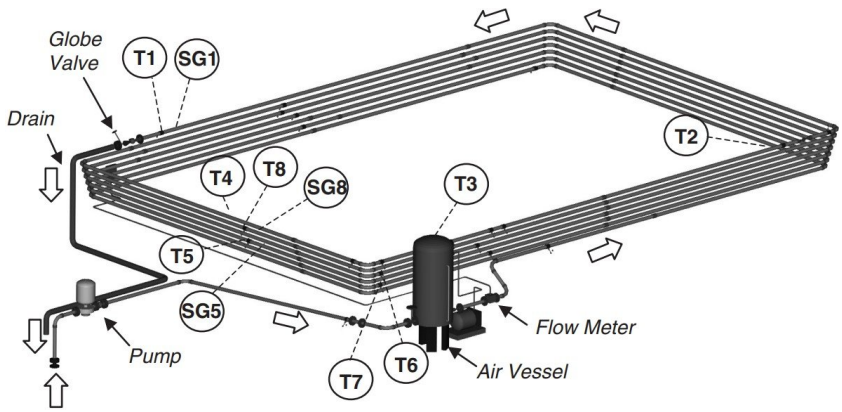

Source: Adapted from Covas et al. (2004).

6.2 Numerical Setup

The experimental setups are more complex than the mathematical model of a reservoir-pipe-valve due to the high control required to generate and measure the hydraulic transient phenomenon. On the other hand, for the numerical experiments, one keeps the mathematical simplified model by applying the fundamental physical aspects of the experimental setups, such as the pipe's total length, the pipe's inner diameter, the pipe's thickness, the pipe's inner wall roughness, the discharge, and the elastic pressure wave speed. Table 6.2 summarizes the experimental setup's physical aspects. In the viscoelasticity experiments case, Covas et al. (2005) generated the Voigt element's properties of the Voigt-Kelvin model they used. But, they need to be tuned since the numerical models and implementations have differences. Hence, the Tab. 6.3 contains the Voigt element's respective data.

The physical properties employed in this analysis include a water density of 998.000 kg/m^3, kinematic viscosity of 1.0034 mm^2/s, and gravitational acceleration of 9.8067 m/s^2. Notably, the copper pipe referenced in the studies by Martins et al. (2016) and Soares et al. (2017) exhibits Young's modulus of 120 GPa, with bulk modulus reported as 1.6095 GPa and 1.6228 GPa, respectively.

In addition to these physical parameters, numerical considerations are critical. The initial numerical parameters for the SPH-based methods and the MOC are delineated in Table 6.1. Specifically for the SPH-based approaches, the values are set as follows: $\alpha_\Pi = 1.8000$, $\beta_\Pi = 0.000$, and $\kappa_s = 1.2000$. However, these parameters vary due to the optimization process using the surface response method, a statistical method described by Montgomery (2013).

Table 6.1 – Numerical aspects of the SPH based methods and the MOC.

Experiment	Parameter	Value	Unit
I II	Δt	1.6700×10^{-5}	s
	Δx	2.0993×10^{-2}	m
	m_b	2.0951×10^{1}	kg
III IV V	Δt	1.6690×10^{-5}	s
	Δx	2.0878×10^{-2}	m
	m_b	2.0836×10^{1}	kg
VI VII	Δt	3.3400×10^{-3}	s
	Δx	1.3259×10^{0}	m
	m_b	1.3232×10^{3}	kg

Table 6.2 – Physical aspects of the experimental data.

Exp.	Q_0 ($\times 10^{-8}$ m^3/s)	h_0 (m)	L (m)	d (mm)	e (mm)	a (m/s)	Authors
I	8500.00	45.59	15.22	20.00	1.00	1255.00	Soares et al. (2017)
II	13300.00	44.64					
III	7170.00	46.14					
IV	9610.00	45.36	15.22	20.00	1.00	1250.00	Martins et al. (2016)
V	12060.00	44.66					
VI	100810	45.46	271.80	50.60	6.30	395.00	Covas et al. (2005)
VII	5600	48.32					

Table 6.3 – Voigt element's properties for the Voigt-Kelvin viscoelastic models applied in the SPH-based models.

Experiment	Unsteady Friction Model	Voigt elements number	ι (GPa^{-1})	μ/G (s)
VI	No	3	0.1044	0.05
			0.1037	0.50
			0.1145	1.50
VII	No	3	0.0801	0.05
			0.1101	0.50
			0.5906	10.00
VI	Ramos et al. (2004)	3	0.0800	0.05
			0.1200	0.50
			0.0001	1.50
VII	Ramos et al. (2004)	3	0.0600	0.05
			0.1300	0.50
			0.1100	10.00

The time step depends on the empirical experiments since the most stable states are around the Courant–Friedrichs–Lewy (CFD) number equal to one. As a result,

$$\Delta t \approx \frac{\Delta x}{a}. \tag{6.1}$$

Table 6.4 – Voigt element's properties for the Voigt-Kelvin viscoelastic models in the MOC-based models.

Experiment	Unsteady Friction Model	Voigt elements number	ι (GPa^{-1})	μ/G (s)
VI	No	3	0.1200	0.05
			0.1160	0.50
			0.0010	1.50
VII	No	3	0.0871	0.05
			0.1507	0.50
			0.6761	10.00
VI	Ramos et al. (2004)	3	0.0750	0.05
			0.0900	0.50
			0.0001	1.50
VII	Ramos et al. (2004)	3	0.0450	0.05
			0.1500	0.50
			0.1100	10.00

Additionally, the transient friction coefficients of the models proposed by Vitkovsky et al. (2000) and Ramos et al. (2004) are also experiment-dependent. Thus, Tab. 6.5 resumes the initial values for the transient friction coefficients used for the SPH based models and Tabs. 6.6 and 6.7 resume the transient friction coefficients used for the MOC based models.

The valve closure maneuver implicates significant numerical errors depending on its numerical model. Hou et al. (2012) pointed out an overshoot in the first pressure wavefront for an instantaneous closure and suggested a pre-smoothing treatment as a mitigation method. However, using a smoothed closure model, the overshoot naturally disappears from the numerical results. A possible model for ball valves is the orifice model, in which the discharge becomes a function of the piezometric head

$$Q = \frac{C_{or}}{\sqrt{1-\beta_{or}^4}} \frac{\pi\, d_{or}^2}{4} \sqrt{2\, g\, h}, \tag{6.2}$$

where C_{or} is the coefficient of discharge, d_{or} is the orifice diameter, and $\beta_{or} = d_{or}/d$ is the diameter ratio of orifice diameter to pipe diameter. Assuming that the experiment is initially at steady-state, the valve entirely opened, then the discharge is

$$Q_0 = \frac{\pi\, d^2}{4} \sqrt{2\, g\, h_{valve}^0}, \tag{6.3}$$

Table 6.5 – Time step and transient friction coefficients for each empirical setup used in SPH based models.

Experiments	Viscoelastic Model	K (-)	K_1 (-)	K_2 (-)
I	No	0.0070	0.0200	0.0070
II	No	0.0085	0.0160	0.0085
III	No	0.0095	0.0180	0.0095
VI	No	0.0095	0.0180	0.0095
V	No	0.0085	0.0180	0.0085
VI	No	0.0236	0.0144	0.0236
VII	No	0.0250	0.0850	0.0250
VI	Yes	0.0250	0.0850	0.0250
VII	Yes	0.0800	0.0800	0.0800

where h^0_{valve} is the initial piezometric head at the valve. Hence, the ratio of Eq. (6.2) to Eq. (6.3) is

$$Q = \frac{C_{or}\,\beta^2_{or}}{\sqrt{1-\beta^4_{or}}}\,Q_0\sqrt{\frac{h}{h^0_{valve}}} = \phi_{or}\,Q_0\sqrt{\frac{h}{h^0_{valve}}}. \tag{6.4}$$

Table 6.6 – Time step and transient friction coefficients for each empirical setup used in MOC based models with the experimental wave speeds as input.

Experiments	Viscoelastic Model	K (-)	K_1 (-)	K_2 (-)
I	No	0.0160	0.0010	0.0095
II	No	0.0160	0.0010	0.0078
III	No	0.0180	0.0010	0.0095
VI	No	0.0120	0.0001	0.0070
V	No	0.0100	0.0001	0.0070
VI	No	0.2066	0.2087	0.2066
VII	No	0.0170	0.0610	0.0170
VI	Yes	0.0170	0.0610	0.0170
VII	Yes	0.0400	0.0500	0.0400

Table 6.7 – Time step and transient friction coefficients for each empirical setup used in MOC based models with the corrected wave speeds as input.

Experiments	K (-)	K_1 (-)	K_2 (-)
I	0.0120	0.0200	0.0120
II	0.0095	0.0200	0.0100
III	0.0130	0.0200	0.0130
VI	0.0120	0.0200	0.0120
V	0.0120	0.0200	0.0120

where ϕ_{or} represents the effect of the valve closure maneuver relative to the initial state. Soares et al. (2017) supplied their closure maneuver data, such that one built the following equations using linear regression:

$$\phi_{or,I} = \begin{cases} -33136210550.00\,t^5 + 15977593421.18\,t^4 - \ldots \\ \ldots - 3082203992.922\,t^3 + 297344207.4208\,t^2 - \ldots \\ \ldots - 14345063.58997\,t \ + 276871.9170941, & \text{if } t \in [0.0939, 0.1015] \text{ s} \\ -3588165639.098\,t^4 + 1497047202.413\,t^3 - \ldots \\ \ldots - 234162994.9103\,t^2 + 16274344.66216\,t - \ldots \\ \ldots - 424034.6404308, & \text{if } t \in (0.1015, 0.1069] \text{ s} \end{cases} \tag{6.5}$$

$$\phi_{or,II} = \begin{cases} 30931597565.25\,t^5 - 15288705063.59\,t^4 + \ldots \\ \ldots + 3020788024.399\,t^3 + 297344207.4208\,t^2 - \ldots \\ \ldots - 14714135.67012\,t \ + 290206.5309442, & \text{if } t \in [0.0939, 0.1022] \text{ s} \\ -7528208028.395\,t^4 + 3157772340.466\,t^3 - \ldots \\ \ldots - 779591437.9822\,t^2 + 156817861.4321\,t - \ldots \\ \ldots - 11828551.88814, & \text{if } t \in (0.1022, 0.1069] \text{ s} \end{cases} \tag{6.6}$$

where $\phi_{or,I}$ and $\phi_{or,II}$ are relative to experiments I and II, respectively, Tab. 6.2. Figure 6.3 represents the empirical data and regression curves Regr1 and Regr2, relative to the two intervals that Eqs. (6.5) and (6.6) have.

Using the experimental data from Martins et al. (2016), one builts the following equations using linear regression:

Figure 6.3: Ball valve closure maneuver empirical data from Soares et al. (2017) and regression curves.

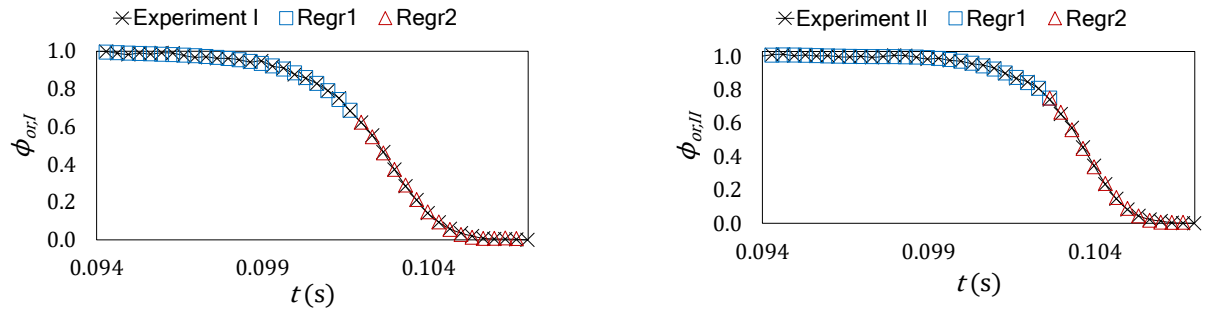

(a) Experiment I (b) Experiment II

Source: Own Authorship.

$$\phi_{or,III} = \begin{cases} -22026895341.00\,t^5 + 32196189399.71\,t^4 - \ldots \\ \ldots - 18824053123.65\,t^3 + 5502869160.653\,t^2 - \ldots \\ \ldots - 804326733.9482\,t\ + 47025451.94893, & \text{if } t \in [0.2886, 0.2976] \text{ s} \\ -1426943047.556\,t^4 + 1722394887.783\,t^3 - \ldots \\ \ldots - 779591437.9822\,t^2 + 156817861.4321\,t - \ldots \\ \ldots - 11828551.88814, & \text{if } t \in (0.2976, 0.3036] \text{ s} \end{cases} \tag{6.7}$$

$$\phi_{or,IV} = \begin{cases} -23633530486.50\,t^5 + 34545374625.25\,t^4 - \ldots \\ \ldots - 20198021539.31\,t^3 + 5904665129.024\,t^2 - \ldots \\ \ldots - 863076152.5143\ t + 50461510.61295, & \text{if } t \in [0.2886, 0.2976] \text{ s} \\ -1552829902.781\,t^4 + 1873132430.433\,t^3 - \ldots \\ \ldots - 847272930.5948\,t^2 + 170323404.6985\,t - \ldots \\ \ldots - 12839110.6795, & \text{if } t \in (0.2976, 0.3036] \text{ s} \end{cases} \tag{6.8}$$

$$\phi_{or,V} = \begin{cases} \quad -25141064389.25\,t^5 + 36749881726.51\,t^4 - \ldots \\ \ldots - 21487505120.24\,t^3 + 6281794071.637\,t^2 - \ldots \\ \ldots - 918224622.1600\;t + 53687303.17074, & \text{if } t \in [0.2886, 0.2976] \text{ s} \\ \quad -1636194166.699\,t^4 + 1972784117.887\,t^3 - \ldots \\ \ldots - 891939979.3917\,t^2 + 179221023.0860\,t - \ldots \\ \ldots - 13503706.84737, & \text{if } t \in (0.2976, 0.3036] \text{ s} \end{cases} \tag{6.9}$$

where $\phi_{or,III}$, $\phi_{or,IV}$, and $\phi_{or,V}$ are relative to experiments III, IV, and V, respectively, Tab. 6.2. Figure 6.4 represents the empirical data and regression curves Regr1 and Regr2, relative to the two intervals that Eqs. (6.7), (6.8), and (6.9) have.

Figure 6.4: Ball valve closure maneuver empirical data from Martins et al. (2016) and regression curves.

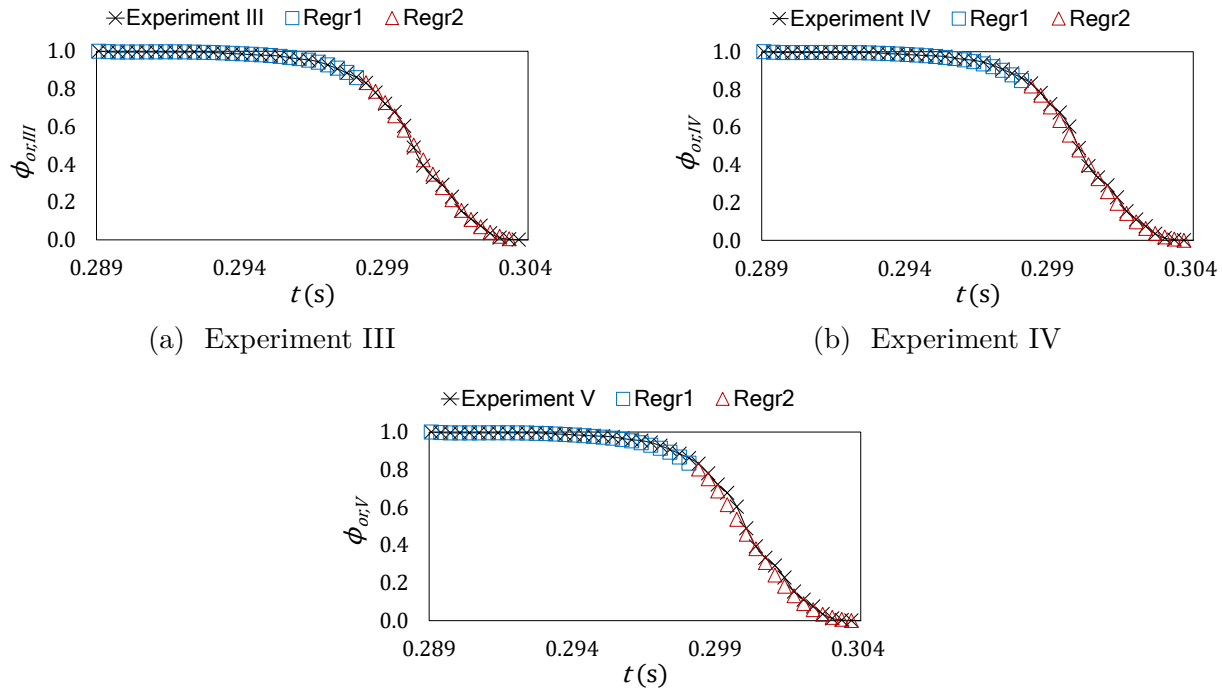

(a) Experiment III

(b) Experiment IV

(c) Experiment V

Source: Own Authorship.

The last set of experimental data is the one of Covas et al. (2005), from which one constructs the following equations of the valve closure maneuver effect:

$$\begin{aligned} \phi_{or,VI} = {} & 1650.9600708\,t^4 - 1143.7226854\,t^3 + \ldots \\ & \ldots + 229.03402032\,t^2 - 12.721545463\,t + \ldots \\ & \ldots + 0.7726266990, \qquad \text{if } t \in [0.1570, 0.3106] \text{ s} \end{aligned} \tag{6.10}$$

$$\begin{aligned}\phi_{or,VII} = {} & 7274.6913770\,t^4 - 5719.5575268\,t^3 + \ldots \\ & \ldots + 1603.2863430\,t^2 - 196.00649247\,t + \ldots \\ & \ldots + 10.014697696, \qquad \text{if } t \in [0.1703, 0.2806] \text{ s}\end{aligned} \tag{6.11}$$

where $\phi_{or,VI}$ and $\phi_{or,VII}$ are relative to experiments VI and VII, respectively, Tab. 6.2. Figure 6.5 represents the empirical data and regression curve Regr.

Figure 6.5: Ball valve closure maneuver empirical data from Covas et al. (2005) and regression curves.

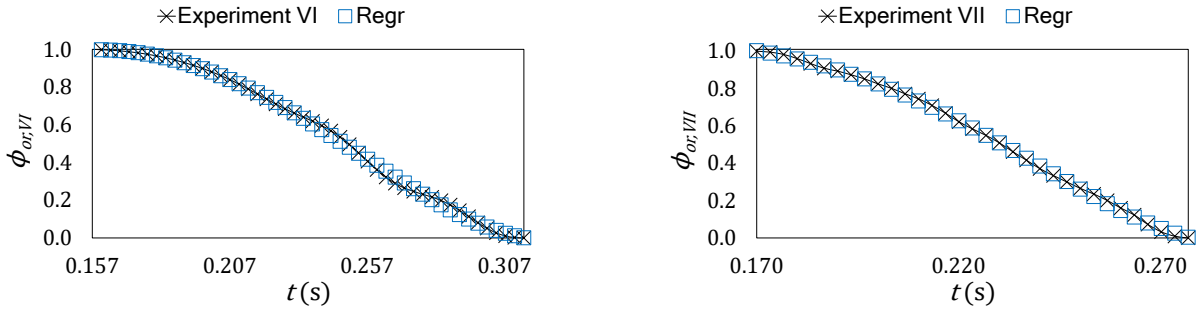

(a) Experiment VI (b) Experiment VII

Source: Own Authorship.

Experiments VI and VII show fluctuations in the reservoir piezometric head over time, requiring fitted equations for characterization. In experiment VI, the reservoir head is described by

$$h_{reservoir}\,(t) = \begin{cases} \quad 0.6002187309\,t^4 - 1.0326029405\,t^3 + \ldots & \\ \ldots + 0.5398833853\,t^2 - 0.0821863478\,t + \ldots & \\ \ldots + 45.4589409830 & \text{if } t \in [0.0000, 1.2031] \text{ s}, \\ \quad -6.1036393206 \times 10^{-7}\,t^6 + \ldots & \\ \ldots + 4.1833212328 \times 10^{-5}\,t^5 - \ldots & \\ \ldots - 1.1172311572 \times 10^{-3}\,t^4 + \ldots & \\ \ldots + 1.4685059103 \times 10^{-3}\,t^3 - \ldots & \\ \ldots - 1.0203549720 \times 10^{-1}\,t^2 + \ldots & \\ \ldots + 4.8445862009 \times 10^{-7}\,t + \ldots & \\ \ldots + 4.5171022079 \times 10^{1} & \text{otherwise}, \end{cases} \tag{6.12}$$

and in experiment VII,

$$h_{reservoir}\,(t) = 48.331537990 + 7.835039175 \times 10^{-3}\,t; \tag{6.13}$$

provides a better fit.

6.3 Error Evaluation

The current work uses two error evaluation types because each gives a specific data perspective. The first error type is the root mean square error (RMSE) defined by

$$RMSE = \sqrt{\frac{1}{T}\sum_{i=1}^{T}(f_i - \langle f_i \rangle)^2}, \tag{6.14}$$

where T is the total number of observed points, $\langle f \rangle$ is the approximated value, and f is the real value. It represents an oscillating signal steady-state or mean value and poses a relatively high weight for wide deviations in the dataset, resulting in sensitivity to outliers (HYNDMAN; KOEHLER, 2006). Additionally, one can normalize the RMSE to facilitate comparisons between datasets or models with different scales. A possible normalization choice is the range of the values, as in

$$NRMSE = \frac{RMSE}{f_{max} - f_{min}}, \tag{6.15}$$

or by the root mean square of the real values, as in

$$RMSPE = \sqrt{\frac{\sum_{i=1}^{T}(f_i - \langle f_i \rangle)^2}{\sum_{i=1}^{T} f_i^2}}. \tag{6.16}$$

The second error type is the mean absolute scaled error (MASE) defined by

$$MASE = \frac{\sum_{i=1}^{T} |f_i - \langle f_i \rangle|}{\sum_{i=1}^{T} |f_i - \overline{f}|}, \tag{6.17}$$

where $\overline{f}$ is the mean value of f. According to Hyndman and Koehler (2006), MASE has the following properties:

a. Independence from scale: MASE scales the error based on the in-sample Mean Absolute Error (MAE) from the naïve prediction method, allowing for meaningful comparisons across different datasets with varying scales.

b. Interpretability: MASE values greater than one indicate that the predictions are, on average, worse than the in-sample one-step forecasts from the naïve method. Values less than one indicate better performance than the naïve method. That makes MASE easy to interpret, as improvements are directly comparable to the naïve method.

c. Applicability: MASE can be applied to different forecasting scenarios, including single-step and multi-step forecasts, making it versatile in various forecasting contexts.

d. Robustness: MASE is less sensitive to outliers compared to other error measures such as Root Mean Squared Scaled Error (RMSSE) and Median Absolute Scaled Error (MdASE), making it more reliable when dealing with datasets containing extreme values.

e. Finite and defined values: MASE always provides a finite and defined value, except in cases where all historical observations are equal, which is an unlikely scenario in practical prediction.

f. Consistency: When the Mean Absolute Scaled Error (MASE) is less than 1, it indicates that, on average, the errors are smaller than those from the naïve method. This consistent improvement provides confidence in the evaluation of prediction methods.

g. Comparison across different scales: Mean Absolute Scaled Error (MASE) enables the comparison of prediction accuracy across series with different scales by providing a universally applied standardized measure.

6.4 Response Surface Methodology (RSM)

Response Surface Methodology (RSM) is an ensemble of mathematical and statistical techniques aimed at optimizing processes where the response is influenced by several variables. This methodology is instrumental in exploring complex relationships where the form of the response surface is not known beforehand. It is extensively applied in industrial and scientific research to model and refine multi-variable equations.

6.4.1 Fundamentals of Response Surface Methodology

The foundation of RSM lies in its systematic approach to empirical model building, exploring the effects of multiple factors and their interactions on a response. The methodology typically begins with the identification of the factors likely to affect the response variable. Following this, a sequence of designed experiments is conducted to generate data that covers the region of interest sufficiently. This exploratory phase is crucial as it sets the stage for a more detailed investigation around the optimum response region (MONTGOMERY, 2013).

A key aspect of RSM is its iterative nature, where initial experiments guide subsequent experiments. This iterative process continues until a satisfactory model of the response surface is obtained, which can then be used to locate the optimum settings of the

process variables. RSM aims not just at finding the settings that optimize the response, but also at understanding the nature of the response surface to ensure robustness and reliability in the process being optimized (MYERS et al., 2009).

Experimental designs employed in RSM are chosen based on their ability to provide clear, unbiased insights into complex multi-variable relationships. The initial phase often uses factorial designs due to their structured way of investigating all possible combinations of the levels of the variables. This is usually followed by more focused designs that allow for the exploration of nonlinear relationships and interactions among the variables.

6.4.2 Experimental Design in RSM

The selection of an appropriate experimental design is critical in RSM because it influences the efficiency of the analysis and the quality of the information obtained. The Central Composite Design (CCD) and the Box-Behnken design are two of the most commonly used designs in RSM. These designs are particularly favored for their ability to fit second-order (quadratic) models efficiently, which are crucial for exploring and optimizing response surfaces that exhibit curvature.

When experimental regions are irregular or when a non-standard model is needed, D-optimal designs are particularly advantageous. These designs are constructed to maximize the determinant of the information matrix thus providing the best possible estimation of the regression coefficients under model constraints. This feature is especially beneficial in constrained experimental regions or when the number of runs needs to be minimized without sacrificing the accuracy of the model.

D-optimal designs are a subset of optimal designs that focus on the efficient estimation of model parameters, particularly when dealing with practical constraints such as limited resources or specific experimental conditions. By strategically placing the design points, these designs help in obtaining the maximum possible information about the parameters, thereby enhancing the reliability of the model predictions.

6.4.3 Polynomial Models in RSM

RSM predominantly uses polynomial models to approximate the true response surface. Initially, a first-order (linear) polynomial model is often employed:

$$y = \beta_0 + \sum_{i=1}^{k} \beta_i \, x_i + \varepsilon, \tag{6.18}$$

where y is the response variable, β_0, βi are the model coefficient, x_i are the independent variables, and ε represents the random error.

This model provides the base understanding of how each factor influences the response. It is particularly useful for identifying the direction of the steepest ascent or descent, which indicates the path along which the response changes most rapidly.

As insights into the system improve, second-order polynomial models are generally required to adequately model the curvature of the response surface:

$$y = \beta_0 + \sum_{i=1}^{k} \beta_i \, x_i + \sum_{i=1}^{k} \beta_{ii} \, x_i^2 + \sum \sum_{i<j} \beta_{ij} \, x_i \, x_j + \varepsilon. \tag{6.19}$$

This model includes not only the main effects but also the interaction effects and quadratic terms, which are crucial for capturing more complex behaviors of the response surface. The inclusion of these terms allows for a more detailed and nuanced understanding of the relationships between the variables, providing a more accurate depiction of the response surface (KHURI; CORNELL, 1996).

6.4.4 Analysis of the Fitted Model

Once the polynomial model is fitted, rigorous analysis follows to assess its adequacy. This analysis includes evaluating the significance of the model terms through Analysis of Variance (ANOVA), assessing the goodness of fit, and performing model diagnostics to identify any potential problems like outliers or influential points. These steps ensure that the model is not only statistically significant but also valid for prediction within the context of the experimental data.

Graphical methods such as contour plots and three-dimensional surface plots are indispensable tools in RSM. They provide visual interpretations of the model, illustrating how the response varies with changes in the input variables. These plots are particularly useful for identifying regions of maximum or minimum response and for understanding the nature of the response surface—whether it is showing a global optimum, local optima, or saddle points.

6.4.5 Optimization Using RSM

The ultimate goal of RSM is to use the developed model to find the optimum conditions that maximize or minimize the response. Techniques like the method of steepest ascent or descent are used initially to move toward the region of the optimum. In this technique, experiments are conducted along the path in the direction of the steepest gradient of the response surface until no further improvement is observed.

Once near the optimum, more sophisticated optimization techniques may be required to fine-tune the model and to precisely locate the optimum. These techniques might include numerical optimization methods, which use algorithms to find the best

settings of the variables based on the fitted model. This step is critical for ensuring that the optimum conditions are both accurate and practical for implementation in the real-world process.

6.5 The Wave Speed Measurement (WSM) Algorithm

The Discrete Fourier Transform (DFT) is an available mathematical tool for computing the wave speed of a signal by decomposing it into its periodic components (HEIDEMAN et al., 1984). This process occurs within the frequency domain, enabling the signal's frequency spectrum analysis. One can compute the wave speed by deriving the wave frequency from this spectral information, knowing the wavelength.

According to Press et al. (2007), the Discrete Fourier Transform (DFT) of a function $g(t)$ is computed at N_f discrete points, denoted as g_k, as expressed in

$$\mathcal{DFT}\left\{g_k\right\} = G_n = \sum_{k=0}^{N_f-1} g_k \exp\left(2\,\pi\,i\,k\,n\,/N_f\right). \tag{6.20}$$

The transformed components, G_n, correspond to the frequency domain representation of g_k. The inverse operation, which reconstructs the time-domain signal from its frequency components, is defined by

$$\mathcal{DFT}^{-1}\left\{G_n\right\} = g_k = \frac{1}{N_f}\sum_{n=0}^{N_f-1} G_n \exp\left(-2\,\pi\,i\,k\,n\,/N_f\right), \tag{6.21}$$

where $i = \sqrt{-1}$ in Eqs. (6.20) and (6.21).

However, both transformations are computationally intensive, requiring $\mathcal{O}(N_f^2)$ operations in a straightforward implementation. To address this inefficiency, Cooley and Tukey (1965) introduced the Fast Fourier Transform (FFT), which significantly reduces the computational complexity to $\mathcal{O}(N_f \log N_f)$. This breakthrough paved the way for the development of numerous other algorithms that maintain the $\mathcal{O}(N_f \log N_f)$ efficiency in calculating the DFT (PRESS et al., 2007).

The frequency spectrum presented in Fig. 6.6 illustrates the decomposition of a signal into its fundamental components, each corresponding to a specific frequency. Typically, the highest amplitude frequency is the most significant contributor to the signal frequency. Consequently, this peak frequency is identified as the fundamental frequency of the signal (KAY, 1993).

According to Smith (2011), the optimal approach for extracting sinusoidal parameters from a dataset involves determining the amplitude, phase, and frequency of each spectral peak obtained from a zero-padded FFT of the data. Zero padding entails

Figure 6.6: Representation of the FFT transformation of an arbitrary function.

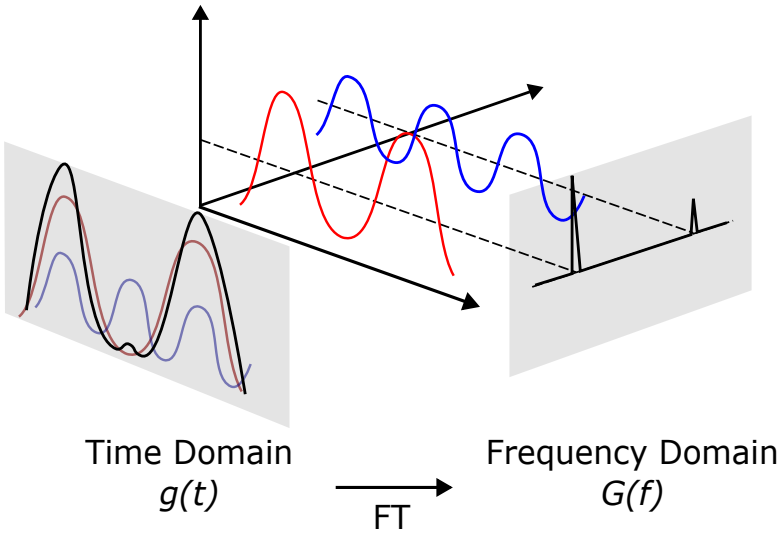

Source: Modified from Gomede (2023).

extending a signal (or spectrum) by appending zeros, allowing the transformation of a dataset of length N_f to a longer length M_f where $M_f > N_f$, and N_f does not need to be a divisor of M_f. Mathematically, zero padding is defined by

$$ZeroPad_{M_f,m_f}(t) = \begin{cases} t(m_f), & |m_f| < N_f/2 \\ 0, & \text{otherwise} \end{cases} \tag{6.22}$$

where m_f ranges over $0, \pm 1, \pm 2, \cdots, \pm M_h$, with $M_h \approx (M_f - 1)/2$ for odd M_f and $M_f/2 - 1$ for even M_f.

Utilizing a zero-padded FFT of the dataset, Smith (2011) have addressed several critical aspects for estimating sinusoidal parameters:

a. Ensure that the data (or window) length is sufficiently long to resolve all sinusoidal components within the signal.

b. Apply adequate zero padding to achieve significant spectrum oversampling, facilitating more straightforward peak interpolation.

c. To refine the peak estimation, Implement quadratic interpolation on the three samples surrounding a dB-magnitude peak in the oversampled spectrum.

d. Evaluate the resulting fitted parabola at its extremum to derive interpolated estimates of amplitude and frequency for each sinusoidal component.

e. Compute a phase estimate for each peak frequency through quadratic or linear interpolating of the unwrapped phase values near the peak.

The initial step in signal processing is the windowing of the data set, which entails selecting a small segment from a larger dataset using a window or tapering function. According to Kumar (2014), a window function is a mathematical construct that takes on a zero value outside a specified interval. Typically, these functions exhibit symmetry about their midpoint, reaching a peak at the center and tapering off toward the edges. Windowing is particularly crucial for non-periodic datasets, as appending them directly in the time domain may introduce discontinuities that get magnified in the frequency domain. This spectral deviation, known as spectral leakage, can distort the frequency representation of the signal. The application of a suitable window function mitigates this spectral leakage (PRESS et al., 2007; SMITH, 2011).

However, it should be noted that the resultant windowed continuous waveform may not accurately represent the original waveform. An inherent trade-off affects both the amplitude and energy of the signal. While window-specific corrections exist to compensate for these effects, simultaneous correction for amplitude and energy is not feasible (PRESS et al., 2007; SMITH, 2011).

Upon applying a window function to a suitably zero-padded sinusoidal signal and executing an FFT, the resulting spectrum, as depicted in Fig. 6.7, reveals a prominent peak at the center, referred to as the main lobe, flanked by adjacent peaks known as side lobes. Focusing on the main lobe in Fig. 6.8, one observes its resemblance to a quadratic function, suggesting that a quadratic polynomial can effectively approximate the main lobe's shape. This approximation holds for any practical window function over a sufficiently small region around the peak due to the convergence of higher-order terms in the Taylor series expansion around the peak to zero as one approaches it.

Figure 6.7: Arbitrary sinusoidal signal in (a) that is windowed in (b).

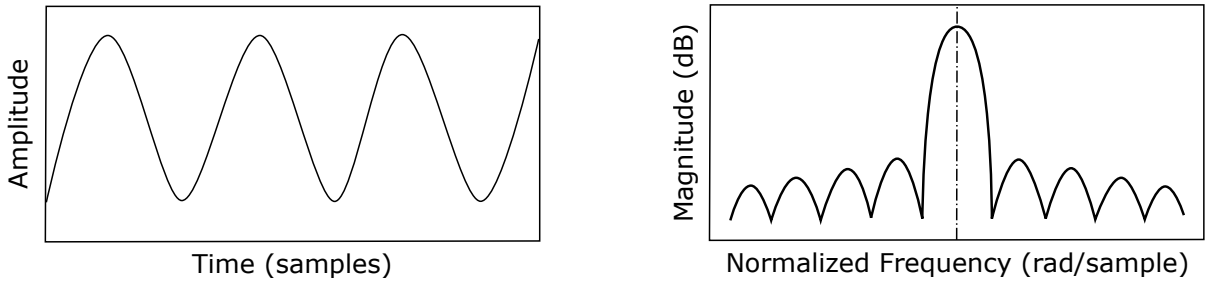

(a) Sinusoidal signal (b) Windowed signal

Source: Own Authorship.

Quadratic interpolation employs three neighboring points, α_f, β_f, and γ_f, surrounding the target peak, p_f, normalized within the interval $[-1, 1]$ as illustrated in Fig. 6.8. The reference point $(0, \beta_f)$ is selected based on its alignment with the estimated sinusoidal frequency. As demonstrated by Press et al. (2007), the sinusoidal frequency estimator,

Figure 6.8: Zoom in on the main lobe of the windowed signal and the superposed quadratic polynomial that pass on the points $(-1, \alpha_f)$, $(0, \beta_f)$, and $(-1, \gamma_f)$, which are the nearest neighbors of the actual main lobe's peak.

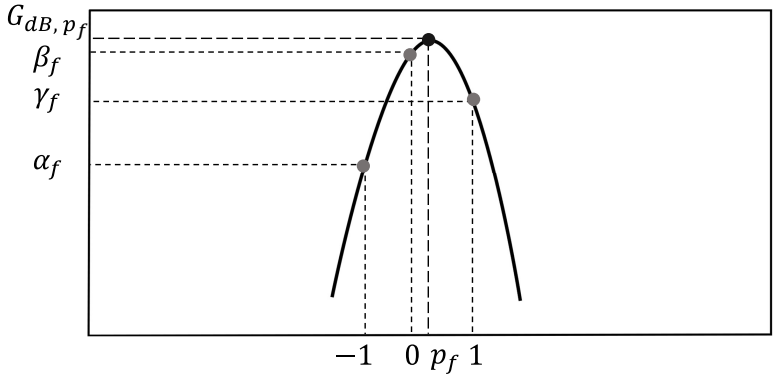

Source: Modified from Smith (2011).

derived from a least-squares approach, corresponds to the frequency that maximizes the magnitude of the DFT, as expressed in

$$\widehat{\omega}_0^* = \arg\left\{\max_{\widehat{\omega}_0} \left|\mathcal{DFT}\left\{g_k\right\}\right|\right\}. \tag{6.23}$$

where $\widehat{\omega}_0^*$ is the least-square estimated frequency in rad/samples, and $\widehat{\omega}_0$ are the frequencies of the discretized sinusoidal signal f_k.

Considering k as the point that yields the least-square estimated sinusoidal frequency, the actual peak can be derived from

$$p_f = \frac{1}{2}\frac{\alpha_f - \gamma_f}{\alpha_f - 2\,\beta_f + \gamma_f} + k, \tag{6.24}$$

or

$$p_f = \frac{1}{2}\frac{G_{dB,k-1} - G_{dB,k+1}}{G_{dB,k-1} - 2\,G_{dB,k} + G_{dB,k+1}} + k, \tag{6.25}$$

where $G_{dB} = \log\left(|G|\right)$, while its magnitude is specified in

$$G_{dB,p_f} = \beta_f - \frac{1}{4}\left(\alpha_f - \gamma_f\right)\left(p_f - k\right). \tag{6.26}$$

or

$$G_{dB,p_f} = G_{dB,k} - \frac{1}{4}\left(G_{dB,k-1} - G_{dB,k+1}\right)\left(p_f - k\right). \tag{6.27}$$

The final estimated frequency of the signal is calculated using

$$\langle f_0 \rangle = f_s \frac{p_f}{N_w}, \tag{6.28}$$

where $\langle f_0 \rangle$ is the estimated frequency in Hz by interpolation, f_s represents the signal acquisition frequency in Hz and N_w indicates the length of the windowed signal. The entire methodology is encapsulated in Algorithm 1, where H_w is an arbitrary window function and $FFT(\cdot)$ represents an arbitrary FFT algorithm.

Algorithm 1 Frequency estimation using FFT and quadratic interpolation.

$$\begin{aligned}
g_{window} &\leftarrow g\, H_w(M_f) \\
G_{window} &\leftarrow \mathrm{FFT}(g_{window}) \\
k &\leftarrow \arg\{\max |G_{window}|\} \\
G_{dB} &\leftarrow \log(|G_{window}|) \\
p_f &\leftarrow \frac{1}{2} \frac{G_{dB,k-1} - G_{dB,k+1}}{G_{dB,k-1} - 2\,G_{dB,k} + G_{dB,k+1}} + k \\
\langle f_0 \rangle &\leftarrow f_s \frac{p_f}{N_w}
\end{aligned}$$

There is a second approach to estimating a signal. It is based on the autocorrelation properties of the function's DFT. Autocorrelation is the correlation of a signal with a delayed copy of itself as a function of delay,

$$(g * g)_k = \frac{1}{N_f} \sum_{m=0}^{N_f - 1} \overline{g_m}\, g_{m+k}. \tag{6.29}$$

The analysis of autocorrelation is a mathematical tool for finding repeating patterns, such as the presence of a periodic signal obscured by noise or identifying the missing fundamental frequency in a signal implied by its harmonic frequencies (PROAKIS; SALEHI, 2002).

According to Todd and Cruz (1996) and Xiao et al. (2007), various autocorrelation-based algorithms for frequency estimation have been developed. The methodology employed in the current work focuses on repetitive pattern identification. Thus, the autocorrelation function, as defined in Eq. (6.27), is computed for finite discrete samples of g_k. This process yields a symmetric function that exhibits a peak at the origin, as illustrated in Fig. 6.9. Furthermore, the autocorrelation preserves the periodic characteristics of the original signal. Based on these properties and considering the positive lags, one determines the frequency using the peak after the first local minimum. Then, use quadratic interpolation to refine the estimated frequency position.

A k-th discrete difference operation is conducted along the lag axis to pinpoint the first local minimum. This operation produces an array where the initial positive entry corresponds to the first local minimum in the autocorrelation. Then, the second peak of the autocorrelation is identified using the $\arg\{\max |\cdot|\}$ function. Afterwards, one applies

Figure 6.9: Autocorrelation result of an arbitrary discrete function g_k.

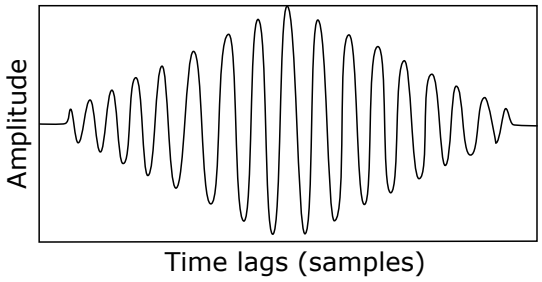

Source: Own Authorship.

quadratic interpolation to determine the lag associated with the estimated frequency. The estimated frequency is subsequently computed using

$$\langle f_0 \rangle = \frac{f_s}{p_f}. \tag{6.30}$$

The process is summarized in Algorithm 2, where $\text{positive} - \text{lags}\,(\cdot)$ takes only the positive lags of an array, $\text{diff}\,(\cdot)$ applies the k-th discrete difference, and $\text{find}\,(\cdot)$ looks for the first lag at which the array values match the input condition.

Algorithm 2 Frequency estimation using autocorrelation and quadratic interpolation.

$$
\begin{aligned}
g_{autocorr} &\leftarrow g * g \\
g_{autocorr} &\leftarrow \text{positive} - \text{lags}\,(g_{autocorr}) \\
g_{diff} &\leftarrow \text{diff}\,(g_{autocorr}) \\
k_0 &\leftarrow \text{find}\,(g_{diff} > 0) \\
k &\leftarrow \arg\left\{\max\left|g_{autocorr,k>=k_0}\right|\right\} + k_0 \\
p_f &\leftarrow \frac{1}{2}\frac{g_{autocorr,k-1} - g_{autocorr,k+1}}{g_{autocorr,k-1} - 2\,g_{autocorr,k} + g_{autocorr,k+1}} + k \\
\langle f_0 \rangle &\leftarrow \frac{f_s}{p_f}
\end{aligned}
$$

This study employs both frequency estimation algorithms on the normalized pressure wave measurements. The average of the two frequencies is utilized to compute the estimated wave speed as described in

$$\langle a \rangle = 4\,L\,\left\langle \overline{f}_0 \right\rangle, \tag{6.31}$$

where L is the pipe length, $\langle a \rangle$ is the estimated wave speed, and $\left\langle \overline{f}_0 \right\rangle$ is the average of the estimated frequencies.

7 RESULTS

The current work results section includes a subsection covering the validation of the CSPH method coupled with the transient friction models against experimental data. The CSPH method is calibrated and evaluated based on the behavior of its crucial parameters. A similar procedure is carried out using only the viscoelastic method, and finally, both friction and viscoelasticity aspects are coupled to the CSPH method for evaluation.

7.1 Elastic Pipe with Unsteady Friction

This section focuses on assessing the unsteady friction component of the numerical scheme developed. The evaluations draw on the experimental setups I, II, III, IV, and V in Tab. 6.2 from Soares et al. (2017) and Martins et al. (2016), which utilized elastic pipelines and highlighted unsteady friction as the dominant influence on pressure wave propagation.

The dimensionless piezometric head facilitates comparison between experimental and numerical outcomes. The unsteady friction models referenced are those developed by Vardy and Hwang (1993), Vitkovsky et al. (2000), and Ramos et al. (2004), which are designated as models 1, 2, and 3, respectively. Moreover, the numerical methods and associated unsteady friction models are commonly referred to using the acronyms -VH, -V, and -R, correlating to Vardy and Hwang (1993), Vitkovsky et al. (2000), and Ramos et al. (2004) accordingly.

This section will encounter notations such as CSPH-VH, which denotes the Corrected Smoothed Particle Hydrodynamics implemented with the unsteady friction model as per Vardy and Hwang (1993). The initial test parameters for the numerical methodologies are in the Tab. (2).

7.1.1 Measuring the Wave Speed: CWSM Algorithm

The WSM algorithm employs a FFT for signal analysis, enabling identification of the signal peak. Two techniques—parabolic interpolation and autocorrelation analysis—are implemented to refine the peak estimation. This methodology facilitates the calculation of an approximate period, which is used to derive wave speed. The definitive wave speed is the average of the values obtained from parabolic interpolation and autocorrelation.

When applied to Experiments I and III, wave speeds of 1264.2657 m/s and 1251.7499 m/s were determined, resulting in deviations of 9. m/s and 1.7499 m/s from the experimental values of 1255 m/s and 1250 m/s, respectively. Thus, assume that the simulation outcomes derived from variations of SPH and MOC retain the essential characteristics

of the corresponding experimental data. Consequently, deviations observed in the experimental measurements are used for correction when applying the WSM algorithm to the simulation data. This methodology is termed the Corrected WSM (CWSM).

For instance, in applying the CWSM to the wave speed obtained from the GSPH simulation for Experiment I, the WSM generates a wave speed of 1278.0462 m/s. When corrected by the deviation factor of 9.2657 m/s associated with Experiment I, this value adjusts to 1268.7805 m/s.

7.1.2 Testing the SPH and MOC algorithms

7.1.2.1 The Correction Effect

Many SPH algorithms initiate the computation by determining particle density, typically using the formulation outlined in Eq. (4.32). However, the ghost particle boundary treatment circumvents the need for density updates since Eqs. (4.33) and (4.34) inherently maintain mass balance. The MOC exhibits a similar characteristic. Conversely, in the CSPH method, it is necessary to compute corrections before applying the balance equations, and these corrections must be updated if particle positions exhibit temporal variations. These adjustments alter the volume of the particles, thereby affecting their density. Consequently, density recalculations are performed using Eq. (4.32) following the scheme of Eq. (4.47), leading to the density distribution depicted in Fig. 7.1. This figure reveals an overall reduction in density, indicating an increase in particle volume, with this phenomenon being more pronounced at the numerical boundaries compared to the interior of the computational domain.

Figure 7.1: Density distribution within the numerical domain of the Experiment I after applying the correction from the CSPH method. The input density was 998 kg/m^3 (water at 20^{o}C).

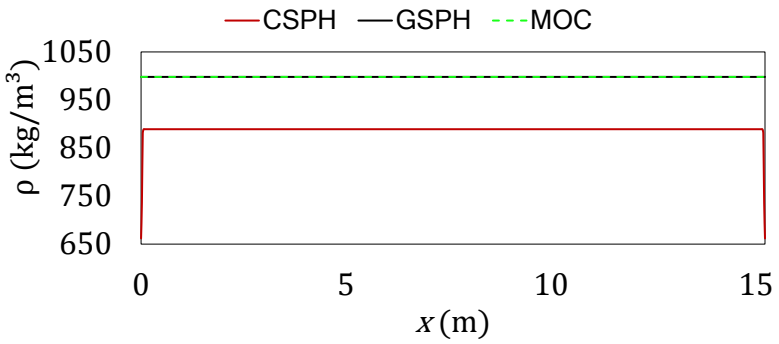

Source: Own authorship.

The impact of the correction embedded in CSPH is a notable change in the numerical pressure wave speed since it depends on the fluid density distribution, Eq. (3.41).

This phenomenon is illustrated in Fig. 7.2, which represents Experiment I alongside the numerical outcomes from the GSPH, CSPH, and MOC methods, all of which operate without an unsteady friction model. CSPH and MOC yield visually similar wave speeds, yet CSPH generates a sinusoidal wave profile, while MOC produces a squarish waveform. Compared to GSPH and CSPH, the GSPH method yields a higher density throughout the domain and at the boundaries, resulting in higher speed values (1268.7805 m/s) than those observed in CSPH (1244.9744 m/s). The same phenomenon occurs in the simulation of Experiment III, Fig. 7.3. The GSPH presents a higher wave speed (1271.9279 m/s), while CSPH and MOC yield a slower wave speed (1247.2177 m/s), which is not visually evident due to the plot time range.

Figure 7.2: Numerical results from GSPH, CSPH and MOC methods without an unsteady friction model, comparing the pressure wave speed with Experiment I.

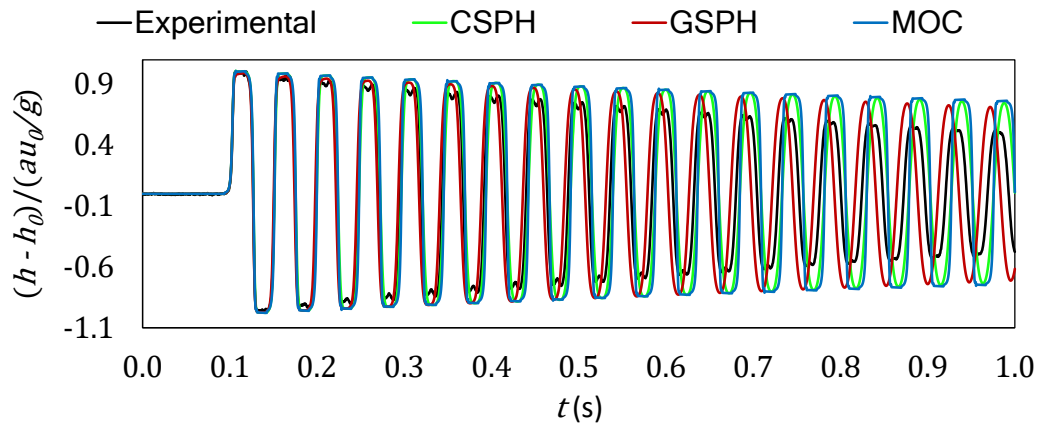

Source: Own authorship.

The variation in numerical wave speeds between GSPH and CSPH is examined in this simulation by applying unsteady friction models. Unsteady friction model 1 is deemed more suitable for this analysis due to its straightforward formulation, lacking the additional variables introduced by models 2 and 3 (K, K_1, and K_2). Figure 7.4 presents the results from Experiment I, showcasing the comparison among GSPH-VH, CSPH-VH, and MOC-VH. The findings indicate that the unsteady friction mechanism contributes a damping effect, thereby reducing the wave speed as anticipated. Specifically, GSPH-VH achieves a wave speed of 1257.9360 m/s, in contrast to CSPH-VH and MOC-VH, which exhibit reduced wave speeds of 1234.8094 m/s.

A similar trend is observed in Experiment III, as depicted in Fig. 7.23, where the numerical simulations leverage unsteady friction model 1. The wave speed recorded for GSPH-VH is 1261.6019 m/s, while CSPH-VH and MOC-VH show values of 1236.5089 m/s. This consistency across experiments underscores the influence of the density distribution

Figure 7.3: Numerical results from GSPH, CSPH and MOC methods without an unsteady friction model, comparing the pressure wave speed with Experiment III.

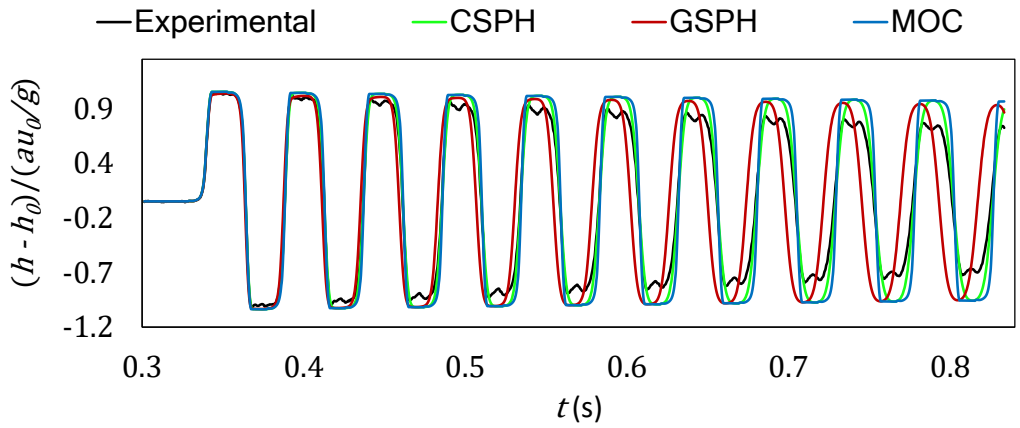

Source: Own authorship.

Figure 7.4: Numerical results from GSPH-VH, CSPH-VH and MOC-VH methods, comparing the pressure wave speed with Experiment I.

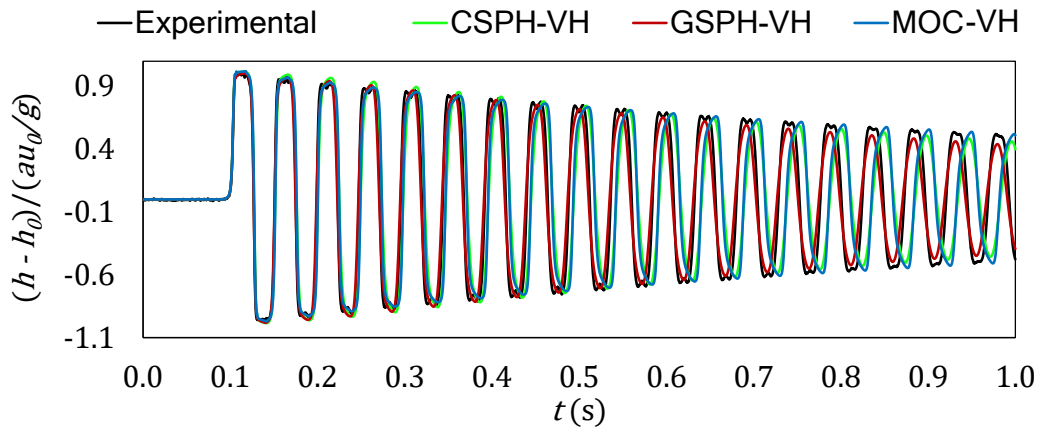

Source: Own authorship.

on wave propagation characteristics in the context of the simulations conducted using GSPH and CSPH.

A potential approach to address the loss of momentum associated with density reduction in the CSPH method is to adjust the numerical wave speed. Assuming that the time derivative of the piezometric head computed using the GSPH aligns with that derived from the CSPH. That leads to:

Figure 7.5: Numerical results from GSPH-VH, CSPH-VH and MOC-VH methods, comparing the pressure wave speed with Experiment III.

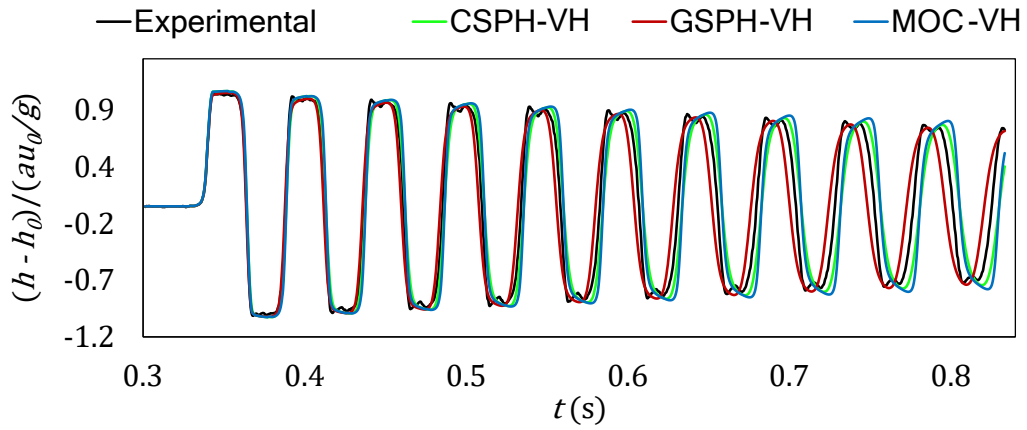

Source: Own authorship.

$$\left\langle \frac{Dh}{Dt} \right\rangle_{a,CSPH}^{t+1} = -\frac{a^2}{g}\phi_{CSPH} \sum_{b\in\mathcal{N}_a} u_{ba}^t \frac{\partial W_{ab}^t}{\partial x_{1,a}^t} \frac{m_b^t}{\rho_b^t} = \\ -\frac{a_0^2}{g} \sum_{b\in\mathcal{N}_a} u_{ba}^t \frac{\partial W_{ab}^t}{\partial x_{1,a}^t} \frac{m_b^t}{\rho_{0,b}^t} = \left\langle \frac{Dh}{Dt} \right\rangle_{a,GSPH}^{t+1}, \tag{7.1}$$

where ϕ_{CSPH} represents the correction factor, a_0 is the experimentally measured wave speed and ρ_0 is the original density,

$$\phi_{CSPH} = \left(\sum_{b\in\mathcal{N}_a} x_{ba}^t \frac{\partial W_{ab}^t}{\partial x_{1,a}^t} \frac{m_b^t}{\rho_b^t} \right)^{-1}. \tag{7.2}$$

Given that particles' mass, position, and density are constant throughout the simulation, we can simplify Eq. (7.4) into

$$\frac{a^2\, m\, \phi_{CSPH}}{\rho} = \frac{a_0^2\, m}{\rho_0} \rightarrow a = \sqrt{\frac{a_0^2\, \rho}{\phi_{CSPH}\, \rho_0}}. \tag{7.3}$$

This simplification enables estimating the required wave speed to counteract the effects of density reduction.

Using the wave speed measured from experimental data by WSM algorithm and Eq. (7.3), one derives compensated wave speed values for more accurate corrections. For Experiment I, an experimental wave speed of 1264.2657 m/s translates to a numerical speed estimate of 1277.2000 m/s. By correcting for the deviation of 9.2657 m/s, we arrive

at a corrected wave speed of 1267.9343 m/s, which closely approximates the speed recorded in the simulation data without employing an unsteady friction model with GSPH, yielding an absolute error of 0.8462 m/s.

Similarly, for Experiment II, the experimental wave speed of 1251.7499 m/s results in a numerical estimation of 1265.3500 m/s. Correcting for the deviation of 1.7499 m/s leads to a compensated wave speed of 1263.6001 m/s. This correction reflects a deviation of approximately 8.3278 m/s from the speed observed in the simulation data using GSPH without an unsteady friction model.

The compensated wave speed variant of the CSPH method will be referred to as CCSPH, which stands for Compensated Corrected Smoothed Particle Hydrodynamics. Figures 7.6 and 7.7 illustrate the numerical results obtained from CCSPH in comparison with experimental data and simulation outputs from both the GSPH and CSPH methodologies. The MASE relative to the GSPH indicates that the CCSPH is 9.29% closer to GSPH in Experiment I and 21.96% in Experiment III, indicating a more substantial alignment of CCSPH with GSPH in Experiment I compared to Experiment III. Utilizing the unsteady model 1, the results shown in Figs. 7.8 and 7.9 exhibit consistent differences between CCSPH and GSPH, with MASE values of 8.66% for Experiment I and 20.96% for Experiment III.

Figure 7.6: Numerical results from GSPH, CSPH and CCSPH methods without an unsteady friction model, comparing the pressure wave speed with Experiment I.

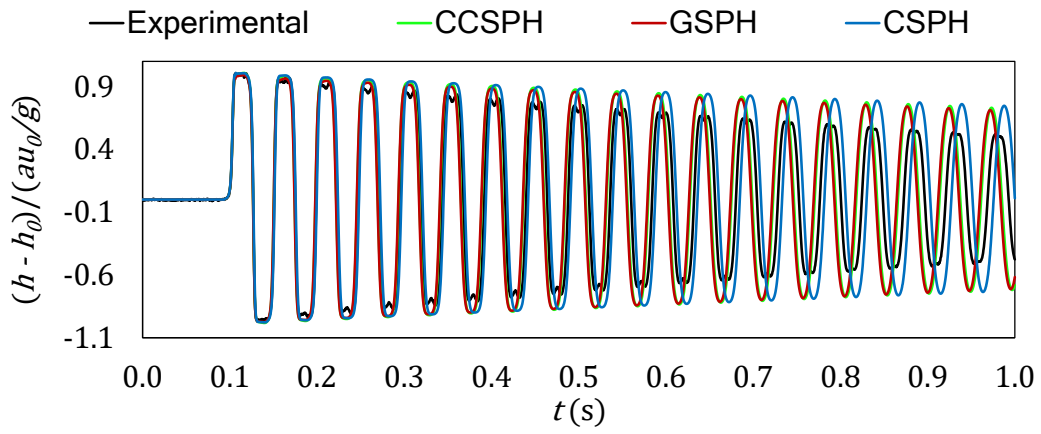

Source: Own authorship.

In the analysis, CCSPH demonstrates performance metrics that are on par with GSPH in Experiment I while outperforming both CSPH and GSPH in Experiment III. Specifically, in Experiment I, the MASE for CCSPH-VH is recorded at 16.08%, compared to 19.49% for GSPH-VH and a significantly higher 57.65% for CSPH-VH. In contrast,

Figure 7.7: Numerical results from GSPH, CSPH and CCSPH methods without an unsteady friction model, comparing the pressure wave speed with Experiment III.

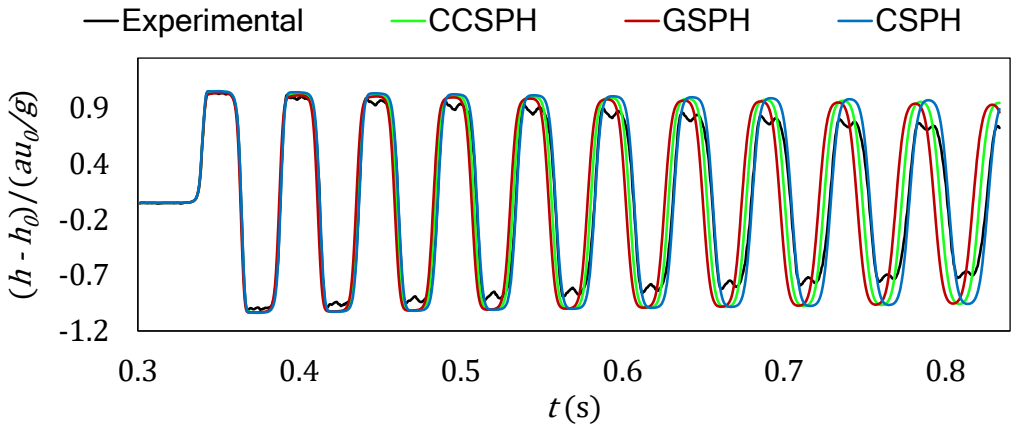

Source: Own authorship.

Figure 7.8: Numerical results from GSPH-VH, CSPH-VH and CCSPH-VH, comparing the pressure wave speed with Experiment I.

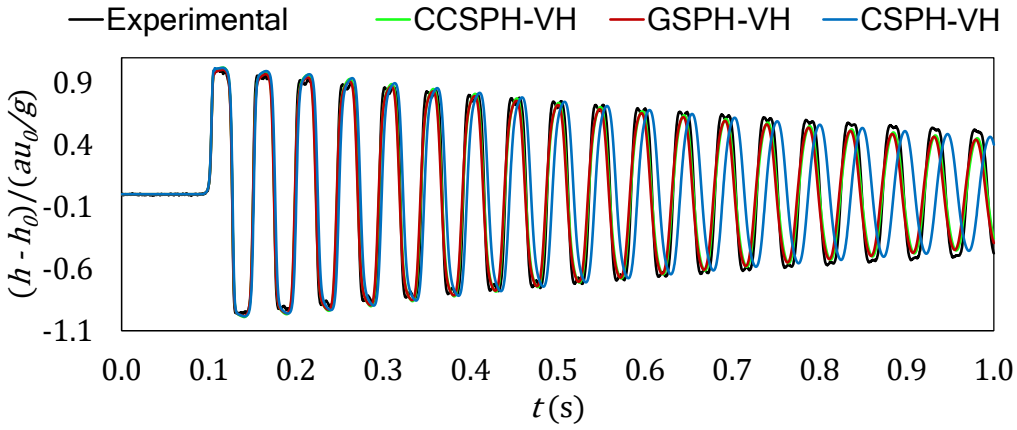

Source: Own authorship.

Experiment III shows improved accuracy, with CCSPH-VH achieving a MASE of 8.92%, GSPH-VH at 23.23%, and CSPH-VH at 27.34%.

Utilizing the CWSM algorithm for wave speed measurement, CCSPH yields values of 1266.5519 m/s in Experiment I and 1261.5511 m/s in Experiment III. These results exhibit deviations of -0.11% and -0.16%, respectively, when compared to the corrected wave speeds derived from Eq. (7.3). Furthermore, when applying the unsteady friction model 1, CCSPH-VH records wave speed values of 1255.6252 m/s and 1251.0888 m/s for Experiment I and III, respectively. These speeds reveal deviations of 0.05% and 0.09%

Figure 7.9: Numerical results from GSPH-VH, CSPH-VH and CCSPH-VH methods, comparing the pressure wave speed with Experiment III.

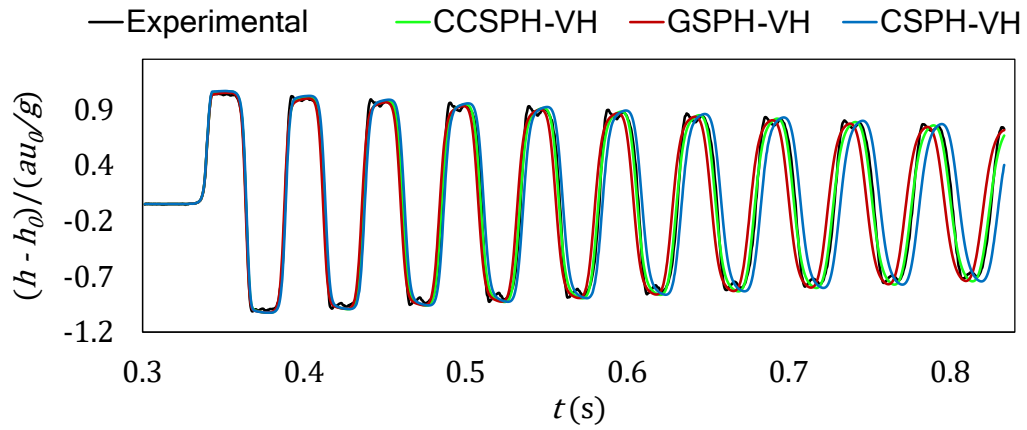

Source: Own authorship.

when juxtaposed with experimental measurements. Thus, it is evident that CCSPH has effectively achieved the intended compensation for reductions in density and momentum.

7.1.2.2 Unsteady Friction Models Aspects in CCSPH

The CCSPH method captured the first pressure wave peak in Figs. 7.10-7.14 with and without the transient friction models. Applying only the quasi-stationary friction model results in numerical results with slight damping and a faster wave speed than the experimental curve. This wave speed difference became visually significant in the ninth wave peak in Figs. 7.10 and 7.11, and in the sixth peak in Figs. 7.12, 7.13, and 7.14.

The transient friction models shown in Figs. 7.10-7.14 provide enhanced damping effects and accurately replicate the decay observed in experimental results, which confirms their effectiveness in modeling pressure wave behavior. Transient model 1 (CCSPH-VH) slows numerical pressure waves more than model 2 (CCSPH-V), especially compared to the quasi-stationary friction approach results. Model 2 shapes pressure waves similarly to model 3 (CCSPH-R). However, since model 2 uses the same coefficient (K) for both local and advective terms, adjustments can only be made to one characteristic of the pressure wave at a time—either the damping rate or the wave celerity. Model 3 resolves the issue by decoupling the local and advective terms with separate coefficients, K_1 and K_2.

Model 1 and quasi-stationary friction are independent of experimental tunning coefficients, while models 2 and 3 are not. In Experiments II (Fig. 7.15a) and V (Fig. 7.15b), which feature higher Reynolds numbers, all models exhibit similar behavior in pressure magnitude decay and wave celerity, regardless of initial conditions. However, the coefficients in models 2 and 3 show that they are influenced by the experimental conditions,

Figure 7.10: Collected data from experiment I vs numerical results with CCSPH for $Q = 8500.00 \times 10^{-8}$ m^3/s.

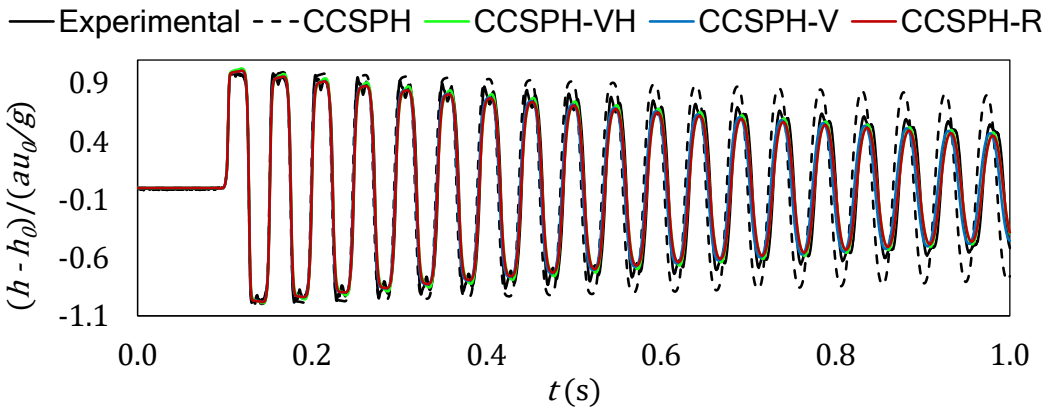

Source: Own Authorship.

Figure 7.11: Collected data from experiment II vs numerical results with CCSPH for $Q = 13300.00 \times 10^{-8}$ m^3/s.

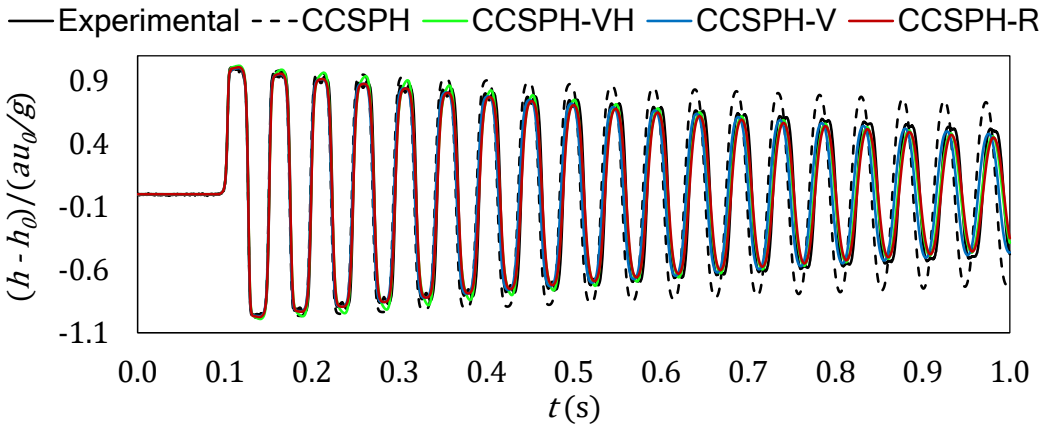

Source: Own Authorship.

as shown in Table 6.5.

The RMSPE and MASE metrics offer an objective evaluation of the results. Tables 7.1 and 7.2 display the application of RMSPE and MASE metrics directly to the piezometric head values, while 7.3 and 7.4 present the metrics applied to the dimensionless piezometric head values. Comparing the metrics before and after the piezometric head scaling, one observes that the RMSPE doubles its value from Table 7.1 to Table 7.3. On the other hand, MASE hardly changes, showing its robustness relative to the scaling process. Hence, MASE better serves the calibration and analysis.

Figure 7.12: Collected data from experiment III vs numerical results with CCSPH for $Q = 7170.00 \times 10^{-8}$ m^3/s.

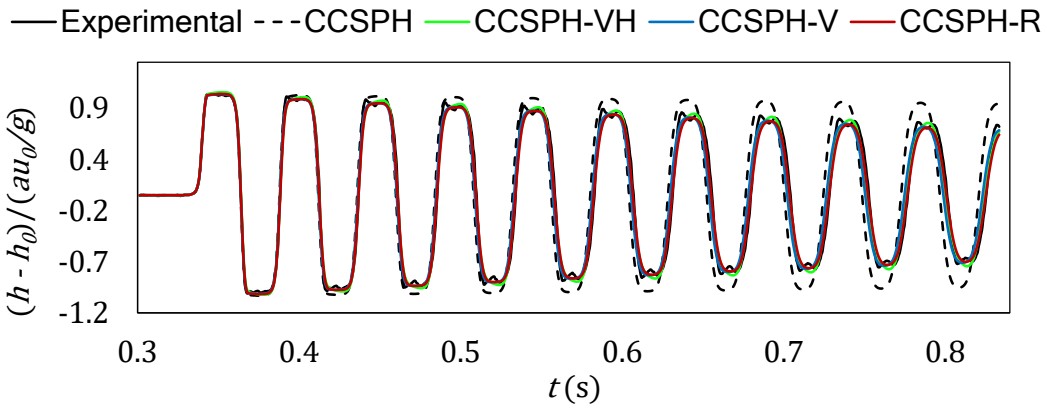

Source: Own Authorship.

Figure 7.13: Collected data from experiment IV vs numerical results with CCSPH for $Q = 9610.00 \times 10^{-8}$ m^3/s.

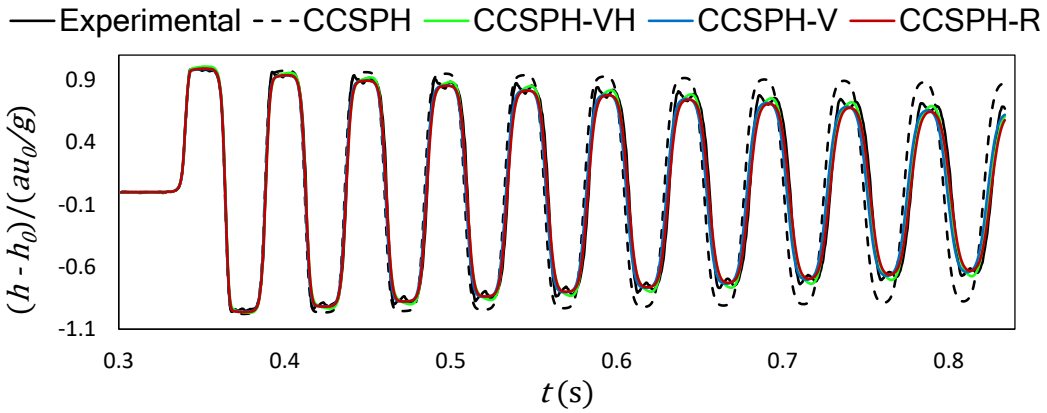

Source: Own Authorship.

The results in Tables 7.2 and 7.4 show that, on average, model 3 has better accuracy with a 10.77% MASE metric compared to models 1 and 2. In experiments III, IV, and V, models 1 and 2 performed better with an average of 9.49% and 13.16%, respectively, while in experiments I and II, models 1 and 2 achieved 15.23% and 25.14%, respectively. The better performance of model 3 may be due to using K_1 and K_2 to control local and advective acceleration separately, in contrast to using only one parameter (K) to control both acceleration terms.

Table 7.1 – RMSPE of the experiments I, II, III, IV and V for each transient friction model in CCSPH considering the piezometric head direct values.

	RMSPE - Experiments				
Models	I	II	III	IV	V
CCSPH-VH	6.62%	9.44%	4.25%	5.65%	6.76%
CCSPH-V	10.68%	20.32%	6.68%	8.73%	10.53%
CCSPH-R	6.44%	8.49%	3.66%	5.09%	5.81%

Table 7.2 – MAPE of the experiments I, II, III, IV and V for each transient friction model in CCSPH considering the piezometric head direct values.

	MASE - Experiments				
Models	I	II	III	IV	V
CCSPH-VH	14.28%	14.44%	9.04%	9.24%	9.51%
CCSHP-V	21.17%	26.45%	12.29%	12.75%	13.28%
CCSPH-R	14.10%	13.22%	7.52%	8.28%	8.00%

Figure 7.14: Collected data from experiment V vs numerical results with CCSPH for $Q = 12060.00 \times 10^{-8}$ m^3/s.

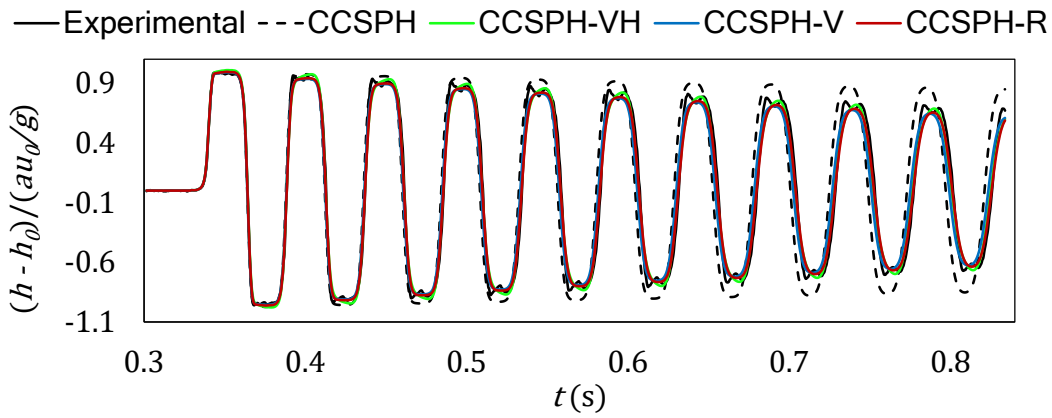

Source: Own Authorship.

Figure 7.15: Close look in the interval [0.70, 0.80] s of the Figs. 7.11 and 7.14, which represents the Experiment II and V. The intend is to subjectively asses the transient friction models in CCSPH relatively to experimental data.

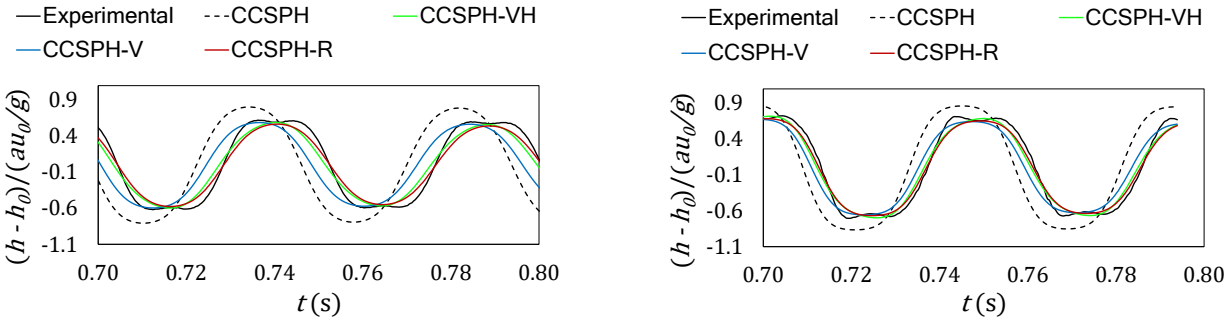

(a) Experiment II (b) Experiment V

Source: Own Authorship.

Table 7.3 – RMSPE of the experiments I, II, III, IV and V for each transient friction model in CCSPH considering the dimensionless piezometric head.

	RMSPE - Experiments				
Models	I	II	III	IV	V
CCSPH-VH	15.97%	16.29%	10.88%	11.33%	11.49%
CCSPH-V	25.74%	35.07%	17.09%	17.52%	17.90%
CCSPH-R	15.54%	14.65%	9.37%	10.21%	9.88%

Table 7.4 – MASE of the experiments I, II, III, IV and V for each transient friction model in CCSPH considering the dimensionless piezometric head.

	MASE - Experiments				
Models	I	II	III	IV	V
CCSPH-VH	16.02%	16.17%	9.38%	9.72%	10.03%
CCSPH-V	23.62%	29.30%	12.87%	13.53%	14.26%
CCSPH-R	16.05%	15.09%	7.99%	8.91%	8.57%

Aside from the numerical parameters aspects, the theoretical fundamentals have a way of estimating the number of wave cycles before the vorticity or the shear pulse entirely defuses radially from the wall region to the pipe's core, perturbing the pre-existing turbulent or steady-state characteristics, thus, invalidating the unsteady friction models.

Hence, using Eqs. (3.95) and (3.96) (GHIDAOUI et al., 2002), experiments I and II may support 42 to 62 wave cycles, or the shear pulse takes 0.52 s to 0.76 s to diffuse. This time scale aligns with the observations of Figs. 7.10 and 7.11, considering especially the quasi-stationary model and model 2. Contrastingly, experiments III-V have diffusion time scales within the interval of 0.56 s and 0.88 s, but they experienced less interference from the shear pulse. Therefore, the numerical results of experiments III-V have more minor errors than those of experiments I and II, as shown in Table 7.4. Additionally, from the calculated diffusion time scales, the transient friction models may have reduced reliability for $t > 0.50$ s, based on the physical parameters of experiments I-V.

Vardy and Brown (1995) and Vardy and Brown (2003) also proposed a time scale called rising time, which is also related to the time required for vorticity diffusion over the cross-section and is defined by Eq. (3.100). Using the beginning of the valve closure as a reference (0.0939 s for experiments I-II and 0.2689 s for experiments III-V), the rising time for experiments I-II is around 0.61 s to 0.90 s. In comparison, experiments III-V are around 0.50 s to 0.86 s. The rising time values agree with the diffusion time scale proposed by Ghidaoui et al. (2002), although it is less conservative regarding reliability.

Ghidaoui et al. (2005) observed that, in general, models 2 and 3 become more accurate for highly turbulent flows relative to model 1 since the weight function becomes less significant. Observing Table 7.4, on average, models 2 and 3 increased in error with the increasing Reynolds number, 2.36% and -0.13%, respectively, while model 1 increased in error, 0.27%. The increase in error in those cases was insignificant but lesser in model 3. This behavior suggests the potential for improved accuracy in highly turbulent flows, as noted by Ghidaoui et al. (2005), but at the expense of adjusting the coefficients K_1, K_2.

The three models' potential robustness can be observed through the absolute difference between the dimensionless piezometric heads obtained numerically and experimentally. In Figs. 7.16a and 7.16b (representing experiments I and II, respectively), it is evident that the errors in model 2 increase faster than in models 1 and 3 since their errors decrease with time. Experiments III-V, which appeared in Figs. 7.17a-7.17c, respectively, showed errors with smaller magnitudes and a less significant increase over time.

7.1.2.3 Unsteady Friction Models Aspects in MOC

Considering the experimental wave speeds of 1255 m/s (Experiments I and II) and 1250 m/s (Experiments II-V) alongside the numerical data in Table , the numerical results show slower wave speeds. The numerical pressure waves are shifted to the right compared to the experimental pressure wave, as shown in Figures 7.18 - 7.22. This issue is less pronounced in the quasi-stationary formulation and is significant for Models 1 and 2. Models 3 and the quasi-stationary model exhibit similar wave speeds, but model 3 requires a substantial reduction in the local term, causing numerical instabilities.

Figure 7.16: Absolute difference between numerical and experimental dimensionless piezometric heads over time of experiments I and II for CCSPH.

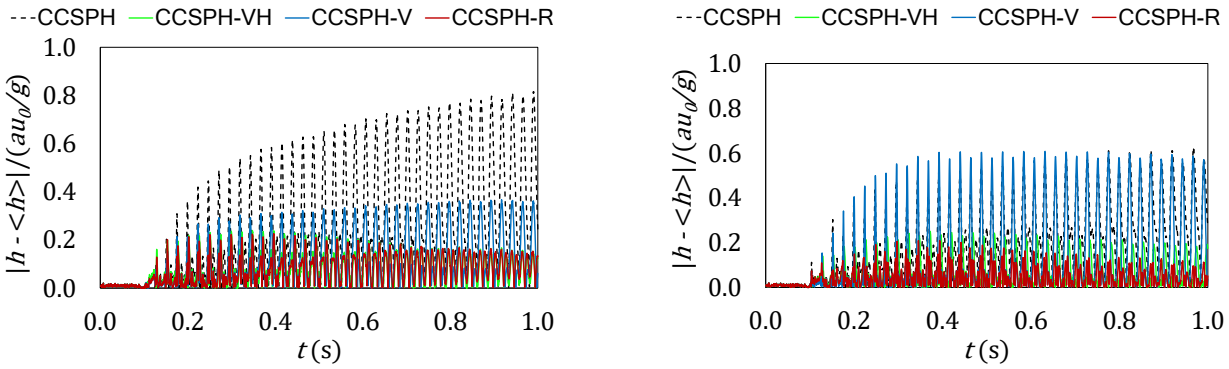

(a) Experiment I

(b) Experiment II

Source: Own Authorship.

Figure 7.17: Absolute difference between numerical and experimental dimensionless piezometric heads over time of experiments III, IV and V for CCSPH.

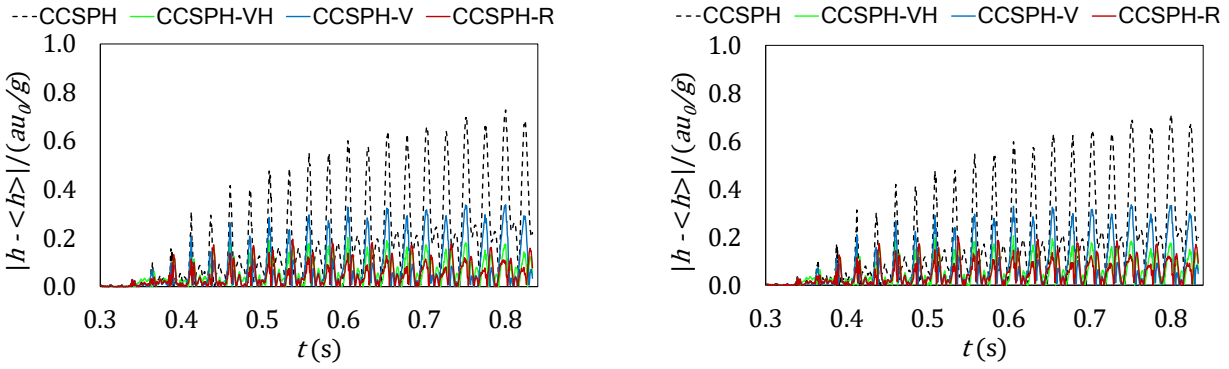

(a) Experiment III

(b) Experiment IV

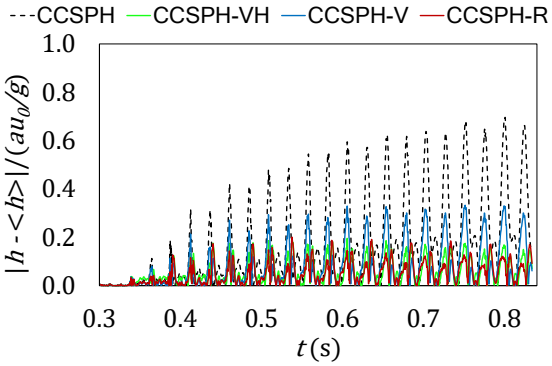

(c) Experiment V

Source: Own Authorship.

Table 7.5 lists the MASE metrics for numerical outcomes using MOC with experimental wave speeds. MOC-R outperforms the others, with an average MASE of 23.69%.

Figure 7.18: Collected data from experiment I vs numerical results with MOC for $Q = 8500.00 \times 10^{-8}$ m^3/s using $a = 1255$ m/s.

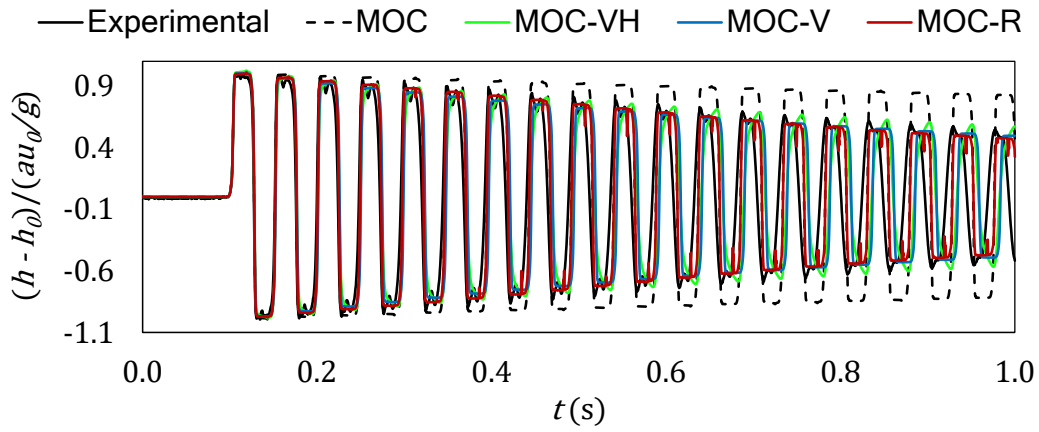

Source: Own Authorship.

Figure 7.19: Collected data from experiment II vs numerical results with MOC for $Q = 13300.00 \times 10^{-8}$ m^3/s using $a = 1255$ m/s.

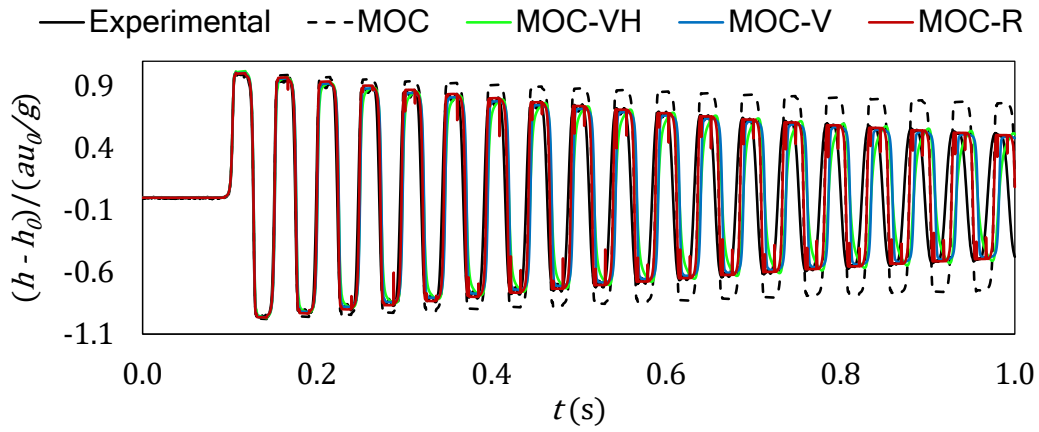

Source: Own Authorship.

MOC-VH and MOC-V have average MASE values of 46.20% and 40.89%, nearly double that of MOC-R. In comparison, CCSPH-R achieves a much lower average MASE of 11.32%, almost half that of MOC-R.

Adjusting the wave speeds to 1278 m/s for Experiments I-II and 1265 m/s for Experiments III-V improves results, aligning them more with the CCSPH outcomes, Figures 7.23 - 7.27. These new speeds are based on Equation (7.3). Model 1 shifts left correctly after the input wave speed change. The wave speed deceleration effect may remain unchanged, but the initial momentum energy increases as expected by model 1

with the higher input speeds. That is an interesting result since model 1 depends only on the initial and boundary conditions and is a theoretical model. Furthermore, with higher input speeds, MOC-R requires values for K_1 closer to the ones observed in CCSPH-R, resulting in stable outcomes, Tabs. 6.6 and 6.7.

Table 7.5 – MASE of the experiments I, II, III, IV and V for each transient friction model in MOC considering the dimensionless piezometric head. The outcomes in the table were obtained using $a = 1255$ m/s for experiments I-II, and $a = 1250$ m/s for experiments III-V.

	MASE - Experiments				
Models	I	II	III	IV	V
MOC-VH	66.68%	61.47%	26.94%	26.40%	49.52%
MOC-V	62.43%	52.23%	27.65%	20.87%	41.26%
MOC-R	35.10%	29.72%	11.99%	10.48%	31.18%

When comparing Tabs. 7.6 and 7.4, MOC with new wave speeds demonstrated better performance than CCSPH. The average MASE for MOC methods—MOC-VH, MOC-V, and MOC-R—were 11.62%, 15.19%, and 8.88%, respectively. In comparison, CCSPH methods—CCSPH-VH, CCSPH-V, and CCSPH-R—had MASE values of 12.26%, 18.72%, and 11.32%, respectively. The average difference of about 2.05% indicates that MOC maintains a wave shape closer to the experimental data over time.

Table 7.6 – MASE of the experiments I, II, III, IV and V for each transient friction model in MOC considering the dimensionless piezometric head. The outcomes in the table were obtained using $a = 1278$ m/s for experiments I-II, and $a = 1265$ m/s for experiments III-V.

	MASE - Experiments				
Models	I	II	III	IV	V
MOC-VH	14.35%	13.90%	10.57%	9.90%	9.39%
MOC-V	17.22%	23.41%	9.70%	10.30%	10.35%
MOC-R	12.43%	8.72%	7.93%	7.80%	7.52%

Although MOC with the system celerities 1255 m/s (Experiments I and II) and 1250 m/s (Experiments II-V) does not result in correct wave celerity through the entire

Figure 7.20: Collected data from experiment III vs numerical results with MOC for $Q = 7170.00 \times 10^{-8}$ m^3/s using $a = 1250$ m/s.

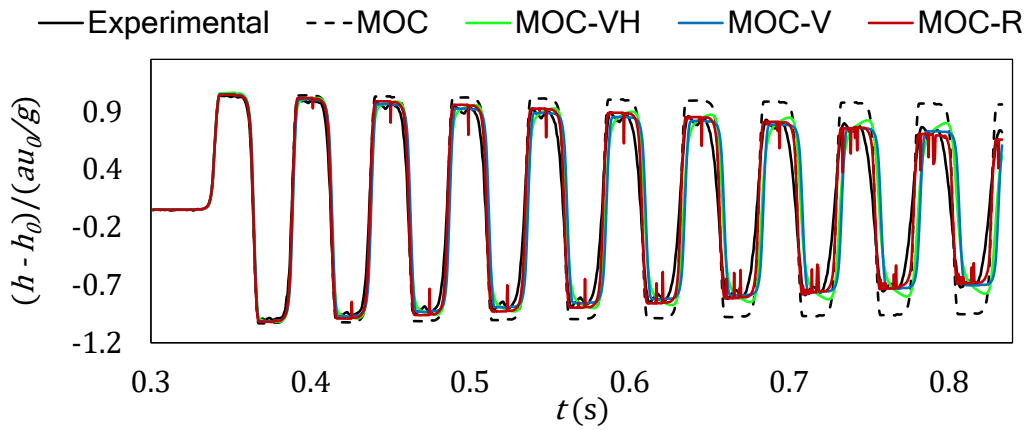

Source: Own Authorship.

Figure 7.21: Collected data from experiment IV vs numerical results with MOC for $Q = 9610.00 \times 10^{-8}$ m^3/s using $a = 1250$ m/s.

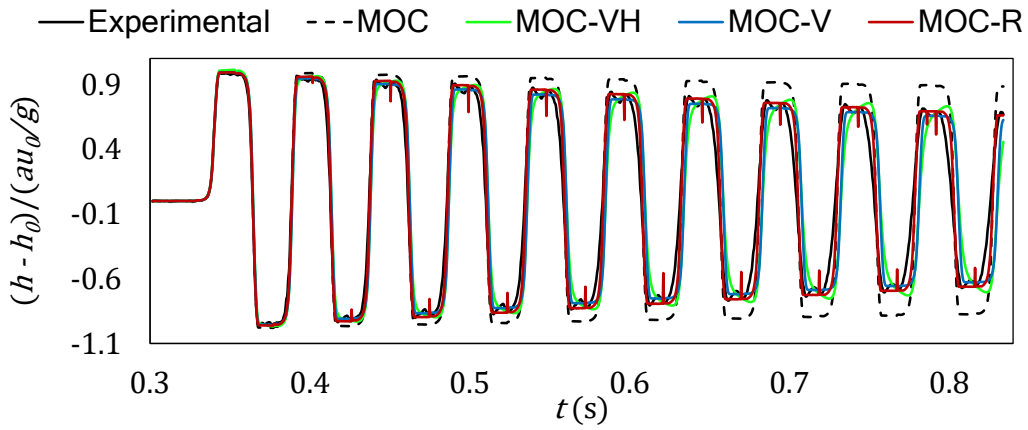

Source: Own Authorship.

time range, it has a subjectively good fit until the eighth wave peak, considering dumping rate and wave celerity.

7.1.3 SPH Parameters Analysis

Understanding the behavior or influence of the numerical parameters on the numerical results is essential for optimizing or calibrating the CCSPH numerical variables and the transient model coefficient. Hence, the response surface method (RSM) can help to analyze the five experiments and find the optimum values for the numerical parameters.

Figure 7.22: Collected data from experiment V vs numerical results with MOC for $Q = 12060.00 \times 10^{-8}$ m^3/s using $a = 1250$ m/s.

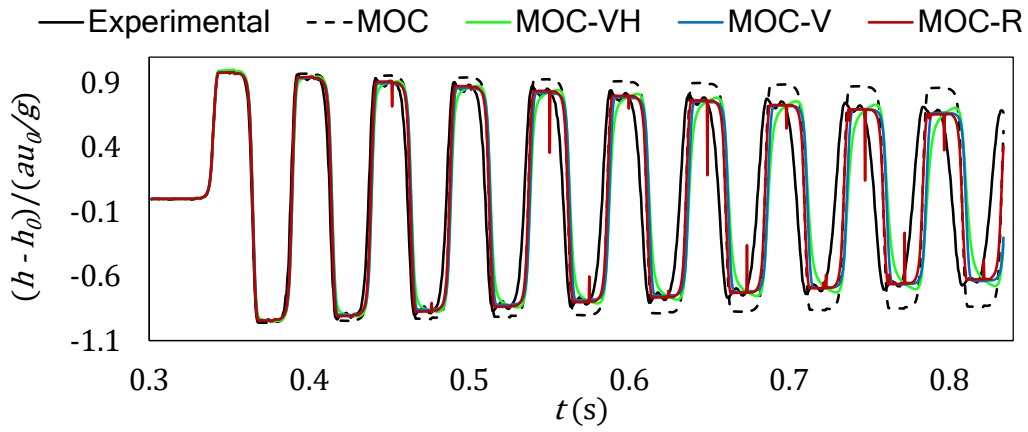

Source: Own Authorship.

Figure 7.23: Collected data from experiment I vs numerical results with MOC for $Q = 8500.00 \times 10^{-8}$ m^3/s using $a = 1278$ m/s.

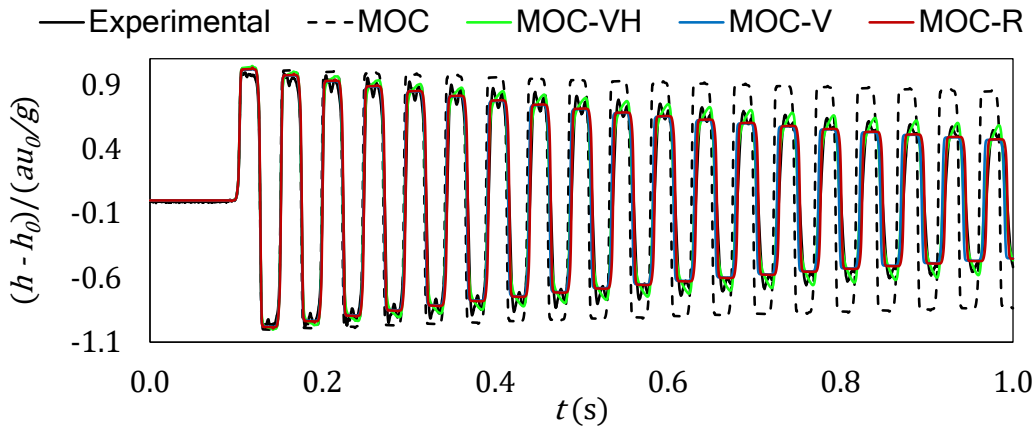

Source: Own Authorship.

The RSM approach requires careful consideration. In this study, model 3 (RAMOS et al., 2004) was chosen due to its superior controllability compared to model 2 (VITKOVSKY et al., 2000) and its potential accuracy in high turbulent flows compared to model 1 (VARDY; HWANG, 1993). The variables under consideration are Δx_1, α, κ, K_1, and K_2. Δx_1 represents the initial distance between particles, influencing the number of particles within the numerical domain. α controls the impact of artificial viscosity in the CSPH method, reflecting the level of inserted numerical diffusion. κ affects the number of neighboring particles that influence the evaluated particle. Finally, K_1 and K_2 determine the transient friction model's celerity and dumpiness. The MASE metric is used to compose

Figure 7.24: Collected data from experiment II vs numerical results with MOC for $Q = 13300.00 \times 10^{-8}$ m^3/s using $a = 1278$ m/s.

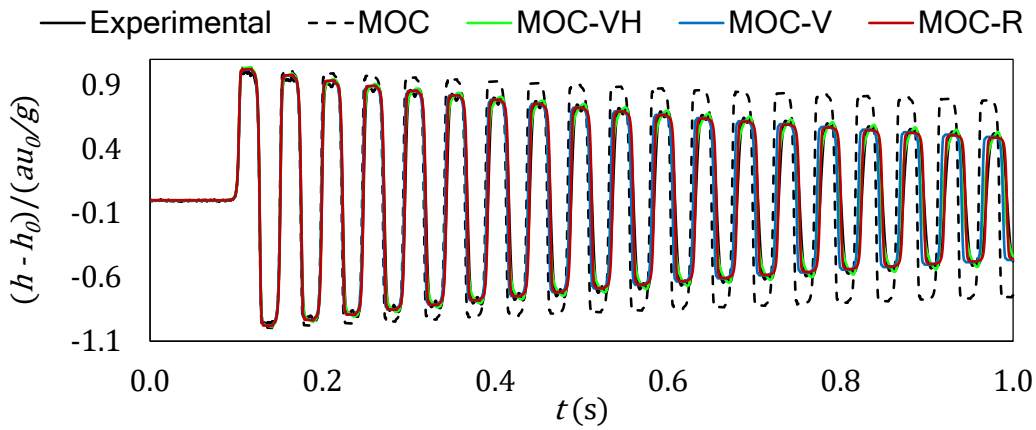

Source: Own Authorship.

Figure 7.25: Collected data from experiment III vs numerical results with MOC for $Q = 7170.00 \times 10^{-8}$ m^3/s using $a = 1265$ m/s.

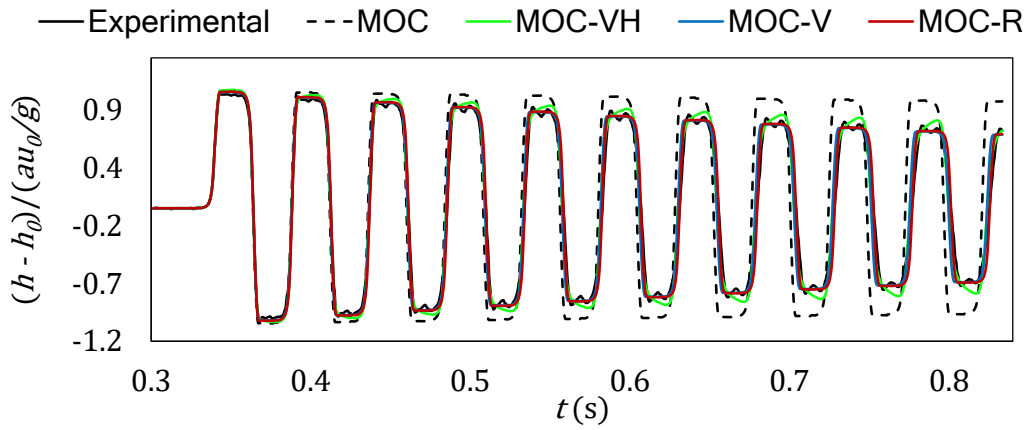

Source: Own Authorship.

the response to create the statistical surface of the variable effects. Additionally, each experiment is considered a replicate with a block effect, and the time step remains constant throughout the runs.

For a central composite and two-level complete factorial design applied to five continuous factors and five replicates (blocking each), the RSM theory leads to 52 base runs, resulting in 260 total runs. The table design comprises 160 cube points, 50 center points in the cube, 50 axial points, and zero center points in the axial. However, 260 simulation runs are time-consuming, implying a need for reduction. The D-optimization

Figure 7.26: Collected data from experiment IV vs numerical results with MOC for $Q = 9610.00 \times 10^{-8}$ m^3/s using $a = 1265$ m/s.

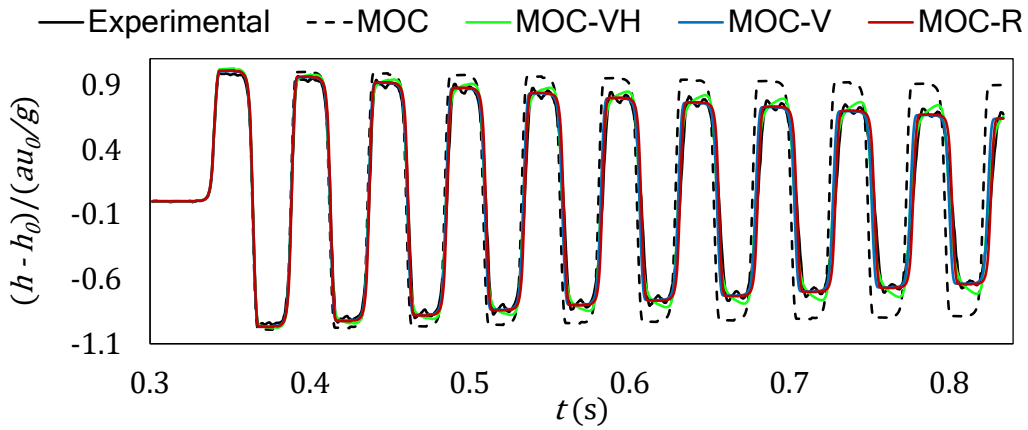

Source: Own Authorship.

Figure 7.27: Collected data from experiment V vs numerical results with MOC for $Q = 12060.00 \times 10^{-8}$ m^3/s using $a = 1265$ m/s.

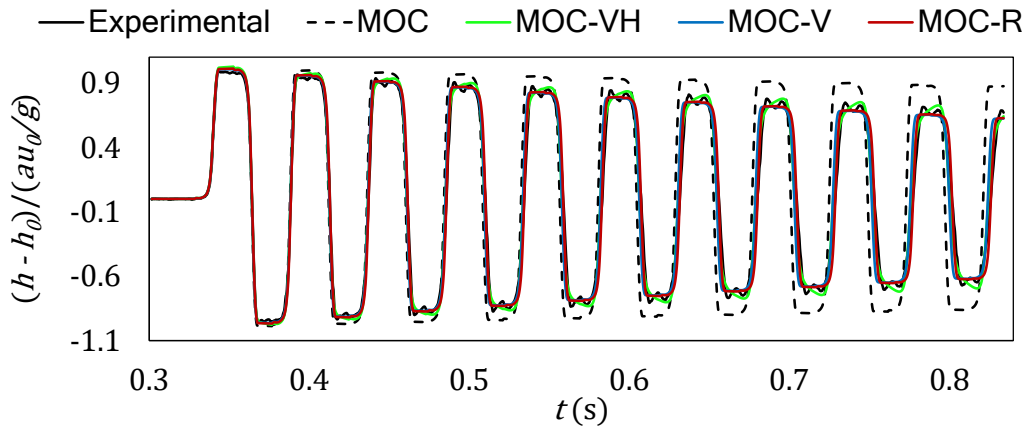

Source: Own Authorship.

technique can reduce the runs to 130, from which only 78 were usable since the other ones were outliers due to the numerical divergence of the numerical parameter combinations. The resulting table design with the error responses is Table 7.7.

The RSM involves creating a hyperdimensional surface using a linear regression based on the data collected from Tab. 7.7. This method selects a representative set of continuous factors from each response's statistical domain of possible factor combinations. The resulting regressive equation is a complete quadratic polynomial that calculates each factor's normalized effects. These normalized effects, represented as T-values, are plotted

against their normal probability values, Fig. 7.28. The significance of the effect for the MASE response is determined by measuring the relative distance between the actual and expected effect probabilities. Therefore, the red dots in Fig. 7.28 are significant as they have large distances, indicating that K_1 and K_2 contribute substantially to errors in the numerical results. Once K_1 and K_2 are optimized, the combination of the number of particles and the artificial viscosity intensity significantly influences the errors, with α carrying more weight than Δx_1.

Table 7.7 – Experimental design table with the MASE response for the RSM.

Blocks	α	Δx_1	K_2	K_1	κ	$MASE\,(\%)$
1	1.5000	0.0350	0.0140	0.0140	1.0000	37.03
1	1.0000	0.0500	0.0080	0.0200	1.0000	48.23
1	1.8000	0.0200	0.0200	0.0200	1.8000	65.21
1	1.8000	0.0500	0.0200	0.0080	1.8000	55.12
1	1.8000	0.0350	0.0140	0.0140	1.5000	60.99
1	1.0000	0.0500	0.0080	0.0200	1.8000	86.90
1	1.0000	0.0200	0.0080	0.0080	1.0000	21.21
1	1.8000	0.0500	0.0200	0.0080	1.0000	36.07
1	1.0000	0.0200	0.0200	0.0200	1.8000	269.00
1	1.8000	0.0200	0.0080	0.0080	1.8000	51.69
1	1.8000	0.0500	0.0200	0.0200	1.0000	50.92
1	1.0000	0.0500	0.0080	0.0080	1.0000	25.18
1	1.8000	0.0200	0.0080	0.0200	1.0000	51.88
1	1.5000	0.0350	0.0140	0.0200	1.5000	71.94
1	1.0000	0.0500	0.0080	0.0080	1.8000	64.14
1	1.0000	0.0200	0.0080	0.0200	1.8000	277.45
1	1.5000	0.0350	0.0140	0.0140	1.8000	63.78
1	1.0000	0.0200	0.0200	0.0080	1.0000	31.55
1	1.0000	0.0500	0.0200	0.0200	1.0000	50.41
1	1.8000	0.0200	0.0080	0.0080	1.0000	38.04
1	1.5000	0.0200	0.0140	0.0140	1.5000	57.84
1	1.8000	0.0500	0.0080	0.0200	1.8000	84.14
1	1.8000	0.0500	0.0080	0.0080	1.8000	61.88
1	1.0000	0.0350	0.0140	0.0140	1.5000	61.31
1	1.0000	0.0200	0.0200	0.0080	1.8000	254.76
1	1.5000	0.0350	0.0080	0.0140	1.5000	65.51

continued on next page

continued from previous page

Blocks	α	Δx_1	K_2	K_1	κ	$MASE\,(\%)$
2	1.8000	0.0200	0.0200	0.0200	1.0000	70.80
2	1.0000	0.0200	0.0080	0.0080	1.0000	30.76
2	1.8000	0.0500	0.0080	0.0080	1.0000	34.07
2	1.5000	0.0500	0.0140	0.0140	1.5000	70.86
2	1.8000	0.0200	0.0200	0.0080	1.0000	63.79
2	1.0000	0.0200	0.0200	0.0080	1.0000	34.82
2	1.5000	0.0350	0.0080	0.0140	1.5000	75.50
2	1.0000	0.0500	0.0080	0.0200	1.0000	57.59
2	1.0000	0.0500	0.0200	0.0200	1.8000	85.24
2	1.0000	0.0200	0.0080	0.0200	1.8000	259.42
2	1.8000	0.0200	0.0080	0.0080	1.8000	62.45
2	1.8000	0.0200	0.0080	0.0080	1.0000	38.70
2	1.5000	0.0350	0.0140	0.0200	1.5000	80.61
2	1.8000	0.0500	0.0200	0.0080	1.8000	63.01
2	1.0000	0.0350	0.0140	0.0140	1.5000	70.28
2	1.0000	0.0200	0.0200	0.0080	1.8000	235.89
2	1.8000	0.0500	0.0080	0.0080	1.8000	71.73
2	1.0000	0.0500	0.0200	0.0080	1.0000	38.26
2	1.8000	0.0200	0.0200	0.0200	1.8000	73.69
2	1.8000	0.0500	0.0080	0.0200	1.0000	56.82
2	1.5000	0.0350	0.0140	0.0140	1.8000	73.29
3	1.5000	0.0200	0.0140	0.0140	1.5000	40.63
3	1.0000	0.0500	0.0200	0.0200	1.0000	34.48
3	1.8000	0.0500	0.0200	0.0080	1.0000	24.23
3	1.0000	0.0200	0.0200	0.0200	1.8000	45.86
3	1.0000	0.0200	0.0080	0.0080	1.8000	39.34
3	1.5000	0.0350	0.0140	0.0140	1.8000	45.60
3	1.5000	0.0350	0.0080	0.0140	1.5000	45.93
3	1.0000	0.0200	0.0200	0.0200	1.0000	31.90
3	1.0000	0.0500	0.0080	0.0080	1.8000	46.29
3	1.5000	0.0350	0.0200	0.0140	1.5000	39.93
3	1.5000	0.0350	0.0140	0.0080	1.5000	35.45
3	1.8000	0.0200	0.0080	0.0200	1.0000	32.51
3	1.8000	0.0500	0.0200	0.0200	1.8000	52.10
3	1.8000	0.0500	0.0080	0.0080	1.8000	44.72
3	1.0000	0.0200	0.0080	0.0200	1.0000	33.86

continued on next page

continued from previous page

Blocks	α	Δx_1	K_2	K_1	κ	$MASE\,(\%)$
3	1.0000	0.0200	0.0200	0.0080	1.0000	20.65
3	1.8000	0.0500	0.0080	0.0200	1.0000	34.85
3	1.8000	0.0500	0.0200	0.0200	1.0000	35.04
3	1.0000	0.0500	0.0200	0.0200	1.8000	52.69
3	1.8000	0.0200	0.0200	0.0080	1.0000	42.39
3	1.8000	0.0350	0.0140	0.0140	1.5000	41.97
3	1.8000	0.0200	0.0200	0.0080	1.8000	31.76
3	1.0000	0.0500	0.0080	0.0080	1.0000	21.30
3	1.8000	0.0200	0.0080	0.0200	1.8000	52.73
4	1.8000	0.0500	0.0200	0.0200	1.8000	51.11
4	1.8000	0.0200	0.0200	0.0080	1.8000	30.60
4	1.8000	0.0350	0.0140	0.0140	1.5000	40.83
4	1.8000	0.0500	0.0200	0.0200	1.0000	35.22
4	1.0000	0.0500	0.0080	0.0200	1.8000	58.33
4	1.0000	0.0200	0.0080	0.0080	1.8000	37.73
4	1.0000	0.0500	0.0200	0.0080	1.0000	23.85
4	1.0000	0.0200	0.0200	0.0200	1.0000	32.13
4	1.5000	0.0200	0.0140	0.0140	1.5000	39.36
4	1.8000	0.0500	0.0080	0.0080	1.0000	20.16
4	1.0000	0.0500	0.0200	0.0080	1.8000	38.05
4	1.8000	0.0500	0.0200	0.0080	1.8000	37.62
4	1.5000	0.0350	0.0140	0.0140	1.0000	25.27
4	1.0000	0.0500	0.0080	0.0200	1.0000	34.15
4	1.5000	0.0350	0.0140	0.0080	1.5000	34.31
4	1.8000	0.0200	0.0080	0.0200	1.8000	51.20
4	1.0000	0.0500	0.0080	0.0080	1.8000	44.78
4	1.5000	0.0350	0.0200	0.0140	1.5000	39.54
4	1.8000	0.0500	0.0080	0.0200	1.0000	33.74
4	1.0000	0.0200	0.0080	0.0080	1.0000	18.07
4	1.8000	0.0200	0.0080	0.0080	1.0000	21.41
5	1.8000	0.0500	0.0080	0.0080	1.0000	19.48
5	1.0000	0.0200	0.0080	0.0200	1.0000	31.32
5	1.5000	0.0350	0.0140	0.0140	1.0000	25.47
5	1.0000	0.0500	0.0200	0.0080	1.8000	37.06
5	1.0000	0.0200	0.0200	0.0200	1.8000	43.70
5	1.0000	0.0200	0.0080	0.0080	1.8000	36.32

continued on next page

continued from previous page

Blocks	α	Δx_1	K_2	K_1	κ	$MASE\,(\%)$
5	1.0000	0.0350	0.0140	0.0140	1.5000	40.36
5	1.5000	0.0350	0.0140	0.0200	1.5000	46.72
5	1.8000	0.0200	0.0200	0.0080	1.8000	29.69
5	1.5000	0.0500	0.0140	0.0140	1.5000	40.99
5	1.8000	0.0500	0.0200	0.0200	1.8000	50.31
5	1.0000	0.0200	0.0200	0.0080	1.8000	30.05
5	1.8000	0.0200	0.0200	0.0080	1.0000	43.23
5	1.5000	0.0350	0.0080	0.0140	1.5000	43.29
5	1.8000	0.0500	0.0200	0.0080	1.0000	25.04
5	1.8000	0.0500	0.0080	0.0200	1.8000	55.63
5	1.0000	0.0500	0.0080	0.0080	1.0000	19.37
5	1.0000	0.0500	0.0200	0.0200	1.0000	34.87
5	1.8000	0.0200	0.0200	0.0200	1.0000	50.81
5	1.8000	0.0200	0.0200	0.0200	1.8000	43.19
5	1.5000	0.0350	0.0200	0.0140	1.5000	39.35
5	1.8000	0.0200	0.0080	0.0080	1.8000	35.96

Figure 7.28: Probability plot of the normalized effect of the factors α, Δx_1, K_2, K_1, and κ. The red line is the expected probability based on a normal distribution, while the dots are the actual probabilities of each factor. The red dots represent the most significant factors for the MASE response.

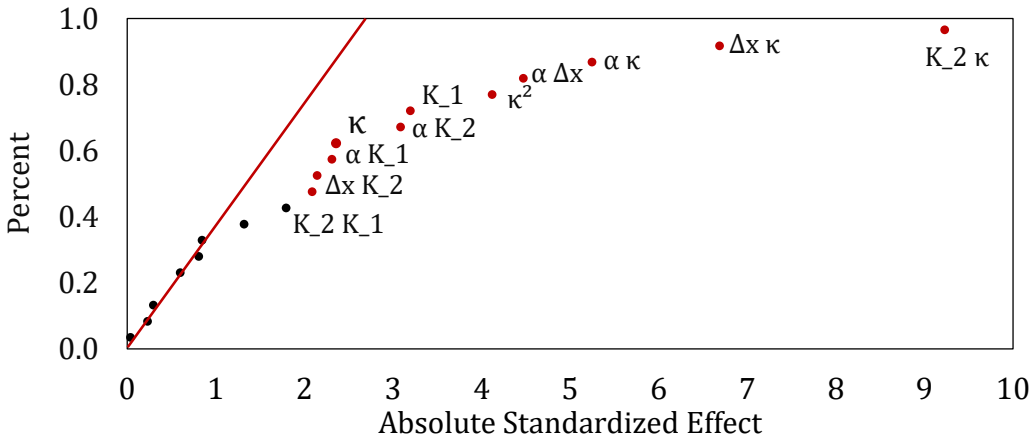

Source: Own Authorship.

Figure 7.29: K_1 and K_2 contour curves of its response surface, reflecting their parabolical behavior and the existing of a minimum pair of values.

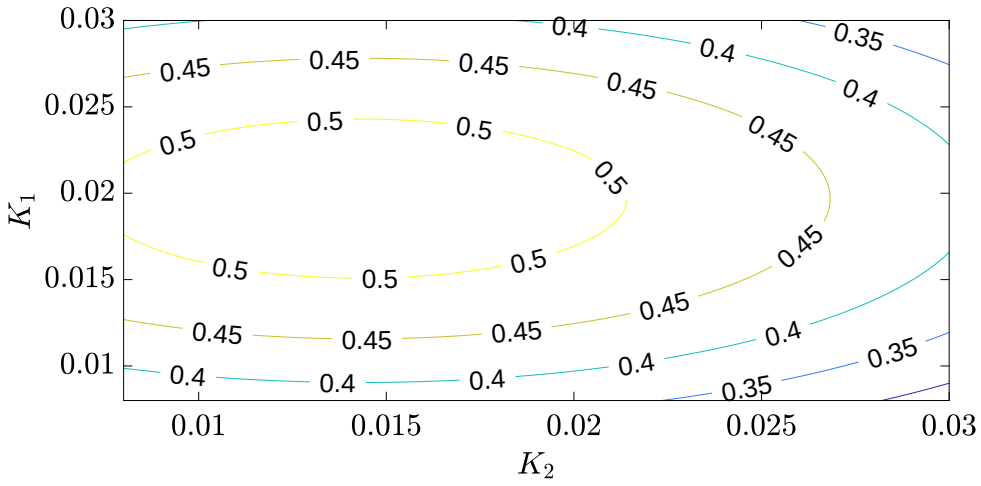

Source: Own Authorship.

Both K_1 and K_2 significantly impact model accuracy, but K_1 has a larger effect compared to K_2, as indicated by their MASE variation ranges ($K_1 - 14.96\%$, $K_2 - 6.14\%$, $\alpha - 8.22\%$, $\Delta x - 8.2433$, and $\kappa - 18.49\%$). The smaller impact of K_2 may result from its combination with α, where their damping effects add with each other. This is reinforced by Fig. fig:6.1.9, which shows that the interaction of αK_2 is more significant than that of $K_1 K_2$, with notable contributions from various combinations involving α and K_2. Reducing the RSM surface to the relationship of α and K_2, the model becomes

$$\langle MASE \rangle = \left(0.126 + 0.782\,\alpha - 2.000\,K_2 - 0.275\,\alpha^2 + 2.03\,\alpha\,K_2\right)^{\frac{1}{2}}. \tag{7.4}$$

Its two minimum values are $\alpha = 1.000$ and $K_2 = 0.008$, or $\alpha = 1.800$ and $K_2 = 0.008$, showing α with a stronger parabolic behavior. At the same time, K_2 remains more flat.

Considering only the K_1 and K_2, RSM enables a reduction to a two-dimensional plane, Fig. 7.29, described by

$$\langle MASE \rangle = \left(0.340 + 9.8\,K_2 + 31.9\,K_1 - 342\,K_2^2 - 810\,K_1^2\right)^{\frac{1}{2}}. \tag{7.5}$$

Three local minimum values occurs when $K_1 = 0.008$ and $K_2 = 0.008$ or $K_1 = 0.008$ and $K_2 = 0.020$ or $K_1 = 0.020$ and $K_2 = 0.008$, with an estimated MASE of 36.00%, 36.27%, and 50.55%, respectively, with 95% confidence interval of (32.51%, 39.66%). There is no absolute minimum, but one local value combination aligns with the initial estimates for K_1 and K_2. Figure 7.29 shows a parabolic relationship between K_1 and K_2, indicating

that lower values are typically found when K_1 and K_2 are on opposite ends of the range $[0.008, 0.020]$.

Following the same analysis, reducing the RSM model to α and Δx_1, the error is described by

$$\langle MASE \rangle = \left(-0.137 + 0.962\,\alpha + 6.000\,\Delta x_1 - 0.283\,\alpha^2 - 3.500\alpha\,\Delta x_1\right)^{\frac{1}{2}}. \tag{7.6}$$

The optimal values for α and Δx_1 are 1.000 and 0.0200, respectively. The reduction in the particles' distance aligns with optimization common sense as it allows for more particles within the numerical domain, resulting in higher resolution that explains more of the physical interactions of the phenomenon. The minimum value for the artificial viscosity indicates less numerical diffusion, which can reduce the dumping on the pressure waves..

Observing the complete model and the five variables, the RSM gives the following equation:

$$\begin{aligned}\langle MASE \rangle = \big(&-0.638 + 0.129\,\alpha + 0.96\,\Delta x_1 + 9.52\,K_2 + 15.53\,K_1 + 1.173\,\kappa + 0.0410\,\alpha^2 \\ &-14.3\,\Delta x_1^2 + 231\,K_2^2 + 96\,K_1^2 - 0.282\,\kappa^2 - 2.355\alpha\,\Delta x_1 + 4.06\,\alpha\,K_2 \\ &-3.06\,\alpha\,K_1 - 0.1029\,\alpha\,\kappa - 74.9\,\Delta x_1\,K_2 + 8.1\,\Delta x_1\,K_1 + 3.515\Delta x_1\,\kappa \\ &-183.5\,K_2\,K_1 - 12.12\,K_2\,\kappa - 1.07\,K_1\,\kappa)^{\frac{1}{2}}.\end{aligned} \tag{7.7}$$

The minimum point of the surface described by Eq. (7.7) is $\alpha = 1.000$, $\Delta x_1 = 0.0200$, $K_1 = 0.0080$, $K_2 = 0.0080$, and $h = 1.0000$. The estimated MASE at the optimal point is 20.92%, with a 95% confidence interval of (18.89%, 23.05%). In experiments I-V, the recorded MASE values are 28.18%, 20.38%, 16.33%, 15.44%, and 14.75%. These values are roughly double those in Table 7.6 but are close to the RSM estimate, with an average difference of 4.81%. The main issue with the proposed RSM's variable combination is the significant reduction in wave speed, suggesting that K_1 should be reduced.. Maybe, by changing the evaluated intervals in RSM, the statical model would better capture the optimum point for every variable since more error responses would be available due to the CCSPH coupled with transient model convergence.

The response surface methodology (RSM) allows the visualization of the factors' behavior by isolating them on a plane. Figure 7.30 shows the α, Δx_1, K_1, K_2, and κ curves. Figures 7.30c and 7.30d highlight the parabolic behavior of variables K_1 and K_2, showing a local maximum and rapid divergence towards the extremes in the K_1 case. The effects of K_1 and κ are more prominent than the other factors. K_1 is strongly related to wave speed control, which results in a wave shift that rapidly increases errors.

Figure 7.30: Average MASE of each numerical parameter analysed by the RSM.

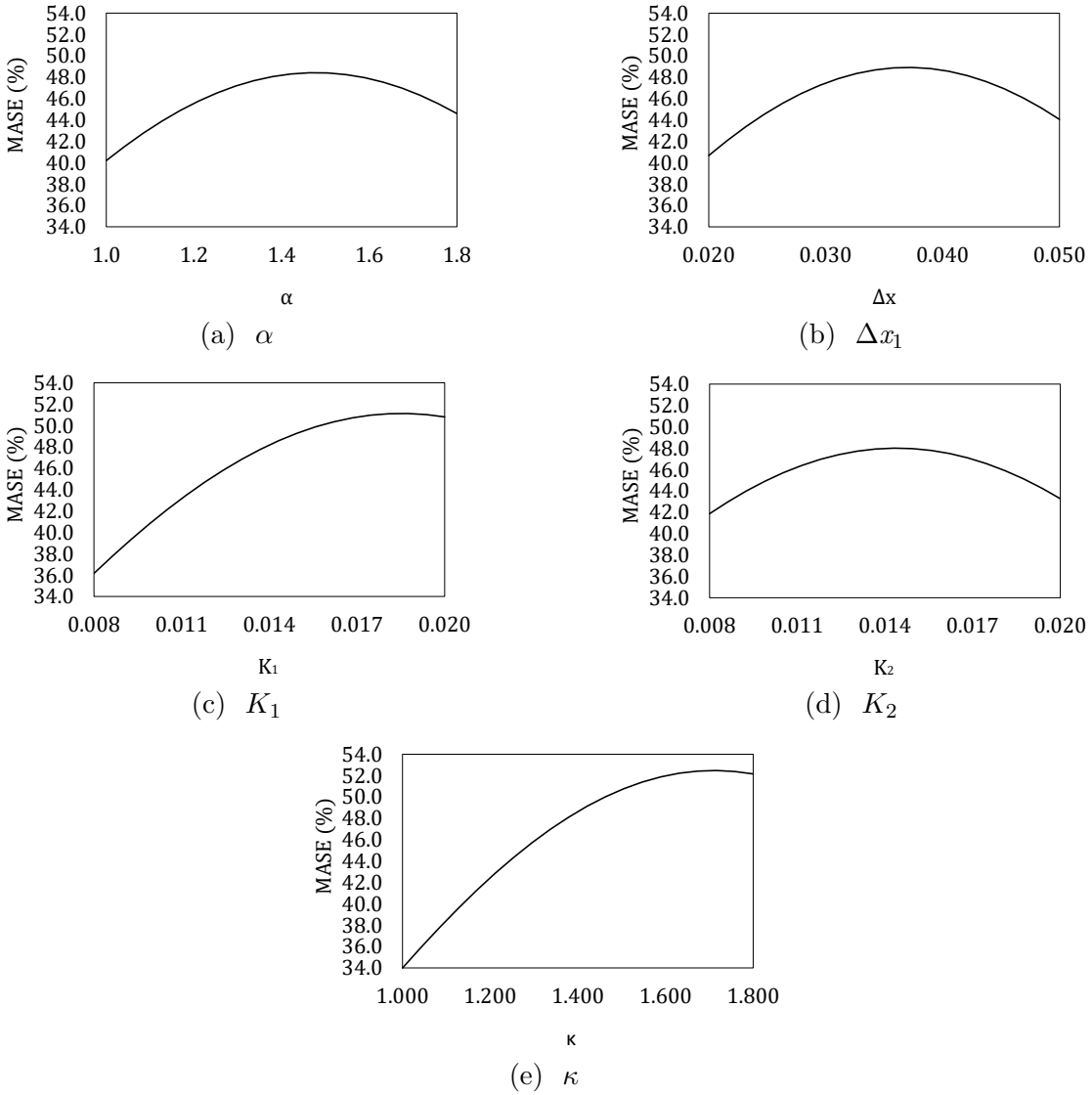

(a) α (b) Δx_1

(c) K_1 (d) K_2

(e) κ

Source: Own Authorship.

The smoothing length factor, κ, dictates the number of neighboring particles and exhibits a parabolic behavior, Fig, 7.30e. Errors decrease towards the extremes, possibly due to the boundary truncation effect. At the numerical domain's boundaries, each particle's support domain becomes unbalanced, impacting the kernel function and causing numerical errors. A small neighborhood may be less sensitive to imbalances but contains less local information. Conversely, a large neighborhood presents the opposite behavior. There is a point where locally available information compensates for numerical errors caused by support domain imbalances.

The variable Δx_1 determines the particle density in the numerical domain and is linked to the Courant number, given by $(a\,\Delta t)\,/\Delta x_1 \leq 1.0$. The extremes from Response Surface Methodology (RSM), $(0.020, 0.050)$, correlate to Courant numbers of 1.00 and 0.50. According to MOC, the first value indicates a stable solution. The second value also

suggests stability, which may explain the parabolic behavior shown in Fig. 7.30b.

7.2 Viscoelastic Pipe with Transient Friction

This study followed the approach of Covas et al. (2005) to fine-tune numerical coefficients for creep compliance using a viscoelastic model and later incorporating unsteady friction model 3. A Gauss-Newton algorithm was applied to a Kelvin-Voigt model with three Voigt elements. For experiment VI, characterized by laminar flow at a discharge of 5600×10^{-8} m^3/s, the retarded times are $\mu_1/G_1 = 0.05$ s, $\mu_2/G_2 = 0.50$ s, and $\mu_3/G_3 = 10.00$ s. In experiment VII, which exhibits turbulent flow with a discharge of 100810×10^{-8} m^3/s, the retarded times are $\mu_1/G_1 = 0.05$ s, $\mu_2/G_2 = 0.50$ s, and $\mu_3/G_3 = 1.00$ s. Covas et al. (2005) found that a retarded time of 0.05 s is optimal for a wave speed of 395 m/s, balancing accuracy and computational efficiency. They also noted that using more than four Voigt elements doesn't enhance accuracy, justifying this work's choice of three components.Moreover, $\alpha = 1.00$, and the roughness changed to 6.20×10^{-3} m.

The creep compliance values from the viscoelastic model for experiments VI and VII are shown in Tabs. 6.3 (CCSPH) and 6.4 (MOC). Figures 7.31 and 7.32 compare the CCSPH and MOC results under this model. Both models produced similar outcomes and matched the experimental data well. The main difference is at the initial pressure wave peak, where CCSPH shows an overshoot, while MOC remains close to the experimental values. This overshoot is likely a characteristic of the CCSPH model, as it also occurs in simulations without the viscoelastic model. In contrast, MOC and MOC-VISC do not exhibit any overshoot.CCSPH demonstrates smoother behavior than MOC in cases without a viscoelastic model, which likely explains the differences in creep compliance values observed between the two numerical models.

CCSPH-VISC and MOC-VISC demonstrated similar accuracy, with MASE values of 9.15% and 11.16% in Experiment VI, and 8.87% and 9.50% in Experiment VII. CCSPH and MOC showed identical accuracy as well, with MASE values of 305.68% and 310.77% in Experiment VI, and 167.25% and 160.93% in Experiment VII.

The Gauss-Newton algorithm optimized the creep compliance values and unsteady friction model coefficients separately. However, using the viscoelastic model and unsteady friction together resulted in negative values for the third Voigt element's creep compliance. This led to a manual tuning process for the coefficients and creep compliance values. The first Voigt element's creep compliance was found to significantly affect pressure wave celerity. Therefore, the manual tuning began by balancing K_1 and ι_1, followed by adjusting K_2, ι_2, and ι_3, with ι_2 greater damping effect than ι_3.

Figures 7.33 and 7.34 present results from CCSPH, CCSPH-R, and CCSPH-R-

Figure 7.31: Collected data from experiment VI compared with the outcomes of CCSPH, CCSPH-VISC, MOC, and MOC-VISC for $Q = 5600.00 \times 10^{-8}$ m^3/s using $a = 395$ m/s.

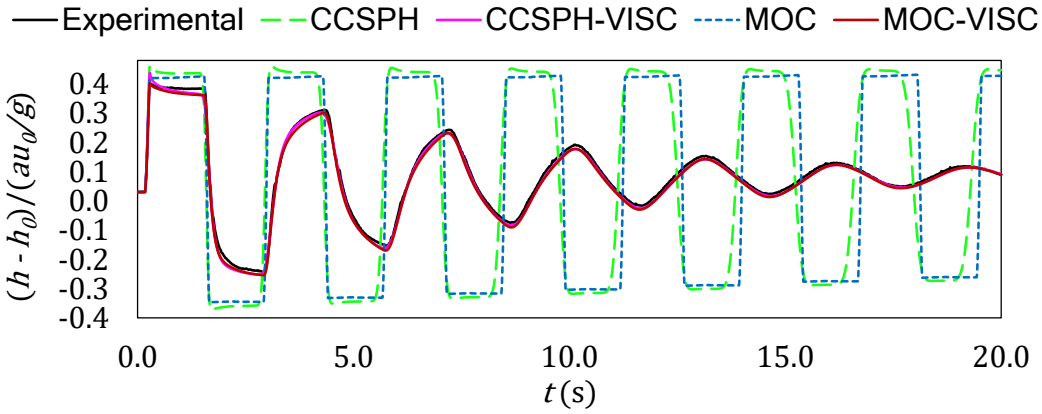

Source: Own Authorship.

Figure 7.32: Collected data from experiment VI compared with the outcomes of CCSPH, CCSPH-VISC, MOC, and MOC-VISC for $Q = 100810.00 \times 10^{-8}$ m^3/s using $a = 395$ m/s.

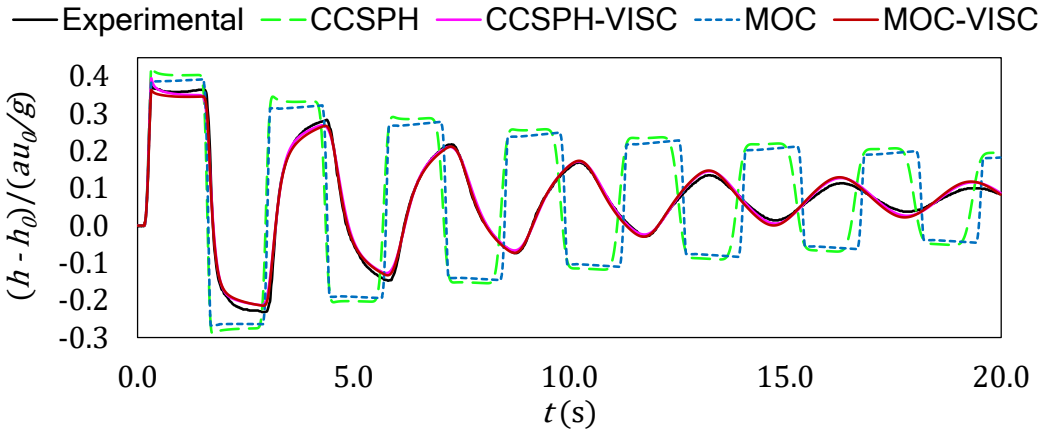

Source: Own Authorship.

VISC, while Figures 7.35 and 7.36 show outcomes from MOC, MOC-R, and MOC-R-VISC. In CCSPH-R and MOC-R, unsteady friction model 3 reasonably matched wave celerity but exhibited excessive damping. It also produced a squarish waveform. Furthermore, MOC-R showed a discontinuity in the initial peaks, which smoothed out over time. Meanwhile, CCSPH-R had an overshoot at the beginning of its first peak.

The CCSPH-R-VISC and MOC-R-VISC also have good accuracy, 11.50% and 11.81% for experiment VI and 8.81% and 10.01% for experiment VII, compared with

CCSPH-VISC and MOC-VISC, 9.15% and 11.16% for experiment VI and 8.87% and 9.50% for experiment VII. The MASE values are resumed in Tabs. 7.8 and 7.9.

Table 7.8 – MASE of the experiments VI and VII considering a dimensionless piezometric head and the CCSPH based numerical methods.

	MASE - Models			
Experiments	CCSPH	CCSPH-R	CCSPH-VISC	CCSPH-R-VISC
VI	305.68%	28.81%	9.15%	11.50%
VII	167.25%	23.95%	8.87%	8.81%

Table 7.9 – MASE of the experiments VI and VII considering a dimensionless piezometric head and the MOC based numerical methods.

	MASE - Models			
Experiments	MOC	MOC-R	MOC-VISC	MOC-R-VISC
VI	310.77%	29.85%	11.16%	11.81%
VII	160.93%	25.92%	9.50%	10.01%

Figure 7.33: Collected data from experiment VI compared with the outcomes of CCSPH, CCSPH-R-VISC, CCSPH-R,and CCSPH-VISC for $Q = 5600.00 \times 10^{-8}$ m^3/s using $a = 395$ m/s.

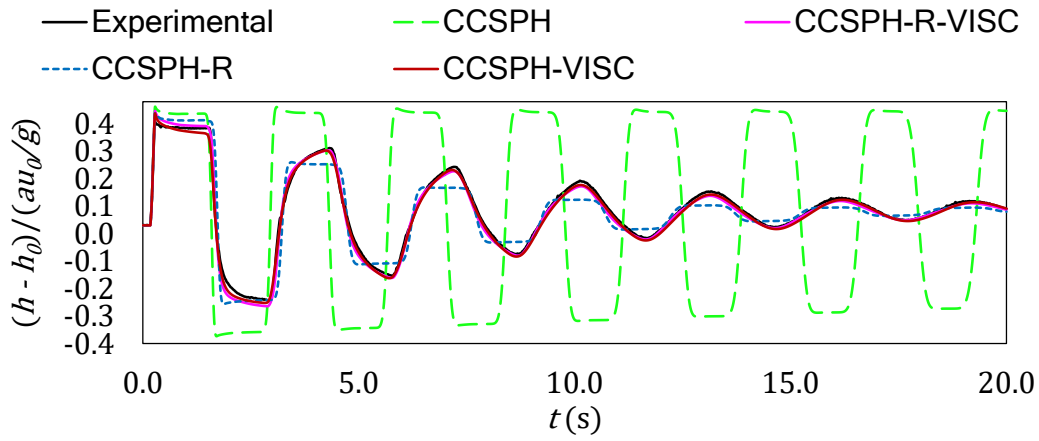

Source: Own Authorship.

The main difference between the viscoelastic and unsteady friction models is the reduced damping at the end of the first wave peak. The laminar flow results visually fit

the experimental data better overall. However, the numerical results in turbulent flow deviate from the experimental damping rate after 10 seconds, likely due to not including a turbulent model.

Figure 7.34: Collected data from experiment VI compared with the outcomes of CCSPH, CCSPH-R-VISC, CCSPH-R,and CCSPH-VISC for $Q = 100810.00 \times 10^{-8}$ m^3/s using $a = 395$ m/s.

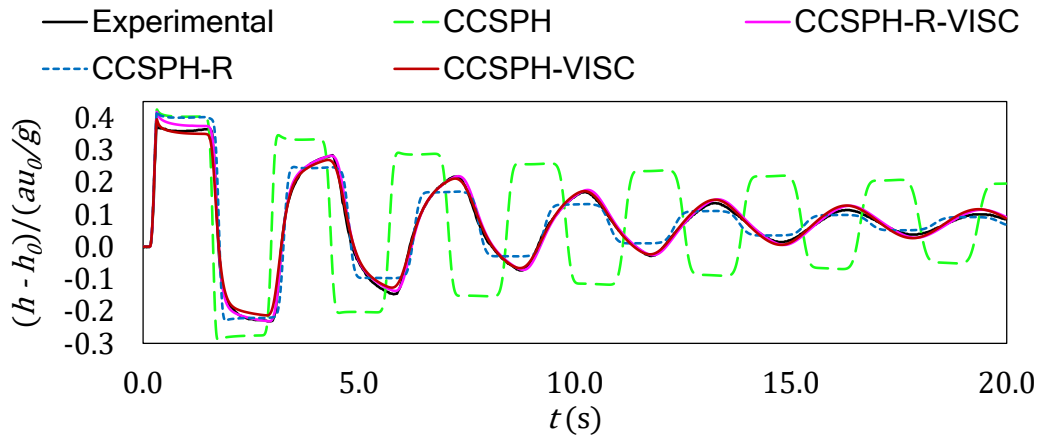

Source: Own Authorship.

Figure 7.35: Collected data from experiment VI compared with the outcomes of MOC, MOC-R-VISC, MOC-R,and MOC-VISC for $Q = 5600.00 \times 10^{-8}$ m^3/s using $a = 395$ m/s.

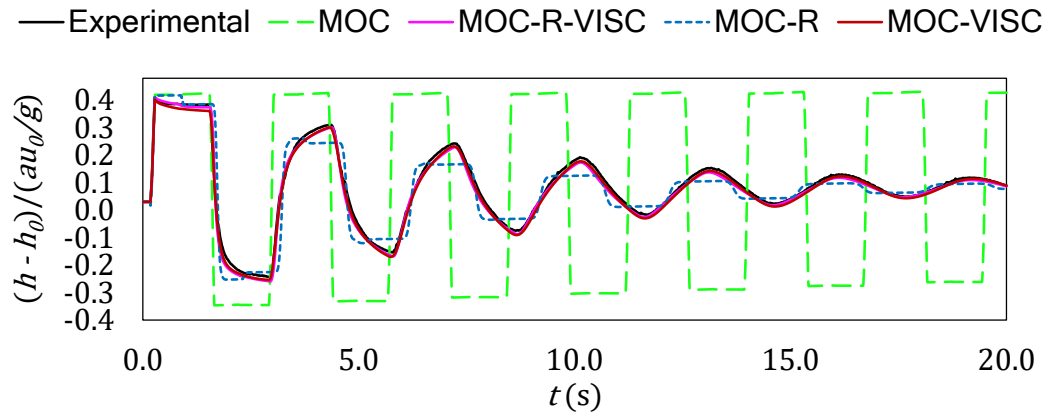

Source: Own Authorship.

The MASE values in Tables 7.8 and 7.9 show that CCSPH-based models are more accurate than MOC-based methods, though the difference is minimal. CCSPH models have an average computational time of about 1.30 seconds, compared to 2.00 seconds for MOC models, which is not significant. These simulations were run on a Windows 11

laptop with an Intel(R) Core(TM) i5-8265U CPU (1.60 to 1.80 GHz) and 12 GB RAM. The code used is entirely written in C++.

Figure 7.36: Collected data from experiment VI compared with the outcomes of MOC, MOC-R-VISC, MOC-R,and MOC-VISC for $Q = 100810.00 \times 10^{-8}$ m^3/s using $a = 395$ m/s.

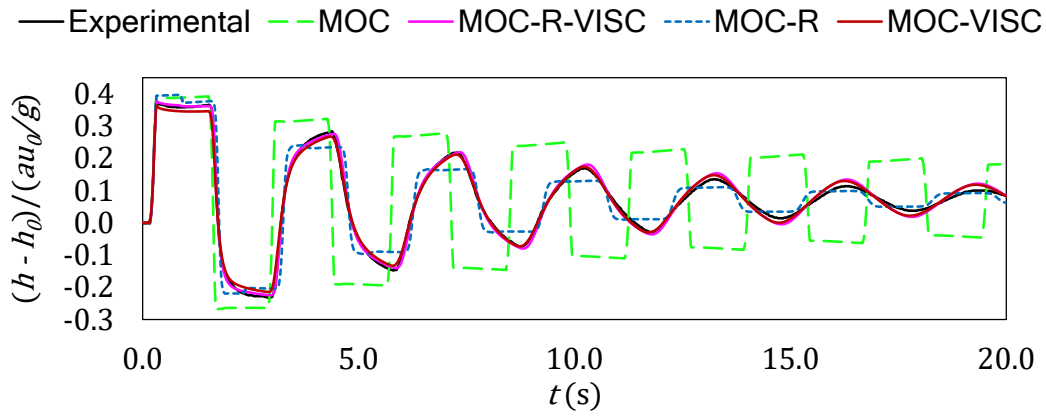

Source: Own Authorship.

CONCLUSION

The current work goal was to apply the CSPH method coupled with transient friction and viscoelastic models to hydraulic transient problems and then analyze the critical numerical parameters using the response surface methodology.

The CSPH model, when applied alongside unsteady friction models, successfully captures the damping ratio of pressure waves but tends to underestimate wave speed, leading to a rightward deviation from experimental observations. Detailed analysis indicated that the normalization process employed in the CSPH framework, intended to mitigate numerical boundary errors, modifies particle volume. This alteration results in a shift in density distribution within the computational domain while maintaining a constant mass, ultimately artificially influencing the momentum of fluid particles. This phenomenon is identified as the primary factor contributing to the underestimation of wave speed.

To address this issue, we introduced a momentum conservation correction, aiming to rectify the artificial momentum change stemming from the density shifts induced by the CSPH adjustments, culminating in developing the CCSPH model. This new model retains the boundary correction capabilities of CSPH, effectively reducing unphysical numerical oscillations while simultaneously correcting its adverse impact on density and momentum conservation.

The CCSPH model demonstrates improved accuracy in wave speed estimation when coupled with unsteady friction models. However, it is crucial to note that this enhanced accuracy is only observed within the temporal framework established by Vardy and Brown (1995), Vardy and Brown (2003), Ghidaoui and Kolyshkin (2001), and Ghidaoui et al. (2002). Beyond this timeframe, inaccuracies arise due to the diffusion of turbulence structures present in the experimental setup, which the current model does not account for, leading to discrepancies in both damping ratio and wave celerity outcomes.

The MOC code, along with unsteady friction models, was validated against experimental data, showing behavior similar to CSPH. Moreover, Ramos et al. (2004)'s model required a minimal K_1 value for optimal fit, which caused numerical instabilities. By adjusting the input wave speed to match the correction in CCSPH, MOC achieved better accuracy across all unsteady friction models, and the coefficients in Ramos et al. (2004)'s model were more stable.

Ramos et al. (2004)'s model exhibited superior accuracy in most experiments, attributed to its unique capability to control local and advective acceleration separately. The analysis of numerical parameters' influence enhanced the models' understanding and provided practical insights. It revealed that well-calibrated coefficients in the model

proposed by Ramos et al. (2004) enabled them to depict experimental data accurately, even beyond the point where vorticity diffused to the pipe's core.

The RSM was used to analyze experimental data and optimize numerical parameters. This approach effectively highlighted how various factors influence numerical results, especially their interactions. Notably, the interaction between parameters α and K_2 significantly affects diffusion in the CCSPH framework, resulting in the attenuation of pressure waves as their effects accumulate.

The parameter K_1 significantly affected wave speed estimation, leading to noticeable changes in wave outcomes. The parameter κ was the most influential factor, primarily because it determines the particle neighbor count, regulating the spatial information available to each particle. This information flow is essential for numerical stability and other dynamics in the simulation.

The CCSPH method was evaluated for simulating water hammer in viscoelastic pipes. The viscoelastic model by Covas et al. (2005) was integrated with the CCSPH code and tested against experimental data from laminar and turbulent flows. The results were accurate, successfully estimating the damping ratio, wave speed, and waveform. Additionally, combining the viscoelastic model with the unsteady friction model from Ramos et al. (2004) yielded similar accuracy.

The evaluation of the MOC code, along with the viscoelastic and unsteady friction models, demonstrated performance similar to that of CCSPH. This was anticipated, given MOC's historical use in water hammer problems and the study of Covas et al. (2005). However, CCSPH proved competitive with MOC regarding both accuracy and computational time.

Building on the findings from this dissertation, several promising directions for future research are worth exploring. One key avenue is the simulation of scenarios where particles can move freely within the numerical domain, which could provide more realistic behavior in fluid dynamics.

In addition to that, three specific approaches are particularly interesting:

1. A development of a three-dimensional version of the SPH method combined with turbulence models.
2. An extension of the CCSPH or SPH with ghost particles, both with unsteady friction models, to tackle intricate water distribution systems made of plastic pipes, which would require a viscoelastic model.
3. Lastly, an inverse approach could be pursued. In this method, we could use pressure data collected over time as the input to measure the flow rate in a pipe during a water hammer phenomenon.

REFERENCES

AFSHAR, M. H.; ROHANI, M. Water hammer simulation by implicit method of characteristic. *International Journal of Pressure Vessels and Piping*, v. 85, n. 12, p. 851–859, 2008. Cited in page 11.

ALLAMPALLI, V. et al. High-accuracy large-step explicit runge–kutta (hale-rk) schemes for computational aeroacoustics. *Journal of Computational Physics*, v. 228, n. 10, p. 3837–3850, 2009. Cited in page 69.

ALLIEVI, L. *Teoria generale del moto perturbato dell'acqua nei tubi in pressione*. 1. ed. Rome, Italy: Assoziazione Elettrotecnica Italiana, 1903. Cited 2 times in page 4 and 5.

ALLIEVI, L. *Allgemeine Theorie über fiber die veränderliche veranderliche Bewegung des Wassers in Leitungen*. 1. ed. Berlin, Germany: Springer-Verlag Berlin Heidelberg GmbH, 1909. ISBN 978-3-642-52015-0. Cited 2 times in page 4 and 5.

ALTOMARE, C.; DOMíNGUEZ, J. M.; FOURTAKAS, G. Latest developments and application of sph using dualsphysics. *Computational Particle Mechanics*, v. 9, n. 1, p. 863–866, 2022. Cited in page 2.

ARLT, H. *Experimentelle Untersuchungen über das instationäre, turbulente Reibungsverhalten bei aufgeprägten Druckimpulsen in einer Rohrleitung mit Kreisquerschnitt*. Phd Thesis (PhD Thesis) — Technische Universität Berlin, 1983. Cited in page 34.

AXWORTHY, D. H.; GHIDAOUI, M. S.; MCINNIS, D. A. Extend thermodynamics derivation of energy dissipation in unsteady pipe flow. *Journal of Hydraulic Engineering*, v. 126, n. 1, p. 276–287, 2000. Cited 3 times in page 6, 31, and 33.

BANKS, H. T.; HU, S.; KENZ, Z. R. A brief review of elasticity and viscoelasticity for solids. *Advances in Applied Mathematics and Mechanics*, v. 3, n. 1, p. 1–51, 2010. Cited 2 times in page 39 and 40.

BENTLEY, J. L. Multidimensional binary search trees used for associative searching. Association for Computing Machinery, New York, NY, USA, v. 18, n. 9, 1975. ISSN 0001-0782. Cited in page 61.

BERGANT, A. et al. Parameters affecting water-hammer wave attenuation, shape and timing - part 1. *Journal of Hydraulic Research*, v. 46, n. 3, p. 373–381, 2008. Cited in page 10.

BERGANT, A. et al. Parameters affecting water-hammer wave attenuation, shape and timing - part 2. *Journal of Hydraulic Research*, v. 46, n. 3, p. 382–391, 2008. Cited in page 10.

BOLTZMANN, L. E. Zur theorie der elastischen nachwirkung. *Sitzungsberichte Kaiserliche Akademie Wissenhaft Wien Mathematische-Naturwissenhaft*, v. 70, p. 275–306, 1874. Cited 2 times in page 7 and 39.

BRUNONE, B.; GOLIA, U. M. Improvements in modelling of water hammer and cavitating flow in pipes: Experimental verification. In: *22nd Convegno Nazionale di Idraulica e Costuzioni Idrauliche*. Italian: [s.n.], 1990. p. 147–160. Cited 3 times in page 14, 12, and 33.

BRUNONE, B.; GOLIA, U. M.; GRECO, M. Modeling of fast transients by numerical methods. In: *Proceedings of International Conference on Hydraulic Transients with Water Column Separation, IAHR-Group*. Delft, The Netherlands: [s.n.], 1991a. p. 273–280. Cited 3 times in page 1, 12, and 33.

BRUNONE, B.; GOLIA, U. M.; GRECO, M. Some remarks on the momentum equation for fast transients. In: *Proceedings of International Conference on Hydraulic Transients with Water Column Separation, IAHR-Group*. Delft, The Netherlands: [s.n.], 1991b. p. 201–209. Cited 5 times in page 1, 6, 7, 12, and 33.

BRUNONE, B. et al. Velocity profiles and unsteady pipe friction in transient flow. *Journal of Water Resources Planning and Management*, v. 126, n. 4, p. 236–244, 2000. Cited in page 36.

BUDINSKI, L. Application of the lbm with adaptive grid on water hammer simulation. *Journal of Hydroinformatics*, v. 18, n. 4, p. 687–701, 2016. Cited in page 11.

BUTCHER, J. C. *Numerical Methods for Ordinary Differential Equations*. 1. ed. New York: John Wiley & Sons, 2008. 187 p. ISBN 978-0-470-72335-7. Cited in page 70.

CARPENTER, R. C. Experiments on waterhammer. *Transactions of the American Society of Mechanical Engineers*, v. 15, n. 1, 1893. Cited in page 4.

CHAUDHRY, M. H. *Applied Hydraulic Transients*. 1. ed. New York: Van Nostrand Reinhold, 1987. Cited in page 5.

CHAUDHRY, M. H. *Applied Hydraylic Transient*. 3. ed. New York, NY, USA: Elsevier, 2014. Cited 5 times in page 1, 14, 20, 23, and 25.

CHEN, J. K.; BERAUN, J. E.; CARNEY, T. C. A corrective smoothed particle method for boundary value problems in heat conduction. *International Journal for Numerical Methods in Engineering*, v. 46, n. 1, p. 231–252, 1999. Cited 3 times in page 12, 48, and 65.

CHENG, Y.-G.; ZHANG, S.-H.; CHEN, J.-Z. Waterr hammer simulation by the lattice boltzmann method. *Transactions of the Chinese Hydraulic Engineering Society - Journal of Hydraulic Engineering*, v. 6, n. 1, p. 25–31, 1998. Cited in page 11.

COOLEY, J. W.; TUKEY, J. W. An algorithm for the machine calculation of complex fourier series. *Mathematics of Computation*, v. 19, n. 1, p. 297–301, 1965. Cited in page 93.

COURANT, R.; HUBERT, D. *Methods of Mathematical Physics*: Volume ii. [S.l.]: John Wiley & Sons, 1962. ISBN 0-471-50439-4. Cited in page 9.

COURANT, R.; HUBERT, D. *Methods of Mathematical Physics: Volume II*: Partial differential equations. 2. ed. New York, United States of America: John Wiley & Sons, 1989. Cited in page 72.

COVAS, D. I. et al. The dynamic effect of pipe-wall viscoelasticity in hydraulic transients. part ii - model development, calibration and verification. *Journal of Hydraulic Research*, v. 43, n. 1, p. 56–70, 2005. Cited 14 times in page 4, 8, 9, 10, 1, 7, 79, 80, 81, 82, 87, 88, 126, and 132.

COVAS, D. I. et al. The dynamic effect of pipe-wall viscoelasticity in hydraulic transients. part i - experimental analysis and creep characterization. *Journal of Hydraulic Research*, v. 42, n. 5, p. 517–532, 2004. Cited 3 times in page 1, 8, and 80.

COVAS, D. I. C. *Inverse Transient Analysis for Leak Detection and Calibration of Water Pipe Systems Modelling Special Dynamic Effects*. Phd Thesis (PhD Thesis) — Imperial College of Science, Technology and Medicine, 2003. Cited 5 times in page 25, 26, 27, 74, and 77.

DAILY, J. W. et al. Resistance coefficients for accelerated and decelerated flows through smooth tubes and orifices. *Trans. ASME*, v. 78, n. 1, p. 1071–1077, 1956. Cited 3 times in page 6, 30, and 33.

DAS, D.; ARAKERI, J. H. Transition of unsteady velocity profiles with reverse flow. *Journal of Fluid Mechanics*, v. 374, p. 251–283, 1998. Cited in page 36.

DUAN, H.-F. et al. Unsteady friction and visco-elasticity in pipe fluid transients. *Journal of Hydraulic Research*, v. 48, n. 3, p. 354–362, 2010. Cited in page 9.

DUISTERMAAT, J. J.; KOLK, J. A. C. *Distributions*: Theory and applications. 1. ed. Boston: Birkhäuser, 2010. ISBN 978-0-8176-4675-2. Cited in page 49.

FRANKE, P. G.; SEYLER, F. Computation of unsteady pipe flow with respect to visco-elastic material properties. *Journal of Hydraulic Research*, v. 21, n. 5, p. 345–353, 1983. Cited in page 8.

FRIZELL, J. P. Pressure resulting from changes of velocity of water in pipes. *Transactions of the American Society of Civil Engineers*, v. 39, n. 1, p. 1–18, 1898. Cited in page 4.

FULK, D. A. *A numerical analysis of smoothed particle hydrodynamics*. Phd Thesis (PhD Thesis) — School of Engineering, 1994. Cited in page 55.

GALLY, M.; GUNEY, M.; RIEUTFORD, E. An investigation of pressure transients in viscoelastic pipes. *Journal of Fluids Engineering, Transactions of the American Society of Mechanical Engineers*, v. 101, n. 1, p. 495–499, 1979. Cited 2 times in page 7 and 8.

GHIDAOUI, M. S.; KARNEY, B. W. Equivalent differential equations in fixed?grid characteristics method. *Journal of Hydraulic Engineering*, v. 120, n. 10, p. 1159–1175, 1994. Cited in page 10.

GHIDAOUI, M. S.; KARNEY, B. W.; MCINNIS, D. A. Energy estimates for discretization errors in water hammer problems. *Journal of Hydraulic Engineering*, v. 124, n. 4, p. 384–393, 1998. Cited in page 10.

GHIDAOUI, M. S.; KOLYSHKIN, A. A. Stability analysis of velocity profiles in water-hammer flows. *Journal of Hydraulic Engineering*, v. 127, p. 499–512, 2001. Cited 3 times in page 6, 36, and 131.

GHIDAOUI, M. S.; MANSOUR, S. G. S.; ZHAO, M. Applicability of quasisteady and axisymmetric turbulence models in water hammer. *Journal of Hydraulic Engineering*, v. 128, p. 917–924, 2002. Cited 4 times in page 36, 37, 111, and 131.

GHIDAOUI, M. S. et al. A review of water hammer theory and practice. *Applied Mechanics Review, Trans ASME*, v. 58, p. 49–76, 2005. Cited 9 times in page 1, 2, 6, 7, 9, 27, 30, 36, and 111.

GINGOLD, R. A.; MONAGHAN, J. J. Smoothed particle hydrodynamics: theory and application to non-spherical stars. *Mon. Not. R. Astron. Soc.*, v. 181, n. 3, p. 375–89, 1977. Cited 6 times in page 3, 48, 55, 57, 58, and 68.

GOLDBERG, D. E.; WYLIE, E. B. Characteristics method using time-line interpolation. *Journal of Hydraulic Engineering*, v. 109, n. 5, p. 670–683, 1983. Cited in page 10.

GOMEDE, E. *The Fourier Transform and its Application in Machine Learning*. 2023. Available at: <https://medium.com/the-modern-scientist/the-fourier-transform-and-its-application-in-machine-learning-edecfac4133c>. Cited in page 94.

GONG, J. et al. Determination of the creep function of viscoelastic pipelines using system resonant frequencies with hydraulic transient analysis. *Journal of Hydraulic Engineering*, v. 142, n. 9, p. 04016023, 2016. Cited in page 9.

GRAY, C. A. M. The analysis of the dissipation of energy in water hammer. *Proceedings of the American Society of Civil Engineers*, v. 79, p. 1176, 1953. Cited in page 9.

HE, S.; JACKSON, J. D. A study of turbulence under conditions of transient flow in a piper. *Journal of Fluid Mechanics*, v. 408, p. 1–38, 2000. Cited in page 36.

HEIDEMAN, M. T.; JOHNSON, D. H.; BURRUS, C. S. Gauss and the history of the fast fourier transform. *Institute of Electrical and Electronics Engineers Audio and Acoustic Signal Processing (IEEE AASP) Magazine*, v. 1, n. 4, p. 14–21, 1984. Cited in page 93.

HENCKY, H. Über die form des elastizitätsgesetzes bei ideal elastischen stoffen. *Zeitschrift für technische Physik*, v. 9, p. 215–220, 1928. Available at: <https://www.uni-due.de/imperia/md/content/mathematik/ag_neff/hencky1928.pdf>. Cited in page 20.

HIRSCHMANN, P. Das impedanzenverfahren mit beruecksichtigung von rohrreibung und visko-elastischem materialverhalten. In: *Mitteilungen aus Hydraulik und Gewaesserkunde der TUM*. Munich: [s.n.], 1978. p. 1–39. Cited in page 8.

HIRSCHMANN, P. Resonanz in visko-elstischen druckleitungen. In: *Mitteilungen aus Hydraulik und Gewaesserkunde der TUM*. Munich: [s.n.], 1979. Cited in page 8.

HOPP-HIRSCHLEY, M.; NIEKEN, U. Fully implicit time integration in truly incompressible sph. *The European Physical Journal Special Topics*, v. 227, n. 1, p. 1501–1514, 2019. Cited in page 68.

HOU, Q. et al. Simulating water hammer with corrective smoothed particle method. In: *BHR Group - 11th International Conferences on Pressure Surges*. Lisbon, Portugal: [s.n.], 2012. p. 171–187. ISBN 978-1-85598-133-1. Cited 3 times in page 2, 12, and 83.

HOU, Q. et al. Lagrangian modelling of fluid transients in pipelines with entrapped air. In: *BRH Group - 12th International Conference on Pressure Surges*. Dublin, Ireland: [s.n.], 2015. p. 215–228. ISBN 978-1-51081-718-0. Cited in page 12.

HOU, Q. et al. Rapid filling of pipelines with the sph particle method. *Procedia Engineering*, v. 31, n. 1, p. 38–43, 2012. ISSN 1877-7058. International Conference on Advances in Computational Modeling and Simulation. Available at: <https://www.sciencedirect.com/science/article/pii/S1877705812010119>. Cited in page 12.

HYNDMAN, R. J.; KOEHLER, A. B. Another look at measures of forecast accuracy. *International Journal of Forecasting*, v. 22, n. 4, p. 679–688, 2006. Cited in page 89.

HöRMANDER, L. *The analysis of linear partial differential operators I*: Distribution theory and fourier analysis. New York: Springer, 1998. (Grundlehren der mathematischen Wissenschaften). ISBN 978-3-642-96750-4. Cited in page 49.

ISERLES, A. *A First Course in the Numerical Analysis of Differential Equations*. 1. ed. London: Cambridge University Press, 1996. 39 p. ISBN 978-0-521-55655-2. Cited in page 70.

JAEGER, C. *Theorie Generale du Coup de Belier*: Application au calcul des conduites a carateristiques multiples et des chambres d'equilibre. 1. ed. Paris: Dunod, 1933. Cited in page 5.

JANG, T. U. et al. Efficient quasi-two-dimensional water hammer model on a characteristic grid. *Journal of Hydraulic Engineering*, v. 142, n. 2, p. 06016019, 2016. Cited in page 11.

JOU, D.; CASAS-VáZQUEZ, J.; LEBON, G. *Extend irreversible thermodynamics*. 4. ed. [S.l.]: Springer, 2010. ISBN 978-90-481-3073-3. Cited 2 times in page 30 and 33.

JOUKOWSKI, N. E. Memoirs of the imperial academy society of st. petersburg. *Proc. American Water Works Association*, v. 24, n. 1, p. 341–424, 1898. Cited in page 4.

JUNG, B. S.; BOULOS, P. F.; WOOD, D. J. Impacts of skeletonization on distribution system hydraulic transient models. In: KABBES, K. C. (Ed.). *World Environmental and Water Resources Congress 2007: Restoring Our Natural Habitat*. Tampa, Florida, United States: [s.n.], 2007. p. 1–10. ISBN 978-0-78440-927-5. Cited in page 1.

JUNIOR, J. F.; VASCO, J. R. G.; SOARES, A. K. Classical transient pipe flow analysis with sph method. In: *XLI Ibero-Latin American Congress on Computational Methods in Engineering: XLI CILAMCE*. Foz do Iguaçu, Parana, Brazil: [s.n.], 2020. p. 1–7. Cited 2 times in page 2 and 12.

KARNEY, B. W.; GHIDAOUI, M. S. Flexible discretization algorithm for fixed-grid moc in pipelines. *Journal of Hydraulic Engineering*, v. 123, n. 11, p. 1004–1011, 1997. Cited in page 10.

KAY, S. M. *Fundamentals of Statistical Signal Processing*: Estimation theory. 1. ed. Upper Saddle River, RJ: Prentice Hall, 1993. ISBN 978-0-13-345711-7. Cited in page 93.

KHORASANIZADE, S.; SOUSA, J. M. M. Improving linked-lists using tree search algorithms for neighbor finding in variable-resolution smoothed particle hydrodynamics. *Communications in Computational Physics*, v. 26, n. 1, p. 57–86, 2019. Cited 2 times in page 59 and 61.

KHURI, A. I.; CORNELL, J. A. *Response Surfaces*: Designs and analyses. 2. ed. [S.l.]: Marcel Dekker, 1996. Cited in page 92.

KUMAR, C. *Development of Efficient Radar Pulse Compression Technique for Frequency Modulated Pulses*. 2014. Available at: <https://core.ac.uk/download/53190479.pdf>. Cited in page 95.

LAI, C. Comprehensive method of characteristics models for flow simulation. *Journal of Hydraulic Engineering*, v. 114, n. 9, p. 1074–1097, 1988. Cited in page 10.

LAI, C. A. *Study of Water Hammer Including Effect of Hydraulic Losses*. Phd Thesis (PhD Thesis) — The University of Michigan, 1961. Cited in page 9.

LIBERSKY, L. D. et al. Strain lagrangian hydrodynamics: a three-dimensional sph code for dynamic material response. *Journal of Computational Physics*, v. 109, n. 1, p. 67–75, 1993. Cited in page 48.

LISTER, M. The numerical solutions of hyperbolic partial differential equations by the method of characteristics. In: RALSTON, A.; WILD, H. S. (Ed.). *In Mathematical Methods for Digital Computers*. New York, NY, USA: John Wiley, 1960. p. 165–179. Cited 2 times in page 9 and 10.

LIU, G. R.; LIU, M. B. *Smoothed Particle Hydrodynamics*: a meshfree particle method. 1. ed. Singapore: World Scientific, 2003a. ISBN 981-238-456-1. Cited 10 times in page 48, 50, 52, 54, 58, 59, 61, 62, 64, and 67.

LIU, M. B.; LIU, G. R. Restoring particle consistency in smoothed particle hydrodynamics. *Applied Numerical Mathematics*, v. 56, n. 1, p. 19–36, 2006. Cited in page 48.

LIU, M. B. et al. Computer simulation of high explosive explosion using smoothed particle hydrodynamics methodology. *Computers & Fluids*, v. 32, n. 3, p. 305–322, 2003a. Cited in page 2.

LOUATI, M.; Mahdi Tekitek, M.; Salah Ghidaoui, M. On the dissipation mechanism of lattice boltzmann method when modeling 1-d and 2-d water hammer flows. *Computers & Fluids*, v. 193, n. 1, p. 103996, 2019. ISSN 0045-7930. Available at: <https://www.sciencedirect.com/science/article/pii/S004579301830584X>. Cited 2 times in page 11 and 12.

LUCY, L. B. A numerical approach to the testing of the fission hypothesis. *Astron. J.*, v. 82, p. 1013–1024, 1977. Cited 5 times in page 3, 48, 55, 57, and 68.

MARTINS, N. M. C. et al. Cfd modeling of transient flow in pressurized pipes. *Computers and Fluids*, v. 126, n. 1, p. 129–140, 2016. Cited 9 times in page 4, 26, 79, 80, 81, 82, 85, 87, and 99.

MEIßNER, E. Das impulsantwortverfahren—ein mathematisches modell zur berechnung instationärer strömungsvorgänge in druckleitungen. *Forsch Ing-Wes*, v. 43, n. 1, p. 115–125, 1977. Cited in page 8.

MENABREA, L. F. Note sur les effects de choc de l'eau dans les conduites. *Comptes rendus de l'Académie des Sciences*, v. 47, n. 1, p. 221–224, 1858. Cited in page 4.

MICHAUD, J. Coups de bélier dans les conduites. Étude des moyens employés pour en atteneur les effects. *Bulletin de la Société vaudoise des ingénieurs et des architectes*, v. 4, n. 3, p. 56–64, 1878. Cited in page 4.

MONAGHAN, J. J. Shock simulation by the particle method sph. *Journal of Computational Physics*, v. 52, p. 374–389, 1983. Cited in page 48.

MONAGHAN, J. J. On the problem of penetration in particle methods. *Journal of Computational Physics*, v. 82, n. 1, p. 1–15, 1989. Cited in page 64.

MONAGHAN, J. J. Smoothed particle hydrodynamics. *Annual Review of Astronomy and Astrophysics*, v. 30, n. 1, p. 543–574, 1992. Cited 3 times in page 48, 55, and 64.

MONAGHAN, J. J. Simulating free surface flows with sph. *Journal of Computational Physics*, v. 110, p. 399–406, 1994. Cited in page 67.

MONAGHAN, J. J.; LATTANZIO, J. C. A refined particle method for astrophysical problems. *Astronomy and Astrophysics*, v. 149, n. 1, p. 135–143, 1985. Cited 2 times in page 3 and 58.

MONTGOMERY, D. C. *Design and analysis of experiments*. 8. ed. New York: John Wiley & Sons, 2013. 478-544 p. ISBN 978-1118-14692-7. Cited 2 times in page 81 and 90.

MYERS, R. H.; MONTGOMERY, D. C.; ANDERSON-COOK, C. M. *Response Surface Methodology*: Process and product optimization using designed experiments. 3. ed. New York: John Wiley & Sons, 2009. Cited in page 91.

NEJAD-ASGHAR, M.; KHESALI, A. R.; SOLTANI, J. Artificial viscosity in simulation of shock waves by smoothed particle hydrodynamics. *Astrophysics and Space Science*, v. 313, n. 4, p. 425–430, 2008. Cited in page 64.

PAL, S.; HANMAIAHGARI, P. R.; KARNEY, B. W. An overview of the numerical approaches to water hammer modelling: The ongoing quest for practical and accurate numerical approaches. *Water*, v. 13, n. 1, p. 1597, 2021. Cited 3 times in page 2, 10, and 11.

PALYANOV, A.; KHAYRULIN, S.; LARSON, S. D. Application of smoothed particle hydrodynamics to modeling mechanisms of biological tissue. *Advances in Engineering Software*, v. 98, n. 1, p. 1–11, 2016. Cited in page 2.

PAN, T. et al. Smoothed particle hydrodynamics with unsteady friction model for water hammer pipe flow. *Journal of Hydraulic Engineering*, v. 148, n. 2, p. 04021057, 2022. Available at: <https://ascelibrary.org/doi/abs/10.1061/%28ASCE%29HY.1943-7900.0001966>. Cited 2 times in page 2 and 12.

PARMAKIAN, J. *Water-Hammer Analysis*. 1. ed. New York: Dover Publications, Inc., 1963. Cited in page 5.

PERKINS, F. E. et al. *Hydro-Power Plant Transients, Part II*. Cambridge, MA, USA, 1964. Cited in page 10.

PRESS, W. H. et al. *Numerical Recipes*: The art of scientific computing. 3. ed. Cambridge, England: Cambridge University Press, 2007. Cited 2 times in page 93 and 95.

PROAKIS, J. G.; SALEHI, M. *Communication Systems Engineering*. 2. ed. Upper Saddle River, New Jersey: Prentice Hall, Inc, 2002. ISBN 0-13-095007-6. Cited in page 97.

RAMOS, H. et al. Surge damping analysis in pipe systems: modelling and experiments. *Journal of Hydraulic Research*, v. 42, n. 4, p. 413–425, 2004. Cited 17 times in page 8, 9, 10, 14, 1, 6, 7, 33, 63, 75, 76, 82, 83, 99, 116, 131, and 132.

RAPP, B. E. Chapter 10 - conservation of mass: The continuity equation. In: RAPP, B. E. (Ed.). *Microfluidics: Modelling, Mechanics and Mathematics*. Oxford: Elsevier, 2017, (Micro and Nano Technologies). p. 265–271. ISBN 978-1-4557-3141-1. Available at: <https://www.sciencedirect.com/science/article/pii/B9781455731411500101>. Cited in page 16.

READ, J. I.; HAYFIELD, T.; AGERTZ1, O. Resolving mixing in smoothed particle hydrodynamics. *Monthly Notices of the Roayal Astronomical Society*, v. 405, n. 1, p. 1513–1530, 2010. Cited in page 65.

RIANDE, E. et al. *Polymer Viscoelasticity*: Stress and strain in practice. 1. ed. Basel, New York, United States: Marcel Dekker, Inc., 2000. Cited in page 1.

RICH, G. R. Water-hammer analysis by the laplace-mellin transformations. *Transactions of the American Society of Mechanical Engineers*, v. 67, n. 5, p. 361–368, 1945. Cited in page 5.

RIEUTORD, E.; BLANCHARD, A. Pulsating viscoelastic pipe flow - water-hammer. *Journal of Hydraulic Research*, v. 17, n. 3, p. 217–229, 1979. Cited 3 times in page 1, 7, and 8.

SCHöNFELD, J. C. Resistance and inertia of the flow of liquids in a tube or open canal. *Appl. Sci. Res.*, v. 169, n. 1, 1949. Cited 4 times in page 5, 7, 8, and 28.

SHAW, M. T.; MACKNIGHT, W. J. *Introduction to polymer viscoelasticity*. 3. ed. Canada: John Wiley & Sons, Inc., 2005. ISBN 978-0-471-74045-2. Cited 3 times in page 1, 7, and 40.

SHIMADA, M. et al. Time-line interpolation errors in pipe networks. *Journal of Hydraulic Engineering*, v. 132, n. 3, p. 294–306, 2006. Cited in page 10.

SHIMIZU, Y.; KHAYYER, A.; GOTOH, H. An implicit sph-based structure model for accurate fluid–structure interaction simulations with hourglass control scheme. *European Journal of Mechanics / B Fluids*, v. 96, n. 1, p. 122–145, 2022. Cited in page 68.

SHUTOV, A.; KLYUCHANTSEV, V. On the application of sph to solid mechanics. In: *All-Russian Conference and School for Young Scientists, devoted to 100th Anniversary of Academician*. Novosibirsk, Russian Federation: Journal of Physics: Conference Series - IOP Publishing Ltd, 2019. v. 1268, p. 012077. Cited in page 2.

SHUY, E. B. Wall shear stress in accelerating and decelerating turbulent pipe flows. *Journal of Hydraulic Research*, v. 34, n. 2, p. 173–183, 1997. Cited in page 6.

SIBETHEROS, I. A.; HOLLEY, E. R.; BRANSKI, J. M. Spline interpolations for water hammer analysis. *Journal of Hydraulic Engineering*, v. 117, n. 10, p. 1332–1351, 1991. Cited in page 10.

SIGALOTTI, L. D. G.; KLAPP, J.; GESTEIRA, M. G. The mathematics of smoothed particle hydrodynamics (sph) consistency. *Front. Appl. Math. Stat.*, v. 7, n. 797455, 2021. Cited 6 times in page 48, 50, 53, 64, 65, and 66.

SMITH, J. O. *Spectral Audio Signal Processing*. 1. ed. Upper Saddle River, New Jersey: W3K Publishing, 2011. ISBN 978-0-9745607-3-1. Cited 4 times in page 93, 94, 95, and 96.

SOARES, A. K.; COVAS, D. I.; REIS, L. F. Analysis of pvc pipe-wall viscoelasticity during water hammer. *Journal of Hydraulic Engineering*, v. 134, n. 9, p. 1389–1394, 2008. Available at: <https://ascelibrary.org/doi/abs/10.1061/%28ASCE%290733-9429%282008%29134%3A9%281389%29>. Cited in page 1.

SOARES, A. K.; MARTINS, N. M. C.; COVAS, D. I. C. Transient vaporous cavitation in a horizontal copper pipe. *Journal of Hydraulic Research*, Taylor & Francis, v. 55, n. 5, p. 731–736, 2017. Cited 8 times in page 4, 79, 80, 81, 82, 85, 86, and 99.

SONG, W. et al. Development of smoothed particle hydrodynamics based water hammer model for water distribution systems. *Engineering Applications of Computational Fluid Mechanics*, v. 17, n. 1, p. 2171139, 2023. Cited 2 times in page 2 and 13.

STREETER, V. L. Valve stroking to control water hammer. *Journal of the Hydraulics Division*, v. 89, n. 2, p. 39–66, 1963. Cited in page 9.

STREETER, V. L.; LAI, C. Water-hammer analysis including fluid friction. *Transactions of the American Society of Civil Engineers*, v. 128, n. 1, p. 1491–1524, 1963. Cited 2 times in page 5 and 9.

STREETER, V. L.; WYLIE, E. B. *Hydraulic Transients*. 1. ed. New York: McGraw-Hill, 1967. Cited in page 5.

SUO, L.; WYLIE, E. B. Impulse response method for frequency-dependent pipeline transients. *Journal of Fluids Engineering*, v. 111, n. 4, p. 478–483, 1989. Cited in page 8.

SUO, L.; WYLIE, E. B. Complex wavespeed and hydraulic transients in viscoelastic pipes. *Journal of Fluids Engineering*, v. 112, n. 4, p. 496–500, 1990. Cited in page 8.

SWAMEE, P. K. Design of submarine oil pipeline. *Journal of Transportation Engineering*, v. 119, n. 1, p. 159–170, 1993. Cited in page 27.

SZEWC, K. et al. A study on application of smoothed particle hydrodynamics to multi-phase flows. *International Journal of Nonlinear Sciences and Numerical Simulation*, v. 13, n. 6, p. 383–395, 2012. Cited in page 2.

THORLEY, A. R. D. *Fluid Transients in Pipeline Systems*: A guide to the control and suppression of fluid transients in liquids in closed conduits. 1. ed. London, England: D. and L. George Ltd, 1991. Cited 2 times in page 14 and 23.

TIAN, W. et al. Numerical simulation and optimization on valve-induced water hammer characteristics for parallel pump feedwater system. *Annals of Nuclear Energy*, v. 35, n. 12, p. 2280–2287, 2008. Cited in page 10.

TODD, R. M.; CRUZ, J. Frequency estimation and the qd method. *Control and Dynamic Systems*, v. 75, n. 1, p. 1–78, 1996. Cited in page 97.

TRIKHA, A. K. An efficient method for simulating frequency-dependent friction in transient liquid flow. *Journal of Fluids Engineering, Trans ASME*, v. 97, p. 97–105, 1975. Cited 4 times in page 11, 16, 7, and 34.

VARDY, A. E. On the use of the method of characteristics for the solution of unsteady flows in networks. In: *In Proceedings of the 2nd International Conference on Pressure Surges, BHRA Fluid Engineering*. City University, London, UK: [s.n.], 1976. p. 22–24. Cited in page 10.

VARDY, A. E. On sources of damping in water-hammer. *Water*, v. 15, n. 3, p. 385, 2023. Cited in page 9.

VARDY, A. E.; BROWN, J. M. B. Transient, turbulent, smooth pipe friction. *Journal of Hydraulic Research*, v. 33, n. 4, p. 435–436, 1995. Cited 6 times in page 7, 36, 37, 38, 111, and 131.

VARDY, A. E.; BROWN, J. M. B. Discussion on wall shear stress in accelerating and decelerating pipe flow. *Journal of Hydraulic Research*, v. 35, n. 1, p. 137–139, 1997. Cited 2 times in page 6 and 7.

VARDY, A. E.; BROWN, J. M. B. Transient turbulent friction in smooth pipe flows. *Journal of Sound and Vibration*, v. 259, n. 5, p. 1011–1036, 2003. Cited 7 times in page 11, 7, 36, 37, 38, 111, and 131.

VARDY, A. E.; HWANG, K.-L. A weighting function model of transient turbulent pipe friction. *Journal of Hydraulic Research*, v. 31, n. 4, p. 533–548, 1993. Cited 15 times in page 3, 8, 9, 10, 1, 7, 34, 35, 36, 37, 63, 75, 76, 99, and 116.

VITKOVSKY, J. P. et al. Advances in unsteady friction modeling in transient pipe flow. In: ANDERSON, A. (Ed.). *Proceedings of 8th International Conference on Pressure Surges, Professional Safe Design and Operation of Industrial Pipe System*. Hague, Netherlands: Engineering Publishing Limited, 2000. p. 471–482. Available at: <http://wiki.loa-cnr.it/Papers/kr10v0.7.pdf>. Accessed on: 25 jan. 2024. Cited 14 times in page 8, 9, 10, 14, 1, 6, 7, 33, 63, 75, 76, 83, 99, and 116.

WESTON, E. B. Description of some experiments made on the province, ri water works to ascertain the force of water ram in pipes. *Transactions of the American Society of Civil Engineers*, v. 14, n. 1, p. 238, 1885. Cited in page 4.

WIGGERT, D. C.; SUNDQUIST, M. J. Fixed-grid characteristics for pipeline transients. *Journal of the Hydraulics Division*, v. 103, n. 12, p. 1403–1416, 1977. Cited in page 10.

WU, K. et al. Energy analysis of a quasi-two-dimensional friction model for simulation of transient flows in viscoelastic pipes. *Water*, v. 14, n. 20, p. 3258, 2022. Cited in page 9.

WU, Y.; CHI, L.; ZHANG, H. Study of resistance distribution and numerical modeling of water hammer in a long-distance water supply pipeline. In: ZYL, K. V. (Ed.). *Water Distribution Systems Analysis 2008*. Kruger National Park, South Africa: [s.n.], 2008. p. 1–10. Cited in page 11.

WYLIE, E. B. Resonance in pressurized piping systems. *Journal of Basic Engineering*, v. 87, n. 4, p. 960–966, 1965. Cited in page 8.

XIAO, Y.-C.; WEI, P.; TAI, H.-M. Autocorrelation-based algorithm for single-frequency estimation. *Signal Processing*, v. 87, n. 6, p. 1224–1233, 2007. Cited in page 97.

XU, F. et al. On methodology and application of smoothed particle hydrodynamics in fluid, solid and biomechanics. *Acta Mechanica Sinica*, v. 39, n. 1, p. 722185, 2023. Cited in page 2.

ZHU, Q.; HERNQUIST, L.; LI, Y. Numerical convergence in smoothed particle hydrodynamics. *The Astrophysical Journal*, The American Astronomical Society, v. 800, n. 1, p. 6, 2015. Cited in page 64.

ZHU, Y.; FOX, P. J. Smoothed particle hydrodynamics model for diffusion through porous media. *Transport in Porous Media*, v. 43, n. 1, p. 441–471, 2001. Cited in page 2.

ZHU, Y.; FOX, P. J. Simulation of pore-scale dispersion in periodic porous media using smoothed particle hydrodynamics. *Journal of Computational Physics*, v. 182, n. 2, p. 622–645, 2002. Cited in page 2.

ZIELKE, W. Frequency-dependent friction in transient pipe flow. *Journal of Basic Engineering, Trans ASME*, v. 90, p. 109–115, 1968. Cited 5 times in page 7, 33, 34, 35, and 37.

ZORICH, V. A. *Mathematical Analysis II*. 5. ed. Berlin Heidelberg, Germany: Springer-Verlag, 2004. Cited in page 20.

ŁUKASZEWICZ, G.; KALITA, P. *Navier–Stokes Equations*: An introduction with applications. 1. ed. Switzerland: Springer International Publishing, 2016. Cited 4 times in page 14, 15, 21, and 24.